High-performance geopolymer and low-carbon cementitious binders using flash-calcined dredged sediments and excavated clays

Ali Alloul

Doctoral School SPI: Engineering Sciences

Doctoral Thesis

To obtain the title of Doctor from the University of Lille awarded by IMT Nord Europe

Specialty: Civil Engineering

Presented and defended by

Ali ALLOUL

High-performance geopolymer and low-carbon cementitious binders using flash-calcined dredged sediments and excavated clays

Thesis date: 17 September 2024

Rapportrice	Siham KAMALI-BERNARD	Professeure, INSA de Rennes
Rapportrice	Naima BELAYACHI	Professeure, Université d'Orléans
Président du jury	Ali ZAOUI	Professeur, Université de Lille
Examinatrice	Elhem GHORBEL	Professeure, CY Cergy Paris Université
Directeur de thèse	Mahfoud BENZERZOUR	Professeur, IMT NORD EUROPE
Codirecteur de thèse	Nor-Edine ABRIAK	Professeur, IMT NORD EUROPE
Encadrant	Mouhamadou AMAR	Enseignant-Chercheur, IMT NORD EUROPE

Laboratoire Génie Civil et géo Environnement (LGCgE)

CERI Matériaux et Procédés, IMT NORD EUROPE

École Doctorate ENGSYS 632 (Univ.Lille, Centrale Lille Institut, IMT Nord Europe)

Abstract

Geopolymer (GP) concrete and low carbon concrete with supplementary cementitious materials (SCMs) are promising solutions to substitute ordinary Portland cement concrete binders. This thesis aims to develop high-performance geopolymer and low-carbon cement concrete using flash-calcined dredged sediments (FCS) and excavated clay materials (FCC). Dredged sediments and excavated materials are widely available and classified as waste materials due to their improper disposal methods. Flash calcination, a heat thermal treatment technique of temperature 750°C is used to eliminate their pollutants, high organic content, and enhance their pozzolanic reactivity, thus enhancing their potential to be used in concrete formulations. These materials are rich in aluminosilicates and can be used as main sources in developing geopolymer binders. Moreover, due to their clayey content they can be used as SCMs in low carbon concrete binders such as limestone flash-calcined clay cement (LFC). The results show that using 16-24 % of FCS and 19-27 % of FCC result in achieving geopolymer binders of high strength and durability with the incorporation of metakaolin and granulated blast furnace slag. For the LFC formulations using 18-26 % of FCS and FCC result in achieving significant strength and durability in comparison to formulations done with metakaolin and to the reference mix done with 100% OPC. The physical, mechanical, microstructural, physicochemical, and durability tests are done on GP and LFC formulations. The formulations done with FCS and FCC result in achieving high performance properties in terms of high strength and durability.

Keywords: High-performance concrete, Geopolymer binders, Limestone calcined clay cement binders (LC3), Dredged sediments, Excavated clays, Flash calcination.

Résumé

Le béton géopolymère et le béton à faible teneur en carbone avec des matériaux cimentaires supplémentaires sont des solutions prometteuses pour remplacer les liants de béton ordinaires au ciment Portland. Cette étude vise à développer des bétons géopolymères haute performance et à faible teneur en carbone en utilisant des sédiments dragués et des matériaux excavés flash-calcinés. Les sédiments dragués et les matériaux excavés sont largement disponibles et classés comme déchets en raison de leurs méthodes d'élimination inappropriées. La flash-calcination, une technique de traitement thermique (750 °C) par la chaleur utilisée pour éliminer leurs polluants, leur teneur élevée en matière organique et améliorer leur réactivité pouzzolanique, améliore ainsi leur potentiel d'utilisation dans les formulations de béton. Ces matériaux sont riches en aluminosilicates et peuvent être utilisés comme sources principales dans le développement de liants géopolymères. De plus, en raison de leur teneur en argile, ils peuvent être utilisés comme matériaux cimentaires supplémentaires dans les liants de béton à faible teneur en carbone tels que le ciment d'argile calcinée au calcaire. Les résultats montrent qu'en utilisant 16 à 24 % de sédiments flash-calcinés et 19 à 27 % d'argiles excavées flash-calcinées, on obtient des liants géopolymères de haute résistance et durabilité avec l'incorporation de métakaolin et de laitier de haut fourneau granulé. Pour les formulations de ciment d'argile calcinée au calcaire, l'utilisation de 18 à 26 % de sédiments dragués flash-calcinés et d'argiles excavées comme argile calcinée permet d'obtenir une résistance et une durabilité significatives par rapport aux formulations réalisées avec du métakaolin et au mélange de référence réalisé avec 100 % de ciment Portland ordinaire. Des tests physiques, mécaniques, microstructuraux, physico-chimiques et de durabilité sont réalisés sur les formulations de béton géopolymère et de ciment d'argile calcinée au calcaire. Les formulations réalisées avec des sédiments dragués et des argiles excavées flash-calcinés permettent d'obtenir des propriétés haute performance en termes de résistance et de durabilité élevées.

<u>Mots-clés</u>: Béton haute performance, Liants géopolymères, Liants cimentaires à base de calcaire et d'argile calcinée (LC3), Sédiments de dragage, Argiles excavées, Calcination flash.

ACKNOWLEDGMENTS

AKNOWLEDGMENTS

First of all, I would like to express my thanks and gratitude for the members of the jury that have agreed to accept reviewing my manuscript. Professor Siham KAMALI-BERNARD of university INSA de Rennes, Professor Naima BELAYACHI of university d'Orleans, president of the jury Professor Ali ZAOUI of university de Lille, Professor Elhem GHORBEL of university CY Cergy Paris.

The work results achieved in this thesis couldn't be done without the help and support of my directors and supervisor. My thesis director Professor Mahfoud BENZEZOUR, I would like to express my gratitude for you for allowing me to be a part of your team and always believing in my work and giving me important feedback that enhanced my knowledge and skills. My thesis co-director Professor Nore-Edine ABRIAK, I would like to thank you for your constant encouragement that allowed me to keep moving forward and giving my best work. A huge thanks and gratitude to my thesis supervisor Doctor Mouhamadou AMAR, you have followed my work step by step and provided me with valuable insights, you have inspired me to be a better researcher and working with you is a great pleasure and I'm honored to have you as my thesis supervisor.

I would like to express my greatest gratitude to my Fiancée Assil Darwish. Thank you for believing in me, your constant support kept me going and allowed me to work hard and focus on my goals. Thank you for everything you have done, your encouragement is very appreciated.

I would like to thank my father and mother for their sacrifices and trusting their son. You have both guided me into this path and made me the man I'm today. I would like to honor both of you by gifting you this achievement and making you feel proud. I would also like to thank my sister Ghida Alloul and her husband Wael Chahine for their constant care and support.

I would like to thank my childhood and best friends Rawad, Ouss, Hadi, and Hassan for their support, you always made things easier for me, so thanks a lot for your encouragement. A special thanks to my small family in Douai: Fatima, Aadel, Mohammad, Zeinab, Hassan, Ghinna, Ahmad, Douaa, Ibrahim, Tamara, Raafa, and Salwa. I would also like to thank my friend Hussein for his constant help.

I would like to thank all my colleagues and technicians at IMT NORD EUROPE for their help and advice. Bader, Elie, Miguelli, Janna, and Joelle, thank you all.
I would like to express my greatest gratitude and help for everyone who helped and supported me during my thesis period. I would like to wish you all the best in your future work.

Best Regards to you all

Summary

Table of Contents

Table of Figures

Tables of Tables

General Introduction

General Introduction

Ordinary Portland cement (OPC) is the most used type of cement in the world and is a key ingredient in concrete which is used in the construction of modern buildings and bridges [1]. It is produced by grinding together a mixture of limestone and clay, and then heating it in a kiln at high temperatures (~1450°C) to produce a material known as clinker. This clinker is then ground into a fine powder and mixed with gypsum to produce the final cement product. The production of OPC is known to have significant environmental impacts. The process of heating the raw materials such as limestone in a kiln requires a large amount of energy, which primarily comes from the burning of fossil fuels leading to the emission of 50% of CO_2 from the manufacturing process of cement. In addition, the CO_2 emissions coming from OPC production is estimated to be 40 percent of the polluting gases [2]. This not only leads to the release of CO_2 into the atmosphere but also contributes to air pollutants such as sulfur and nitrogen oxides. Furthermore, the construction mining industry, of its raw materials can lead to a negative impact on the destruction of environment landscapes.

The use of alternative materials as cement substitutes is gaining attraction in the construction industry due to the environmental impacts associated with the production of OPC. For example, dredged sediments and excavated clays, when treated through processes like flash calcination, can serve as aluminosilicate sources for developing geopolymer binders [3][4] or as viable alternatives to OPC substitution to produce low carbon concrete such as limestone calcined clay cement [5]–[9].

High-performance concrete stands out as a specialized form of concrete, showcasing enhanced mechanical properties and durability when compared to traditional concrete [10]. Its distinguishing features include elevated compressive strength, minimal permeability, and outstanding resistance to chemical assaults, abrasion, and the effects of freeze-thaw cycles. An effective strategy for achieving high-performance concrete involves incorporating alternative binders and supplementary cementitious materials (SCMs) during the concrete production process [11][12].

In this research attempt, the focus is on advancing high-performance concrete by either utilizing flash-calcined dredged sediments and flash-calcined excavated clays in the production of geopolymer concrete or as sustainable cementitious components for substituting OPC in concrete

formulations. The sediments used in this study are dredged from the Noyelles-sous-Lens (NSL) river whereas excavated clays are extracted from the Grand Paris express project.

Sediments are formed by the accumulation of particles, varying in size, or precipitated material that has undergone individual transportation processes [13]. In France, around 50 million cubic meters of sediments are dredged annually, where they are subsequently stored, treated, and/or discharged into the sea [14]. Depending on their pollution levels, including heavy metals and hydrocarbons, sediments may be regarded as waste, raising concerns about their disposal. Various approaches for treatment and utilization are currently under exploration. These include the consideration of their use in geopolymer binders [15]–[18] and as SCMs [19][15][16].

The Grand Paris express projects, a series of large-scale construction attempts taking place in the Greater Paris area, have resulted in the excavation of substantial amounts of clay. In France, the large quantities of excavated soil generated each year are estimated to be 130 million tons [22]. Excavated clays from construction projects are classified as waste materials [23]. However, recognizing the potential of these excavated clays and understanding their characteristics is crucial to utilizing them effectively. Studies showed that excavated clays from construction projects have the potential to be transformed into a valuable resource through their use as SCMs [24]–[26] .

Flash calcination involves quickly exposing finely divided materials to high temperatures in the presence of air. Professor Salvador [27] initiated and developed this technique, initially applying it to activate certain clays like Kaolinite to give them pozzolanic properties [28]. When applied to specific clay categories, such as kaolin, the process results in dehydroxylation, eliminating hydroxyl (-OH) bonds [29][30]. While direct calcination can achieve similar outcomes, the associated energy costs are often prohibitive [31]. The instantaneous nature of flash calcination, however, leads to partial material destruction, creating an amorphous state and enhancing product reactivity [31].

In this thesis, flash calcination is adopted for the treatment of dredged sediments and excavated clays. This adaptation aims to activate specific sediment and clay phases, especially clayey ones such as kaolin, using the same principle.

In 1979, Davidovits [32] proposed an alternative method for OPC called “geopolymer” that are defined as inorganic polymer that display exceptional physical and chemical properties. They are typically synthesized through a reaction between aluminosilicates and an alkaline activator, resulting in a three-dimensional network structure. Geopolymers are a type of inorganic polymer

that is synthesized through a reaction between materials that are rich in silicon (Si) and Aluminum (Al) and an alkaline activator, such as sodium or potassium silicate [33]–[35]. These materials exhibit a wide range of applications due to their high strength, durability, and resistance to fire, chemicals, and extreme temperatures [32]. The properties of geopolymers are directly influenced by the raw materials used and the synthesis conditions. Usually Metakaolin, granulated blast furnace slag, and fly ash are used as binders however different studies mention using other types of aluminosilicates such as dredged sediments or excavated clays [18][36]. These alternative aluminosilicates have shown promising results in geopolymer synthesis, indicating a potential for expanding the range of raw materials used in the production of geopolymers. This variation of raw materials may also contribute to reducing the environmental impact of geopolymer production by utilizing materials that are readily available and often considered as waste or by-products of other processes such as dredged sediments or excavated clays.

Limestone Calcined Clay Cement (LC^3) binders are increasingly being used in the construction industry as sustainable alternatives to traditional cement binders. These binders are composed of a combination of calcined clay, limestone, and cement clinker, which not only reduces the environmental impact of manufacturing but also enhances the performance and durability of concrete structures. In recent years, there has been a growing interest in the use of LC^3 binders due to their potential to lower CO_2 emissions and contribute to a more sustainable construction sector as clinker content can be reduced to 50% [37]. The combination of calcined clay and limestone as SCMs shows promising results in reducing the overall carbon footprint of concrete production. Additionally, the use of these binders has the potential to improve the long-term strength and durability of concrete, making them an attractive option for various construction applications. As research and development in this field continue, it is expected that LC^3 binders will play a significant role in the transition towards greener and more environmentally friendly construction practices [9][38]–[40].

This thesis aims to enhance the value of dredged sediments and excavated clays, typically considered waste, by subjecting them to flash calcination. Following this process, the materials are utilized as key components in creating two high-strength, durable binders: geopolymer and LC3. This report aims to establish a synthesis of the scientific and experimental work carried out as a part of this thesis. First of all, the problem is identified followed by setting a main objective. Part 1 focuses on the bibliography relating to different scientific and technical aspects as well as the

treatment method. Part 2 illustrates the scientific methodology which includes the materials used, the characterization methods, and impact of the treatment technique on their characteristics. Part 3 shows the results obtained, their analysis and discussion. Finally, the conclusion will highlight the strongest results of this work.

Chapter 1. Bibliography

Chapter 1. Bibliography

1.1. Concrete

1.1.1. Concrete definition

Concrete is a versatile construction material composed of a mixture of cement, water, aggregates (such as sand and gravel), and sometimes additives or admixtures. It is renowned for its strength, durability, and ability to mold into various shapes.

Concrete has been utilized for construction purposes for thousands of years. One of the earliest known uses dates to ancient civilizations like the Egyptians and Mesopotamians, who used a form of concrete made from a mixture of lime and gypsum. During the Roman Empire, concrete became more widely used and advanced [41]. The Romans developed a variation known as Roman concrete, made by mixing lime, volcanic ash, and water [42]. This mixture was exceptionally durable and strong, enabling the construction of magnificent structures such as the Colosseum and the Pantheon (*Fig. 1*).

Modern concrete structures include bridges, dams, skyscrapers, highways, and stadiums. One notable example is the Hoover Dam, built in the 1930s, which still stands as a marvel of engineering today. Concrete remains an essential material in construction due to its remarkable qualities and versatility. The mentioned examples of concrete structures represent just a few among countless others, showcasing the enduring impact and utility of this material.

Fig. 1. Colosseum and Hoover Dam concrete structure.

As we look to the future, concrete will undoubtedly remain a cornerstone of construction and infrastructure, facilitating the creation of awe-inspiring architectural wonders and vital public works. Its role in shaping the world around us is integral, and its enduring impact on human progress cannot be understated.

1.1.2. History of High-performance concrete

High Performance Concrete (HPC), also known as High Strength Concrete (HSC), refers to a type of concrete that exhibits superior mechanical and durability properties compared to conventional concrete [43]. This type of concrete is characterized by its high compressive strength and enhanced durability [44].

The first development and implementation of High Strength Concrete (HSC) was carried out in Chicago for several tower constructions in 1960's [45]. The HSC exhibited a modest compressive strength, around 60 MPa, but was two times higher compared to the ready-mix concrete of the time. The principal benefit was the decrease of the columns' cross-sections therefore a gain of space. Usually, HSC is required for tall buildings [46][47][48], rigid pavements [49], and long-span bridges [50]. Examples of HPC structures are Ile de Re bridge, Arche de la défense, or Burj khalifa tower (Fig. 2).

Fig. 2. Ile de Re bridge, Arche de la défense, or Burj khalifa tower.

HPC mix designs, properties, and applications were developed in France [51]–[54] having a compressive strength of around 60 to 80 MPa used in precast industry but still uncommonly cast in situ [45].

As per the CEB-fip Model Code 1990 [55], concrete qualifies as HPC when its compressive strength on cylinders exceeds 60 MPa after 28 days. In North American standards "ACI1992" [56], high-strength concretes are defined as those achieving a compressive strength of at least 41 MPa on cylinders at 28 days. Presently, various standards, including "EC22005" [57], "SIA262" [58], incorporate HPC with compressive strengths reaching up to 100 MPa.

1.1.3. High performance concrete mix design

Initially, a standard concrete mix comprises cement, water, and aggregates. In the case of HPC, the choice of cementitious material becomes pivotal, and careful attention must be paid to the water-to-binder ratio, which significantly influences concrete performance. Moreover, the selection of aggregate types and the balance between fine and coarse aggregates are crucial factors in achieving high-performance concrete. Furthermore, typical HPC mix designs often incorporate superplasticizers to decrease water requirements while preserving the desired workability.

- Supplementary cementitious materials

In France and Switzerland, cement type CEM I 52.5R is used for HPC mixes [45]. Usually, the cement used for normal strength concrete is < 350 kg/m^3 while that for HPC is between 350 and 600 kg/m^3. To obtain this density, supplementary cementitious materials (SCMs) are substituted by OPC. The SCMs used are silica fume, fly ash [59], ground blast furnace slag [60], or natural pozzolanic materials like metakaolin [61] are used [45]. The incorporation of these SCMs will improve the workability of the concrete and refine the pore structure. Sun et al. [62] stated that enhanced packing density can decrease the heat generated during hydration, leading to improved mechanical properties and durability. Consequently, this can result in reduced permeability and porosity.

The inclusion of GBFS has been extensively studied for its application in the development of high-performance concrete. Moula et al. [63] conducted a study examining the influence of GBFS on the hydration reaction of cement and its subsequent impact on the mechanical properties of concrete. The findings indicate that replacing cement with GBFS can lead to a reduction in early concrete strength, but a comparable compressive strength is maintained after 28 days. In the research by Yazici et al. [64], a significant decrease in 2-day compressive strength was observed with a 40% slag replacement, although the 28-day compressive strength closely resembled that of the reference mix. Pyo and Kim [65] reported a 39% and 18% decrease in early compressive strength at 1 and 3 days, respectively. Studies have also highlighted that GGBS reduces the heat of hydration [66], consequently leading to a decrease in the compressive strength of UHPC at 3 days or earlier due to the lower reactivity of slag [28]. Pyo and Kim [65] noted that slag retards the early-age hydration process and setting time, resulting in lower early strength. It is worth noting

that slag contributes to enhancing the late-age compressive strength of UHPC through its latent hydraulic reaction. The formation of hydration products during the GGBS reaction proves beneficial in minimizing porosity and enhancing the packing density of UHPC. This densification of the concrete matrix contributes to increased long-term strength and durability [67]. Yu et al. [66] reported a 10% increase in compressive strength when GGBS replaced 30% of the cement at day 28. Numerous studies have explored the partial substitution of cement with ordinary slag to boost the compressive strength of UHPC at later stages [63][68][69][70][71][72]. The delayed strength gain in UHPC due to the slower hydration of slag can be addressed by using finely ground slag.

Metakaolin (MK) is recognized as a highly reactive pozzolan that positively influences the performance of concrete, particularly in the context of high-performance concrete (HPC). When combined with materials such as Fly ash (FA) or Ground Granulated Blast Slag (GGBS), MK demonstrates favorable characteristics [73]. Several studies highlight the incorporation of MK into concrete, emphasizing its ability to enhance stability, albeit at the expense of reduced fluidity, requiring more water for proper consistency [74]. In investigations by Sfikas et al. [72], a decrease in workability was noted, accompanied by an increase in mechanical strength when MK was added to Self-Consolidating Concrete (SCC). Siddique and Kaur [75] explored the substitution of different percentages of cement with MK, finding a decreasing trend in strength characteristics beyond a 15% substitution, with 10% identified as the optimal replacement level. Kadri et al. [76] concluded that MK contributes to concrete strength through pozzolanic reactions with calcium hydroxide, promotion of ordinary Portland cement hydration, and a filler effect. The improvement in mechanical performance is linked to MK's role in increasing the formation of calcium-silicate hydrate (CSH) gel, resulting in a denser structure [72].

In the context of developing high-performance concrete, studies by Wild et al. [72] and Courard et al. [72] have investigated the feasibility and effectiveness of using MK as a substitute for Portland cement in the production of High-Performance Concretes (HPC). These studies contribute to the long-term sustainability of the construction industry, exploring the potential of natural materials like metakaolin in enhancing the properties of HPC when compared to ordinary Portland cement (OPC).

- Aggregates

The optimal size of coarse aggregate varies for different strength levels, aiming to achieve the highest compressive strength per unit mass of cement. Generally, smaller aggregates lead to increased compressive strength, while utilizing larger aggregates allows for a higher Young's modulus, improved creep, and shrinkage behavior [53]. The Maximum Paste Thickness (MPT) concept, introduced by de Larrard and Tonda [51], focuses on the distance between two coarse aggregates and its impact on concrete compressive strength based on various mixtures.
De Larrard emphasized that decreasing MPT enhances strength, achievable by reducing the maximum size of aggregates. However, for compressive strength exceeding 80 MPa, aggregate strength begins to dominate concrete strength. The packing density of aggregates influences concrete properties, with denser packing density correlating with better workability and compressive strength, as noted by de Larrard [51].

- Water to binder ratio

A significant factor contributing to the excellent performance of concrete is the water-to-binder (W/B) ratio. High-performance concrete typically favors a low W/B less than 0.4 [77]. The preference for a lower W/B ratio comes from the fact that it implies a reduced amount of water in the concrete mix, resulting in a more densely packed structure with fewer void spaces. Furthermore, a low W/B ratio helps minimize shrinkage and cracking during hydration since less water is available for evaporation.
Additionally, a low W/B ratio improves the bonding between cement particles and aggregates, thereby enhancing the overall mechanical properties of the concrete. Research indicates that incorporating supplementary cementitious materials like silica fume, metakaolin, and fly ash can further elevate the performance of high-performance concrete, enabling even lower W/B ratios [78]. These supplementary materials react with free lime in the concrete mix, forming additional hydration products that contribute to strength and durability.
It is crucial to emphasize that selecting an appropriate W/B ratio is vital in the design of high-performance concrete. However, achieving a balance between a low W/B ratio and maintaining workability is essential. The use of admixtures or adjustments to the particle size distribution of aggregates, it is possible to attain a lower W/B ratio without compromising workability. Careful consideration of the water-to-binder ratio empowers construction professionals to create high-

performance concrete with superior strength, durability, and resistance to various environmental factors.

1.1.4. Environmental impact of concrete

The building materials industry ranks as the third-largest CO_2-emitting industrial sector globally, contributing to 5 to 10% of total anthropogenic CO_2 emissions [79]. Concrete manufacturing, including cement and gravel extraction, is a major contributor to this sector's carbon footprint. Additionally, the building materials sector significantly impacts natural resource consumption, with civil works and construction activities utilizing 60% of materials extracted from the lithosphere. In Europe, mineral extraction for buildings amounts to approximately 4.8 tons per inhabitant annually, and the depletion of natural aggregates near cities is increasing transportation distances [80].

Efforts to mitigate the environmental impact of cement production include exploring improvements in manufacturing processes, using alternative fuels, and substituting clinker material with mineral additions to reduce CO_2 emissions. Another strategy involves reducing the volume of concrete required for construction by enhancing its performance [81]. While increasing mechanical strength may raise CO_2 emissions per cubic meter of concrete, studies, such as those by Habert et al. [81], demonstrate that the net environmental impact can be reduced. For example, using high-performance concrete in bridge construction with a strength of around 80 MPa resulted in a 20% reduction in the overall global warming impact, as indicated by Life Cycle Assessment. Similar studies suggest that high-strength concrete, ranging from 100 to 120 MPa, offers an efficient compromise between performance and cement quantity, leading to decreased CO_2 emissions [45].

1.2. Ordinary Portland cement

Cement is the main component of concrete and the most widely used construction material in the world [82]. According to the European standard NF EN 197-1 [83], cement is a hydraulic binder, meaning it is a finely ground mineral material that, when mixed with water, forms a paste that sets and hardens due to reactions and hydration processes. After hardening, it retains its strength and stability even underwater.

Portland cement was first invented in 1824 by firing a mixture of limestone and clay at 1200 °C [84]. Since that day, manufacturing techniques and performance have continuously improved. Indeed, the temperature proposed by Aspdin was lower than that used today in the cement industry (1450 °C). Compared to the initial hydraulic binder, using a higher firing temperature allows for a reduction in the calcination time and enhanced control over the setting and mechanical strengths developed by the binder [85].

France ranks as the 20th global producer of cement, with a clinker production of 14.2 million tons in 2012 and 18 million tons of cement. France is also the leading producer of Portland cement in Europe [86].

1.2.1. Ordinary Portland cement composition

Portland cement is produced through the grinding of clinker with sulfates, commonly using gypsum or anhydrite. The manufacturing process of clinker and Portland cement can be outlined schematically, as illustrated in Fig. 3.

Fig. 3. Cement manufacturing

The primary oxides found in Portland cement include CaO (calcium oxide), SiO_2 (silicon dioxide), Al_2O_3 (aluminum oxide), and Fe_2O_3 (iron (III) oxide). These oxides are distributed among four main phases that make up the clinker:

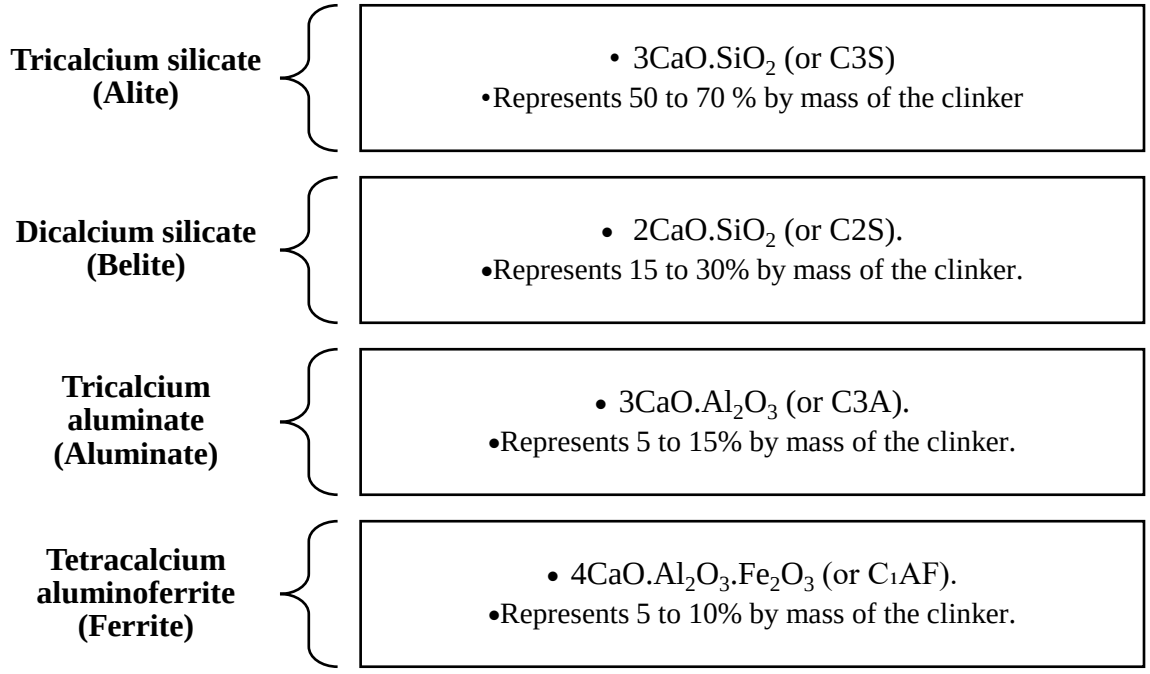

When these clinker phases encounter water, they undergo hydration with different kinetics. In other words, they react with water at different rates. This hydration process is a crucial step in the setting and hardening of Portland cement, leading to the formation of hydrated cementitious compounds that contribute to the strength and durability of concrete. The specific reactions and kinetics of each phase play a significant role in the overall performance of the cementitious system.

1.2.2. Clinker 4 main phases

- **Tricalcium silicate (Alite)**

The primary clinker phase is alite, which manifests in 7 distinct polymorphic forms influenced by temperature. These forms include three triclinic polymorphs (designated as T1, T2, and T3), three monoclinic polymorphs (designated as M1, M2, and M3), and one rhombohedral polymorph (designated as R) [87]. This phenomenon is termed polymorphism. Fig. 4 provides a visual representation of the 7 alite polymorphs corresponding to varying temperatures.

Fig. 4. Polymorphs of alite as a function of temperature [82].

At room temperature, pure alite exists in the T1 polymorph. However, during the formation of alite within an industrial clinker, the presence of minor elements stabilizes certain monoclinic polymorphs, primarily M1 and M3 [88], at the expense of the theoretical triclinic polymorph. Additionally, the presence of magnesium tends to stabilize the M3 polymorph, while the presence of SO_3 promotes the formation of M1 [88]. Fig. 5 illustrates the relationship between the SO_3 content, MgO content, and the transformations of alite polymorphs.

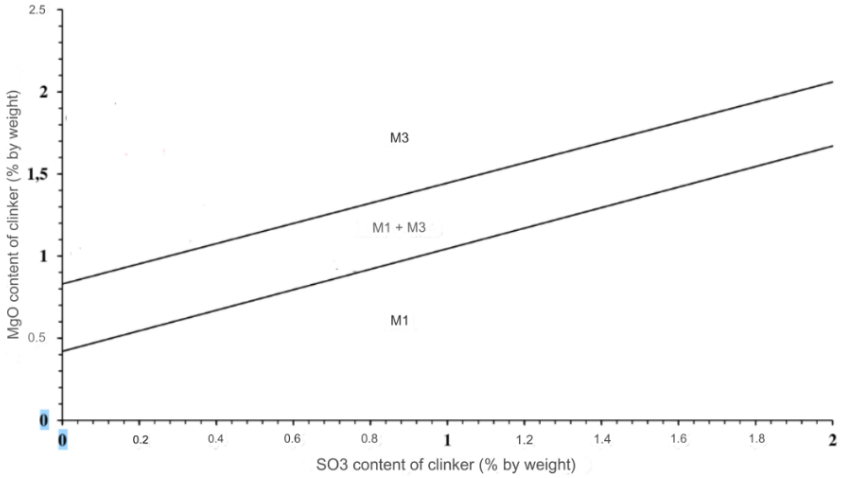

Fig. 5. The relationship between the SO_3 content, MgO content, and the transformations of alite polymorphs in the clinker [88].

- **Dicalcium silicate (Belite)**

The belite, or dicalcium silicate, is the second major component of clinker. It has 5 different polymorphs whose formation also depends on temperature: α (hexagonal), α'H (orthorhombic), α'L (orthorhombic), β (monoclinic), and ϒ (orthorhombic) [89]. Fig. 6 illustrates the relationship between temperature and the formation of C2S polymorphs [90].

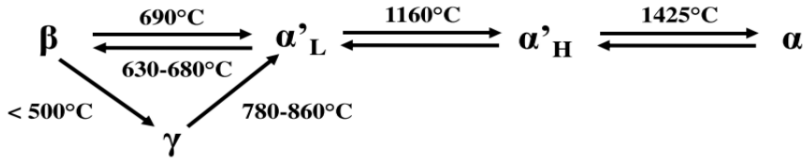

Fig. 6. The relationship between temperature and the formation of C2S polymorphs [82].

The structure of belite consists of an assembly of $SiO4^{4-}$ tetrahedra linked by calcium ions Ca^{2+} in octahedral sites [89][87]. The α, α', and β polymorphs are relatively similar and are obtained

through displacement, particularly through a change in the orientation of $SiO4^{4-}$ tetrahedra and movements of Ca^{2+} ions [90]. The ϒ polymorph results from slow cooling from α-C2S. At room temperature, the ϒ-C2S structure is the most stable form; consequently, it is less reactive. In industrial clinker, belite is primarily in the β form and contains 4 to 6% minor elements such as aluminum, iron, and potassium [90].

- **Tricalcium aluminate (Aluminate)**

In the case of a pure compound, tricalcium aluminate (C3A) does not exhibit temperature-dependent polymorphism [87]. Pure C3A exists in a cubic form. However, the introduction of minor elements into the crystal lattice, such as sodium, iron, and silicon, can alter the symmetry of the crystal lattice. The replacement of Ca^{2+} by two Na^{+} ions facilitate the transition from a cubic system to monoclinic or orthorhombic systems depending on the substitution rate [91]. Indeed, when the total alkali content is low, C3A is in the cubic form. On the other hand, when the total alkali content is higher, the orthorhombic form predominates. This form can contain up to 20% minor elements.

- **Tetracalcium aluminoferrite (Ferrite)**

The tetracalcium aluminoferrite should be considered as a solid solution containing C2A and C2F [89], with a chemical formula of $2CaO(Al_xFe_{1-x})_2O_3$ where $0 < x < 0.7$. The limit for x is set at 0.7 due to the instability of C2A under certain pressure conditions [91]. In the crystalline structure, iron and aluminum share positions between tetrahedral and octahedral sites based on the composition and conditions during the phase formation. This phase, in turn, can incorporate up to approximately 10% minor elements [87].

- **Quantification of mineral phases in clinker – "Bogue Formula"**

The mass percentage of each mineral phase in the clinker can be estimated using the Bogue formula [92] with the following equations:

- $C3S = 4.07 * (CaO_{Total} – CaO_{free\ lime}) - 6.72 * Al_2O_3 – 1.43 * Fe_2O_3$ Eq. 1
- $C2S = 8.60 * SiO_2 + 1.08 * Fe_2O_3 + 5.07 * Al_2O_3 - 3.07 * (CaO_{Total} – CaO_{free\ lime})$ Eq.2
- $C3A = 2.65 * Al_2O_3 – 1.69 * Fe_2O_3$ Eq. 3
- $C4AF = 3.04 * Fe_2O_3$ Eq. 4

A fundamental assumption of the equations in the Bogue formula is the purity of the mineral phases in the clinker and the non-incorporation of foreign ions. This explains why the total mass sum of mineral phases, including the free lime content, does not reach 100%.

1.2.3. Cement hydration

The various chemical mechanisms associated with the hydration of cement phases are extensively explained and detailed in numerous works, such as "Cement Chemistry" by Taylor [87] or "Lea's Chemistry of Cement and Concrete" edited by P. C. Hewlett [93]. The process of cement hydration initiates when cement encounters water, and it involves several chemical reactions with the anhydrous phases of the clinker.

The reactions between alite and belite with water primarily result in the formation of compounds responsible for the specific mechanical strength of cement: hydrated calcium silicates (C-S-H) and portlandite ($Ca(OH)_2$). Dissolving the anhydrous phases leads to the solution's saturation, followed by the germination and growth of C-S-H on one hand, and the precipitation of portlandite on the other, stemming from the concentration of calcium and hydroxide ions. The reaction of alite is faster than that of belite. The equations below describe these phenomena:

$$C_3S + zH \rightarrow C_xSH_y + (3 - x)CH \quad \text{Eq. 5}$$

$$C_2S + zH \rightarrow C_xSH_y + (2 - x)CH \quad \text{Eq. 6}$$

Where, z= y + 3 – x and z= y + 2 – x for alite and belite respectively.

The anhydrous phases of the clinker exhibit different hydration kinetics (Fig. 7), resulting in distinct kinetics of hydrate formation [93].

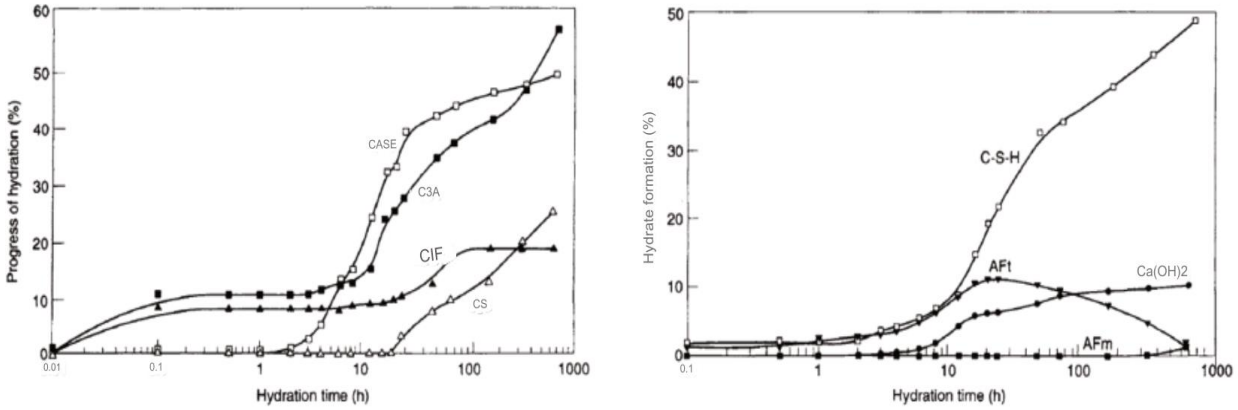

(a) Hydration of the anhydrous phases of the clinker

(b) Formation of the main hydrated phases

Fig. 7. Kinetics of hydration and formation of reaction products [93].

The reaction between cement and water is an exothermic process, releasing heat. Various techniques can be employed to measure the heat generated during this reaction. Isothermal calorimetry involves recording both the heat flow and cumulative heat of a sample throughout hydration. This method allows for data collection from the initiation of hydration, precisely when the cement contacts water. Heat flow curves are unique to each material and can vary between different types of cement. These curves provide insights into and characterize the distinct hydration reactions, breaking down into multiple phases. This concept is elucidated by Taylor [87] and further expanded upon by Gartner et al. [94], Bullard et al. [95], or Jansen et al. [96].

The heat flow curve (Fig. 8) during the reaction between Portland cement and water is divided into four stages, each corresponding to different reactions and marked by distinct chemical modifications:

1. **Initial Period:** Begins from the moment cement and water come into contact.
2. **Induction Phase:** Characterized by a period of thermal inertia.
3. **Acceleration Phase:** Ends with the silicate reaction peak, marked by rapid formation of C-S-H (hydrated calcium silicates) and portlandite.
4. **Deceleration Phase:** Represents a slowing down of the dissolution of silicates, and during this phase, aluminate reactions can be observed in the heat flow curve.

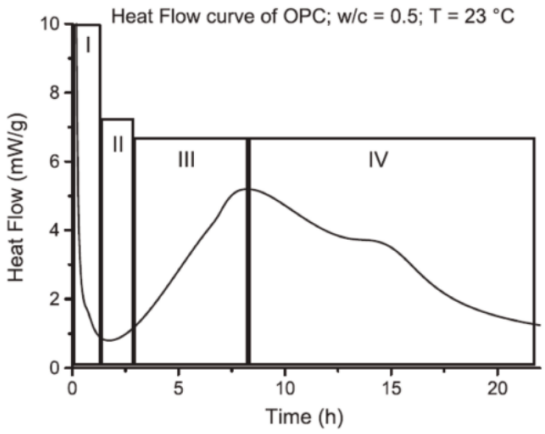

Fig. 8. Evolution of the heat flow during the reaction between Portland cement and water [96].

The nucleation of C-S-H and portlandite initiates from the early moments (phases I and II) with the dissolution of alite. The acceleration phase sees a rapid formation of C-S-H and portlandite. In the beginning of the deceleration phase, a portion of the water has been consumed by the initial hydration reactions, and the dissolution of silicates slows down.

Aluminate reactions, indicated by a shoulder in the deceleration phase, correspond to the disappearance of sulfates and the swift consumption of C3A (tricalcium aluminate). The hydration reactions of aluminates and ferrite yield similar hydration products.

The reaction of aluminate (C3A) is fast and, if poorly controlled, can lead to the phenomenon of false setting in cement. The addition of sulfates to the clinker helps regulate the setting, and the reaction between C3A and sulfates produces ettringite.

$$C3_A + 3C\bar{S}H_2 + 26H \rightarrow C_6A\bar{S}_3H_{32} \qquad \text{Eq. 7}$$

If the sulfate concentration is insufficient, and gypsum has completely disappeared, ettringite transforms into monosulfates of calcium after reacting with the remaining aluminates. describes the reaction of ettringite with aluminate.

$$C_6A\bar{S}_3H_{32} + 2C_3A + 4H \rightarrow 3C_4A\bar{S}H_{12} \qquad \text{Eq. 8}$$

In the case of ferrite, aluminum atoms are substituted by iron atoms in ettringite and monosulfates, forming the phases referred to as AF_t (Al_2O_3-Fe_2O_3-trisulfate) and AF_m (Al_2O_3-Fe_2O_3-monosulfate).

1.2.4. Role of sulfates

The impact of sulfate content on the hydration and mechanical characteristics of Portland cement has been extensively demonstrated and affirmed over time. Lerch [97] and Bentur [98] conducted studies illustrating the effects of sulfate on hydration, highlighting the presence of an optimum level of mechanical strength depending on the sulfate content in the cement. The optimal sulfation level is significantly influenced by experimental conditions, with each system having its unique optimal composition. While various parameters contribute to determining the optimum, hypotheses regarding the origin of this sulfate optimum differ.

According to Gunay [99], two primary hypotheses have emerged to explain this phenomenon: the kinetic effect [97] and the microstructural effect. The kinetic hypothesis suggests that reaching the optimum sulfation occurs when the hydration of silicates and the dissolution of aluminates happen simultaneously. Isothermal calorimetry tests can help identify each of these reactions, thus determining the optimal sulfation for a cementitious system. The second hypothesis, termed microstructural, posits that the optimal sulfate content corresponds to the quantity required for ettringite formation to fill the pore space left by C-S-H [99].

It is crucial to emphasize that the optimal sulfation is system-dependent and is associated with the relative proportions between C3A and calcium sulfates. The hydration of C3A influences that of C3S in the presence of calcium sulfate, directly impacting mechanical properties.

1.3. Geopolymer

1.3.1. Geopolymer and geopolymerization

The term “geopolymer” was first defined by the French scientist Professor Davidovits in 1979 as an alternative material for ordinary Portland cement (OPC) [35] but with reduced Greenhouse emissions [100]. Geopolymer is defined as an inorganic polymer that is obtained by the chemical reaction happening between alumino-silicate source and alkaline reagents [35]. This process is called geopolymerization which results in polycondensation reaction that yields three-dimensional tecto-aluminosilicate with the general empirical formula:

$$M_n[-(SiO_2)_Z - AlO_2]_n * wH_2O \quad \text{Eq. 9}$$

Where M is a cation (K, Na, Ca) and n is the degree of polycondensation and z is 1, 2, 3 or >>3 [35].

Davidovits proposed that geopolymer materials are made up of tetrahedral units that are linked to polymeric precursors by sharing oxygen atoms that yield the formation of poly(sialate), where sialate is an observation of silico-oxo-aluminate (Si-O-Al) [35]. The sialate network consists of SiO_4 and AlO_4 tetrahedral linked by sharing all oxygen atoms. Positive ions (Na^+, K^+, Ca^{2+}, etc.) must be present to balance the negative charge of Al in 4-fold coordination [101][102]. The three-dimensional silico-aluminate structures known as the geopolymer terminology is defined by the type of sialate as represented in Fig. 9.

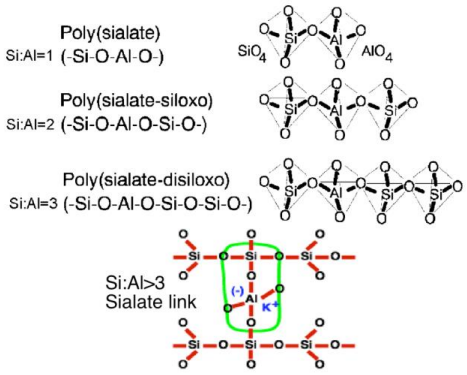

Fig. 9. Geopolymer terminology [101].

Additionally, Davidovits clarified that the atomic ratio of Si:Al plays a crucial role in determining the chemical, physical, and mechanical characteristics of materials resembling ceramics. A Si:Al ratio of 1 is conducive to the formation of bricks and ceramics, while a ratio of 2 facilitates the

creation of low CO_2 cement and energy-efficient concretes. When the Si:Al ratio is 3, it promotes the development of fire and temperature-resistant compounds used in the production of prototypes and tooling. A Si:Al ratio exceeding 3 results in the production of paints and coatings that exhibit resistance to corrosion and high temperatures. Maintaining a Si:Al ratio between 20 and 35 is ideal for producing advanced composites comprising carbon fiber, which possess fire and heat-resistant properties. These classifications are summarized in Fig. 10 [103].

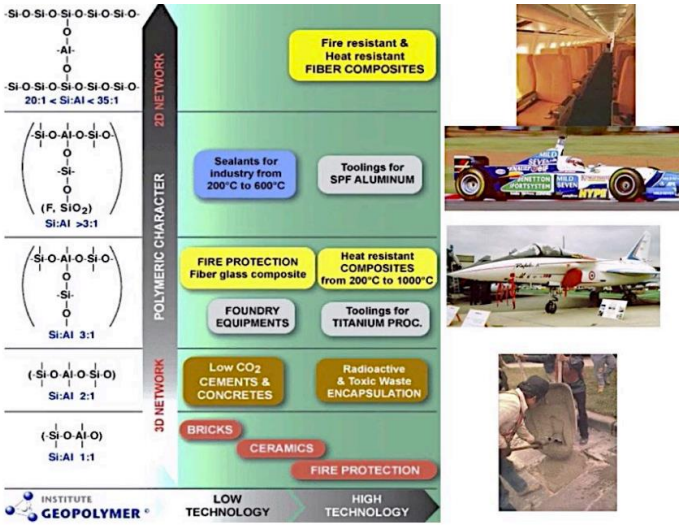

Fig. 10. The atomic ratio Si: Al in the poly(sialate) structure determines the properties and application fields [103].

Prior to explaining the stages of geopolymerization and distinguishing between alkali-activated materials and geopolymers as referred to by Davidovits, the reaction between alumino-silicate sources and alkaline reagents is referred to as alkali activation. In the 1950s, Glukhovsky [104] proposed a comprehensive mechanism for the alkali activation of alumino-silicate materials, which comprises three stages: (a) destruction-coagulation, (b) coagulation-condensation, and (c) condensation-crystallization. Subsequently, various authors expanded Glukhovsky's theory to explain the geopolymerization reaction [105][106][107] . This extension of the theory prompted Duxson et al. [102] to outline the key factors governing the transformation of a solid aluminosilicate source into a synthetic alkali aluminosilicate, simplifying the representation of the geopolymerization reaction as depicted in Fig. 11.

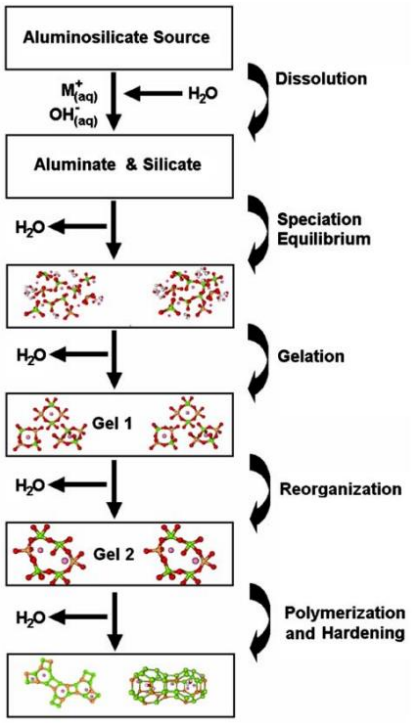

Fig. 11. Simplified Conceptual model for geopolymerization [102].

On the other hand, Davidovits [103] has explained the geopolymerization mechanism by the following six steps:

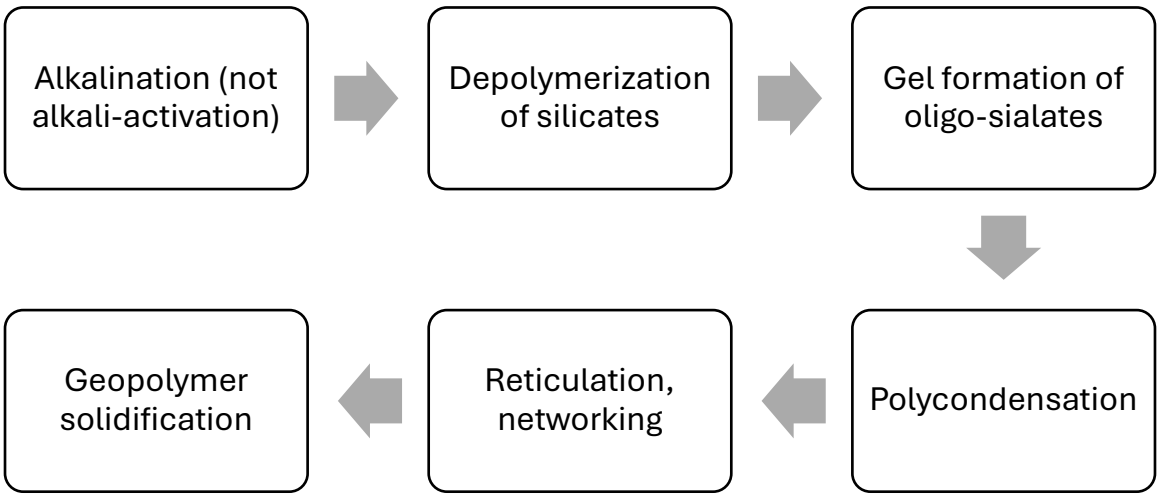

Moreover, Davidovits [103] has clarified that referring to geopolymers as alkali-activation is an inaccurate terminology. He emphasizes that alkali-activation is the initial stage of the geopolymerization process. Additionally, he points out that alkali-activated materials rely on a low-molecular chemistry with small molecules and do not exhibit polymer-like characteristics, unlike geopolymers, which are characterized by high molecular structures or macromolecules. Furthermore, Davidovits has explained that the substances involved in this process do not require activation since they are inherently super-reactive, and the alkaline reagent serves primarily as a hardening agent. Davidovits has showed an example to clarify the difference between alkali-activated slag without the presence of metakaolin upon conducting the nuclear magnetic resonance (NMR) as shown in Fig. 12. The author explained, to continue the geopolymerization reaction, a networking element such as metakaolin should be added to interact with the free cations thus ending with a Si(Q_4) stable specie and three-dimensional network rather than Si(Q_2).

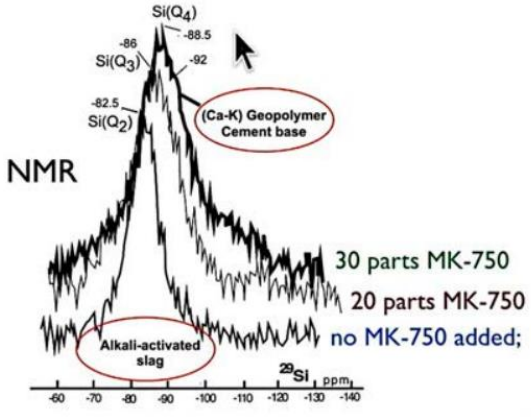

Fig. 12. From alkali activated slag to geopolymer cement [103].

1.3.2. Raw materials and alkaline reagents

Geopolymers are typically crafted by employing materials rich in aluminosilicates, such as kaolinite and clays. The primary components utilized in geopolymer synthesis are usually metakaolin, well-known for its elevated SiO_2 and Al_2O_3 mass concentrations and minimal CaO content. In 1975, Davidovits developed geopolymer using Metakaolin (MK-750), highlighting its high reactivity in an alkaline medium [108]. MK-750 subsequently became a reference material in geopolymer development, serving for quality control and the selection of reactive raw materials [108]. Subsequently, low calcium fly ash gained preference in geopolymer concrete formulations

over high calcium fly ash due to the potential interference of high calcium content with the polymerization process and alteration of the microstructure [109][110][111][112]. Furthermore, successful manufacturing of geopolymer concrete using low calcium fly ash has been achieved when silicon and aluminum oxides constituted approximately 80% by mass, with a Si-to-Al ratio of about 2 [109]. On the other hand, different studies have mentioned using slags as they are incorporated into geopolymer formulations to create MK/fly ash -slag based geopolymers [113]–[121]. Unlike fly ash and metakaolin, slags have a notable CaO content. The classification of MK, fly ash, and slags is based on their SiO_2, Al_2O_3, and CaO content, as depicted in Fig. 13.

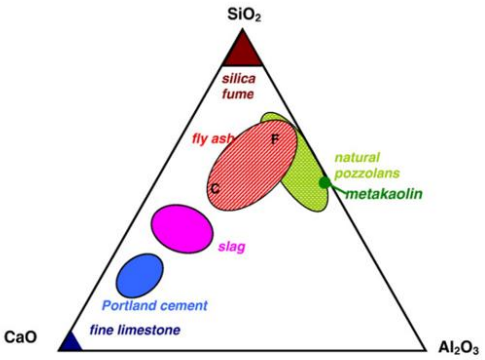

Fig. 13. CaO- $A_{l2}O_3$- SiO_2 diagram for metakaolin, fly ash, and slag [122].

Furthermore, various studies have highlighted the distinctions between metakaolin (MK) and fly ash-based geopolymers. The mechanical characteristics of geopolymers based on metakaolin are frequently superior to those derived from fly ash. Additionally, there are variations in porosity; typically, metakaolin-based geopolymers exhibit more isolated pores, while fly ash-based geopolymers have more interconnected pores. These differences must be considered, considering the potential variations for each type of geopolymers based on the initial formulation [123]. Deventer et al. [124] conducted a comparison of the structures of geopolymers synthesized from metakaolin or fly ash as the aluminosilicate source and either sodium hydroxide or alkali silicates as the activating solution, utilizing scanning electron microscopy as shown in *Fig. 14*. *Fig. 14*(a) represents the geopolymer derived from fly ash, whereas *Fig. 14*(b) illustrates the geopolymer based on metakaolin. The metakaolin-based geopolymer displays a more consistent appearance with minimal indications of unreacted materials. In contrast, the fly ash-based geopolymer exhibits a significant presence of unreacted materials.

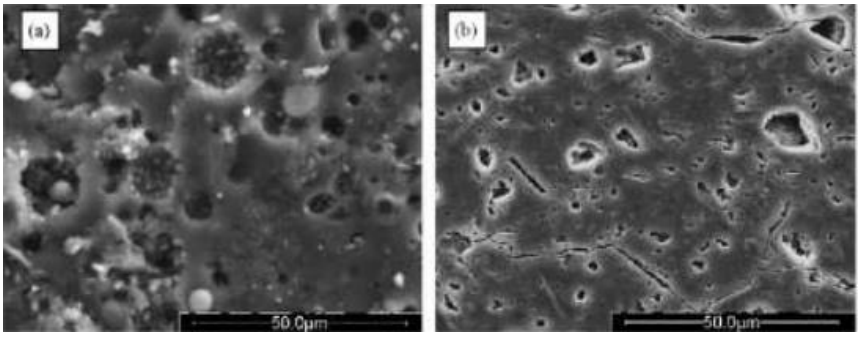

Fig. 14. Scanning electron microscopy for (a) fly ash geopolymer and (b) metakaolin geopolymer [124].

The addition of ground granulated blast furnace slag (GGBFS) is important in both cementitious binders and geopolymer concrete. In cementitious binders, GGBFS acting as a supplementary cementitious material offers significant impact on the concrete performance and offers economic and environmental benefits compared to Portland cement production contributing to reduced CO_2 emissions [125]. GGBFS, known for its latent hydraulic properties, can enhance early cement hydration when used with Portland cement. Despite its low reaction rate with water, GGBFS cements exhibit drawbacks such as lower early strength and longer setting times, which can be mitigated with specific approaches. Understanding the early-age behavior of cementitious materials is crucial for improving construction quality and durability. However, the use of GGBFS in geopolymer formulations can enhance its early-age strength and overall performance, but the effectiveness depends on various factors, including the nature of GGBFS, alkaline reagent, and curing conditions.

In addition to the materials rich in aluminosilicates, an alkaline reagent is used to start the geopolymerization reaction. The commonly used alkaline reagents include a combination of sodium hydroxide (NaOH) and potassium hydroxide (KOH), along with sodium silicate or potassium silicate [109]. Indeed the quality and concentration of the alkaline reagent used is an important factor to determine the final structure of the cured material [126][127]. Duxson et al. [127] has mentioned the relationship between the compressive strength of geopolymer formulations with metakaolin and different alkaline silicate solutions with different concentrations. The author [127] has summarized the results in *Fig. 15*. The compressive strength of alkali ratios (Na, Na75, Na50, Na25, and K) increases as the Si/Al ratio rises from 1.15 to 1.90, but a slight decrease is noted beyond Si/Al = 1.90. Despite different alkali compositions, specimens

exhibit similar compressive strengths at a given Si/Al ratio, indicating a 10–20% difference in mechanical properties, typical for chemically analogous glasses without ionic diffusion [127][128]. Notably, K specimens show higher strength than Na specimens in the mid Si/Al range, where alkali effects have been observed previously.

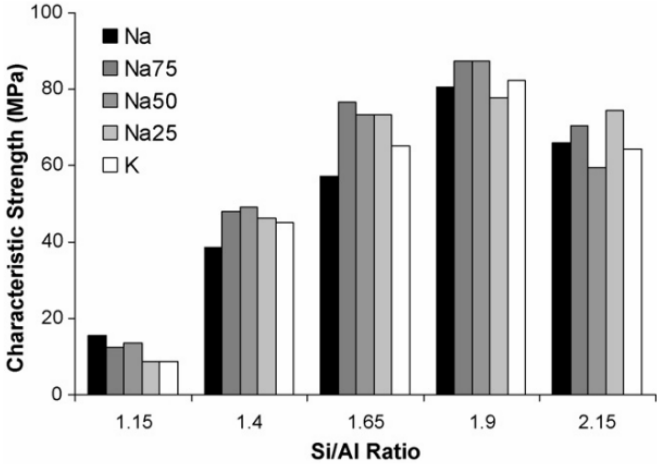

Fig. 15. Compressive strength of geopolymer specimens with different alkaline solutions [127].

Moreover, studies showed that the degree of gel formation is more important in potassium-based rather than sodium-based geopolymers [129][130]. Xu and Deventer [131] elaborated that geopolymer based on KOH exhibits greater compressive strength than geopolymer based on NaOH. Nevertheless, Alosno et al. [132] also demonstrated that the compressive strength of NaOH-based geopolymer can surpass that of KOH-based geopolymer, depending on variations in curing temperature, curing time, or the alkali activator/aluminosilicate ratio.

1.3.3. Factors influencing the geopolymerization reaction

The literature discusses the effect of molar concentrations, silica to aluminum, water quantity, and curing temperature on the geopolymer behavior.

1.3.3.1. Influence of molar ratios

Among the factors influencing the properties of geopolymer matrices are the molar concentrations of alumino-silicate sources, alkalinity, and mixing water. Various studies on the molar ratios of Si_2O/Al_2O_3, Na_2O/SiO_2, H_2O/Na_2O, and Na_2O/Al_2O_3 can be found in the literature

[133][134], highlighting the advantage of optimizing the ratios between these values as follows; where M= Na, K, or Li.

$$0.2 < M_2O/SiO_2 < 0.48$$

$$3.3 < SiO_2/Al_2O_3 < 4.5$$

$$10 < H_2O/M_2O < 25$$

$$0.8 < M_2O/Al_2O_3 < 1.6$$

1.3.3.2. Influence of Si/Al

Duxson et al. [130] highlighted the correlation between the Si/Al ratio and the mechanical properties of geopolymers synthesized from metakaolin and a sodium silicate solution. The author has explained linking microstructure to mechanical strength. For Si/Al ratio below 1.4, large, interconnected pores are observed, along with the presence of destabilizing precipitates and traces of unreacted materials, resulting in low mechanical strength. For a Si/Al ratio above 1.65, smaller isolated pores and a more homogeneous binder are observed. The optimum strength is found for a Si/Al ratio of 1.9, corresponding to a slight reduction in porosity. Beyond this ratio, mechanical strength could decrease as this modification comes at the expense of Si-O-Al bridges responsible for network cross-linking. The decrease in mechanical strength beyond a Si/Al ratio of 1.9 could also be explained by a faster geopolymer setting, leading to an early reduction in reactant mobility. Additionally, as the Si/Al ratio increases, metakaolin is less dissolved, increasing the proportion of unreacted material, countering the effect of more numerous Si-O-Si bridges.

1.3.3.3. Influence of water quantity

The polymerization process is influenced by the amount of water used during the synthesis of geopolymers. It should not be too low to ensure proper mixing of reactants and facilitate ionic transfer. Conversely, it should not be too high to avoid diluting the reactants, hindering the interaction of oligomers, and thus slowing down polymerization [135]. An excess of water leads to a significant loss of mechanical strength. Moreover, since water does not participate in the geopolymerization reaction, an excess of water may result in the formation of larger pores and a greater porous volume [136].

1.3.3.4. Influence of curing temperatures

The crucial parameters in geopolymerization are temperature, relative humidity, and curing time. The temperature plays a significant role in accelerating the kinetics of geopolymerization reactions. To accelerate the geopolymerization reaction, geopolymers can be stored at temperatures ranging from 50°C to 80°C after the mixing process, involving the addition of the alumino-silicate source [137]. However, the accelerated reactions significantly impact the final properties of the material, particularly its mechanical strengths [138]. At room temperature, reactions proceed at a regular pace, resulting in comparatively lower mechanical strengths. Conversely, excessively high temperatures can lead to cracking in the geopolymer, negatively affecting its physical properties [139]. Cracking can also be a consequence of overly rapid drying, a situation that typically arises when the geopolymer is not properly sealed during the curing process and is placed in an environment with a relative humidity range of 30% to 70% [140].
Another experiment done by Rovnaník et al. [141] demonstrates that curing at high temperatures doesn't improve mechanical strength if the curing time is too short as 1 hour. A longer curing time equals to 4 hours is necessary to observe an effect. The results of this study are summarized in Fig. 16. The compressive strength, whether measured at an early stage or on the final material, undergoes significant changes depending on the curing conditions applied to the samples. Elevated temperatures (60°C and 80°C) enhance the strength during the early stages. For other temperature settings, attaining the ultimate compressive strength requires a longer duration. Nevertheless, the strength values at 28 days are higher. The rapid establishment of the network at higher temperatures results in products of lower quality. Conversely, at lower temperatures, the network has sufficient time to organize, leading to improved material strengths. Another explanation proposed in this study suggests that curing at higher temperatures would result in larger pores and a greater porous volume. Additionally, this finding underscores that temperature plays a role in influencing the porosity of geopolymers.

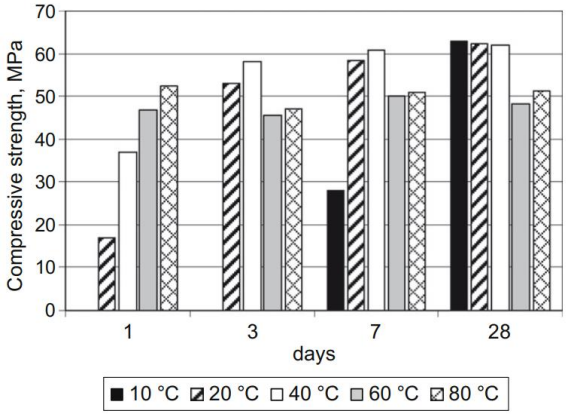

Fig. 16. Evolution of the compressive strength of sodium-based metakaolin geopolymers subjected to curing at 10, 20, 30, 40, 60, and 80 °C [141].

Another study conducted by Fernandez-Jimenez [142] illustrated this influence along with the impact of curing time on the total porosity and pore distribution of geopolymers based on fly ash and sodium hydroxide as shown in Fig. 17. The total porous fractions vary significantly, ranging between 29% and almost 35%. After 5 hours of curing, the geopolymers at 85°C and 120°C exhibit similar total porosities. After 7 days, the samples at 85°C have a slightly lower total porosity than those at 120°C. However, the pore distribution is influenced by the temperature and curing duration, as the quantity of finer pores (less than 0.1 μm) increases with these parameters.

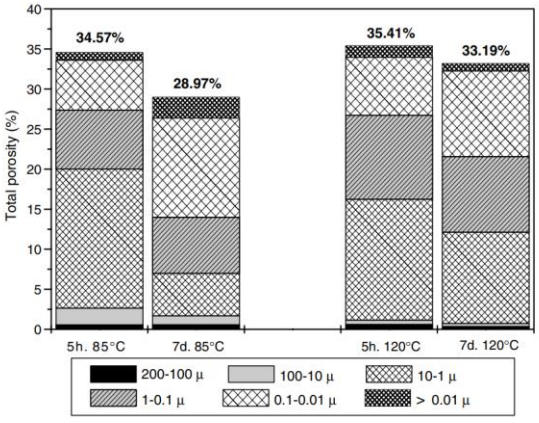

Fig. 17. Changes in the total porosity and pore distribution of sodium-based fly ash geopolymers stored at different temperatures over time, measured through mercury intrusion [142].

1.3.3.5. Influence of curing time

A recent study highlighted changes observed in porosity (pore size, volume, and specific surface area) between 3 days and 6 months after their synthesis [143]. Two geopolymers, one sodium-based and the other potassium-based, were compared. Both materials were analyzed through nitrogen adsorption measurements to characterize the evolution of porosity and specific surface area as mentioned in Table 1.

Table 1. Specific surface area, pore volume and pore diameter measured by nitrogen adsorption for sodium and potassium geopolymers at different aging times: t = 3, 7, 14 d and 6 months [143].

Time	Sodium geopolymer			Potassium geopolymer		
	$S_{BET}(m^2/g)$	$D_{pore}(\dot{A})$	$V_{pore}(cm^3/g)$	$S_{BET}(m^2/g)$	$D_{pore}(\dot{A})$	$V_{pore}(cm^3/g)$
3 d	62	112	0.23	155	62	0.34
7 d	58	102	0.19	145	60	0.30
14 d	54	102	0.18	123	65	0.28
6 months	36	107	0.13	106	73	0.26

Irrespective of the nature of the alkali reagent either sodium or potassium, the pore volume and specific surface area of these two geopolymers decrease between 3 days and 6 months after their synthesis, thus indicating curing time affects the microstructure of the geopolymer.

1.3.3.6. Geopolymer CO_2 emissions vs. OPC CO_2 emissions

Davidovits conducted a study comparing the carbon dioxide (CO_2) emissions and energy consumption associated with Ordinary Portland Cement (OPC) production versus geopolymer production [144]. The comparison involved assessing the quantity of cement permitted with a 100-gram allowance for CO_2 emissions. The author explained that the production of all oxides involves the calcination of carbonates, such as calcium carbonate ($CaCO_3$) for OPC and sodium carbonate (Na_2CO_3) and potassium carbonate (K_2CO_3) for geopolymer cement. Analyzing the theoretical yield for cements produced with a 100-gram CO_2 allowance, as depicted in Fig. 18. Davidovits concluded that the chemical properties enable the manufacture of 5 to 10 times more geopolymer than OPC.

Beyond its environmental advantages, geopolymer production also offers economic benefits. The utilization of industrial by-products as raw materials has the potential to reduce the cost of building materials, thereby making construction more cost-effective. Additionally, the decreased energy consumption in the production process not only contributes to lower CO_2 emissions but also results in cost savings for manufacturers. This, in turn, could lead to more competitive pricing for geopolymer-based products. The study also included a cost estimation for construction materials, factoring in CO_2 taxes on energy alone and on both energy and chemical CO_2 emissions, as illustrated in Table 2 and Fig. 18.

Table 2. Estimation of cost increase or decrease for construction materials assuming CO_2 taxes on energy alone and on energy+chemical-CO_2 emission [144].

Material	**CO_2 tax energy alone**	**CO_2 tax energy + chemical CO_2**
Portland cement concrete	+ 20%	+50%
Blended Portland cement concrete 50% Portland/50% by-products	+ 20%	+ 35%
Steel	+ 20%	+ 30%
Wood	0%	0 to – 30%
Geopolymer cement concrete	+ 10%	+ 15%

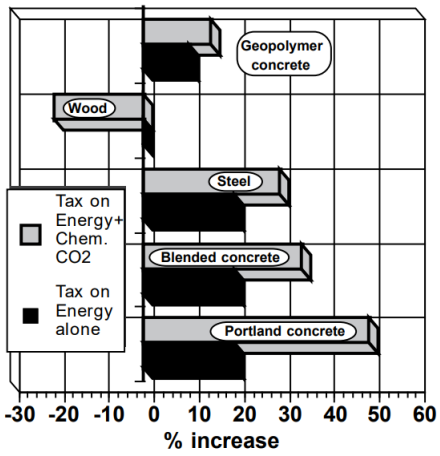

Fig. 18. Estimation of cost increase or decrease for construction materials assuming CO_2 taxes on energy alone and on energy+chemical-CO_2 emission [144].

Moreover, Turner et al. [145] conducted a study that highlighted a substantial contrast in carbon dioxide (CO_2) emission rates between geopolymer concrete and Ordinary Portland Cement (OPC) [146][147]. The research estimated a significant reduction in CO_2 emissions from geopolymer concrete, ranging from 80% less than OPC to 26-45% lower than OPC concrete. Turner et al. [145] further investigated CO_2 emissions, specifically considering the production of 40 MPa concrete, the manufacture of alkaline reagents, and the curing of geopolymer concrete at 50 °C for 24 hours. The author presented a summary of the CO_2 emissions calculations in Fig. 19. However, it is essential to note that not all geopolymer concretes necessitate high-temperature curing, which results in lower energy consumption and CO_2 emissions. This can lead to even lower CO_2 emissions than those indicated in Turner et al. [145] study.

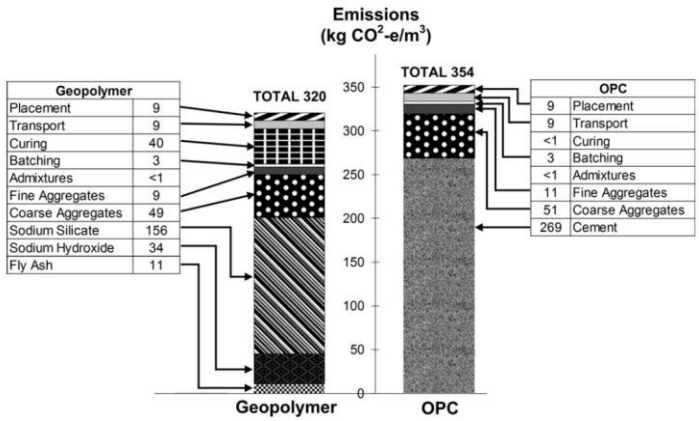

Fig. 19. Summary of CO_2 emissions for grade 40 concrete mixtures with OPC and geopolymer binders [145].

In relation to the study conducted by Turner et al. [145], Davidovits [148] pointed out inaccuracies in the terminology and CO_2 emission calculations, particularly concerning the production of sodium silicate glass. Davidovits corrected the initially reported value of 156 kg CO_2/m^3 to 69.01 kg CO_2/m^3. Turner et al. [145] initially estimated the total CO_2 emissions at 320 kg CO_2/m^3 for fly ash-based geopolymer concrete. However, Davidovits argued that properly industrialized fly ash-based geopolymer concrete should undergo ambient curing, adding an extra 40 kg CO_2/m^3 for heat curing. Consequently, Davidovits asserted that the corrected CO_2 emissions value should be 169 kg CO_2/m^3, contrasting with the initially reported 320 kg CO_2/m^3.

Finally, Davidovits [148] explained that the life cycle greenhouse gas emissions of Geopolymer Type 2 concrete are significantly lower, approximately 62-66 % less than emissions from the reference concrete. Moreover, the Type 2 geopolymer cement exhibits an approximately 80% lower emitted greenhouse gas intensity compared to an equivalent amount of ordinary Portland cement binder used in reference concrete of similar strength. Davidovits [148], elaborated that these findings align with data previously published by the Geopolymer Institute, indicating reductions in the range of 70 to 90%.

1.3.4. Geopolymer applications

The University of Queensland's Global Change Institute (GCI) is the world's first building to successfully use geopolymer concrete for structural purposes (Fig. 20). The 4-story high building, for public use, comprises 3 suspended geopolymer concrete floors involving 33 precast panels. They are made from slag/fly ash-based geopolymer concrete coined Earth Friendly Concrete (EFC), a Wagner's brand name for their commercial form of geopolymer concrete.

Brisbane West Well camp Airport (BWWA), Toowoomba, Queensland, is Australia's first greenfield public airport to be built in 48 years. BWWA became fully operational with commercial flights operated by Qantas Link in November 2014. See our News dated of October 14, 2014, 70,000 tons Geopolymer Concrete for airport (Fig. 20).

Fig. 20. First geopolymer building (year 2014) and Brisbane West Wellcamp Airport (BWWA).

Other studies are using geopolymer concrete in different construction approaches such as in apron, pavements, retaining walls, sewer pipes, aircraft pavements, and walls Fig. 21.

Fig. 21. Use of geopolymer concrete.

1.4. Low carbon Concrete

1.4.1. Authorized cementitious binders

As binding solutions, certain cements defined by the standards NF EN 197-1 [83] and NF EN 197-5 [149] already exhibit a reduced carbon footprint compared to Portland cement due to a substitution of clinker content. These various cements and their footprint are illustrated in Fig. 22. The figure below presents the carbon footprints derived from the environmental product declarations (EPDs) of various types of cement available on the SFIC website [150]. The values shown in this graph are based on the updated EPDs of the cements as of June 2022, considering a carbon footprint for blast furnace slag with an economic allocation. In May 2022, the DHUP (Department of Housing and Urban Planning) published a report recommending the inclusion of

an economic allocation between pig iron and blast furnace slag at a rate of 1.4% for blast furnace slag, equivalent to 83 kg CO2 eq./ton (this value does not include emissions related to grinding).

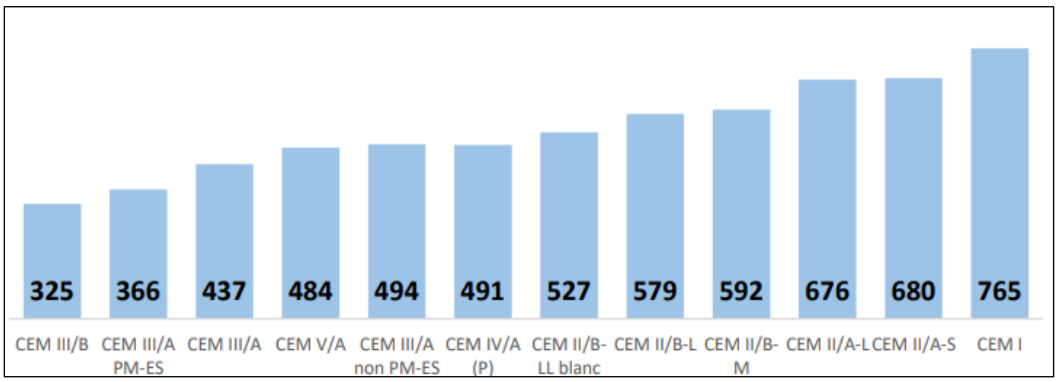

Fig. 22. Carbon footprint associated with the production of various types of standardized cements [150].

The nomenclature of cements defined by NF EN 197-5 [149] standards is as follows:

- CEM I: Portland cement containing as principal constituent at least 95% clinker.
- CEM II: Composite Portland cement containing at least 50% clinker, combined with other constituents among those listed below.
- CEM III: Blast furnace, containing 5 to 65% clinker, combined with blast furnace slag.
- CEM IV: Pozzolanic cement, containing 45 to 89% clinker, combined with pozzolanic constituents (silica fume, natural or calcined pozzolan, or fly ash).
- CEM V: Composite cements containing 20 to 64% clinker, combined with 18 to 49% slag and 18 to 49% natural or calcined pozzolan, or fly ash.
- CEM VI: Composite cements containing 35 to 49% clinker, combined with 31 to 59% blast furnace slag and 6 to 20% of another constituent.

Overall, the observed decrease in carbon footprint in the previous figure is almost proportional to the clinker content within the mix [151].

The cements considered of lowest carbon footprint are those in which a high clinker content is replaced by supplementary materials such as silica fume, natural pozzolan, calcined natural pozzolan (including calcined clays), siliceous fly ash, calcareous fly ash, and limestone.

1.4.2. Substitution of cement by mineral additions

This thesis focusses on replacing clinkers with mineral additions such as limestone additions and calcined clays such as metakaolin or calcined excavated clays. The abundance of the utilized materials is observed by Scrivener et al. [152] as shown in Fig. 23.

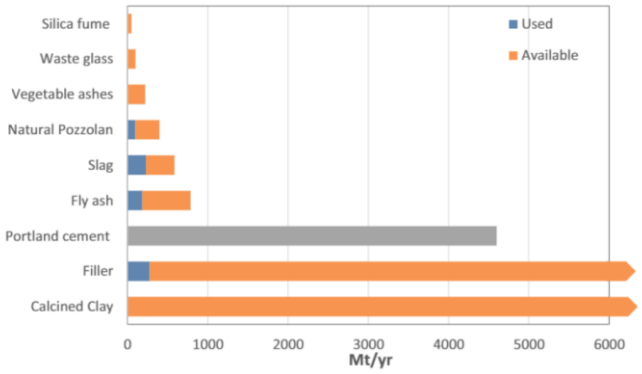

Fig. 23. Estimation of the mineral additions by Scrivener et al. [152].

Due to their chemical nature and manufacturing processes, both limestone additions and metakaolin (calcined kaolinitic clay) present reduced carbon footprints between 40 and 60 kg CO_2 equivalent per ton for limestone additions and 139 kg CO_2 equivalent per ton for metakaolin [151]. The incorporation of limestone additions and calcined clays into concrete is thus an interesting avenue for formulating decarbonized binders. A chapter in this thesis study is dedicated to the design of low carbon concrete, namely as limestone calcined clay cement with evaluation of the mechanical, rheological, and microstructural properties of the designed formulations. Three types of clays are utilized as metakaolin, dredged sediments, and excavated millstone clay.

1.4.3. Limestone

The limestone additions are defined by the NF P 18-508 standard [153] as dry products, obtained by grinding and/or selection, from deposits of limestone rocks that may be dolomitic, massive, or loose. They are mainly composed of calcium carbonate with the formula $CaCO_3$, and the content determines the purity of the obtained addition. The map presented in Fig. 24 lists the quarries for the exploitation of carbonate rocks in metropolitan France in 2015 [154].
The map excludes carbonate rock quarries for use in cement production but serves to highlight the widespread availability of this resource throughout the French territory. Exploiting limestone for

use as an additive could potentially increase, becoming locally accessible to all concrete industry professionals. In 2015, it is estimated that 20.3 million tons of limestone were extracted, contributing to a total estimated production of carbonate rocks at 37.3 million tons. According to a report by BRGM [154], there are also numerous untapped deposits in the territory. However, environmental regulations restrict access to these deposits.

The production of limestone for use as an additive in concrete is estimated to be between 4 and 10 million tons per year (Cerib data). A gradual growth in both demand and production is also observed. Aggregate producers are beginning to enter the limestone additive market [150].

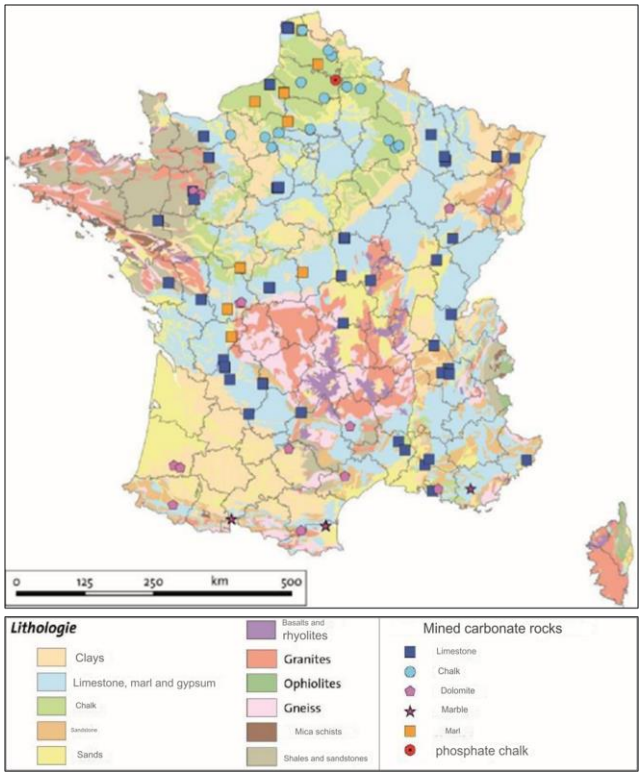

Fig. 24. Distribution of carbonate rock quarries in France [154].

1.4.3.1. Limestone production method

Initially, limestone rocks are extracted from quarries using explosives or hydraulic excavators, depending on the hardness and friability of the rock. However, the latter method is generally preferred to minimize significant rock degradation. Following the cutting operations, the obtained blocks are sent to the factory for processing (Fig. 25).

The extracted rocks are then crushed or ground, screened, and sometimes washed to eliminate pollutants and clays. Through mechanical grinding, it is possible to obtain aggregates of various sizes, and even fillers with dimensions less than 80 µm [151].

Fig. 25. Limestone blocks.

1.4.3.2. Incorporation of limestone into cementitious binders

The limestone powders obtained from the previously mentioned processes can be used as a filler (aggregate of which most grains pass through a sieve of 0.063 mm [155]), type I addition (inert addition [156]), or as the primary or secondary constituent of cement [151].

To be considered a filler, the crushed limestone must meet granulometric criteria prescribed by the EN 12620 standard [155]: 100% passing through a 2 mm sieve, 85% to 100% passing through a 0.125 mm sieve, and 70% to 100% passing through a 0.063 mm sieve. In this case, it is used as a granulometric corrector with the aim of increasing the compactness of the granular skeleton.

As a component of cement, limestone must meet the requirements indicated by the NF EN 197-1 standard [83], namely:

- Calcium carbonate content greater than or equal to 75% by mass.
- Clay content less than 1.20 g/100 g (methylene blue test).
- Total organic carbon content is either less than 0.20% by mass (classified as "LL") or less than 0.50% by mass (classified as "L").

The compliance of limestone as a type 1 addition is governed by the prescriptions of the NF P 18-508 standard [157]:

- Minimum 70% passing through a 0.063 mm sieve.
- Blaine specific surface area greater than or equal to 220 m^2/kg.
- Activity index greater than or equal to 0.71.
- Total carbonate content (limestone and dolomite) is greater than 90%.
- Total calcium carbonate $CaCO_3$ content greater than 65%.
- Other chemical characteristics (content of organic matter, chlorides, sulfates, alkalis).

Finally, according to the NF EN 197-1 [83] and NF EN 197-5 standards [149], it is possible to incorporate different mass fractions of limestone according to different types of cement:

- Portland limestone cement:
  - CEM II/A-L or CEM II/A-LL: 6 to 20% by mass.
  - CEM II/B-L or CEM II/B-LL: 21 to 35% by mass.
- Portland composite cement:
  - CEM II/A-M: 6 to 20% by mass.
  - CEM II/B-M: 21 to 35% by mass.
  - CEM II/C-M: 6 to 20% by mass.
- Composite cement:
  - CEM VI: 6 to 20% by mass.

The use of limestone in cementitious materials is widespread and regulated by a strict normative framework. In the context of this study, the incorporation of type 1 limestone additions, sometimes exceeding normative limits, is the subject of research.

1.4.4. Metakaolin

Metakaolin stands out as the most widely utilized source of calcined clay, and its availability is abundant in France. Additionally, it is employed as the calcined clay component in formulations that incorporate limestone and calcined clay.

According to a report from BRGM published in 2018, there were 41 quarries extracting kaolin or kaolinic clays in France in 2017 [158]. In the same year, the authorized production was 2,085 kt for kaolin and 2,135 kt for kaolinic clays. In comparison, the overall annual production is 400 to 450 kt [158].

As shown in the map presented in Fig. 26, the extraction sites for kaolin and kaolinic clays are relatively evenly distributed across the country. It can be envisioned that in the case of an increase in demand for kaolin for incorporation into concrete, its production would tend to rise.

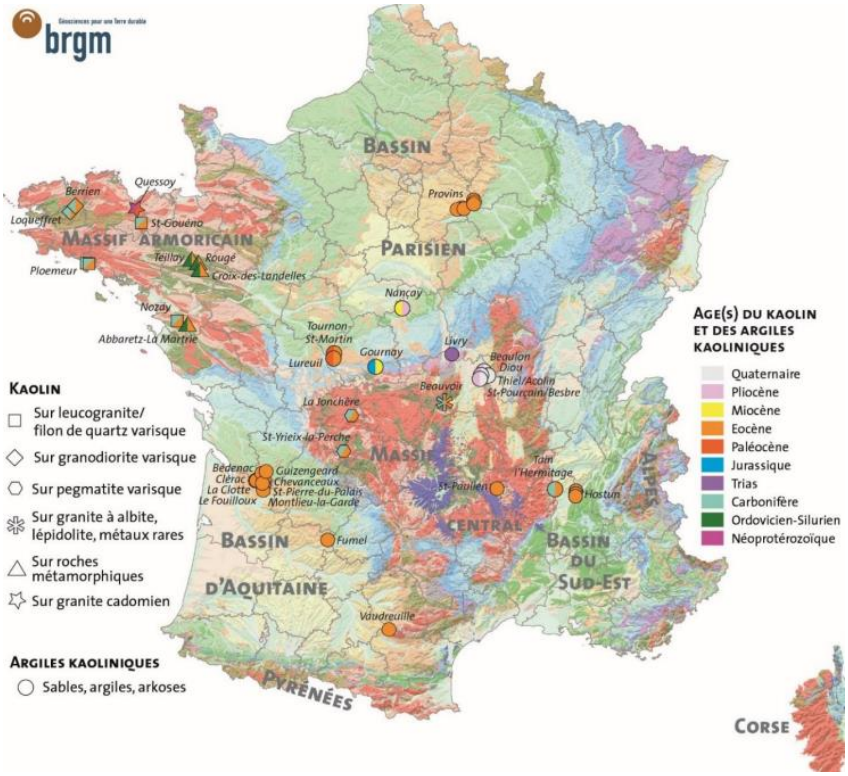

Fig. 26. Availability of kaolin clay in France [158].

1.4.4.1. MK production

Metakaolin is obtained by firing a kaolinic clay at a temperature between 600 °C and 900 °C. In this temperature range, a dehydroxylation reaction occurs as illustrated below.

$$Al_2O_3 * 2SiO_2 * 2H_20 \rightarrow Al_2O_3 * 2SiO_2 + 2H_2O \quad \text{Eq. 10}$$

During this reaction, the crystallization water is gradually eliminated, progressively deteriorating the crystallinity of kaolin. An amorphous "meta-phase" is then obtained [159]. Depending on the quantity of amorphous phases formed, the produced metakaolin is more or less reactive.

Various calcination methods exist, such as fluidized bed furnaces, fixed bed reactors, or rotary kilns. Murat and Bachiorrini [160] tested these methods to evaluate the ideal calcination temperature. They determined that metakaolins obtained at a temperature between 700 °C and 800 °C were the most reactive, providing optimal strengths when mixed with lime at 7 and 28 days.

These calcination processes are time-consuming and represent a significant energy consumption. More recently, the flash calcination process has been developed. In a few seconds, the kaolin is calcined using a flame raised to 900 °C. This method is now the most widely used as it offers better efficiency and more reactive metakaolins. Cassagnabère et al. [161] compared the reactivities of metakaolin obtained by fluidized bed and flash calcination. They observed by XRD analysis that the level of amorphization of metakaolins obtained was higher with flash calcination. Additionally, the manufacturing process influences the morphology of the obtained metakaolins. The fluidized bed calcination process followed by grinding produces angular and protruding particles. Through grinding and then flash calcination, the particles are more vitrified and spherical. However, Garcia-Diaz [160] observed that flash calcination led to the formation of porous agglomerates. It will be seen later in this manuscript that these agglomerates have a detrimental effect on the reactivity of metakaolin and the functional properties of the resulting products, especially rheological properties.

The chemical composition of the chosen kaolin also influences the properties of the resulting metakaolin. Depending on its purity (kaolinite content), the produced metakaolin will have different reactivity. Cassagnabère et al. [161] compared metakaolins obtained by firing kaolins from different sources. The quality of metakaolin can be characterized by its SiO_2/Al_2O_3 ratio. They determined that a ratio of 1.51 corresponded to a metakaolinite content of 68%, compared to 53% for a ratio of 2.67. They also estimated that the optimal ratio is 1.18. A higher ratio, therefore, indicates a high impurity content and hence lower reactivity.

1.4.4.2. Incorporation of MK into cementitious materials

Metakaolins used in cementitious materials must comply with the specifications of the NF P 18-513 standard [162]. They are defined into two types: Type A with high activity (minimum activity index of 100%) and Type B with medium activity (minimum 90%). This standard also defines other requirements, including:

- A sum of mass content of silica (SiO_2) and alumina (Al_2O_3) of at least 90%.
- Fixation of calcium hydroxide $Ca(OH)_2$ of at least 700 mg/g of metakaolin (modified Chapelle test).

According to the NF EN 197-1 standard, pozzolanic materials can be used in the composition of standardized cements, provided they have a minimum reactive SiO_2 content of 25 % by mass. The NF EN 197-1 [83] and NF EN 197-5 [149] standards define the contents of calcined natural pozzolans for the formulation of standard cements:

- CEM II/A, B, or C: maximum 20%, 35%, or 50%, respectively.
- CEM IV/A or B: same for 35% to 55%.
- CEM V/A or B: same for 30% to 49%.

Due to its reactive nature, metakaolin can be incorporated into cement at higher levels than limestone addition. Ideally, this incorporation should be limited based on the metakaolin's ability to react with the formed portlandite.

1.4.5. Limestone calcined clay cement (LC3)

It emerges from the literature review incorporation of metakaolin, and limestone filler has advantages on the performance of concrete as will be discussed in the upcoming chapters.
To substitute a larger amount of cement with these additions, ternary blends can be created known as limestone calcined clay cement (LC3). In recent years, research has been conducted on the synergistic effects between these two additions. For instance, the fluidizing effect of limestone filler can partially offset the high-water demand of metakaolin. Conversely, the beneficial effect on mechanical properties and certain durability properties exerted by the pozzolanic reaction can compensate for the dilution effect of limestone filler [151].
A new type of cement, LC3 (Limestone Calcined Clay Cement), consists of a blend of 50% clinker, 15% calcined clay, 30% limestone filler, and 5% gypsum. It is considered to achieve performance equivalent to CEM I at 28 days. Recently, this composition has been included in the NF EN 197-5 standard [149]. According to this standard, the LC3 binder is classified as Portland cement composite (CEM II/ C-M) as illustrated in Fig. 27.

Main types	Notation of the products (types of cement)		Composition (percentage by mass a)										
			Main constituents										Minor additional constituents
			Clinker	Blast-furnace slag	Silica fume	Pozzolana		Fly ash		Burnt shale	Limestone		
						natural	natural calcined	siliceous	calcareous				
	Type name	Type notation	K	S	D [b]	P	Q	V	W	T	L [c]	LL [c]	
CEM II	Portland-composite cement [d]	CEM II/ C-M	50-64	‹---------- 36-50 ----------›									0-5
CEM VI	Composite cement	CEM VI (S-P)	35-49	31-59	–	6-20	–	–	–	–	–	–	0-5
		CEM VI (S-V)	35-49	31-59	–	–	–	6-20	–	–	–	–	0-5
		CEM VI (S-L)	35-49	31-59	–	–	–	–	–	–	6-20	–	0-5
		CEM VI (S-LL)	35-49	31-59	–	–	–	–	–	–	–	6-20	0-5

[a] The values in the table refer to the sum of the main and minor additional constituents.

[b] In case of the use of silica fume, the proportion of silica fume is limited to 6-10 % by mass.

[c] In case of the use of limestone, the proportion of limestone (sum of L, LL) is limited to 6-20 % by mass.

[d] The number of main constituents other than clinker is limited to two and these main constituents shall be declared by designation of the cement (for examples, see Clause 6).

Fig. 27. Percentage by mass of CEM II/ C-M binder [149].

1.4.5.1. Limestone calcined clay cement (LC3) impact on rheology

The combination of limestone addition and metakaolin seems to decrease the negative effect on rheological properties of using MK alone [151]. Muzenda et al. [163] prepared cement pastes using binary and ternary blends (W/C ratio of 0.45). When metakaolin is used, the shear threshold and plastic viscosity measurements are consistently higher than those of the reference. The LC3 blend shows intermediate values between the reference and this binary blend. According to them, the fineness of metakaolin and its tendency to form flocs explain the reduction in the initial and time-dependent workability of the blends. These observations were also made by Ez-zaki et al. [163], who also prepared cement pastes using binary and ternary blends (W/C ratio of 0.5). According to Vance et al. [164], it is primarily metakaolin that governs the properties of these types of blends. Additionally, when a finer limestone filler is used, plastic viscosity increases due to increased blend compactness.

Avet and Scrivener [165], for example, observed that an LC3-based concrete requires twice as much superplasticizer as a Portland cement-based reference for the same Abrams cone slump (W/C ratio of 0.43). According to Nair et al. [166], superplasticizer particles can be trapped in the spaces between metakaolin layers, rendering it ineffective. The behavior of LC3-based mixes also

depends on the water content. Nair et al. [166] observed that these mixes exhibited a rheofluidizing behavior for a W/C ratio greater than 0.4. For lower water contents, the plastic viscosity of the mix remains constant despite an increasing shear rate. In terms of maintaining rheological performance, the lower the water content, the more rapidly the slump reduction measured on fresh concrete decreases. The authors were unable to achieve slump retention similar to a Portland cement-based reference for an LC3 mix. Finally, the presence of metakaolin imparts a thixotropic behavior to the blend. Hou et al. [166] indeed observe this type of behavior, associating it with the gradual formation of flocs at rest. The longer the resting time, the more they estimate that the amount of water trapped by the flocs is significant. From these various studies, it is evident that the rheological properties of LC3-type blends are improved compared to binary blends with Portland cement and metakaolin. Nevertheless, the obtained workability can be problematic as it is reduced by metakaolin, although partially compensated by limestone filler, especially when the mix has low water content.

1.4.5.2. Limestone calcined clay cement (LC3) impact on mechanical strength

The hydration interactions of metakaolin and limestone addition can allow for the substitution of Portland cement with higher dosages of mineral additions than in the case of binary mixes [151]. Ferreiro et al. [167] estimated that, for this purpose, the mass ratio between metakaolin and limestone addition (MK: LL) should be 2:1. They found that it is for this ratio that the best mechanical strengths at early ages and at 28 days are achieved. According to them, the various mechanisms involved in the development of strengths in this type of mix can be classified in increasing order as follows: filler effect, hydration synergies between limestone addition and metakaolin, pozzolanic reaction.

Antoni et al. [168] substituted Portland cement with mixes (denoted MK-Bx) up to a rate of 60% (mass ratio MK:LL of 2:1). The results obtained on standardized mortar specimens (W/C of 0.5) are presented in Fig. 28. It can be observed that it is possible to achieve similar or even higher compressive strength compared to the reference up to a content of 60% at 28 days. However, the strengths obtained at 24 hours are significantly reduced due to dilution effects. Concrete based on Portland cement and LC3 has been compared by Dhandapani et al. [169]. The last also determined that LC3-based concretes exhibited better compressive strengths (for similar W/C ratios and paste volumes) at all test ages, except at 2 days.

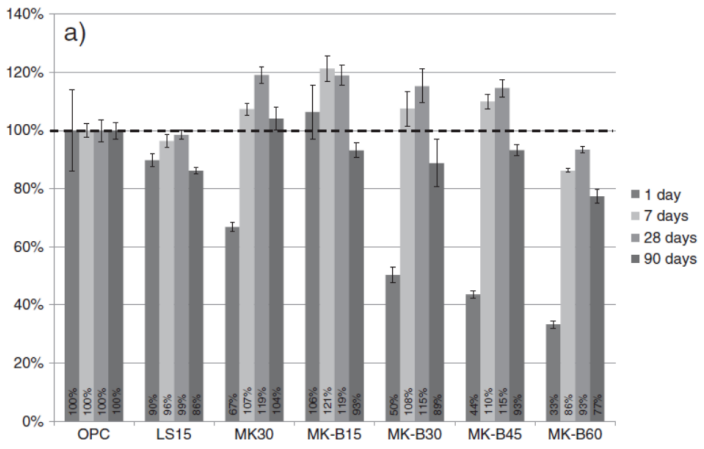

Fig. 28. LC3 compressive strength [168].

Other authors do not make the same observations at 28 days. Roziere et al. [169], for example, observe that for a substitution rate of 30%, the strength obtained at 28 days is equivalent to 83% of that of Portland cement alone (mortars at W/C of 0.5). For a substitution rate of 45%, the strength is reduced to only 65%. However, they observe that for a 30% substitution of cement with metakaolin alone, the obtained strength is only 74%, demonstrating the relevance of ternary mixes in this case.

These differences may arise from the purity of the metakaolins used. Nied et al. [169] determined that a purer metakaolin leads to higher strengths at 28 days for a mix of 60% cement, 30% metakaolin, and 10% limestone addition. However, at an early age, the purity of metakaolin has little impact. Finally, they state that the optimal MK: LL mass ratio depends on the purity of the metakaolin used.

1.5. Dredged sediments

1.5.1. Definition of sediments

The term sediment has various meanings [86]. YANNICK [170] defines it as an accumulation of mineral and organic dredged materials. AMAR [31] describes sediments as fine mineral particles come from dredging operations in seas and rivers. In the context of marine activities, sediments refer to fine, contaminated materials that are dredged at a rate of 56 million m^3 per year in France [171][172]. These materials are categorized as waste with high moisture content and organic matter [173][174][175]. As per the Waste Framework Directive 2008/98/EC

dated November 19, 2008, once dredged sediments are deposited on land, they are officially categorized as waste [176]. The specific designation of sediments, whether riverine or marine, depends on the nature of the dredging environment [177]. Another definition of dredged sediments pertains to their sedimentation mode, describing them as a collection of particles resulting from the earth's disintegration, the precipitation of suspended matter carried by water or air [178], or materials originating from three stages: erosion, transport, and deposition. Sediments are typically identified by their physico-chemical properties, such as grain size, mineralogical composition, water content, and organic matter (OM) [176]. They may also contain varying levels of pollutants, posing challenges for direct utilization in certain applications. Consequently, a thorough physico-chemical and environmental characterization is essential to determine the most appropriate management approach, including offshore disposal, onshore storage, treatment, valorization, etc. [176]. Fig. 29 depicts a dredging operation of sediments in a water current.

Fig. 29. Dredging sediment operation [179].

1.5.2. Origin of sediments

Sediments can exhibit diverse characteristics depending on their origin and nature [86]. According to SCHNEIDER [180], sediments can be distinguished based on endogenous and exogenous origins. Endogenous origin refers to internal sources within the environment, typically involving plant and animal debris. On the other hand, exogenous origin results from external inputs, encompassing natural sources like soil erosion, decomposition of animal or plant matter, as well as anthropogenic contributions such as suspended matter, organic materials, nutrients, and micropollutants due to agricultural, industrial, and domestic discharges directly into the

neighboring environment. Furthermore, BEAUCHAMP [181] proposed a definition based on physical or chemical origin:

- Detrital sedimentary rocks arise from the breakdown of rocks or organisms, including conglomerates, sands, and sandstones.
- Chemically derived sedimentary rocks result from the precipitation of dissolved substances in water, such as rock salt (a saline rock composed of K_2CO_3), limestone rocks, and flint.
- Biochemical sedimentary rocks originate from the synthetic activity of organisms, including coals and continental limestone (continental limestone rocks).

Moreover, sediments are generally associated with climatic, geological parameters, or more frequently, with the power of water currents [176] as shown in Fig. 30.

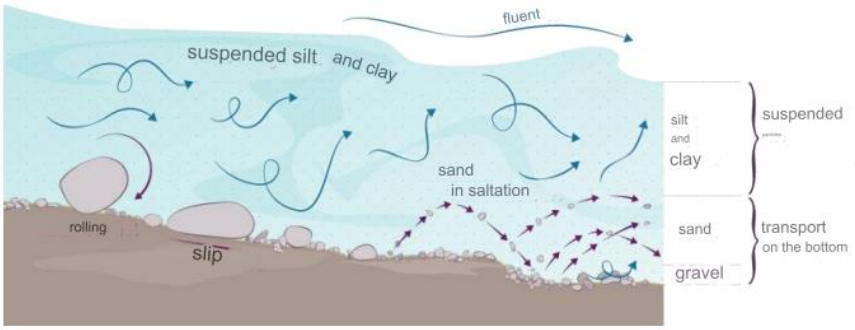

Fig. 30. Transport of sediment particles by water currents [182].

The latter induces erosion, transportation, and sedimentation of soils and rocks. The force of the water current creates both a mechanical force that alters rocks due to friction and a strong capacity for the dissolution of chemical elements present in soil and rocky materials, as well as organic matter. AMAR et al. [20] mentioned the recommended parameters and characterization methods used to study the sediments properties as shown in Table *3*.

Table 3. Recommended characterization methods for sediments [20].

	Parameters	Characterization methods	Standards
Physical characterization	Granulometry	Laser particle size distribution	NF ISO 13320-1
	Density	Helium pycnometer	NF EN 1097-7
	Specific surface area	Brunauer-Emmett-Teller	NF EN ISO 18757
	Water content	Water content test	NF P94-050
	Clay content	Methylene blue value test	NF P94-068
	Plastic limit	Casagrande apparatus	NF P94-051
	Liquid limit	Rolled thread method	NF P94-051
	Mass Loss	Loss on ignition	NF EN 15169 NF EN 12879
Chemical characterization	Chemical elements Oxide elements	XRF	-
	Carbon content	TGA	-
	Mineral and organic pollutants	Leaching test	NF EN 12457-2
Mineralogical Analysis and Microscopy	Identification of minerals	XRD	-
	Quantitative determination of mineral	XRD Rietveld	-
	Morphology	SEM	-
Investigation methods for material and mortars	Resistance	Mortar formulation	NF P 196-1, NF P18-400
	Strength	Compression and flexural test	NF P 196-1, NF P18-400
	Pozzolanicity	Pozzolanic activity tests: (Chapelle, Frattini, Conductimetry)	NF EN 196-5 NF EN 196-6 ASTM C619-A

The main distinguishing features of sediments include their mineralogical composition, grain size, water content, and organic matter. These characteristics offer insights into the deposition process of sediments and their subsequent evolution.

1.5.3. Composition of sediments

Sediment forms a diverse matrix, with its solid component being identifiable and consisting of both mineral elements and organic material [183]. These compounds play a role in shaping the physical, mechanical, and environmental attributes of the sediment. Additionally, SCHNEIDER [180] identified the essential characteristics of sediments based on their granulometry, mineral composition, water content, organic material, and their micro pollutants. The smallest fractions in sediments are responsible for many of the properties. These fractions called "fines" are commonly accepted as corresponding to the phase less than 63 µm. AMAR [184] and Brahim [176] used the ternary diagram of fine soils to assess the sediment characteristics (Fig. 31).

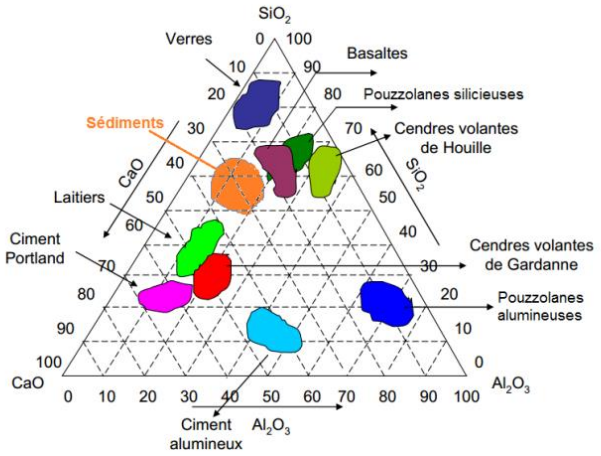

Fig. 31. Ternary diagram for sediment classification by Keil RANKIN.

These relate to the following characteristics [185].

- Mineral matrix (quartz, feldspars, or carbonates).
- Clays, fraction less than 2 µm (kaolinite, montmorillonite, illite or smectite).
- Organic fraction (plant debris, microorganisms, humin, fulvic and humic acids).
- Relative high-water content, presence of organic and mineral pollutants.

1.5.3.1. Granulometry Composition

The sediment's grain size essentially consists of a coarse mineral part (sandy fraction) and a fine part (mud fraction) [185].

- The coarse fraction of sediments with a diameter greater than 63 µm consists mainly of sands and inorganic silicate materials. Sandy sediments have low cohesion, a small contact surface between different sediment particles, and little affinity to contaminants [186].
- The fine fraction of sediments with a diameter less than 63 µm is mainly composed of clay with a diameter between 0.2 µm and 2 µm, and silt with a diameter between 2 µm and 63 µm. This fine fraction generally contains clays and organic materials [187].

The sediment's grain size plays a major role in the capacity to fix contaminants, allowing for the selection of appropriate treatment solutions for different sediments. Indeed, Gosselin et al. [188] conducted their study on sediments from Hamburg and Montreal, and their results showed that contamination of coarse particles is almost negligible, while the fine fraction accumulates more than 70% of contamination [184].

1.5.3.2. Water Content

The water content of sediments is a highly variable fraction, usually dependent on the dredging technique. Generally, three types of water are distinguished: free water, capillary water, and film water. The water filling the voids between solid particles represents a content ranging from 100% to 300% by mass [189]. The water is based on the bonds formed with the particles, categorized into four types:

- Free water: This corresponds to the quantity of water that circulates freely between the particles. It can be separated from solid grains through simple settling or drying.
- Capillary water: This amount of water is linked to fines through capillary forces, occupying very fine interconnected pores (a few microns).
- Bound water: The quantity of water bound or attached to the surface of the particles is part of their chemical composition. Dehydration is only possible through thermal treatments exceeding 105°C.
- Colloidal water: This is the water that forms hydrates by reacting with various elements present in the soil (water between clay layers or in gypsum).

1.5.3.3. Organic materials

The origin of organic matter in sediments is highly diverse, comprising plant residues, humic colloids, or microorganisms. These organic materials undergo continuous decomposition by microbial biomass (microflora: bacteria, fungi, and microfauna). The organic fraction typically constitutes between 2% and 30% of the mass of the mineral fraction in sediments. It is important to note that the fraction of organic matter varies significantly based on the sediment dredging environment, as well as sedimentation time and the kinetics of organic phase decomposition. Generally, they are grouped into four classes [189][190].

- Living organic matter (active biomass).
- Fresh organic matter (plant debris, organisms).
- Evolving plant compounds.
- Humus and stable organic compounds.

The organic phase influences several characteristics of the system, including the mobility and bioavailability of pollutants, especially non-ionic organic materials [191]. Other parameters related to the system impact the chemical balance and the nature of interactions with organic matter [191].

- The pH of the system.
- The redox potential.
- The nature and quality of ionic changes in the environment.
- The nature of organic matter compounds (humic acid, fluidic).

1.5.3.4. Inorganic materials

Inorganic materials are composed of minerals primarily derived from terrestrial erosion and shell debris. The major inorganic components include carbonates, silicates, and clays, with a highly variable size range from colloidal to sandy fractions. Silicates are highly stable anionic chemical groups with a structure based on tetrahedra of $[SiO4]^4$.

Clays are hydrated aluminum silicates with a sheet-like structure and a significant swelling capacity [192][190].

The carbonates found in the sediment are mostly calcite ($CaCO_3$), potentially including magnesite ($MgCO_3$), dolomite ($CaCO_3.MgCO_3$), sodium carbonate ($Na_2CO_3.10H_2O$), and siderite (Fe_2CO_3) [193]. Additionally, inorganic particles are typically coated with iron and manganese hydroxides

and organic substances, providing them with a high adsorption capacity for both mineral and organic contaminants [170].

1.5.3.5. Inorganic and organometallic contaminants

According to Le Hecho et al. [191], inorganic contaminants in sediments include:

- Metals
- Certain salts (sulfates, phosphates, nitrates, chlorides, and ammonium)
- Cyanides

Heavy metals in sediments can originate from the erosion of rocks, soils where they are naturally present, but primarily from human activities. Some elements are essential to living organisms in trace amounts, such as Ti, V, Cr, Mn, Fe, Co, Ni, Cu, Zn, As, Mo, Sn, and Sb, but become toxic at high doses [191]. On the other hand, elements like Pd, Ag, Cd, Au, Hg, and Pd are toxic to living organisms even at low doses [191].

1.5.3.6. Sediment pollutants

The sediments pollutants are divided into categories. The types of sediments pollutants could be either mineral pollutants or organic pollutants.

1.5.3.7. Sediment mineral pollutants

As soon as sectors for the recovery of materials such as sediments emerged, the problem of the contaminants present arose. Due to their fine nature, the presence of organic matter, microbiological activity, sediments tend to store substances, some of which have a pronounced toxic nature: heavy metals, Polycyclic aromatic hydrocarbons (PAHs), Polychlorinated biphenyls (PCB), Tributyltin (TBT), pesticides and various biocides [194]. For MAC FARLANE [195], the origin of this pollution is among other things the fallout from industrial activities, atmospheric pollution, household waste, etc. The main physicochemical properties of sediments which control the interactions between the dredged sediment and the contaminants are according to ALZIEU [194]:

- the quantity and type of fine particles
- the pH of the environment
- redox potential
- the quantity and nature of the ions present
- the composition of organic matter
- salinity

SCHNEIDER [180] suggests that some of these materials are carcinogenic and mutagenic. Among them, mercury (Hg- teratogenic effects on kidneys), lead (Pb- effect on intelligence), Arsenic (As- effect on skin cancer), cadmium (Cd- accumulation in the renal cortex) are the most toxic to human health [191]. The presence of many of these mineral pollutants influence the correct formation of the cement matrix such as Zinc (Zn), copper (Cu) or Lead (Pb).

- Traces of heavy metals

Metallic elements are present in trace amounts in sediments as they are components of numerous rocks. They are non-biodegradable with potential mobility and complexation, and an infinite lifespan. Their origin is linked to human activities such as industrial waste storage, urban activities, agricultural practices, and pollution from atmospheric fallout [176]. The primary trace metal elements include cadmium, chromium, copper, lead, mercury, nickel, selenium, and arsenic [196]. To assess the toxicity of these substances, it is crucial to determine the total content of each element, as well as their chemical form and leaching behavior. The most encountered trace elements in sediments are Arsenic (As), chrome (Cr), Cadmium (Cd), Mercury (Hg), Nickel (Ni), Lead (Pb), and Zinc (Zn).

- Polycyclic aromatic hydrocarbons (PAHs)

Polycyclic aromatic hydrocarbons (PAHs) are aromatic ring structures connected with carbon atoms [196][194]. According to NEFF, they may have various sources, including:

- Secretion by living organisms through biosynthesis.
- Usage of fossil fuel-based materials such as petroleum and its derivatives (gasoline, diesel, etc.), as well as coal.

- Pyrolysis of organic materials at high temperatures, which can occur in forest fires or during the combustion of coal and oil.

PAHs can accumulate in sediments due to their lipophilic properties, and the levels can vary. BAUMARD [196] previously identified the total PAH contents reaching 20 µg/g in sediments at Ajaccio port. Ultimately, PAHs can exert ecotoxicological effects and impact the cellular mechanisms of living organisms. They have the potential to cause carcinogenic or mutagenic abnormalities, especially in mammals. Notably, around 16 molecules have been declared toxic by the "Environment Protection Agency" in the United States, including naphthalene, acenaphthylene, acenaphthene, fluorene, phenanthrene, and others.

- Polychlorinated biphenyls (PCB)

These are long-chain, high-molecular-weight organochlorine compounds resulting from the chlorination of biphenyls to form compounds with chemical formulas of the type $C_{10}H_{(10-n)}Cl_n$. The degree of chlorination leads to products with different physico-chemical characteristics, including thermal stabilization, viscosity, and thermal properties. PCBs were industrially produced in France between 1930 and 1987. The ending of production and the restriction of the use of these compounds followed an awareness of their harmful environmental effects.

These products have numerous isomers (approximately 209) distinguished by the number and position of chloride (Cl) atoms attached to the biphenyl (structural isomers) [197]. These compounds find applications in various fields such as paints, surface treatments, and inks, resulting in specific physico-chemical properties, including semi-volatile compounds, hydrophobicity, and structural stability [194]. The World Health Organization (WHO) has proposed toxic equivalent factors for dioxins, dioxin-like PCBs, and furans. These factors enable the measurement of the relative toxicity of different congeners and, consequently, the assessment of risks to humans. To prevent the impact of these pollutants on the ecosystem, the decree of June 14, 2000, establishes threshold quantities of these derivatives in sediments with two levels, N1 and N2.

- Tributyltin (TBT)

Tributylin compounds (TBT) have a chemical formula of $(n\text{-}C_4H_9)_3S_n\text{-}X$, where X represents an anion or anionic group of unit charge. Among the well-known derivatives of TBT

such as TBT oxide (TBTO), TBT benzoate (TBTB), TBT chloride (TBTCl), and TBT phosphate (TBT-P) [197]. In water, these compounds have weak associations with suspended matter. Moreover, their adsorption kinetics on sediments are very slow and sometimes reversible under mild sediment agitation.

The lifespan of TBT varies depending on the environment. In water, it ranges from a few days to weeks, influenced by factors promoting compound degradation, such as photolysis or microbiological activities. On the other hand, in solid phases, TBT remains relatively stable, potentially persisting for several years [194][197]. TBT derivatives negatively impact the balance of the ecosystem (marine and freshwater), as well as the reproduction of aquatic species.

Despite these concerns, their use is necessary in industries, particularly to ensure the longevity of boats by protecting their hulls against the growth of living organisms. However, there is a significant risk of these compounds spreading into marine and freshwater environments [194].

1.5.4. Regulations regarding dredging operations and management

Dredging operations and sediment management are subject to an authorization or declaration regime (Articles L.214-1 to L.214-6 of the Environmental Code) [198], granted based on decision criteria primarily established according to sediment contamination levels. These criteria are initially proposed by the Study and Observation Group on Dredging and the Environment (GEODE), relying on scientific studies and French or international data, for various classes of contaminants [199]. They are determined based on contaminant levels in sediments, an estimation of their bioavailable fraction, or specific concentrations. These standards then become tools for management and decision-making, utilized in the processing of dredging permits and discharges into the sea. This section aims to mention certain provisions (national and international) concerning dredged sediments.

1.5.4.1. International Regulations

- OSPAR Convention

The OSPAR Convention (OSPAR derived from "Oslo-Paris") is the Convention for the Protection of the Marine Environment of the North-East Atlantic. In force since March 25, 1998, it replaces the Oslo Convention (1972) and the Paris Convention (1978).

- London Convention

The London Convention entered into force on August 30, 1975. The London Convention is the convention on the prevention of marine pollution by dumping of waste (London Convention, 1972). It does not apply when human lives or ship safety are at stake. This convention also does not consider the storage of materials for purposes other than disposal.

- Barcelona Convention

The Barcelona Convention, adopted on February 16, 1976 (subsequently amended on June 10, 1995), primarily focuses on the protection of the Mediterranean Sea. The principles outlined in this convention enable the assessment of pollution and the connection between socio-economic development and environmental quality. The main objective is to promote sustainable projects and protect the environment of the Mediterranean. International regulations are country specific. Overall, various dredging, utilization, or sediment storage operations are conducted in accordance with pollutant thresholds and effects assessed based on usage.

1.5.4.2. National Regulations

The valorization of sediments in France is increasingly regulated by legislation and ministerial orders. Pollutant thresholds and the validation of analysis methods remain the focus of each regulatory development.

The French regulations regarding the management of dredged material immersion were initially defined by the decree of June 14, 2000, and subsequently strengthened by other decrees. The concentration of leachable transition metals remains a determining factor in sediment classification. The Study and Observation Group on Dredging and the Environment (GEODE) has proposed contamination thresholds N1 and N2 levels thresholds for chemical compounds of sediments intended for immersion as shown in Table 4 and Table 5. If the levels of contaminant content fall below the N1 threshold, dredging and disposal activities would be allowed without the need for additional investigations. Conversely, if the contaminant content surpasses the N2 threshold, there is a likelihood of prohibiting dredging and sea disposal operations, as this prohibition represents the least harmful management solution for the environment.

Table 4. Guide values for levels 1 and 2 for metals (mg/kg dry weight) [198].

Contaminant (mg/kg)	N1	N2
Arsenic (As)	25	50
Cadmium (Cd)	1.2	2.4
Chrome (Cr)	90	180
Copper (Cu)	45	90
Mercury (Hg)	0.4	0.8
Nickel (Ni)	37	74
Lead (Pb)	100	200
Zinc (Zn)	276	552

Table 5. Guide values for levels 1 and 2 for polychlorobiphenyl (PCB) congeners (mg/kg) [198].

Contaminant (mg/kg)	N1	N2
PCB total	0.5	1
PCB Congener 28	0.025	0.05
CB Congener 52	0.025	0.05
PCB Congener 101	0.05	0.1
PCB Congener 118	0.025	0.05
PCB Congener 138	0.05	0.1
PCB Congener 153	0.05	0.1
PCB Congener 180	0.025	0

Unlike the offshore disposal of dredged materials, the on-land deposition of sediments, especially regarding their physico-chemical quality, is not yet well-defined by French regulations. In the context of the 2008 Environmental Round Table, the Circular of July 4, 2008, concerning the procedure for sediment management during maritime and river dredging or clearing operations, clarified the following points:

- Definitions of dredging and clearing, and the legal framework applicable to works and operations involving dredging or clearing and thus sediment management.

- The legal framework for resuspension and/or immersion techniques; the possibility of marketing surplus materials and the applicable procedures.
- Procedures applicable when surplus materials are not marketable and when on-land management needs to be considered, including:

  - The state of consideration regarding the distinction between hazardous and non-hazardous sediments.
  - Procedures for on-land management of sediments not characterized as hazardous waste.

In the absence of comprehensive regulations, it is commonly accepted to consider the reference levels prescribed by legislation for the spreading of sludge from sewage treatment plants as shown in Table 6.

Table 6. Admissible limit concentrations in sewage sludge before spreading [198].

Contaminants	Maximum allowable concentration in sludge (mg/kg dry weight)	Maximum allowable concentration in soils (mg/kg dry weight)
Cadmium	15	2
Chromium	1000	150
Copper	1000	100
Mercury	10	1
Nickel	200	500
Lead	800	100
Zinc	3000	300
Cr + Cu + Ni + Zn	4000	-
PCB	0.8	-
Fluoranthene	5	-
Benzo(b) Fluoranthene	2.5	-
Benzo(a)pyrene	2	-

1.5.5. Dredging of sediments

Dredging sediments is an essential process in maintaining navigable waterways, harbors, and ports [200]. It involves the removal of sediment, such as silt, sand, and gravel, from the bottom of bodies of water to ensure safe passage for ships and prevent the accumulation of sediment that can lead to shoaling and reduce water depth. Dredging operations typically involve the use of specialized equipment, such as dredges, which scoop or suction up sediments from the water bottom [201]. These sediments are then transported either via pipeline or barges to designated disposal sites or reclamation areas. In France, sediments are dredged at a rate of 56 million m^3 per year in [171][202][182][203]. The highest volumes of dredged sediments are concentrated in major ports. In 2011, the seven major marine ports (Dunkirk, Le Havre, Rouen, Nantes, La Rochelle, Bordeaux, Marseille) accounted for approximately 88% of the total volume [201]. The three main estuary ports (Rouen, Nantes – Saint – Nazaire, and Bordeaux) represent an annual average of 25 million cubic meters of sediments, including 6.5 million cubic meters of sand and 9.3 million cubic meters of muddy sediments. The five major maritime ports (Dunkirk, Calais, Boulogne, Le Havre, and La Rochelle) dredge an average annual volume of 6.2 million cubic meters of sediments, consisting of about 20% sand and 80% mud.

1.5.6. Dredging sediment problems

Dredging sediments involves the removal of accumulated materials such as sand, silt, and clay from water bodies to maintain navigation channels or to create new ones. However, the process of dredging sediments is not without its problems. One of the major problems of dredging sediments is the potential for harmful environmental impacts. When sediments are dredged, they can contain pollutants and contaminants such as heavy metals, pesticides, and industrial waste. These pollutants can be released into the surrounding water, causing water pollution, and harming aquatic ecosystems.

Furthermore, the disposal of dredged sediments can also pose challenges. Many countries have strict regulations regarding disposing of dredged sediments, requiring them to be treated or stored in designated areas. If the sediments are contaminated, they may not be eligible for beneficial use and must be disposed of properly and environmentally responsible [178].

In addition to the environmental impacts, dredging operations can also have social and economic implications [201]. Moreover, the release of contaminants during dredging activities can lead to health concerns for waterways near cities and industrial sites [201]. To address these complex issues, it is essential to consider a holistic approach that factors in environmental, social, and economic considerations. This may involve implementing advanced sediment treatment technologies, conducting thorough environmental impact assessments before dredging, and engaging with local communities to understand their concerns and potential impacts [201].

Furthermore, investing in research and development to identify innovative and sustainable solutions for managing dredged sediments could pave the way for a more environmentally friendly and socially responsible approach to dredging activities. By addressing the problems associated with dredging sediments at their root, it is possible to minimize negative impacts and work towards a more sustainable coexistence with aquatic ecosystems and the communities that depend on them.

One of the key methods for treating dredged sediments for their use as valorized materials in the construction industry is sediment stabilization. This method involves treating the sediments to reduce their mobility and potential for releasing contaminants. Techniques such as solidification and stabilization can be employed to bind the particles together and immobilize contaminants, making the sediments safer for reuse.

Another important treatment method is sediment washing, which involves the use of water or other solvents to remove contaminants from the sediments. This process can significantly reduce the levels of pollutants in the sediments, making them suitable for various construction applications.

In addition to these treatment methods, thermal treatment can be considered to remediate contaminated sediments [1][16][21][36][37]–[39]. This involves the application of heat to destroy organic contaminants and reduce the concentrations of certain inorganic contaminants, making the sediments suitable for reuse in construction activities. Thus, employing these treatment methods, the dredged sediments can be effectively transformed into valorized materials that can be safely used in the construction industry, contributing to sustainable resource management, and reducing the environmental burden associated with sediment disposal. When considering advanced treatment methods for dredged sediments, one option to explore is flash calcination. Flash calcination is a high-temperature process that involves heating the sediments for a short duration in a controlled environment. This rapid heating process can effectively remove organic contaminants and reduce the concentration of inorganic pollutants, making the sediments suitable

for reuse in construction applications. The flash calcination method offers a fast and efficient way to remediate contaminated sediments and transform them into valuable materials.
By embracing advanced treatment methods like flash calcination and integrating them into dredging operations, it is possible to mitigate the environmental impacts of sediment disposal and create opportunities for the beneficial reuse of dredged materials.

1.5.7. Dredging sediment valorization

The valorization of dredged sediments in the construction industry involves finding innovative ways to treat and reuse these sediments, turning them into valuable construction materials that can be used in various applications Treated sediments by either calcination or flash calcination can activate the pozzolanic reactivity of their clayey content and then can be used in geopolymer concrete formulations or as supplementary cementitious materials (SCMs).

1.5.7.1. Valorization of dredging sediments in geopolymer applications

Merely relying on fly ash, slags, and metakaolin is inadequate for substituting OPC production [208]. Assi et al. [209] proposed that geopolymer concrete could only replace 7% of the annual OPC concrete production. On a global scale, the cumulative fly ash production over the past seventy years is comparable to two years of cement production [210]. Consequently, additional materials must be incorporated into geopolymers; otherwise, the existing worldwide concrete production could be entirely replaced within a span of 7.4 years [15]. Generally, fly ash is used in geopolymer formulations due to its high content of aluminosilicates. Despite the widespread use of FA in GP formulations because of its high SiO_2/Al_2O_3 ratio, this study advocates for the use of FCS instead. Hemalatha et al. [211] conducted research on the attributes of FA and found that for FA class F, the range of SiO_2 and Al_2O_3 is between 37-62.1 and 16.6-35.6, respectively. On the other hand, for FA class C, the range of SiO_2 and Al_2O_3 is between 11.8-46.4 and 2.6-20.5, respectively. As a result, the average $SiO_2/Al2O_3$ ratio for FA class C is 2.51, while that for FA class F is 1.89. The FCS used in this research has a SiO_2/Al_2O_3 ratio of 3.5, which is typically higher than that of FA, thus achieving higher strength [33][212][213][214]. Moreover, in France dredged sediments are widely available and present at a rate of 56 million m^3 per year [33][171][172][182][203]. Therefore, using sediments in geopolymer binder precursors is highly recommended due to its high availability and high content of aluminosilicates.

The use of sediments in geopolymer binders is becoming increasingly interesting for researchers.

Another study done by Lirer et al. [215] discussed replacing sand by sediments in geopolymer formulations, the results of the study showed a more compact microstructure than the composite material made by only sand and thus better compressive strength results as shown in Table 7.

Table 7 . Compressive strength of fly ash geopolymer with sediment or sand [215].

Specimens	sf (MPa)	E50 (MPa)	Yd (kN/m³)
GEO_FA_DR 10	26.2 + 0.13	2561 + 0.2	13,3
GEO_FA_DR 20	24 + 0.06	1940 + 0.10	12,9
GEO_FA_DR 30	15.1 + 0.23	1600 + 0.23	13,5
GEO_FA_DR 50	13.7 + 0.07	1952 + 0.07	13,8
GEO_FA_S 10	25 + 0.05	2737 + 0.23	13,6
GEO_FA_S 20	24.7 + 0.07	2700 + 0.18	14,4
GEO_FA_S 30	11 + 0.09	837 + 0.12	14,4
GEO_FA_S 50	10.7 + 0.02	1137 + 0.20	14,6
GEO_FA	30.5 + 0.09	2810 + 0.45	14,3
GEO_DR	1.9 + 0.16	483 + 0.16	13,5

Finaly, a study done by Mahfouz et al. [216] showed replacement of fly ash by dredged sediments, the results of the study showed that the compressive strength increased upon replacing 15, 30, and 50 percent of fly ash by dredged sediments as shown in Fig. 32.

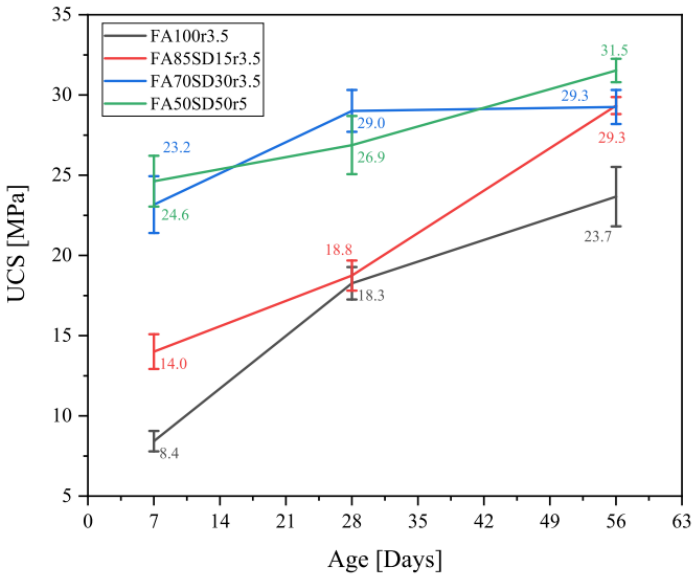

Fig. 32. Compressive strength (MPa) for fly ash geopolymer formulations with sediments [216].

1.5.7.2. Valorization of dredging sediments as SCMs

Other than incorporating sediments in geopolymer formulations, AMAR et al. [20] discussed various applications for sediment valorization as shown in Table 8. The authors highlighted that certain studies utilize treated sediments as supplementary cementitious materials (SCMs) in mortar, concrete, and brick formulations, while others incorporate treated sediments as substitutes for sands and aggregates.

Table 8. Use of sediments in previous works [20].

Authors	Material origin/nature	Study purpose
Achour et al. (2019) [217]	Dredged marine sediment from the Dunkirk Harbor	Evaluation of the performance and the durability of concrete blocks incorporating 12.5% and 20% of dredged sediments. Sediment addition should be limited to 12.5% of the concrete mix to ensure the integrity of mechanical properties
Zhao et al. (2018) [218]	Dredged marine sediment from the Dunkirk Harbor	Study of the use of raw sediment in partial substitution of cement in the manufacture of mortars and concretes It was demonstrated that concrete C30/37 could be designed with 20%

		cement replaced by sediment without the use of admixture
Limeira et al. (2010a. 2011) [219]	Dredged marine sand (DMS) from the Port of Sant Carles de la Rapita (Tarragona, Spain)	The study aimed to assess DMS as an addition (its influence on cohesion and fluidity) or as a fine granular corrector (its influence on compressive strength) Strength resistance improvement in mortars compared to the control mix was identified.
Ozer-Erdogan et al. (2016) [220]	Samples were dredged from Istanbul Ambarl Port, Mersin Erdemli Fishery Harbor, Izmir PETKIM Container Port, and Samsun Port	Sediments are used as a fine aggregate in the ready mixed concrete Incorporation of untreated sediments in concrete decreases the mechanical performances due to the presence of sulfates and chlorides ions
Maherzi et al., (2020) [221]	River sediment from Aire sur la Lys (North of France)	River sediment is used and valorized Use of sediment in substitution of natural sand in resin mortars has been shown interesting Mechanical performance and physicochemical properties of products was satisfying
Xu et al. (2014b) [222]	Urban river sediments were produced by a dredging project in Qinhuai River (China)	The feasibility of the use of urban river sediments as a primary raw material to produce high-insulation brick is established Bricks with 50% urban river sediments fired at 1050 °C
Liu et al. (2016) [223]	Yellow River sediment comes from Huayuankou	Microstructure and performance of stabilized earth bricks prepared from the Yellow River sediment is studied Compressive strength and softening coefficient of stabilized earth bricks is further improved by a polymer bonding agent
Junakova et al. (2015) and Junakova	Sediments dredged from the Klusov and Ruzin	Focus on the possibility of reusing sediment from two Slovak reservoirs as an alternative raw material in concrete production. Mixtures containing 40%

and Junak (2017b) [224]	reservoirs situated in Eastern Slovakia	of binder replacement by the sediment satisfied the strength requirements
Tang et al. (2011) [225]	Fine sediment deposits dredged from the Shihmen Reservoir in Taiwan, China.	The investigation revealed the sediments contain all the necessary elements to enable the bloating and calcining processes within the commercial kiln Sediment-based materials designed have presented compressive strengths comparable to normal density concretes and were 29%-35% lighter.
Ennahal et al. (2020) [226]	Marine sediment from Dunkirk Grand Marine Harbor (France)	Use of sediment as lightweight aggregates as a partial replacement for natural sand in mortar formulations
Mymrin et al. (2017) [227]	Sediment dredged from Brazilian seaports (seaport of Paranagua in Parana state)	Use of dredged sediments of the Atlantic Ocean (up to 60 wt %) to develop a construction material such as bricks and blocks.
Mezencevova et al. (2012) [228]	Sediments dredged from the Savannah Harbor (USA)	The sediment was used as a raw material to produce fired bricks. The compressive strength of bricks made from 100% of dredged sediment and fired at 1000 °C follows ASTM brick criteria for the lowest grade (NW) building bricks. The compressive strength is improved when natural clay is mixed with sediment and met the requirements for severe weathering (SW) building bricks.
Komnitsas (2016) [229]	Marine sediment from the ports of Souda in China, Crete and patras in NW Peloponnese, Greece	Marine sediments were valorized with construction and demolition waste through alkali activation Sediment from the port of Patras can be alkali-activated to produce building materials while the one from Souda port acquire a lower strength (5 MPa).

Wei et al. (2018) [230]	Harbor sediment from Taichung Harbor in Taiwan, China	Preparation of lightweight aggregate from sediment, hazardous steel fly ash.

1.6. Clay materials

1.6.1. Clays definition

Clays are minerals resulting from the alteration of any type of rock forming on the Earth's surface. Clay rocks consist of at least 50% silico-aluminous minerals, often incorporating several non-clay minerals into their composition, such as silica sands, carbonates, oxides, and metallic hydroxides. These rocks are soft and fragile in the dry state and become plastic in the presence of water [231].

The crystalline structure of clays is composed of two basic entities: tetrahedral [T] sites of silicon atoms and octahedral [O] sites of aluminum atoms. The stacking of one or more types of layers forms a sheet. The spaces between the sheets are called interlayer spaces, occupied either by cations or by hydroxyl groups that compensate for the negative charges. This mineral family is called phyllosilicates [232].

1.6.2. Raw Clays

In this paper, the term "clay" refers to a material obtained through extraction, comprising one or more clay minerals (primarily kaolinite and illite) along with additional components like quartz or limestone. Kaolinite and illite clays belong to the phyllosilicate family, constituting approximately 75% of the Earth's crust [233].

Kaolinite is one of the most important minerals due to its wide range of use in applications [234]–[237]. Kaolins are rocks that are formed fundamentally by minerals from the kandite group such as kaolinite, dickite, nacrite and halloysite, accompanied by impurities of quartz, mica, anatase, rutile, ilmenite and small amounts of tourmaline, zircon, and other heavy minerals [235].

Kaolinite ($Al_2Si_2O_5(OH)_4$) is a 1:1 phyllosilicate characterized by the combination of a tetrahedral silica sheet and an octahedral alumina sheet, forming a single layer. In kaolinite, adjacent layers are linked by three hydroxyl groups, while the fourth one remains within the kaolinite layers [235] as shown in Fig. 33.

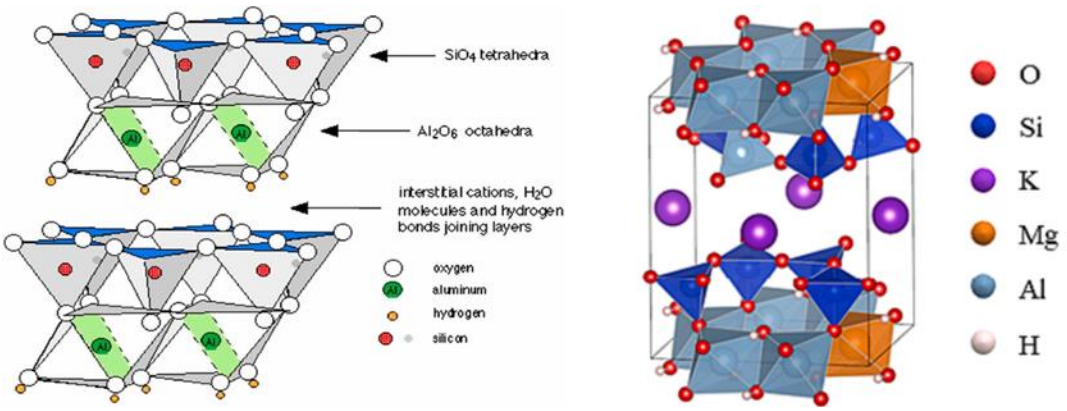

Fig. 33. Kaolinite structure [238] and Illite structure [239].

Illite sheets consist of three layers: two tetrahedral surrounding an octahedral [27]. In illite, isomorphic substitutions, such as replacing aluminum with iron or silicon with aluminum, are common.

1.6.3. Calcined Clays

The calcination process applied to clays serves to thermally activate the clay by disrupting and dehydroxylating its crystalline structure [233]. Elevated temperatures lead to the elimination of hydroxyl groups. The dehydroxylation of kaolinite, a well-characterized phenomenon, occurs within the temperature range of 450 to 600°C, resulting in the formation of an amorphous phase known as metakaolin [232][240][241][242][243]. It is this disordered structure of metakaolin that imparts reactivity to clay [244].To maintain reactivity, the calcination temperature for kaolinite should not exceed 950°C, as beyond this point, metakaolinite transforms into mullite [245][240]. In the case of illite, dehydroxylation primarily occurs from 550°C [246], and optimal pozzolanic activity for calcined illite (also referred to as metaillete) is observed at a calcination temperature of 930°C, as per the study by He et al. [247]. When dealing with a composite clay material containing both kaolinite and illite, a compromise on the calcination temperature is necessary to prevent mullite formation while activating the illite.

The structure of calcined clay plays a crucial role in determining its reactivity. As elucidated in the research by Alujas et al. [248], the pozzolanic reaction is heavily influenced by the degree of structural disorder induced by calcination through clay dehydroxylation. The calcination of hydroxyl groups in clay gives rise to the potential for pozzolanic activity [249]. To assess structural

disorder, powder nuclear magnetic resonance (NMR) serves as a valuable analysis technique. In the case of calcined clays, it is particularly important to monitor the evolution of aluminum groups, employing magic angle spinning (MAS) ^{27}Al NMR spectroscopy. This technique reveals, for instance, that pozzolanic reactivity is closely associated with the presence of aluminum in [V] coordination in the material [249]. A comparison of MAS ^{27}Al NMR spectra between kaolinitic clays and other clays like illite or montmorillonite after calcination at different temperatures allows for the illustration of differences in reactivity among these clays (Fig. 34).

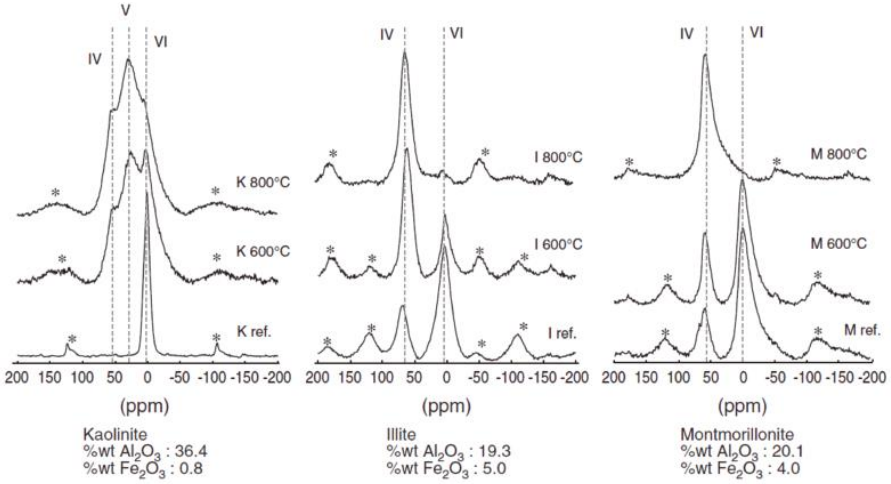

Fig. 34. MAS NMR 27 AL for Kaolinite, Illite, and Montmorillonite [249].

1.6.4. Excavated clays from Grand Paris Express (GPE) Project

Born in 2010, the Grand Paris Express (GPE) project embodies the vision of the sustainable development and planning project for the Ile-de-France metropolis is going to 2030 (Fig. 35). This project is deployed along two main axes: (i) a transport network, the Grand Paris Express, with 205 kilometers of additional rail network planned by 2030; (ii) an objective of building 70,000 new homes per year.

The Société du Grand Paris is tasked with implementing the following key infrastructures:

- 200 km of predominantly underground rail lines (except for sections of lines 18 and 17 Nord).
- 68 new stations, most of which are in relatively dense urban contexts and feature interconnections with existing networks (RATP, SNCF).
- Numerous ancillary structures are spaced approximately every 800 meters along the infrastructure, to meet technical and safety needs of the operational transport network.

- 6 operational centers to ensure the maintenance of both the infrastructure and rolling stock.

However, since the start of the project, the GPE recorded around 23.4 million tons of excavated materials for a carbon footprint of 123 $KTeCO_2$, representing 10% of the GPE's total carbon footprint [250]. Challenges related to excavation management in Ile-de-France (Paris region) and for the work of the GPE are several. They are notably economic, environmental, regulatory, or even competitive. The excavated material from the GPE construction sites can be classified as either inert or hazardous material, therefore they are classified as waste products. Moreover, this classification increased the annual waste volume in Ille-de-France by 10 to 20%.

Fig. 35. Grand Paris Express Project [250].

The excavated soils generated from the GPE project are Coarse limestone, Backfilling sand, Beauchamp sand, and Millstone clays **(**Fig. 36**)**. Millstone clay is carefully chosen, subjected to flash calcination treatment, and then integrated into geopolymer formulations, and used as a substitute for cement as supplementary cementitious materials (SCMs).

Fig. 36. Excavated soils from GPE project [250].

1.6.5. Valorization of excavated clays

Excavated clays are commonly generated each year because of underground space development during construction projects as a byproduct of excavation activities. The waste produced from construction activities encompasses various materials such as concrete, ceramics, asphalt, wood, paper, glass, and excavated soil [16]. The large quantities of excavated soil generated each year, such as the 130 million tons produced in France [17], are also considered waste due to the disposal methods required. Usually excavated clays typically have a high-water content and are not suitable as a construction material. However, there has been a growing effort to find new reuse applications for excavated clay as a sustainable construction material.

After calcination, excavated clays can be used in making geopolymer mixes because it's rich in aluminosilicates. It can also be added to cement mixes, helping cut down on the use of new materials and supporting the environment.

Different studies have used different types of clays as the main source in geopolymer binder precursor and achieving high mechanical and durability properties. Mainly, Metakaolin or calcined kaolin is the best source of silicon and aluminum and is the major material used for the geopolymer matrix [251]. Other than metakaolin, excavated clays from various landfills also have a potential to be used in geopolymer formulations after subjecting them to calcination. For example, Ettahiri et al. [252] studied four types of clays and developed geopolymer formulations of high strength as shown in Fig. 37.

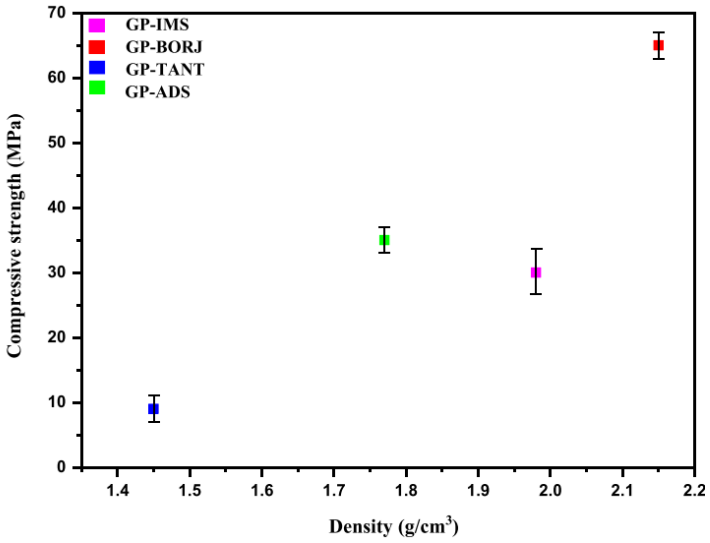

Fig. 37. Compressive strength (MPa) of geopolymer formulations developed with calcined clays [252].

Another study done by Bature et al. [253] used calcined clays from grinding basalt coming from Ireland, the study shows development of geopolymer formulations with high strength (Fig. 38).

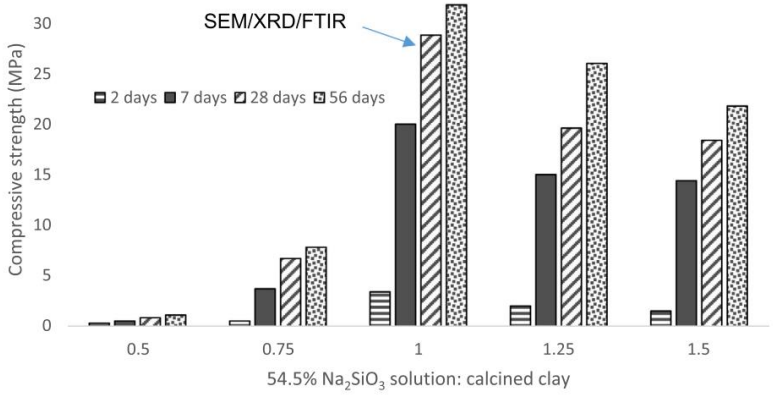

Fig. 38. Compressive strength (MPa) of geopolymer formulations using calcined clays [253].

Moreover, various types of calcined clays have been extensively examined, along with their impact on the mechanical properties of binders, whether binary or ternary [254][255]. Numerous scientific studies [152][256][257][258] have demonstrated the advantages of using metakaolin, and by extension, clays containing predominantly kaolinite, in hydraulic binders, particularly in terms of mechanical properties.

A study conducted by Barbhuiya et al. [259], limestone calcined clay cement (LC3) mortar, with 20% and 30% replacement of Ordinary Portland Cement (OPC) with a combination of calcined

clay and limestone, demonstrated comparable compressive strengths to OPC mortar, with only a slight decrease. The control sample using OPC had the highest strength at all ages, but LC3 mortars exhibited promising mechanical properties. LC3, especially in low to medium-strength applications, emerges as a sustainable alternative to OPC (Fig. 39).

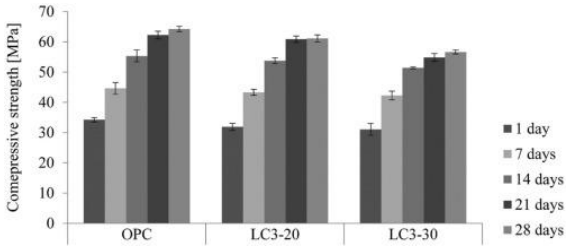

Fig. 39. Compressive strength of mortar using calcined clay [259].

Additionally a study conducted by AVET et al. [260] indicated the relationship between the compressive strength and calcined kaolinite content. The study revealed that as the percentage of kaolinite clay increased the compressive strength increased as well as indicated in Fig. 40.

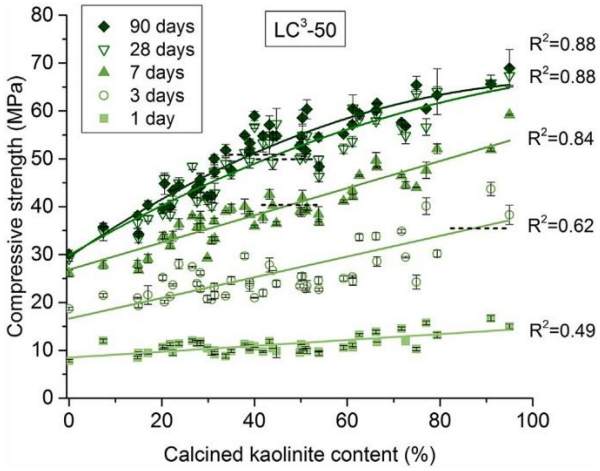

Fig. 40. Compressive strength of LC3 mortar formulations with different clay content (%) [260].

1.7. Flash calcination

Incineration or calcination is a heat-based method employed for treating dredged material. This process involves heating the material to high temperatures (600°C – 1200°C) to eliminate organic contaminants, remove all water, and make certain metallic pollutants inert [31]. The estimated cost of this method is between 40 to 120 € per ton of dry matter [261].

The Flash calcination method is a quick, high-temperature heat treatment technique for fine materials. Initially employed for activating certain clays like kaolinite [262] and clay phases in sediments [31], its principle involves removing excess water through calcination. While traditional rotary ovens are effective for clay activation, they have long process times and high energy costs. Hence, there is encouragement to explore more cost-effective calcination methods [31].

1.7.1. Flash calcination steps

The Flash calcination unit (Fig. 41) used in this thesis is installed at IMT Nord Europe research center (CERI MP). The furnace is capable of calcining approximately 25 kg of material per hour at temperatures up to 900 °C.

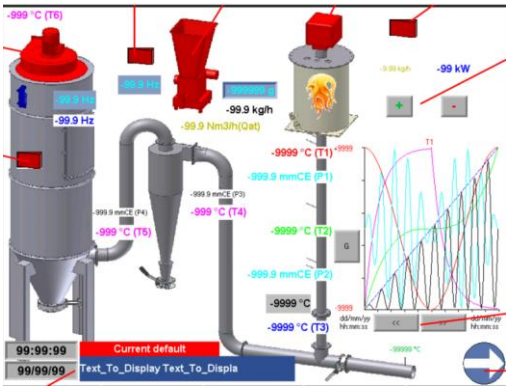

Fig. 41. Flash calcination sketch.

Initially, the materials intended for flash calcination undergo drying at 40°C for 16 hours. This process is conducted to determine their initial organic matter content following the pr EN 17685-1 [263] standard and to eliminate any existing water. This approach was chosen to avoid potential effects from steaming at 105°C.

The products are crushed (separated) using an automatic RETSCH RS200 type crusher initially set at 1000 rpm for 2 minutes or by using a jaw crusher equipped with a sieve at its base. This yields a fine product (maximum aggregate diameter Dmax < 10µm) with controlled particle size. Predetermined quantities of dredged sediment and excavated clays are then prepared, weighed, and introduced into an oven preheated to a specific temperature of 750°C.

Afterwards, the materials are introduced into the combustion chamber through a stream of compressed air. Subsequently, the material particles are heated at high temperatures for a fraction

of a second. Finally, the calcined material is collected at the bottom in a cyclone due to the gravitational force of the material. The methodology of flash calcination is shown in Fig. 42.

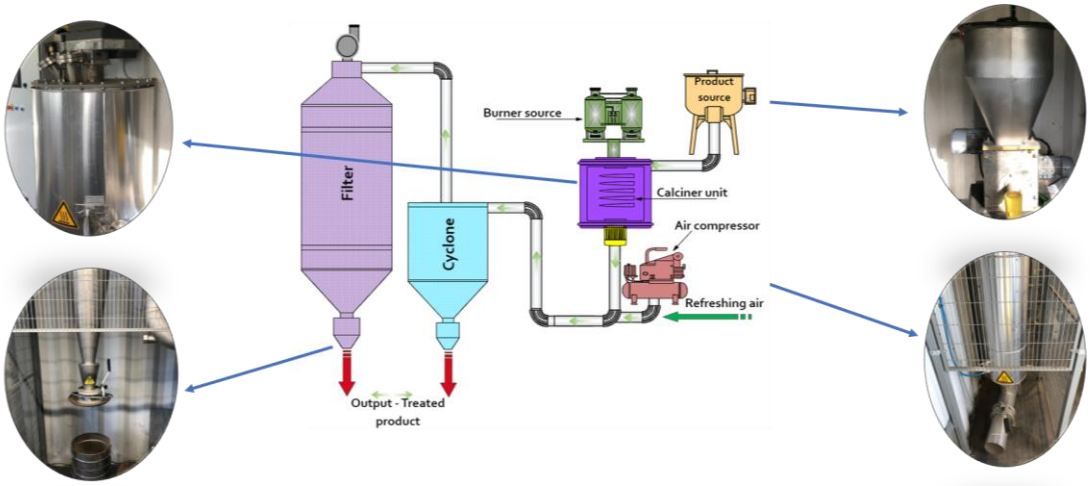

Fig. 42. Methodology of flash calcination [20].

1.7.2. Impact of flash calcination treatment

Flash calcination is a rapid heating and cooling process applied to materials like metakaolin and sediment. This treatment, typically conducted in a flash calcination furnace, has a substantial influence on the material's characteristics. For instance, when applied to dredged sediment, flash calcination enhances reactivity and performance, bringing about alterations in chemical composition and mineralogy. It significantly boosts pozzolanic reactivity, indicating the material's ability to react with lime and contribute to cementitious system strength [31].

Calcined sediments exhibit superior properties compared to raw sediment, including heightened compressive strength and increased porosity. The process improves the material's microstructure, leading to enhanced mechanical performance and resistance development. Additionally, flash calcination reduces material porosity through the pozzolanic reaction. Overall, it proves advantageous for materials like sediment by activating pozzolanic reactivity and enhancing their role in cementitious systems [31].

In the case of metakaolin, flash calcination induces dehydroxylation of kaolinite, resulting in amorphous phase formation and structural transformation. This enhances pozzolanic reactivity, improves particle packing, and reduces water demand in concrete mixtures. The heightened reactivity leads to more efficient consumption of calcium hydroxide, forming additional

cementitious binder and enhancing concrete durability. The refined microstructure contributes to concrete densification, ultimately improving mechanical properties like compressive strength and reducing permeability. Flash calcination thus plays a crucial role in elevating metakaolin's properties, making it valuable for sustainable and high-performance concrete applications.
Metakaolin holds significance across industries, including construction, ceramics, and geopolymer production. Its impact is evident in the calcination and flash calcination processes, common methods for metakaolin production [264].

- **Calcination impact on Metakaolin**

During the calcination process, metakaolin undergoes a thermal treatment that transforms it into a highly reactive pozzolanic material. This involves the dehydroxylation of kaolinite, resulting in metakaolin [265]. Calcination temperature is critical, influencing reactivity and performance. Higher temperatures yield metakaolin with heightened reactivity and improved pozzolanic properties, while lower temperatures may result in reduced reactivity and pozzolanic activity.

- **Flash Calcination impact on Metakaolin**

Flash calcination, a rapid heating process, transforms kaolinite into metakaolin. This process is much faster than traditional methods, taking only seconds [27]. Metakaolin produced through flash calcination exhibits higher dehydroxylation rates, resulting in improved pozzolanic properties. These metakaolins contribute to the enhanced strength and durability of concrete structures [266]. The choice between traditional rotary kiln calcination and rapid flash calcination influences the physical properties and performance of metakaolin as a supplementary cementitious material.

- **Flash Calcination impact on sediments**

A study done by CHU et al. [267] shows the effect of flash calcination on sediments at different temperatures 650 °C, 750 °C, and 800 °C. The study reveals the following findings:

- Flash calcination removes the organic content in raw sediments thus eliminating the effect of late hydration.
- Flash calcination increases the BET specific surface area and density of sediments.

- Flash calcination transforms kaolin to metakaolinite with the formation of anhydrite.
- Flash calcination activates the pozzolanic reactivity of sediments.
- The compressive strength results with flash-calcined sediments showing higher strength compared to raw sediments.
- Flash calcination reduces the metallic trace of elements found in sediments, especially zinc content.

Another study done by Snellings et al. [268] reveals the impact of flash calcination on the properties and pozzolanic reactivity of flash-calcined dredging sediments when producing SCMs for the production of low CO_2 blended cements. The study revealed the following:

- Flash calcination reduced the total organic carbon content by more than 85%.
- The clay minerals were entirely dehydroxylated, clay activation was complete.
- The pozzolanic reactivity of calcined dredged sediments was found to be inferior to metakaolin but superior to siliceous fly ash.

1.7.3. Impact of calcination treatment on dredged sediments and excavated clays in Geopolymer binders

Calcination treatment has a grave importance on the dredged sediments when used in GP formulations in terms of mechanical strength and durability.

A study done by Slimanou et al. [15] compare the impact of using uncalcined and calcined sediments of amounts (0, 5, 10, 15, and 20 wt%) in metakaolin based geopolymer pastes. The author has summarized the compressive strength and water absorption results in Fig. 43. The findings reveal that as the proportion of both untreated and treated dredged sediments rises from 5 to 15% in MK-based geopolymers, there is a gradual increase in compressive strength, peaking at 20.5 and 22 MPa respectively. Notably, variations in sediment ratios indicate that formulations containing treated sediment exhibit higher compressive strength compared to those with untreated sediment. Additionally, water absorption tests demonstrate superior durability for formulations incorporating treated sediments across different sediment percentages. Consequently, formulations utilizing treated sediments exhibit enhanced strength and durability characteristics.

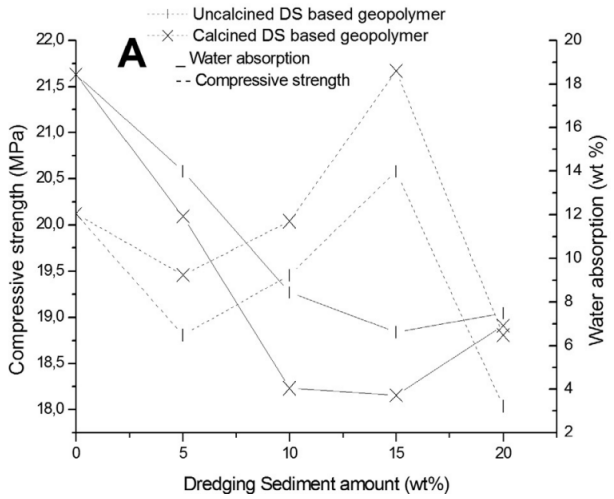

Fig. 43. Compressive strength and water absorption results of uncalcined and calcined sediments with different percentages [15].

Another study done by Ferone et al. [17] shows that calcined clay sediments can be used as a suitable source of polycondensation reactions and develop good mechanical properties. The author has used two types of sediments abbreviated as OC and SA with varying calcination temperatures. The results showed that as the calcination temperature increased, the compressive strength increased as indicated in Table 9.

Table 9. Ferone results on calcined sediments geopolymer [17].

Sample	Compressive strength (MPa)
OC400/N	1.73 ± 0.56
OC400/N/ GBS	14.65 ± 0.99
OC400/N/SS	3.44 ± 0.31
OC400/N/SS/GBS	6.26 ± 0.51
OC750/N	6.20 ± 0.96
OC750/N/GBS	28.10 ± 0.10
OC750/N/SS	6.95 ± 0.59
OC750/N/SS/GBS	14.97 ± 0.41
SA400/N	2.00 ± 0.99
SA400/N/GBS	6.65 ± 0.99
SA400/N/SS	4.40 ± 0.89

SA400/N/SS/GBS	32.19 ± 0.37
SA750/N	8.25 ± 0.15
SA750/N/GBS	35.70 ± 0.70
SA750/N/SS	12.17 ± 0.17
SA750/N/SS/GBS	38.90 ± 0.80

A study done by ESSAIDI et al. [269] reveals the effect of calcination temperature used on two types of clays and their effect on the compressive strength results (Fig. 44). The study revealed that as the calcination temperature increased from 25 °C to 700 °C, the compressive strength increased significantly from a strength < 5MPa to 12.5 and 20 MPa. The strength continued to increase as the calcination temperature increased to 800 °C resulting in a maximum compressive strength of 25 MPa. As the calcination temperature continued to increase to 850-900 °C the compressive strength decreased but still achieved higher results than that of uncalcined samples (25°C).

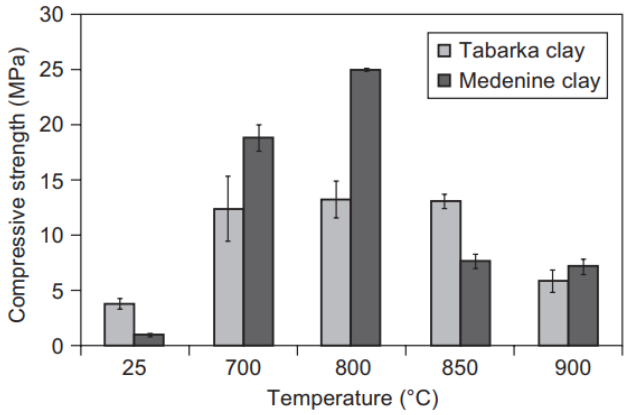

Fig. 44. Effect of calcination temperature on compressive strength results [269].

Another study done by Nmiri et al. [270] confirms the previous results. The study reported the compressive strength results of potassium and sodium geopolymers. The kaolinite clay used was calcined at different temperatures (550, 700, 900, and 1100 °C) and their corresponding compressive strength was evaluated. The results are tabulated below. For both types of geopolymer the compressive strength results are the highest when the calcination temperature was equal to 550 °C and 700 °C whereas the compressive strength decreased when the calcination temperature increased to either 900 °C or 1100 °C.

Table 10. Effect of calcination temperature on geopolymer compressive strength [270].

Calcination temperature of kaolinitic clay °C	Potassium geopolymers				Sodium geopolymers			
	Compressive strength (MPa)	Water porosity (%)	Density (g/cm³)	% water absorption	Compressive strength (MPa)	Water porosity (%)	Density (g/cm³)	% water absorption
550	10.2	24.5	1.95	15.2	13.9	22.2	1.91	13.4
700	34.4	24.3	1.96	14.1	29.9	22.1	2.14	12.9
900	5.2	27.2	1.86	16.9	11.4	25.2	1.98	15.0
1100	4.1	28.3	1.94	17.4	10.4	26.0	1.91	15.4

Chapter 2. Materials and Methods

Chapter 2. Materials and methods

2.1. Materials

Dredged sediments and excavated clays are waste materials. These materials undergo flash calcination at IMT NORD at a temperature of 750 °C then are valorized in geopolymer formulations and in creating limestone calcined clay cement (LC3) formulations.

The first objective of this thesis is to use flash-calcined sediments (FCS) and flash-calcined excavated clays (FCC) as a substituting of metakaolin (MK) with incorporation of ground granulated blast furnace slag (GGBFS) in geopolymer formulations.

The second objective is in the valorization of FCS and FCC in low-carbon cement binders such as limestone calcined clay cement (LC3). The performance of the LC3 with FCS and FCC is evaluated based on reference formulations with MK being selected as the calcined clay material.

The materials' characterization is carried out in the upcoming section.

2.1.1. Dredged sediments

The sediment is extracted from the Noyelles-sous-Lens (NSL) river located in northern France, approximately 20 kilometers away from the IMT NORD EUROPE laboratories (Fig. 45). Upon arrival at the laboratory, the sediments are contained in 50-liter containers, and they have not undergone drying, sieving, or removal of their water content.

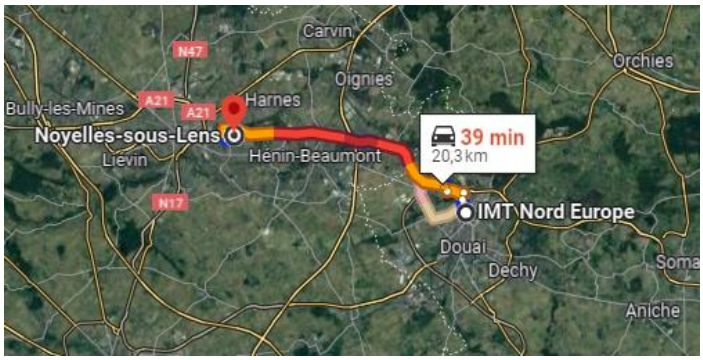

Fig. 45. Noyelles-sous-lens location.

Initially, before undergoing flash calcination, the sediments may contain rocks acquired during the extraction process from the river. To address this, the sediments are initially subjected to drying in a 40°C oven to remove only the free water content without affecting the elimination of their organic

content at this temperature. Subsequently, the rocks are eliminated prior to the grinding process. The resulting products are crushed or separated using either an automatic RETSCH RS200 type crusher set initially at 1000 rpm for 2 minutes or a jaw crusher equipped with a sieve at its base. This process produces a fine product (with a maximum aggregate diameter Dmax < 10µm) with a controlled particle size. At this stage, physico-chemical and mineralogical characterizations are conducted on the raw sediments (RS). Additionally, after flash calcination, the flash calcined sediments (FCS) undergo similar physico-chemical and mineralogical analyses to investigate the impact of flash calcination on the material's characteristics. The dredged sediments, both in their raw and flash calcined states, are depicted in Fig. 46.

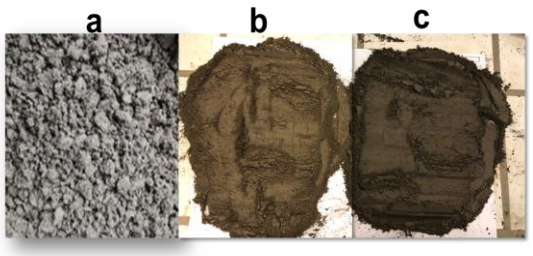

Fig. 46. (a) dredged sediments, (b) raw sediment, (c) flash-calcined sediments.

2.1.2. Excavated millstone clay

The millstone clays extracted for the Grand Paris Express (GPE) project (see Figure in the bibliography section) are acquired through excavation. Similar to dredged sediments, the millstone clays are delivered to the laboratory without undergoing any drying or grinding processes. Consequently, the excavated millstone clays undergo the same procedures as the dredged sediments before being subjected to flash calcination. The excavated millstone clays, in their raw state (RC) and after undergoing flash calcination (FCC), are illustrated in Fig. 47.

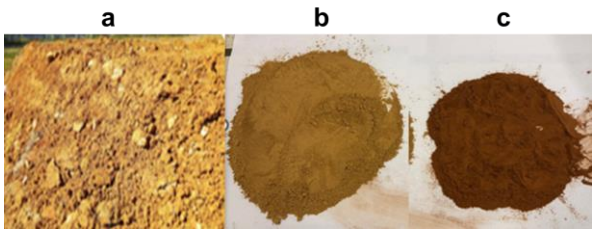

Fig. 47.(a) excavated millstone clay, (b) raw millstone clay, (c) flash-calcined millstone clay.

2.1.3. Metakaolin, ground granulated blast furnace slag, limestone, and ordinary Portland cement

The metakaolin (MK) utilized in this investigation is sourced from ARGICEM and subjected to flash calcination at 750°C. The ground granulated blast furnace slag (GGBFS) employed in this study is procured from ECOCEM. Limestone powder (LS) is derived from the crushing and grinding of natural limestone. The ordinary Portland cement (OPC) utilized is CEM I 52.5 R, supplied by EQIOM France.

2.1.4. Sand

The sand employed in this research is crushed calcareous sand with a particle size of 0-4 mm, supplied by BOCAHUT in the north of France, and it has a density of 2630 kg/m^3. The sand specifications were done according to the standard NF P 18-545 [271] .It was oven-dried at 105 °C for 16 hours then after cooling it was allowed to be used in mixing.

2.1.5. Aggregates

The aggregates used in this study are classified as coarse aggregates having particle size limited to 4-10 mm and 10-20 mm, supplied by BOCAHUT in the north of France (Fig. 48). The coarse aggregates have a density of 2720 kg/m^3. Their specifications were done according to the standard NF P 18-545 [271]. A mixture of both aggregates is used in concrete formulations to ensure achieving high strength and allowable workability.

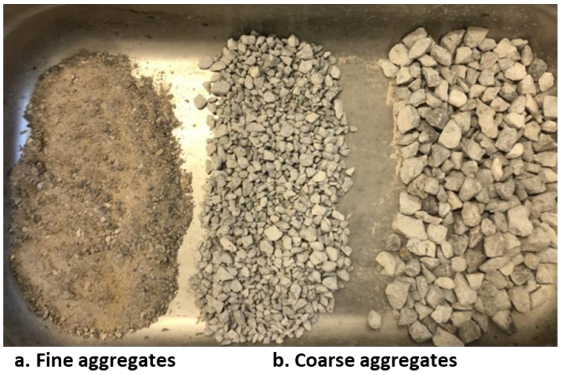

Fig. 48. Fine and coarse aggregates used.

2.1.6. Alkaline reagent (AR)

The alkaline reagent (AR) used for initiating the geopolymerization reaction with the precursor binder is potassium silicate, which was marketed by Woellner® under the brand name Geosil 14157 (Fig. 49). It is a user-friendly product because it does not involve the handling of hydroxides. The composition by weight (%) of the AR is summarized in Table 11.

Table 11. Composition of the AR by weight (%).

Composition of Geosil 14517 solution			
components	K_2O	SiO_2	H_2O
% wt.	21.73	23.27	55.27

Fig. 49. Alkaline reagent (Geosil 14157).

2.1.7. Superplasticizer

The superplasticizer incorporated in LC3 formulations is CHRYSO® Fluid Optima 100, employed to reduce the water content while maintaining the necessary workability.

2.2. Materials characterization methods

Material characterization is conducted on all utilized materials, with a particular focus on both raw and flash-calcined materials, aiming to highlight the influence of flash calcination on the characteristics of the materials.

2.2.1. Materials physical characterizations

2.2.1.1. Water content

The quantification of RS, RC, FCS, and FCC water content are carried out in accordance with the NF P94-050 standard [272]. This parameter is crucial for formulation and allows for the assessment of the consistency of dredging materials. In this study, the determination was performed at different temperatures, specifically at 105 °C, to compare the temperature's influence. The mass mc of an empty metal container is established beforehand. A sample of material is taken, and its initial mass, referred to as the wet mass $mh{+}c$, including that of the metal container, is determined by weighing. The ensemble is then placed in an oven at 105 °C until the mass becomes constant. Subsequently, the mass of the dry sample with the container $ms{+}c$ is determined. The water content $w(\%)$ of the sample is calculated as shown below.

$$W(\%) = \frac{m_{h+c} - m_{s+c}}{m_{s+c} - m_c} \times 100 \qquad \text{Eq. 11}$$

2.2.1.2. Absolute density

The absolute density of materials refers to the mass of a substance per unit volume, without considering pores or voids. This measurement is often used to assess the density of a solid or granular material. It is expressed in kilograms per cubic meter (kg/m³). The absolute density is measured using helium pycnometer type Accupyc 1330 (Fig. 50) according to the NF EN 1097-7 standard [273].

Fig. 50. Helium pycnometer to measure materials' absolute density.

2.2.1.3. BET surface area

The measurement of BET (Brunauer-Emmett-Teller) is carried out in accordance with the NF ISO 9277 standard [274]. The assessment of the mass area, or specific surface area, of

solids through gas adsorption is performed using the BET method using 3FLEX 3500 machine (Fig. 51).

Fig. 51. Measuring BET using 3FLEX 3500 flex.

2.2.1.4. Organic content

The organic matter (OM) present in sediments can have diverse origins. Several authors [275][276][277] have explored the study of these substances and classified them into three evolving fractions: fulvic acids, humic acids, and humins. The findings of these studies seem to confirm that the presence of organic matter can lead to various issues when incorporating dredged sediments into a cementitious matrix. Indeed, the humic acids that constitute the organic matter in sediments play an inhibitory role in cement hydration through two actions:

Adsorption and water retention, potentially resulting in a reduction of the effective water necessary for the complete hydration of the cement.

Combination of humic acids with free lime to form calcium humates. These reactions reduce the quantity of hydration products (C-S-H and portlandite CH) and, consequently, can lead to a decrease in mechanical properties and durability.

The quantity of organic matter in sediments and clays is determined through a loss-on-ignition test, conducted according to the European standard NF EN 15169:12 [278]. The principle involves heating sediment samples in suitable crucibles in an oven up to (550 ± 25) °C. The difference in mass before and after the heating process is used to calculate the loss-on-ignition according to the following formula:

$$Loss\ of\ ignition = \frac{m(c)-m(b)}{m(c)-m(a)} \times 100 \qquad \text{Eq. 12}$$

- m(a): mass of the empty crucible in grams.
- m(b), the mass of the crucible containing the ignited sediment, in grams.
- m(c), the mass of the crucible containing the sample, in grams.

2.2.1.5. Granulometry analysis

Generally, the particle size distribution for fine powders is determined through laser granulometry. The test was conducted using a laser apparatus, the LS 13320 Beckman Coulter model (Fig. 52). For dry testing, the required powder quantity ranges from approximately 0.5 to 5 g, and the specified particle size range varies from 0.5 to 3000 µm. Three test measurements were analyzed for each material to ensure result repeatability.

Fig. 52. Laser granulometry using LS 13320 Beckman Coulter.

2.2.2. Materials physicochemical characterization

The physicochemical characterization for sediments and clays are X-ray fluorescence (XRF), X-ray diffraction (XRD), thermogravimetric analysis (TGA), and scanning electron microscopy (SEM).

2.2.2.1. X-ray fluorescence

This is a technique that allows for the analysis of the chemical elements present in a material and the determination of their respective quantities. When the material is irradiated with

X-rays, it re-emits energy in the form of X-rays, presenting a characteristic spectrum of the sample's chemical composition. By analyzing this spectrum, one can deduce the elemental composition (mass concentrations). The X-ray fluorescence (XRF) of a sample is defined as its ability to emit its own radiation when subjected to X-ray irradiation. Atoms are partially ionized by the removal of an electron. The return to the ground state occurs by filling the electron vacancy with a photon electron. Depending on the considered electronic transition, each atom, and thus each chemical element, has its own photon energy and wavelength. By analyzing the energy spectrum that includes the radiation emitted by all atoms in the material, particularly studying the peak areas, it is possible to obtain a semi-quantitative chemical analysis of the compound. The determination of major elements by XRF spectrometry was carried out using a wavelength dispersive XRF, S4 BRUCKER (Fig. 53).

Fig. 53. X-ray fluorescence using S4 BRUKER.

2.2.2.2. X-ray diffraction

The mineralogical characterization is performed on dried and ground materials (<50 µm). It is mainly carried out through X-ray diffraction (XRD) analysis using a Bruker D2 diffractometer (Fig. 54) equipped with a cobalt anode ($\lambda K\alpha 1$ = 1.74 Å). A fixed divergence slit of 0.6 mm was utilized, and the samples were scanned for 2θ angles ranging from 5° to 80° with a step size of 0.02° and a counting time of 1s. The data were collected at 40 kV and 30 mA.

Fig. 54. X-ray diffraction using D2 Phaser BRUKER.

2.2.2.3. Thermogravimetric analysis (TGA)

The TGA test is done on paste formulations using Netzsch machine model STA 449 F3 Jupiter + QMS Aeolos 403 °C (Fig. 80). It involved increasing the temperature from 40°C to 105°C at a rate of 2°C/min to remove excess water from the samples. The temperature was held constant for 2 minutes at 105°C to stabilize the mass loss before increasing the temperature from 105°C to 1000°C at a rate of 10°C/min to analyze the mass loss at different temperatures.

TGA curves can be used to identify different phases according to various mass loss intervals associated with certain reactions (dehydration, decarbonation, oxidation, etc.). *Table 12* summarizes the characteristic peaks found in TGA according to Nozahic [279].

Table 12. Mineral classifications according to TGA peaks [279].

Composition	Temperature °C	Type of Composition
CSH (rich in lime)	90	Dehydration
CSH (less basic)	125	
CSH et Ettringite	100-180	
CSH	140	
Ettringite	130	
CAH et CASH	180-240	
C_2AH_8	180	
C_4AH_{13}	270	
$Ca(OH)_2$	470	
$Ca(OH)_2$	450-500	
$Ca(OH)_2$	400-600	
Wood	200-380	Combustion
Hemicellulose	250-300	
Cellulose	300-350	
Oil	250-400	Oxidation
	400-550	Combustion
$CaCO_3$ Mode I	780-990	Decarbonation
$CaCO_3$ Mode II	680-780	
$CaCO_3$ mode III	550-680	

2.2.2.4. Scanning electron microscopy (SEM)

The utilization of scanning electron microscopy (SEM) involves the examination of the inner structure of materials at an exceptionally high level of detail. This technique enables a powerful level of magnification, reaching up to 500,000 times, allowing for a comprehensive investigation and analysis of the microscopic components of mortar [206]. The test was done using MEB JEOL diffractometer D2 (Fig. 55).

Fig. 55. SEM using JEOL diffractometer D2.

2.2.2.5. Materials Pozzolanic characterization

To evaluate the pozzolanic reactivity of FCS and FCC, Chapelle test is done before and after flash calcination, followed by conducting the test on MK. As indicated by the standard NF P18-153 [162], to study the pozzolanic activity of the powder materials, a reaction should take place with quicklime (CaO). Firstly, 250 ml of distilled water is boiled to remove the CO_2, then the decarbonized water is added to the mixture of (1g of powder and 2 g of CaO) in an Erlenmeyer flask. The solution will be maintained at a temperature of 85°C for 16 hours under constant stirring using magnetic stirrers. After 16 hours, the system is cooled and 60 g of dissolved sucrose in 250 ml of water is added to the solution under continuous stirring for 15 mins. Then, the solution is filtered, and (25 ± 0.2) ml of clear solution is removed. Finally, titration is carried out with 0.1M HCl using phenolphthalein as a color indicator. The apparatus is shown below (Fig. 56).

Fig. 56. Chapelle test setup.

2.2.3. Effect of flash calcination on materials' characteristics

The physical and mineral characterizations are shown in Table 13 and Table 14, respectively. This study didn't conduct trials to reach an optimum flash calcination temperature for the tested materials, however a study done by Chu et al. [280] shows that flash calcination at 750 °C is optimum for sediments for Noyelles-sous-lens. The author has studied the properties of sediments flash-calcined at three different temperatures, 650 °C, 750 °C, and 800 °C. Comparing the amount of hydrates formed and the fixation of Ca $(OH)_2$, flash calcination at 750 °C showed the best results. Also, it's important to note that even though flash calcination at 800 °C can remove organic content more than that done at 750 °C by 5 %, however at 800 °C, the density has decreased due to recrystallization of mineral phases [280][281], and the specific surface area has decreased from lowering the melting temperature of the material [280][282] . Similar to the flash calcination of sediments at 750 °C, the same temperature is used for millstone clay. The transformation of clay into MK is a common method that could be done by either calcination or flash-calcination. Nicolas et al. [283] mentioned that the transformation of clay into MK at 700 °C can be done with flash calcination. Also, according to the mineralogical composition XRD, MK, and FCC have very similar mineralogy as shown in Fig. 62 and Fig. 63, therefore flash calcination at 750 °C is effective for RC treatment.

Flash calcination at 750 °C with a duration of one tenth of a second was able to eliminate the water content and organic content in both raw sediment (RS) and the raw millstone clay (RC). The flash-calcined materials exhibited complete elimination of water content, and the organic content was reduced by 99% and 94%, respectively. For both materials, their density was higher after flash calcination. That of RS has increased from 2.33 g/m³ to 2.60 g/m³, while that of RC increased from 2.49 g/m³ to 2.71 g/m³. Faure et al. [8] have mentioned in a study about using calcined sediments as SCMs, that raw dredged sediments have an organic fraction that decreases their density. Therefore, the high elimination of the organic content of RS and RC by flash calcination at 750 °C led to an increase in the material's density.

The BET surface area for RS showed a sharp increase from 7.48 m²/g to 27.45 m²/g after flash calcination. However, the BET surface area for RC decreased slightly from 34.36 m^2/g to 33.01 m^2/g. This behavior difference between RS and RC is because pre-treated sediments had a smaller surface area and a higher organic content. Also, their organic content was equal to 13.5%. Ramaroson et al. [284] has stated that the high temperature of normal calcination could increase

the surface area with the increase of temperature up to a maximum of 400 °C. The last has mentioned that this increase is explained by the loss of organic content which generate pores into the sediment particles, thus increasing the surface area [284]. Although flash-calcination has a temperature of 750 °C, however during this process, the organic material is rapidly burned off, leaving behind a porous structure with a higher surface area, thus increasing their pozzolanic reactivity. RC had a small percentage of organic content equal to 8.6%. After eliminating it, the BET was only slightly affected. This suggests that the BET surface area may remain constant for some materials after flash calcination if the material being calcined is already highly porous and has a high surface area before the calcination process. Volet et al. [285] has explained the porous structure of clayey material such as kaolin and metakaolin. The author has deduced that both clayey materials have a disordered porous matrix. Therefore, the porous structure of RC is the explanation why the BET surface area wasn't affected.

Table 13. Physical characteristics of the used materials.

Physical characteristics	**RS**	**FCS**	**RC**	**FCC**	**MK**	**OPC**	**LS**	**GBFS**
Density g/m^3	2.33	2.60	2.49	2.71	2.60	3.15	2.73	2.88
BET m^2/g	7.48	27.45	34.36	33.01	13.59	1.26	1.26	2.70

The chemical analysis demonstrates that the percentage of major oxides remained almost the same after flash calcination, as shown in Table 14. According to the ASTM C618, the class N pozzolan should have the sum of (SiO_2, Al_2O_3, Fe_2O_3) is > 70%, and the LOI is <10% by mass. FCS has a summation of SiO_2, Al_2O_3, and Fe_2O_3 approximately equal to 67 %, but that of FCC is equal to 87%. Therefore, FCC satisfies the requirements of ASTM C618 standards for class N pozzolan. FCS is not very far from meeting this requirement, but different studies have mentioned the pozzolanic activity of flash-calcined sediments [20][268][205][284].

Table 14.Chemical composition for the materials used.

Chemical composition (%)	**RS**	**FCS**	**RC**	**FCC**	**MK**	**OPC**	**LS**	**GBFS**
Silicon dioxide, SiO_2	41.06	44.49	60.45	61.64	58.6	20	0.47	31.87
Aluminum oxide, Al_2O_3	12.08	12.66	18.27	18.58	31.17	5.10	0.21	12.84
Ferric oxide, Fe_2O_3	6.72	9.5	6.63	6.87	3.0	3.40	0.08	0.43

Calcium oxide, CaO	20.15	21.89	2.02	2.85	1.26	63.5	65.39	39.73
Magnesium oxide, MgO	0.99	2.0	0.75	0.77	5.98	0.80	0.54	10.0
Sulphur trioxide, SO_3	0.2	0.20	-	-	-	-	-	-
Sodium oxide, Na_2O	2.0	2.0	-	-	-	-	-	-
Potassium Oxide, K_2O	1.90	1.90	-	-	-	-	-	-
LOI	13.5	0.20	8.60	0.57	-	-	29.0	-

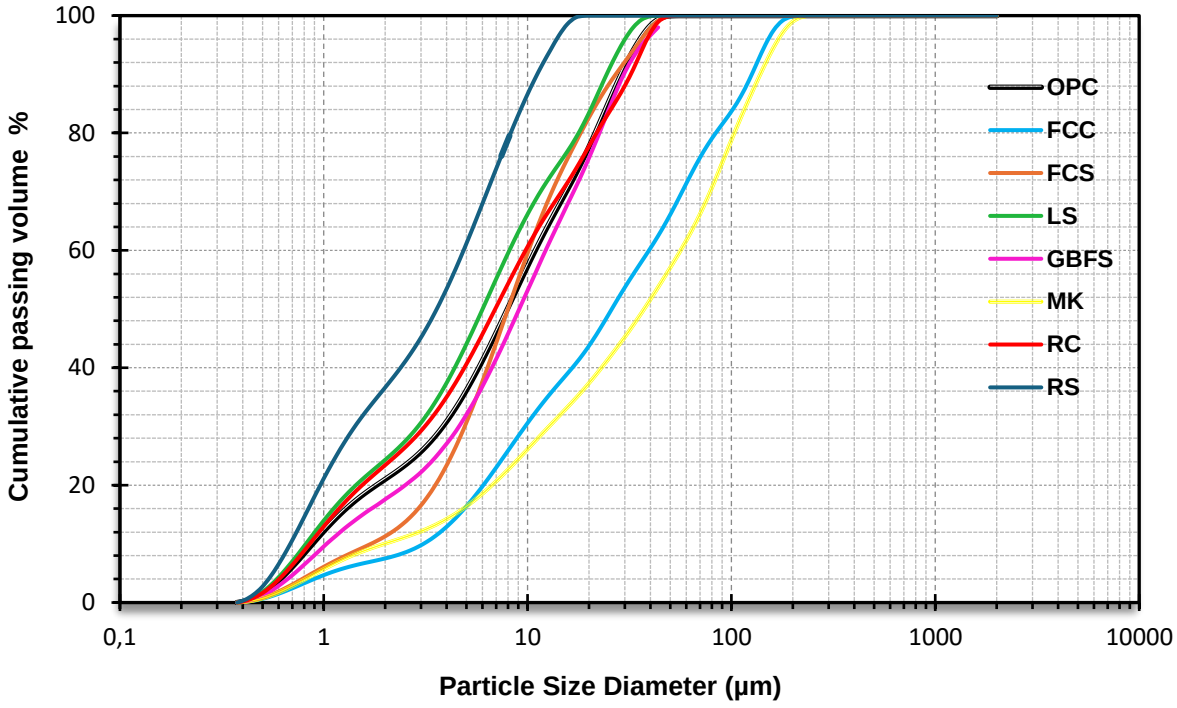

Fig. 57. Particle size diameter for MK, GBFS, OPC, LS, raw (RS, RC) and flash-calcined materials (FCS, FCC).

As shown in Fig. 57, the PSD was higher after flash calcination. For example, the D50 for both sediment and millstone clay has increased from 3.58 µm and 6.95 µm to 8.01 µm and 25.92 µm, respectively. This increase is related to the increase in the BET surface area of sediment and millstone clay resulting in very-fine particles that agglomerate together and increase the PSD. Chu et al. [280] conducted a study that yielded similar results for sediments, which they attributed to the agglomeration of clay minerals rather than sintering during the calcination process [286]. For clays, a study by Skibsted et al. [287] has mentioned the agglomeration phenomenon. The author has deduced calcination of clays at high temperatures will achieve ultra-fine particles that will join and increase their PSD [287].

The TGA/DTG analysis reveals the impact of flash calcination on different phases of sediment and millstone clay. In sediment analysis (Fig. 58), three main phase transformations are observed. Initially, a phase from 100 °C to 400 °C indicates the presence of water and organic matter in the RS, contrasting with the FCS, where no mass loss occurs in this temperature range, demonstrating the effect of flash calcination in removing water content and organic matter. The second phase, occurring between 400 °C and 600 °C, indicates the dehydroxylation of kaolinite in RS only, while no significant change in mass loss is recorded for FCS, suggesting the formation of metakaolin. This is supported by XRD results, showing the disappearance of the kaolinite peak in RS after flash calcination. The final phase, from 600 °C to 800 °C, indicates the decarbonation of $CaCO_3$. The presence of $CaCO_3$ affects the hydration of calcined sediment-based mixtures; when in contact with water, CaO transforms into $Ca(OH)_2$. FCS exhibits a sharper loss for the decarbonation of $CaCO_3$ at a slightly higher temperature.

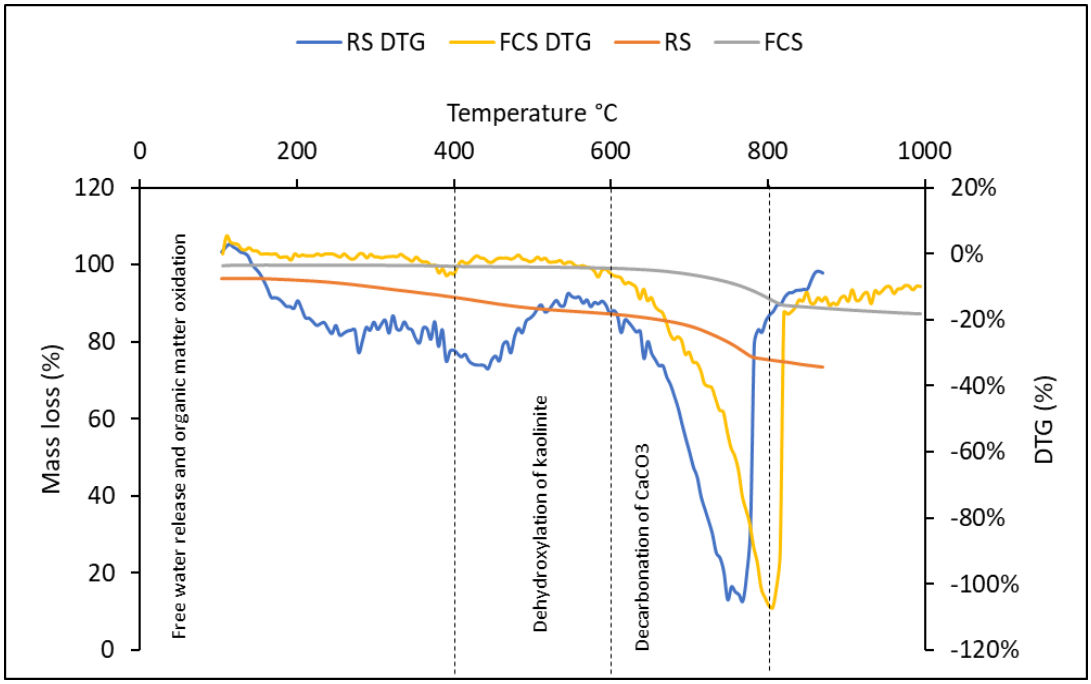

Fig. 58. TGA/DTG of RS and FCS.

Fig. 59 illustrates the TGA/DTG analysis for raw clay (RC) and flash-calcined clay (FCC). RC exhibits 3 major peaks. The first peak, between 200 °C and 300 °C, indicates the rapid loss of absorbed water. The second peak, between 400 °C and 500 °C suggests the dehydroxylation of minerals. The third peak, approximately about 720 °C indicates the decarbonation phase. In contrast, the analysis of the FCC curve shows lower mass loss than the RC due to calcination at

750 °C. Also, the FCC only indicates the presence of a small peak at 700 °C, indicating the effect of flash calcination.

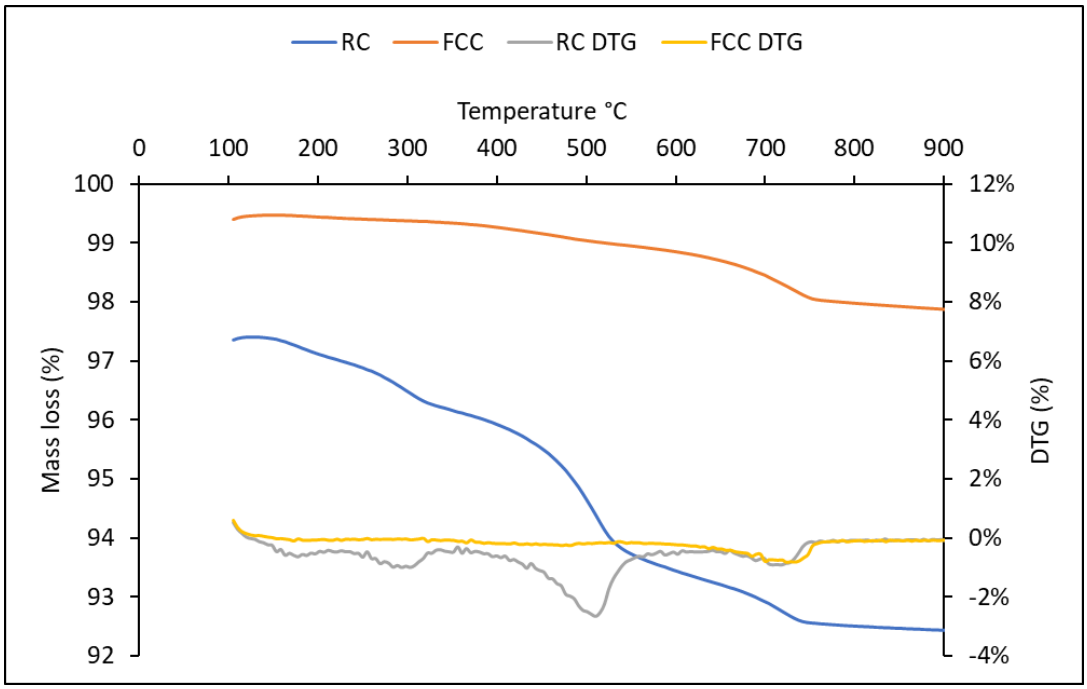

Fig. 59. TGA/DTG of RC and FCC.

The utilization of scanning electron microscopy (SEM) involves the examination of the inner structure of materials at an exceptionally high level of detail. It is evident that there are notable differences in the SEM analysis of RS and RC as shown in Fig. 60. Specifically, following flash-calcination, the particles have clearly undergone a transformation, adopting a more uniform and spherical shape. Additionally, there is a greater degree of particle cohesion observed after flash-calcination, with increased joining between the particles. Various studies have conducted analyses using SEM for both raw and flash-calcined materials. One such study, conducted by AMAR et al. [206], demonstrates that the irregular shapes of particles present in the raw sediments are identified as Pyrite, indicating the necessity for thermal treatment. The author of the study also notes that after flash-calcination, the particle shape becomes more spherical. These particles have been identified as flash-calcined kaolin clay [206][288], originating from the agglomeration process of submicron particles [206][289]. Consequently, the findings of this study are consistent with other research, as evidenced by the observed increase in BET surface area and particle size distribution (PSD) resulting from the agglomeration phenomenon, which were analyzed through SEM examinations of both raw and flash-calcined materials.

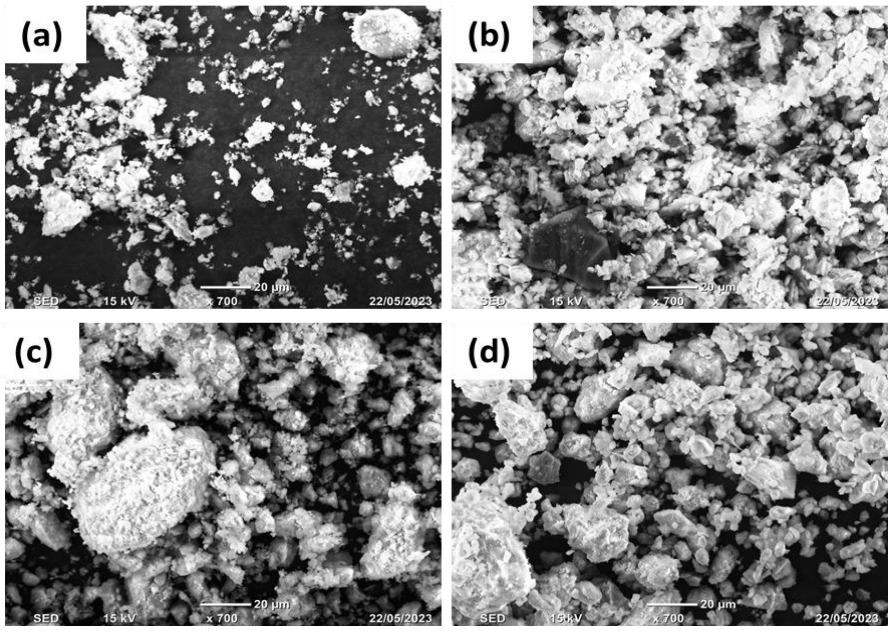

Fig. 60. Scanning electron microscopy for raw materials and flash-calcined materials: (a): RS, (b): FCS, (c): RC, (d): FCC.

The XRD analysis results are presented in Fig. 61, Fig. 62, Fig. 63, Fig. 64, Fig. 65, and Fig. *66*. This test can detect mineralogical changes after flash calcination and provide insights into the transformation behavior and thermal stability of minerals in RS and RC. Calcite (C) can decompose into CaO and CO_2, resulting in a decrease in the intensity of its diffraction peaks in XRD analysis, while quartz (Q) is stable and less affected by flash calcination. RS and RC consist mainly of quartz and kaolinite (K), with calcite present only in RS. Flash calcination caused a decrease in the intensity of the calcite peak in FCS, but the quartz remained the same in both FCS and FCC. Anhydrite (A) formation was observed in FCS due to the reaction of CaO from the decomposition of $CaCO_3$ and sulfate to form $CaSO_4$ [280][290]. Flash calcination also transformed kaolin to metakaolin, leading to a decrease in the intensity of the kaolin peak in XRD patterns for both RS and RC. The primary mineral composition of MK is quartz with an amorphous alumina-silica phase [291] and a phase of kaolinite at 21˚, whereas GBFS exhibits an amorphous phase between 25 and 35° 2Θ. The LS powder is crushed and ground from natural limestone and its only mineral composition is calcite. The OPC powder mostly comprises alite (Al), belite (B), and pentlandite crystals (P).

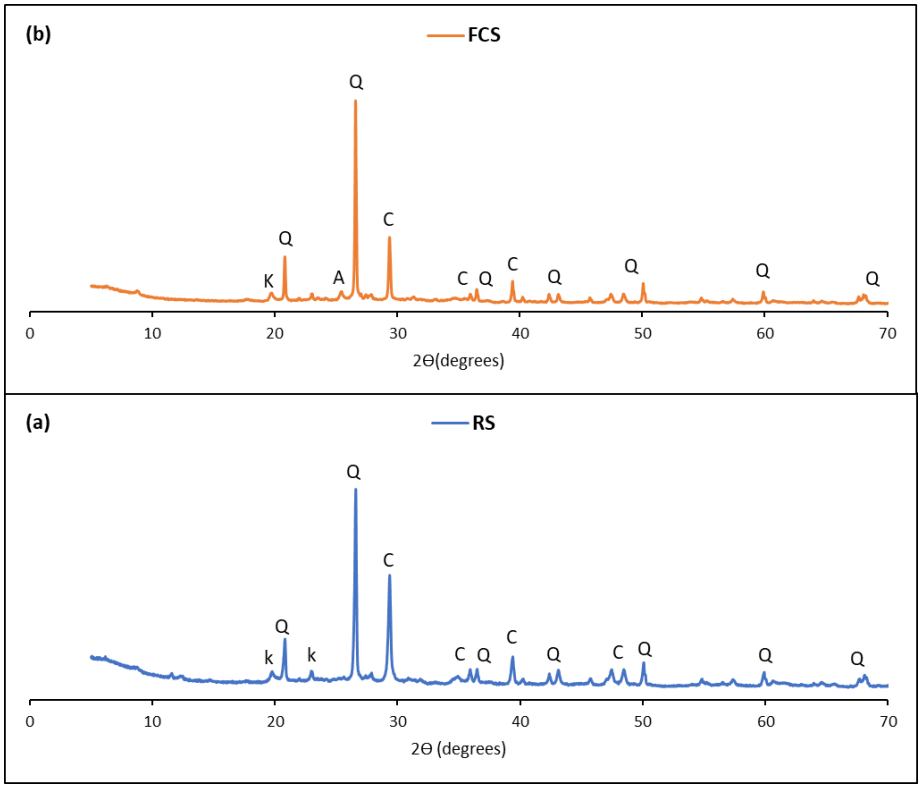

Fig. 61. XRD for (a) RS and (b) FCS.

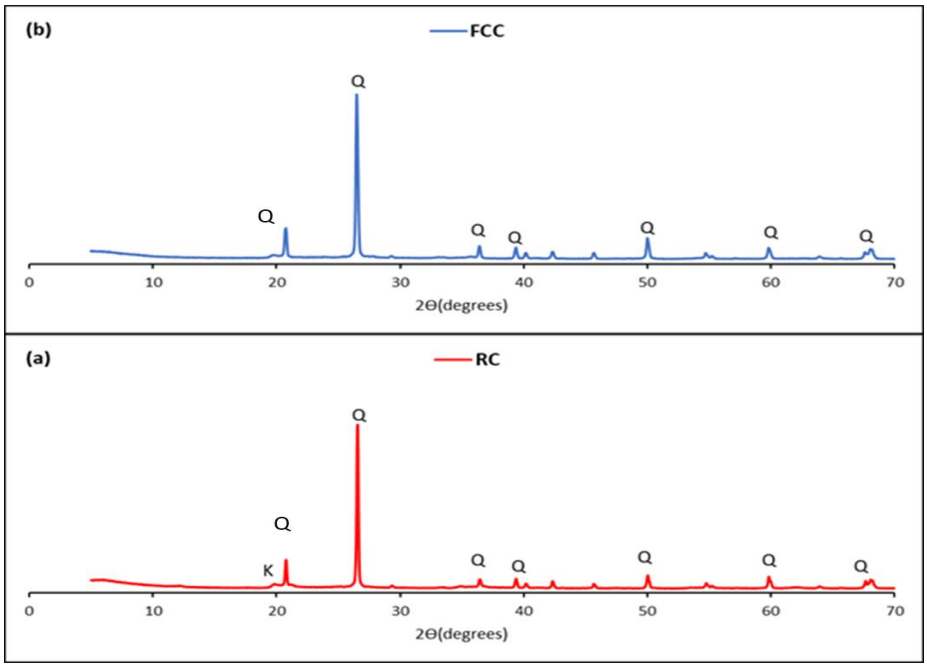

Fig. 62. XRD for (a) RC and (b) FCC.

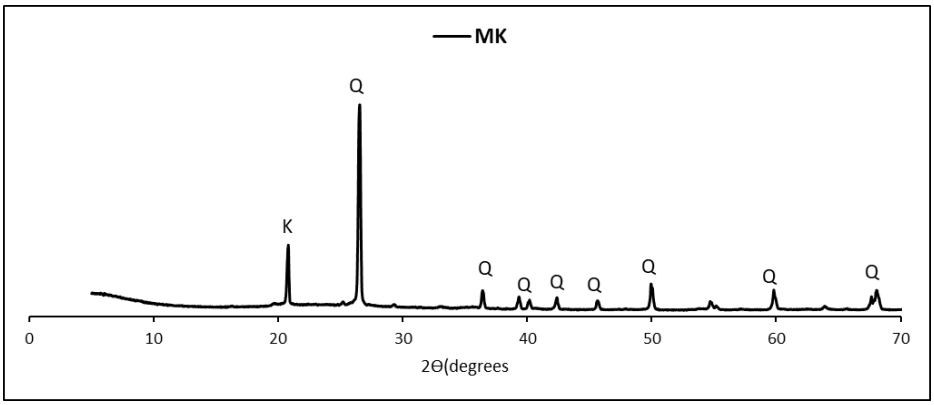

Fig. 63. XRD for MK.

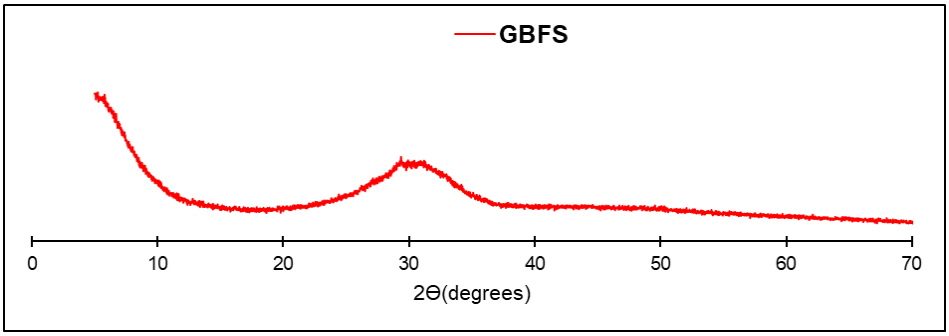

Fig. 64. XRD for GBFS.

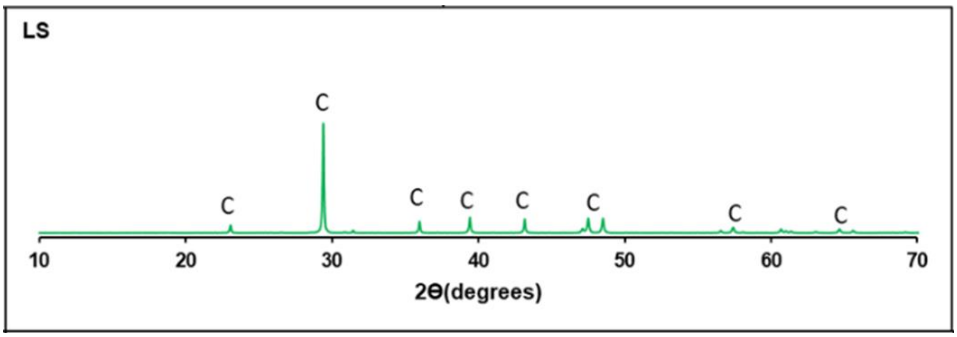

Fig. 65. XRD for LS.

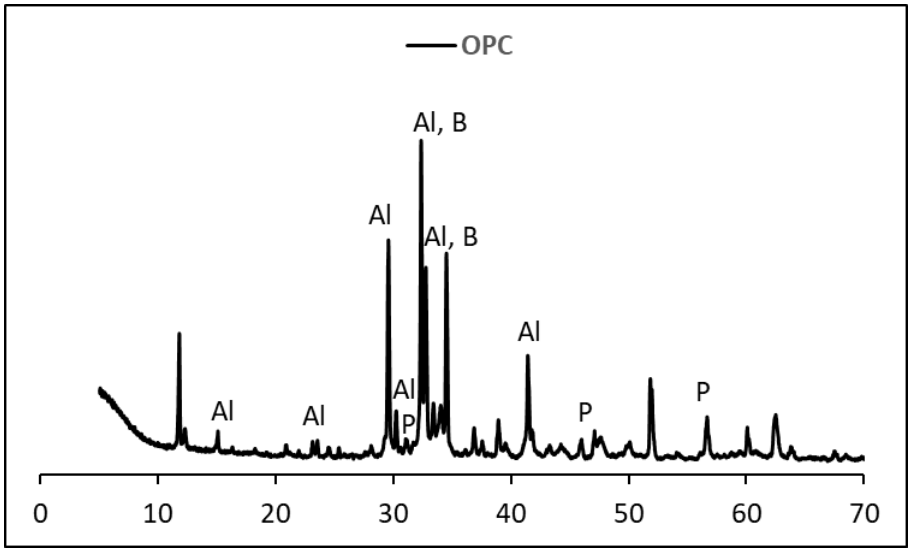

Fig. 66. XRD for OPC.

Upon conducting Chapelle test, unlike raw materials both flash calcined materials have registered positive values of $Ca(OH)_2$ with MK demonstrating the highest of all equal to 1286.35 mg of $Ca(OH)_2$, as shown in Table 15. FCC has registered 257.27 mg of $Ca(OH)_2$ which is slightly higher than FCS, with 233.88 mg of $Ca(OH)_2$. Therefore, FCC tends to be more pozzolanic than FCS which is compatible with the chemical analysis results. The negative $Ca(OH)_2$ values for LS is due to their high CaO percentages, as shown by the XRF results in Table 14. The high percentages of CaO may have caused the dispersion of Ca ions into the solution which prevented the fixation of $Ca(OH)_2$.

Table 15. Chapelle test results.

Materials	MK	FCS	FCC
Mass (mg) of $Ca(OH)_2$ fixed	1286.35	233.88	257.27

Then, according to Chapelle's test results, both FCS and FCC showed pozzolanic reactivity but are not superior to MK.

2.3. Geopolymer binder using flash-calcined dredged sediments and excavated clays

The geopolymer study is divided into two Parts. The objective of the first subject is creating geopolymer mortar with flash-calcined sediments cured under ambient conditions. The study

includes GP mortar formulations having FCS, MK, and GBFS with varying alkaline reagent -to-binder (AR/B) ratios. Different methods are investigated to optimize the AR/B ratio. After optimization, further tests are conducted on the optimized formulations.

The second objective is a comparative analysis of ambient-cured metakaolin geopolymer and flash-calcined soils geopolymer. The study includes a second set of GP formulations on mortar and concrete scales with setting the same AR/B for all GP formulations with investigating their physical, mechanical, mineralogical, microstructural, and durability properties.

2.3.1. Geopolymer mortar with flash-calcined sediments cured under ambient conditions

This section focuses on the development of GP mortar that can be cured under ambient conditions using a combination of FCS, MK, GBFS, and potassium silicate (K_2SiO_2) as an AR. The binder precursor composition was selected by maintaining a Si/Al =2. The AR/B was calculated while maintaining an atomic ratio of K/Al =1 with assuming different reactivity percentages of the Al_2O_3 of the FCS. The study investigates the effect of the alkaline reagent-to-binder ratio (AR/B) and precursor composition on the mechanical and durability properties of the GP mortar. Optimum formulations were selected based on the highest compressive strength and resistance to water boiling test. The results indicate that the lowest AR/B ratio and formulations with higher GBFS percentages have better performance. Porosity test and microstructural analysis tests such as X-ray diffraction (XRD) and Fourier transform infrared spectroscopy (FTIR) was conducted to ensure the stability of the GP formulations exposed to a sulfuric acid attack test, while nuclear magnetic resonance (NMR) tests validate the Q^4(1Si, 3Al) network and their assigned Si/Al ratio.

2.3.1.1. Methodology

The GP binder precursor is designed from MK, FCS, and GGBFS resulting in 12 formulations. The mix design of the 12 formulations is summarized in Table 16. The objective of this chapter is to result in 3 optimum GP formulations having high strength and durability compared to the reference mix MK0 with the optimum alkaline reagent to binder ratio (AR/B). The three GP formulations with FCS are (S24K76G0, S20K70G10, S16K64G20). These formulations will be tested using varying (AR/B) ratio to determine which performed best. The top performing formulations were then studied further. The following were investigated:

- To examine how GBFS impacts GP performance, three variations were created, containing 0%, 10%, and 20% GBFS. The amount of FCS and MK were adjusted proportionally while maintaining a constant Si/Al ratio of 2 based on the chemical composition of the materials coming from X-ray fluorescence test (XRF).
- To determine the required AR/B for each formulation in MK/GBFS based geopolymers. Davidovits [66] suggests using the below equation. The equation's denominator comprises the total percentage of Al_2O_3 that reacts, which is the sum of Al_2O_3 that reacts with the AR related to the precursor composition. Since sediments are considered waste from marine activities, their corresponding Al_2O_3 reaction is unknown. To account for this, four different assumed percentages of Al_2O_3 reaction are used, which result in four different AR/B ratios (R1, R2, R3, R4) and a total of 12 GP formulations for each family.
- The compressive strength and resistance to water boiling of 12 GP formulations were examined to identify the most effective one. As a result, one AR/B was chosen, and further testing is being conducted on the top three formulations to determine their efficacy.

To achieve the optimal design using the materials described, two main parameters need to be determined: the percentage of FCS, MK, and GBFS used, and the AR ratio required for complete polymerization of the precursor binder's aluminosilicates. A Si/Al ratio of 2 is recommended to produce low CO_2 cements and concretes with a rigid 3D structure [103]. To examine the effect of GBFS on GP performance, three GBFS percentages are selected, and the corresponding FCS and MK percentages are calculated to achieve a total Si/Al ratio of 2. For example, selecting 0% GBFS necessitates 24% FCS and 76% MK, while choosing 20% GBFS results in 16% FCS and 64% MK. Finally, the AR/B ratio is determined to achieve an atomic ratio of K/Al = 1, following the formula discussed by Davidovits [292].

$$\frac{nk_2O}{nAl_2O_3} = \frac{mk_2O * MAl_2O_3}{Mk_2O * mAl_2O_3} = 1 \qquad \text{Eq. 13}$$

Where nk_2O/nAl_2O_3 - the number of moles ratio, mk_2O - the mass of K_2O (grams) according to the percentage present in the AR. M Al_2O_3 - the molar mass in (g/mol). MK_2O - the molar mass in (g/mol), and mAl_2O_3 - the mass of Al_2O_3 reacting (grams).

In this section, the authors of this paper have discussed the calculation of the percentage of Al_2O_3 in the different materials used in the precursor binder. The values of Al_2O_3 for FCS found in Table 14 are used to calculate the total mass of Al_2O_3 in the precursor. However, Davidovits [292] note

that not all of the Al_2O_3 in GBFS and FA is reactive, with only 50% of the Al_2O_3 in GBFS and 30% in FA being reactive. Similarly, the percentage of Al_2O_3 reacting with the binder materials and AR in FCS is unknown, so it is assumed to be 30%, 50%, 70%, or 100%. Therefore, the mass of Al_2O_3 is related to the component of the binder and the summation percentage of Al_2O_3 reacting. Different percentages of Al_2O_3 will result in different activator -to- binder (AR/B) ratios, which will be optimized based on the results of the GP. The sand -to- binder (S/B) ratio is kept constant for all formulations equal to 2.64.

Table 16. Mix proportions for GP mortars

	% Weight			Ratios			kg/m³				
Mix Composition	**FCS**	**MK**	**GBFS**	**AR/B**	**S/B**	**%Al_2O_3 FCS**	**FCS**	**MK**	**GBFS**	**S**	**AR**
S24K76G0R1	24	76	0	1.05	2.64	30	116	369	0	1281	509
S24K76G0R2	24	76	0	1.08	2.64	50	115	365	0	1269	519
S24K76G0R3	24	76	0	1.11	2.64	70	114	362	0	1257	528
S24K76G0R4	24	76	0	1.15	2.64	100	113	357	0	1241	541
S20K70G10R1	20	70	10	0.99	2.64	30	99	347	50	1309	491
S20K70G10R2	20	70	10	1.02	2.64	50	98	344	49	1296	501
S20K70G10R3	20	70	10	1.04	2.64	70	98	341	49	1287	507
S20K70G10R4	20	70	10	1.07	2.64	100	97	338	48	1275	517
S16K64G20R1	16	64	20	0.93	2.64	30	81	324	101	1338	471
S16K64G20R2	16	64	20	0.95	2.64	50	81	322	101	1329	478
S16K64G20R3	16	64	20	0.97	2.64	70	80	320	100	1320	485
S16K64G20R4	16	64	20	0.99	2.64	100	79	318	99	1311	492

To evaluate the durability of the optimized GP formulations (S24K76G0R1, S20K70G10R1, and S16K64G20R1) an acid attack test with 2% H_2SO_4 was conducted on both mortar and paste samples after 28 days of curing. The acid solutions were replenished every 7 days. The mortar mixes were analyzed for mass loss, compressive strength loss, porosity, and pH variation, while X-ray diffraction (XRD) and Fourier transform infrared spectroscopy (FTIR) were conducted on the paste samples exposed to acid and control paste samples.

To evaluate and investigate the effect of acid attack test on the pore structure of the GP formulation, mercury intrusion porosity test is done according to standard ISO 15901-1:2016 [67] on both unexposed and exposed mortar samples.

Finally, nuclear magnetic resonance (NMR) was used to identify silico-aluminate species (^{29}Si and ^{27}Al) on mortar specimens of age 28 days to assess the environmental impact of the GP samples.

2.3.1.2. Mixing procedure

The GP specimens were produced using a 5 L mixer, which was operated at maximum speed during the mixing process. The mixing sequence involved adding FCS to the alkaline activator for 10 minutes to ensure geo-polymerization of the particles, followed by the addition of MK for 5 minutes, and then GBFS for 3 minutes. The sand was then added for 5 minutes to ensure the homogeneity of the mixture. The mixing procedure is summarized in Fig. 67. This specific mixing sequence was adopted since the precursor binder materials have different degrees of reactivity; hence dry binder powders could not be mixed together before adding the AR. The mixture was poured into two layers in polyester molds, with each layer compacted for 1 minute using a vibrating table. The molds were closed with plastic bags and cured at room temperature (20°C) under ambient conditions. The samples were demolded at the time of the compressive strength test.

Fig. 67. GP mixing procedure.

2.3.2. A comparative analysis of ambient-cured metakaolin geopolymer and flash-calcined soils geopolymer

This section focuses on advancing the development of geopolymer mortar and concrete while maintaining the same mix design for the binder composition utilized in the first section. FCS and FCC are explored as substitutes for MK, incorporating GBFS, with the continued use of

potassium silicate as the alkaline reagent (AR). Seven GP mortar formulations are examined with varying AR/B ratios (0.4, 0.6, 0.8), while keeping the total W/B ratio constant at 0.45. The initial formulation involves only MK, followed by three formulations using FCS, MK, and GBFS, and another three using FCC, MK, and GBFS. The optimal AR/B ratio, determined based on workability and compressive strength results, is found to be 0.8.

To assess the reactivity of FCS and FCC and their impact on compressive strength, calorimetry tests and mercury porosity tests are conducted. The study of FCS and FCC effects on the geopolymerization matrix involves SEM/EDS, TGA/DTG, and NMR tests. Durability assessments for GP mortar formulations include acid attack, high-temperature resistance, and freeze-thaw tests. The durability of GP concrete is evaluated through a water absorption test. Lastly, the environmental impact was by conducting leaching test.

2.3.2.1. Methodology

The study involved the creation of six different formulations using the same alkaline reagent to binder (AR/B) ratio. Various AR/B ratios were experimented with for each GP formulation to achieve the optimal blend in terms of both workability and compressive strength. The tested AR/B ratios included 0.4, 0.6, and 0.8. The total W/B ratio is kept constant equal to 0.45 for all GP, including the amount water content found in the AR. It was determined that the optimal AR/B ratio across all formulations was 0.8. These formulations were compared to a reference mix, MK0, which consisted of 100% MK. The first set of formulations (S1, S2, S3) contained varying percentages of flash-calcined materials (FCS) and MK. The second set (C1, C2, C3) included flash-calcined clays (FCC) along with MK. All formulations maintained a total Si/Al ratio of 2, following Davidovits' guidance [103] for geopolymer cements and concretes with low-CO_2 emissions and reduced energy demand as calculated in Part I. The mix design of the GP mortar formulations are summarized in Table 17, Table 18, and Table 19.

To assess the strength of the developed mortar, compressive strength measurements were conducted and compared to the reference mix MK0. The study also explored the effects of incorporating ground granulated blast furnace slag (GBFS) on the strength and durability of geopolymer mortar. Nurruddin et al. [293] discussed the behavior of GBFS on the setting time, workability, and initial strength behavior of GP concrete cured under ambient conditions. The

results showed that GBFS enhances the geopolymerization process at ambient curing and yields positive strength development at an early age.

The mercury porosity test was performed on all formulations to investigate the impact of GBFS on pore structure and its correlation with compressive strength results.

Durability assessments included acid attack, high-temperature resistance, and freeze-thaw tests. Acid exposure involved monitoring mass loss, compressive strength loss, and pH variation in mortar mixes. X-ray diffraction (XRD) and Fourier transform infrared spectroscopy (FTIR) were employed on paste samples subjected to acid exposure. For high-temperature resistance, mortar samples were heated up to 800 °C and resulting mass loss and compressive strength were evaluated. The accelerated freeze-thaw test was done on GP mortar samples after 28 days of curing at ambient conditions according to Procedure B in agreement with the ASTM C666-97 [294].

On day 28, thermogravimetric analysis (TGA) was conducted on geopolymer paste samples to examine the decomposition behavior influenced by flash-calcined materials. Followed by calorimetry test to study the reaction of the binder designed with AR and its relation to early high compressive strength.

Finally, all GP mortar formulations are transformed into concrete formulations, maintaining constant AR/B= 0.8 ratios and the 2 % of freely added water from the binder mass. The aggregate (coarse and fine) is set to be equal to 70% of the total GP mass or equals to 68% of the total GP volume.

Mix designs were optimized for high strength, using 0-4 mm fine aggregates, 4-10 mm, and 10-20 mm coarse aggregates, the total aggregates represent 70% of the total concrete mass. Generally, it is suggested that 10 to 12 mm is the appropriate maximum size of aggregates for making high strength concrete, however adequate performance and economy can also be achieved with 20 mm to 25 mm maximum size graded aggregates by proper proportioning [295]. On the other hand, to achieve concrete with good workability, the European guidelines for self-compacting concrete (EFNARC Guidelines) [296] prefer the usage of coarse aggregates up to 50% of the total aggregates with size limited to 20 mm to reduce the friction. Therefore, the percentage of coarse aggregates is set equal to 60% from the total aggregate mass which comprise both strength and workability. Also, due to the viscosity of GP concrete mix caused by the AR, the aggregates of 20 mm are used without limiting the aggregates size to 10 mm to decrease the friction between the aggregates and the binder and ensure maintaining a proper workability performance of the mixture.

The existing literature on the utilization of geopolymer binders for creating high-strength concrete is limited. Conversely, research conducted by the Portland Cement Association [297] indicates that in normal strength concrete, enlarging the coarse aggregate size leads to a reduction in the required mixing water. This results in a lower water-cement ratio, ultimately achieving greater strength. However, in high-strength concrete, the larger size of coarse aggregate tends to diminish concrete strength. In contrast, the utilization of smaller aggregates (19, 12.5, 9.5 mm) proves adequate to attain the desired strength. This study has unveiled a correlation among the cement density in kg/m^3 of the concrete, the maximum size of aggregate used (mm), and compressive strength (MPa). According to the research, for concrete with approximately 400 kg/m^3 of cement without retarding admixtures, the maximum compressive strength is attained when employing a maximum size of aggregates equal to 19 mm. This demonstrates higher strength compared to using a maximum size of aggregates equal to 9.5 mm, as depicted in Fig. 68.

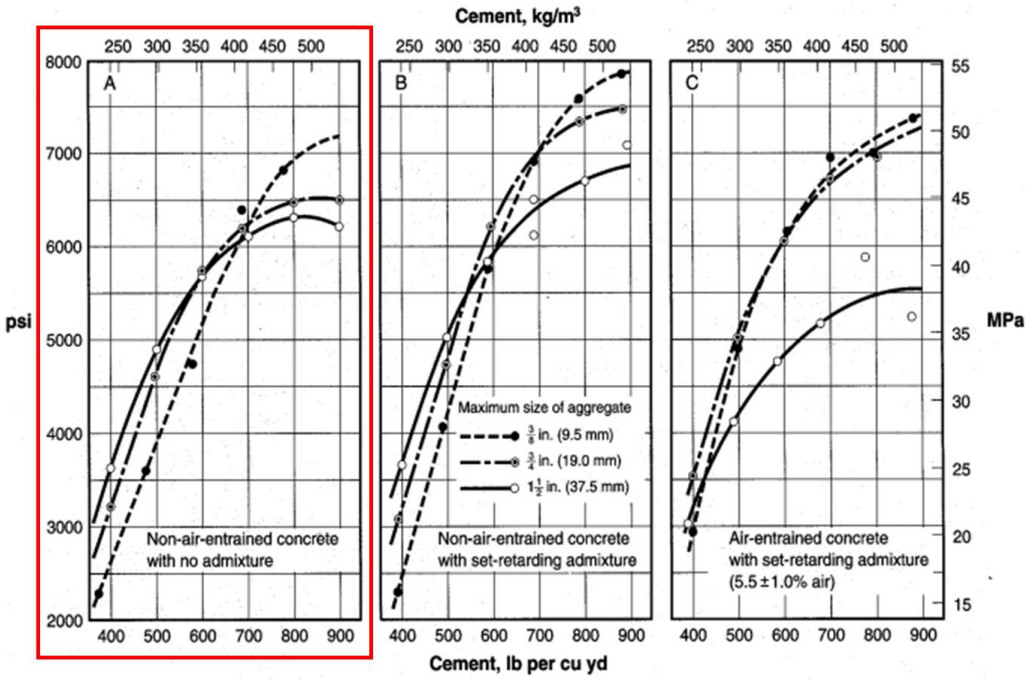

Fig. 68. Effect of cement content on compressive strength at 28 days for various maximum sizes of aggregate in different types of concrete [297].

All GP concrete formulations, the GP binder content represents around 400 kg/m^3 from the total GP mass, therefore with the findings of the high strength concrete study the maximum size of aggregates is limited to 20 mm. The GP concrete mix design is illustrated in Table 20.

Water absorption tests were conducted on the concrete to assess its microstructure.

SEM/EDX tests were employed to investigate microstructure and composition differences among geopolymer binders.

The Nuclear magnetic resonance (NMR) was employed to identify silico-aluminate species (^{29}Si and ^{27}Al) present in the geopolymer formulations.

Finally, a leaching test was conducted to assess the GP impact on the environment if used in construction activities.

Table 17. Mix proportions for GP mortars with AR/B= 0.4.

Mix symbol	**kg/m³**					
	FCS/FCC	**MK**	**GBFS**	**Sand**	**AR**	**W**
MK0	0	535	0	1413	214	128
S1	128	407	0	1413	214	128
S2	107	375	54	1416	215	129
S3	86	344	107	1419	215	129
C1	145	392	0	1416	215	129
C2	124	360	54	1418	215	129
C3	97	334	108	1420	215	129

Table 18. Mix proportions for GP mortars with AR/B= 0.6.

Mix symbol	**kg/m³**					
	FCS/FCC	**MK**	**GBFS**	**Sand**	**AR**	**W**
MK0	0	531	0	1403	319	64
S1	128	404	0	1403	319	64
S2	107	373	53	1406	320	64
S3	85	342	107	1409	320	64
C1	141	389	0	1406	320	64
C2	123	357	53	1409	320	64
C3	96	331	107	1411	320	64

Table 19. Mix proportions for GP mortars with AR/B= 0.8 (Optimum formulation).

Mix symbol	kg/m³					
	FCS/FCC	MK	GBFS	Sand	AR	W
MK0	0	522	0	1379	418	10
S1	125	397	0	1379	418	10
S2	105	366	52	1382	419	10
S3	84	336	105	1384	419	10
C1	141	382	0	1382	419	10
C2	121	351	52	1384	419	10
C3	95	326	105	1386	420	10

Table 20. Mix proportions for GP concrete.

	Mix proportions (kg/m³)								
Mix symbol	**FCS**	**FCC**	**MK**	**GBFS**	**CA 10-20 mm**	**CA 4-10 mm**	**Sand**	**AR**	**W**
MK0	0	0	400.1	0.0	509.7	509.7	679.6	320.1	0.01
S1	96.0	0	304.1	0.0	509.7	509.7	679.6	320.1	0.01
S2	80.1	0	280.5	40.1	510.5	510.5	680.6	320.5	0.01
S3	64.2	0	256.8	80.3	511.2	511.2	681.6	321.0	0.01
C1	0	108.2	292.5	0.0	510.6	510.6	680.7	320.6	0.01
C2	0	92.3	268.8	40.1	511.2	511.2	681.6	321.0	0.01
C3	0	72.3	249.1	80.3	511.8	511.8	682.4	321.4	0.01

2.3.2.2. Mixing procedure

The GP concrete is prepared by using two mixers separately. First, the GP binder is prepared using a 5 L mixer. The GP binder prepared by mixing sequence involved adding FCS or FCC to the alkaline reagent (AR) potassium silicate for 10 mins to ensure geo-polymerization of the particles, followed by the addition of MK for 5 min, and then GBFS for 3 min. Afterwards, the GP binder prepared is added to the concrete mixer as shown in Fig. 69 with the sand already added and mixed for 3 mins at high speed, followed by adding the coarse aggregates to the mixer with the additive water which is 2 % of the binder mass added and mixed for 3 mins at high speed to ensure the homogeneity of the mixture. For the GP mortar the same mixing procedure is done but with adding the sand directly into the 5 L mixer with the extra water quantity. For the GP concrete,

the mixture was poured into two layers of concrete molds of a diameter equal to 10 cm and height of 20 cm with vibration for one minute happening between each layer. Also, for the mortar formulations, polyester molds were used for molding. The mixture was poured into two layers vibrating for one minute on the vibrating table between each layer. All samples are cured at room temperature (20 °C) under ambient conditions.

Fig. 69. Concrete mixing procedure.

2.4. Limestone flash-calcined clay cement (LFC) binder

The aim of this research is to create a binder using flash-calcined limestone sediment and millstone clay cement (LFC). The focus of the study is on developing high-strength and durable mortar and concrete with valorized waste materials (FCS and FCC), aiming to reduce the amount of waste and CO_2 emissions associated with OPC production. The performance of the newly designed binders is compared to a reference mix that uses metakaolin (MK) instead of FCS or FCC, as MK is a well-known pozzolanic supplementary cementitious material. The evaluation of the binder's performance includes workability tests on both mortar and concrete, mechanical strength tests, porosity tests, physicochemical analyses (XRD, TGA, FTIR), and durability tests (acid attack tests). Additionally, the environmental impact is assessed through leaching tests.

2.4.1. Methodology

To develop an environmentally friendly cement binder called limestone flash-calcined clay cement binder (LFC) or LC3 binder, different proportions of clinker, supplementary cementitious materials (SCM), and limestone (LS) were utilized, with clinker accounting for 64%, SCM ranging from 18-26%, and LS ranging from 10-18%. The LFC binders are classified as CEMII/C-M according to the standard as explained in NF EN 197-5 standard [149] and illustrated in Fig. 27.

A total of nine formulations, three from each category, were prepared, alongside a reference mix composed entirely of ordinary Portland cement (OPC).

Before evaluating the LFC formulations done with MK, FCS, and FCC, mortar formulations are done only by substituting OPC with either MK, FCS, or FCC to study their impact on workability and compressive strength without the additional LS.

After conducting mechanical compressive strength tests on all LFC formulations, the top-performing formulations from each category were selected for further assessment of their physical, durability, physicochemical, and microstructural properties. These optimal LFC formulations were then translated into concrete formulations, and their compressive strength was evaluated.

For physical testing, workability assessments were conducted on both mortar and concrete in their fresh states, measuring slump flow diameter.

To compare the microstructural properties of mortar containing metakaolin (MK) and those containing flash-calcined clay (FCS) and flash-calcined marble dust (FCC) on day 28, a mercury porosity test was conducted on the three mixes with the highest MK/flash-calcined materials percentages (C1, C4, C7), which coincided with the formulations exhibiting the highest compressive strength.

Additionally, on day 28, TGA, XRD, and FTIR tests were conducted on paste samples (C1, C4, C7) to investigate the differential impact of LFC with MK compared to that with FCS and FCC.

To understand the effect of MK, FCS, and FCC on the hydration reaction, calorimetry test was done on the mortar formulations (C0, C1, C4, C7) for 7 days.

The durability test, performed on a mortar scale, involved subjecting the mixes to an acid attack test, with monitoring of mass loss, compressive strength loss, and pH variation. X-ray diffraction (XRD) and Fourier transform infrared spectroscopy (FTIR) were employed on paste samples exposed to acid to analyze physicochemical changes.

Finally, to assess the environmental impact of the LFC mixes, a leaching test was carried out.

2.4.2. Mix design

First, nine formulations are prepared by substituting 10, 20, and 30% of OPC by either MK, FCS, or FCC with having the same S/B =3, W/B= 0.33, and SP equal to 2% by mass of the binder. These formulations are (MK10, MK20, MK30, FCS10, FCS20, FCS30, FCC10, FCC20, and FCC30) as shown in Table 21 .This study follows the guidelines of standard NF EN 197-5

[298] to determine the mix proportions of CEM II/C-M cement. According to the standard, CEM II/C-M cement should have a cement ratio ranging from 50% to 64%, calcined material ranging from 36% to 50%, and limestone limited to 6% to 20% by mass. The mix formulations in this study are designed accordingly and are presented in Table 22. The study evaluates nine different formulations along with a reference mix called C0, which consists of 100% OPC by mass.

The first set of formulations, labeled as C1, C2, and C3 adhere to a limit of 64% OPC, 18-24-26% MK, and 10-14-18% LS. The second set of formulations, referred to as C4, C5, and C6, also have a limit of 64% OPC, but with 18-24-26% FCS and 10-14-18% limestone LS. The third set of formulations, named C7, C8, and C9 are limited to 64% OPC, 18-22-26% FCC, and 10-14-18% limestone LS.

High-performance concrete is a specialized type of concrete that contains a reduced amount of water compared to the binder. This composition is necessary to achieve specific mechanical properties such as high compressive strength and excellent durability with minimal maintenance. In Europe, HPC is classified as concrete with a compressive strength exceeding 60 MPa after 28 days and a low water-to-binder ratio (<0.4) [77]. To achieve a mortar with high strength, the water-to-binder ratio (W/B) is set to 0.33 with the addition of the SP to compensate for the workability. The sand-to-binder ratio (S/B) is equal to 3 and is chosen constant with the percentage of SP added (2% of the total binder mass) for all formulations to compare the effect of each SCM on the mortar properties such as workability and mechanical strength under the same conditions.

Table 21. Initial mix proportions of substituting OPC by MK, FCS, and FCC.

Mix kg/m^3	**OPC**	**MK**	**FCS**	**FCC**	**Water**	**Sand**
MK10	502.64	55.85	-	-	184	1675
MK20	445.12	111.28	-	-	184	1669
MK30	388	166.29	-	-	183	1663
FCS10	502.65	-	55.85	-	184	1675
FCS20	445.12	-	111.28	-	184	1669
FCS30	388	-	166.29	-	183	1663
FCC10	503.08	-	-	55.89	184	1677
FCC20	445.89	-	-	111.48	183	1672
FCC30	389.04	-	-	166.73	183	1667

Table 22. Mix proportions for LFC mortar (kg/m³).

Mix kg/m³	OPC	MK	FCS	FCC	LS	Water	Sand
C0	560	-	-	-	-	185	1682
C1	354	144	-	-	55	183	1661
C2	354	122	-	-	78	183	1661
C3	355	100	-	-	100	183	1662
C4	355	-	144	-	55	183	1661
C5	355	-	122	-	78	183	1661
C6	355	-	100	-	100	183	1662
C7	355	-	-	144	55	183	1665
C8	355	-	-	122	78	183	1665
C9	355	-	-	100	100	183	1665

To produce the LFC concrete, the LFC mortar formulations that demonstrated the highest compressive strength were adapted to a concrete scale. The transition involved maintaining the parameters used in the mortar formulations while introducing 10 mm coarse aggregates into the mixture, as illustrated in Table 23. The size of aggregates is limited to 10 mm to ensure achieving high-strength concrete while the addition of 2% of the SP ensures achieving a proper workability of the concrete mixture.

Table 23. LFC concrete mix design (kg/m³).

Mix kg/m³	OPC	MK	FCS	FCC	LS	Coarse Aggregate	Sand	water
C0	664.9	0.0	0.0	0.0	0	1256.70	837.8	219.40
C1	390.10	158.50	0.0	0.0	0.0001	1152.0	768.0	201.10
C4	390.10	0.0	158.50	0.0	0.0001	1152.0	768.0	201.10
C7	390.10	0.0	0.0	158.90	0.0001	1154.90	768.0	201.60

2.4.3. Mixing procedure

To achieve consistency, the dry mixture undergoes a thorough 60-second blending process in a 5-liter mortar mixer. Subsequently, water is introduced along with the superplasticizer (SP) for the next 30 seconds. Following this, sand is incorporated and mixed at high speed for 90 seconds. The process pauses briefly to scrape material off the mixer walls before resuming mixing for an additional 60 seconds at high speed. This method is replicated for concrete, utilizing a concrete mixer, and introducing aggregates after the sand for a 3-minute duration to ensure the uniformity of the concrete mix.

All specimens are molded using steel molds and left at room temperature (20 °C) for 24 hours. Concrete specimens, molded in concrete molds with a diameter of 10 cm and height of 20 cm, undergo the same procedure. After one day, the samples are extracted from the molds and submerged in water for the curing process.

2.5. Lab experiments

2.5.1. Workability on mortar

The workability of GP was evaluated following European standard NF EN 1015-3 [299]. The slump diameter of the fresh mortar was measured using the flow table Fig. 70. The fresh mix was added to the cone and compacted for 25 strokes with a rod. Then, the cone was steadily removed, and 15 compactions were done using the flow table.

Fig. 70. Measuring slump diameter using flow table.

2.5.2. Workability on concrete

The assessment of concrete workability was evaluated following ASTM C143/C143M-12 [300].The fresh concrete’s slump flow diameter was determined utilizing the Abraham cone,

adhering to the specified standard. The process involved introducing the fresh mixture into the Abraham cone in three layers, compacting each layer with a steel rod 25 times. Subsequently, a spatula was used to level the surface. Following the swift removal of the cone, the slump flow diameter was measured (Fig. 71).

Fig. 71. Measuring slump flow diameter of concrete.

2.5.3. Compressive strength on mortar/ concrete

The compressive strength was measured according to European standard NF EN 196-1 [301] for mortar samples of dimensions 4×4×16 cm for ages 7 and 28 days, with an average value of three specimens tested (Fig. 72). Also, the compressive strength was done following the European standard NF EN 12390-3 [302] on concrete specimens with a diameter of 10 cm and a height of 20 cm on days 1,3, 7, and 28 days as shown in Fig. 73.

Fig. 72.Compressive strength on mortar formulations.

Fig. 73. Examples of concrete cylinders after compressive strength test.

2.5.4. Mercury porosity test

The pore structure of the mortar samples of the same composition but different curing conditions was performed following the mercury porosity method as prescribed by the ISO 15901-1:2016 standard [303]. The pore size distribution diameter is classified as macropores, meso/micropores, nanopores and molecular pores as shown in *Fig. 74* [130], [304]–[309]. The pores in this study are classified int4 categories (d< 10 nm), (10 nm<d< 100 nm), (100 nm<d<10 µm), and (d>10 µm). The percentage of the specified diameter range is calculated as shown below in the equations.

$$V\ d\_pore < 10\ nm\ (\%) = \frac{Total\ intrusion\ volume - Vintrusion\ d > 10\ nm\ (mL/g)}{Total\ intrusion\ volume(mL/g)} \times 100 \quad \text{Eq. 14}$$

$$V\ 10\ nm < d\_pore < 100\ nm\ (\%) = \frac{Vintrusion\ d > 10\ nm\ (mL/g) - Vintrusion\ d > 100\ nm\ (mL/g)}{Total\ intrusion\ volume(mL/g)} \times 100 \quad \text{Eq. 15}$$

$$V\ 100\ nm < d_{pore} < 10\ \mu m(\%) = \frac{V\ intrusion\ d > 100\ nm\ (mL/g) - Vintrusion\ d > 10\ \mu m\ (mL/g)}{Total\ intrusion\ volume(mL/g)} \times 100 \quad \text{Eq. 16}$$

$$V\ d_{pore} > 10\ \mu m(\%) = \frac{Vintrusion\ d > 10\ \mu m\ (mL/g)}{Total\ intrusion\ volume\ (mL/g)} \times 100 \quad \text{Eq. 17}$$

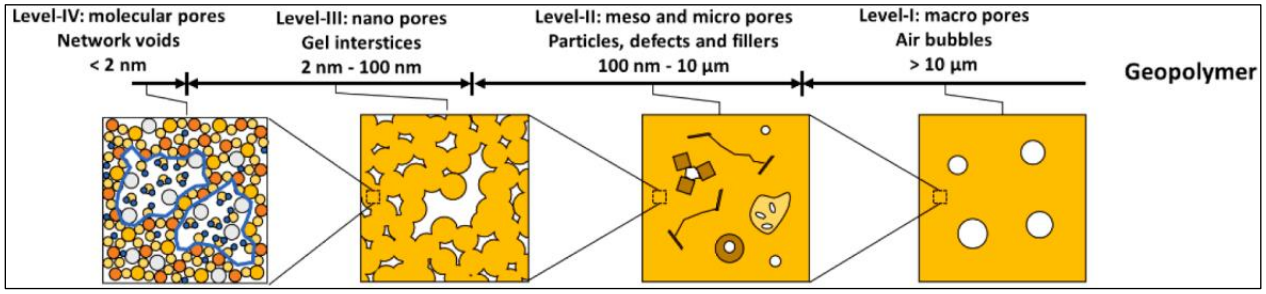

Fig. 74. Geopolymer classification [130], [304]–[309].

2.5.5. Water boiling resistance test

According to Davidovits [292], the water boiling test is a quick method to evaluate the strength of hardened geopolymers. The author suggests that geopolymers with complete condensation should be able to withstand this rigorous test, while solid samples made with incompletely condensed or non-reactive ingredients will break apart during the experiment. The test was conducted by placing mortar samples in boiling water for 15 minutes, followed by compressive strength tests to study the percentage strength loss in comparison with the strength of normal mortar samples aged 28 days. An average value of three samples was recorded.

2.5.6. Acid attack test

To study the durability of the three GP formulations, an acid attack test of 2% H_2SO_4 was carried out based on Aiken et al. [310] procedure. After 28 days of curing, three mortar specimens from each mix were submerged in 2% sulfuric acid of pH equal to 1.11 for 28 days. The acid was replenished every 7 days to maintain its effect due to the alkaline nature of the GP while measuring the pH of the solution, and a visual inspection was recorded every 7 days to study the damage progress caused by the acid. The mass change was measured, and compressive strength tests were conducted after 28 days to study the strength of the GP specimens after the test. An average value of three specimens was recorded for mass change and compressive strength tests.

2.5.7. Freeze-thaw test

The accelerated freeze-thaw test was done on GP mortar samples after 28 days of curing at ambient conditions according to Procedure B in agreement with the ASTM C666-97 [294]. The standard states that the temperature should vary from 4.4 °C to -17.8 °C whereas for the rapid freezing thaw method the thawing time should be at least 20% of the freeze-thaw cycle time. The GP samples were de-molded, and their mass was measured before subjecting them to the freeze-thaw cycles. For each freeze-thaw cycle, the samples were first immersed in tap water and placed in a cooling chamber at a temperature of 4 ± 2 °C for 6 hours. Afterward, the samples were removed and placed in a freezer at a temperature of -18 ± 2 °C for 18 hours. The samples were subjected to 0, 7,14, 28, and 42 freeze-thaw cycles. After each cycle, the samples were placed at room temperature, then their mass change and compressive strength were recorded. This method for

freeze-thaw test was done by a study conducted by Pilehvar et al. [311] with the same freeze-thaw time. Also, another study done by Rashad et al. [312] used the same method but with equal freeze-thaw timing. The GP mortar samples undergone freeze-thaw test are displayed in Fig. 75.

Fig. 75. GP mortar samples upon freeze-thaw test.

2.5.8. High-temperature resistance test

The second durability test is the high-temperature resistance test. This test was done on all GP mortar formulations of age 28 days. The mass and compressive strength were measured for all GP formulations before and after conducting the test. The GP mortar samples were added into a furnace (Fig. 76) and heated in the temperature range of 200 °C, 400 °C, with a heating range of 25 °C/min, then the temperature increased from 400 °C to 800 °C with a heating range of 5 °C/min and stayed constant for two hours. Afterwards, the samples are cooled for 1 h to room temperature, then the mass and compressive strength are measured.

Fig. 76. Oven used for high-temperature resistance test.

2.5.9. Water absorption test

The water absorption test was done following the standard ASTM C1585-13 [313]. The test was conducted on specimens of 100 mm diameter and 50 mm height obtained from the original cylinders after 28 days of curing at room temperature. Afterward, the samples were subjected to conditioning as stated by the standard ASTM C1585-3. The specimens were sealed using duct tape from the sides and the upper surface as shown in Fig. *77*. The water absorption rate was assessed at the times shown in Table 24.

Fig. 77. Concrete specimens before and after sealing.

Table 24. Times and Tolerances for Measurements Schedule [314].

Time	60 s	5 min	10 min	20 min	30 min	60 min	Every hour up to 6 h	Once a day up to 3 days	Day 4 to 7 3 measurements 24 h apart 2 h	Day 7 to 9 1 (one) measurement 2 h
Tolerance	2 s	10 s	2 min	2 min	2 min	2 min	5 min	2 h	2 h	2 h

The initial and secondary rate of water absorption (mm/s$^{0.5}$) are measured using the following equation:

$$I = \frac{m_t}{a*d} \qquad \text{Eq. 18.}$$

Where:

- *I = the absorption.*
- *m_t = the change in specimen mass in grams, at the time t.*

- *a = the exposed area of the specimen in* mm^2.
- d = the density of the water in g/mm^3.

2.5.10. SEM/EDX test

After 28 days of curing of the GP mortar samples, a microstructural examination using the Zeiss Auriga 40 scanning electron microscope (SEM) was performed. The SEM specimens were derived from fractured chips extracted from the samples. These samples underwent a thorough process of drying, embedding in epoxy resin, and polishing to achieve a smooth surface, facilitating optimal SEM imaging and chemical analysis. The Zeiss Auriga 40 SEM (Fig. 79) is equipped with a range of detectors, including Secondary Electron Detectors (SED), Backscatter Detectors (BSD), and Energy-Dispersive X-ray Spectroscopy (EDS) detectors, allowing comprehensive imaging and analysis under varying vacuum conditions. SEM utilizes a focused beam of high-energy electrons to interact with the sample, generating signals that provide crucial information about external morphology, chemical composition, and textural details. using the FEI Quanta 400 instrument. This instrument operated at an accelerating voltage of 12.5 kV, enabling detailed observation of the microstructural characteristics of the GP formulations on mortar scale. Olympus software was used for image processing to study the highlight the microcracks and unreacted particles. The samples preparation is shown in *Fig. 78*.

Fig. 78. Samples preparation for SEM.

Fig. 79. Zeiss Auriga 40 SEM machine.

2.5.11. TGA/DTG test

The TGA test is done on paste formulations using Netzsch machine model STA 449 F3 Jupiter + QMS Aeolos 403 °C (*Fig. 80*). It involved increasing the temperature from 40°C to 105°C at a rate of 2°C/min to remove excess water from the samples. The temperature was held constant for 2 minutes at 105°C to stabilize the mass loss before increasing the temperature from 105°C to 1000°C at a rate of 10°C/min to analyze the mass loss at different temperatures. The same method is used by Chu et al. [60] on flash-calcined sediments to analyze the bound water content and $Ca(OH)_2$ content.

Fig. 80. Netzsch machine model STA 449 F3 Jupiter + QMS Aeolos 403 °C.

2.5.12. Calorimetry test

The heat of hydration is measured on fresh mortar samples according to European standard NF EN 196-9 [315] by using the calorimetry apparatus (Fig. 81). The time of addition of the alkaline reagent was taken as the starting time for mortar formulation. Therefore, the mixing time was taken into consideration while the test kept running for 7 days recording one reading per minute. Finally, the released heat from the mortar reaction was plotted versus time to study the effect of the material added to the binder precursor on the reaction rate and correlate it with the compressive strength results.

Fig. 81. Calorimetry test.

2.5.13. XRD on paste specimens

The XRD was done on paste specimens for various formulations to analyze their chemical properties. Also, it was done on specimens subjected to durability tests such as the acid attack test to study the effect of the test on the integrity of the specimens. The X-ray diffraction (XRD) was done using DIFFRACTOMETRE D2 PHASER-BRUKER, equipped with Cu Kα radiation, λ=1.5406 Å with the angle acquired 2θ from 5° to 80° and a step size of 0.02.

2.5.14. FTIR on paste specimens

Similar to the XRD, the FTIR test was done on the paste specimens of different GP formulations or LFC formulations for the same purpose.

Fourier Transform Infrared Spectroscopy (FTIR) analysis was conducted using Thermo Scientific Nicolet iS20 (Fig. 82). The spectra were gathered in the wavenumber range of 600 cm^{-1} to 4000 cm^{-1} at a resolution of 4 cm^{-1}.

Fig. 82. FTIR apparatus.

2.5.15. NMR test

The nuclear magnetic resonance (NMR) spectroscopy is a valuable tool in identifying silico-aluminate species (^{29}Si and ^{27}Al) in GP samples. This technique has been described as powerful in identifying these elements [35][316][317]. In this study, the test was conducted on GP mortar samples that were cured for 28 days and subsequently crushed into a powder form for analysis. The ^{29}Si and ^{27}Al analysis were conducted using a Brucker 300-600 MHz NMR system.

2.5.16. Leaching test

To assess the potential environmental impact of the GP formulations and LFC formulations, leaching tests were conducted on mortar samples according to the NF EN 12457-2: 2022 standard [318]. The leachates were analyzed using an Inductively Coupled Plasma Optical Emission Spectrometer (ICP-OES 5100, Agilent Technologies) to determine the concentration of heavy metals and other potentially harmful elements. The leaching was performed at a liquid -to- solid (L/S) ratio of 10 L/kg dry matter and distilled water as leaching solution. The solution was agitated for 16 hours (Fig. 83). The leaching limit values for inert waste (IW) and non-hazardous waste (NHW) specified in Directive 1999/31/EC were used to verify material compliance. The trace of elements were recorded based on the average of two values with considering their mean standard deviation.

Fig. 83. Leaching test on designed formulations.

Chapter 3. Results and Discussion – Geopolymer Binders

Chapter 3. Results and Discussion – Geopolymer binders

3.1. Results: Geopolymer mortar with flash-calcined sediments cured under ambient conditions

This section unveils the findings from the examination of Geopolymer mortar using flash-calcined sediments and subjected to ambient curing conditions. The primary objective is to identify the optimal AR/B ratio that maintains both strength and durability. Following the determination of the optimum AR/B ratio, a durability assessment was carried out through an acid attack test. Physicochemical properties were analyzed using XRD and FTIR tests, while the NMR test was employed to detect the presence of a well-structured geopolymer matrix.

3.1.1. Compressive strength test

Fig. 84 displays the compressive strength for all GP formulations. For all GP formulations, the compressive strength has increased linearly from day 1 to day 60. However, the GP formulations have gained most of their strength from day 1 to day 7. A study done by Garcia et al. [319] shows that geopolymer alkalized with K^+ solution will have their strength increase from day 3 to day 7 and then remain constant from day 7 to day 14 and increases again at day 28. This compressive strength development explanation is the case for the GP in this study. For example, S24K76G0R1 showed an increase from day 1 to day 7 from 21 MPa to 33 MPa, at day 14 it remained 33 MPa and then it increased to 38 MPa on day 28. The explanation provided by Garcia et al. [319] states that in the early stages, aluminosilicates dissolve from the binder precursors, followed by a polycondensation reaction that leads to the development of an interconnected structure and a gradual increase in compressive strength. However, in geopolymer that is alkalized with K+, a decrease in compressive strength occurs after 14 days of curing time due to the decrease in water content, which results in a slower dissolution rate of aluminosilicates. The author elucidated this kinetic behavior by examining the results of calorimetry and XRD [319].

The compressive strength for all GP formulations with the lowest AR/B has shown a higher compressive strength since day 7. For example, S24K76G0R1, S20K70G10R1, and S16K64G20R1 have shown compressive strengths of 33 MPa, 38 MPa, and 44 MPa, respectively. At day 60 these compressive strengths have continued to increase and stayed the highest to reach 40 MPa, 43 MPa, and 47 MPa. On the second hand, S24K76G0R4, S20K70G10R4, and

S16K64G20R4 have shown the lowest compressive strengths equal to 36 MPa, 40 MPa, and 41 MPa, respectively. Therefore, as the AR/B increases, the W/B is increasing, thus decreasing the compressive strength. Hadi et al. [320] has concluded that when increasing the AR/B ratio, the compressive strength is going to decrease but increases workability.

Clearly, GBFS content influences compressive strength. As the GBFS proportion has increased from 0 % to 20 %, the compressive strength increases independent of the AR/B ratio. At day 28, that of S24K76G0R1 was equal to 38 MPa, but that of S16K64G20R1 was 41 MPa, therefore as the GBFS content increases, the FCS and MK content decrease, thus a better performance in compressive strength is found. This is true due to the CaO content found in GBFS which has a significant effect in increasing the compressive strength [320][321][322][323][118]. According to Lee et al. [324] increasing the content of GBFS results in a decrease in pore volume and an increase in the density of the GP matrix. This aligns with the forthcoming findings which indicate that S16K64G20R1 displays the least amount of porosity, while S24K76G0R1 exhibits the highest.

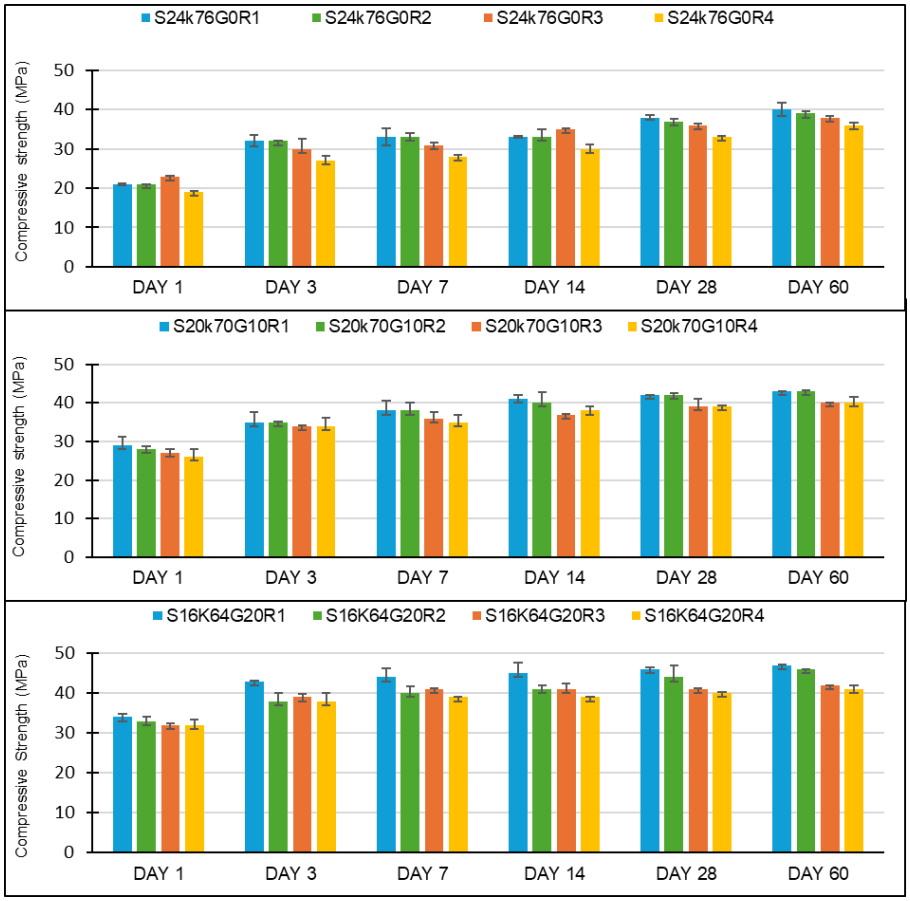

Fig. 84. Compressive strength at days 1, 3, 7, 14, 28, and 60.

3.1.2. Water boiling test

The objective of this experiment was to evaluate various GP mortar formulations with different binder percentages and AR/B ratios to assess their durability and optimize the AR/B ratio. All GP samples had a change in color form black to grey as displayed in Fig. 85 .

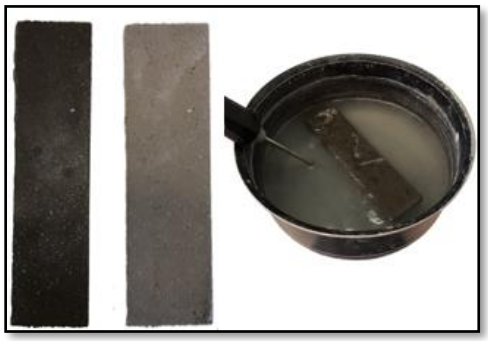

Fig. 85. Water boiling test.

Some of the formulations, including S24K76G0R1, S20K70G10R1, and S16K64G20R1, did not experience any reduction in strength. However, an increase in the AR/B ratio resulted in a proportional loss in strength. For instance, S24K76G0R2 experienced a 3.5% decrease in strength, while S24K76G0R3 and S24K76G0R4 had losses of 4.2% and 7.7%, respectively. Similar trends were observed in other GP formulations. The density of the mixture decreased as more AR was added to the GP formulations while the binder percentage remained constant, leading to a decrease in the durability of the GP mortar as the AR/B ratio increased. Previous studies [325][326]–[328] have shown that increasing the binder dosage increases the mixture density, thus can improve strength and durability with a constant AR/B ratio. However, in this study, only the AR content was varied while the binder percentage was kept constant, resulting in a less dense mixture. Therefore, S24K76G0R1, S20K70G10R1, and S16K64G20R1 were the best formulations in terms of strength and durability, so the optimum AR/B ratio is (R1) for the 3 formulations.

It is imperative to note the impact of GBFS on the durability of GP. Various GP formulations have exhibited a decrease in strength, with some formulations demonstrating greater strength loss than others as displayed in Fig. 86. For instance, S24K76G0R2 displayed a more pronounced strength reduction compared to S20K70G10R2, while S16K64G20R2 exhibited the least amount of strength loss. This trend is also observed in other formulations with higher AR/B ratios. As the proportion of GBFS in the GP increases, the material becomes more resistant to strength loss. This

is attributed to the higher content of calcium and magnesium in GBFS, which can react with aluminosilicate sources used in geo-polymerization, forming additional reaction products, and ultimately resulting in a denser and more durable geopolymer matrix.

The presence of MK in significant amounts in these geopolymer formulations plays a vital role in resisting boiling temperatures. Saif et al. [329] conducted a study on the impact of MK on concrete exposed to elevated temperatures. The authors noted that MK assists in forming gels that fill the micropores in the matrix, preventing an increase in concrete sorptivity when subjected to high temperatures, and consequently enhancing its durability.

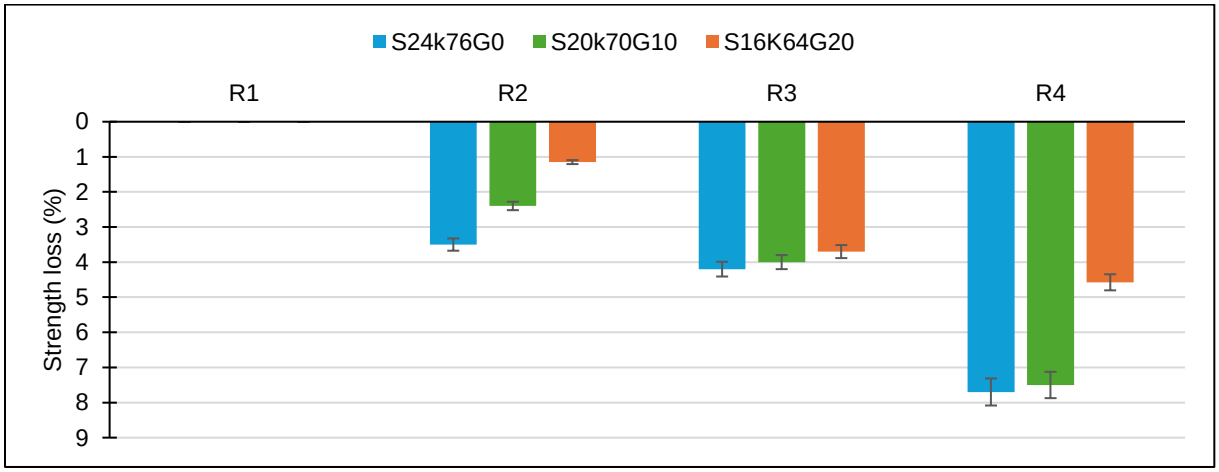

Fig. 86. Compressive strength loss (%) after water boiling test.

3.1.3. Workability test

The workability of each GP formulation is related to the AR/B ratio. The alkaline reagent contains approximately 55% water and 45% dry content. Therefore, as the AR/B ratio increases, the water -to- binder ratio (W/B) contained in the mix increases accordingly. GP mortar formulations without GBFS have the highest AR/B ratio. Thus, S24k76G0(R1, R2, R3, R4) has the highest slump flow diameter as shown in Fig. 87. Additionally, as the assumed percentage of Al_2O_3 reacting for FCS increases, the AR/B ratio also increases, which is true for all the GP mortar formulations. For instance, GP formulations with 0% GBFS have S24k76G0R4 with a slump flow diameter of 23.7 cm. Formulations with 10% and 20% of GBFS have S20K70G10R4 and S16K64G20R4, respectively, with their highest slump flow diameters equal to 22.3 cm and 22 cm. Various studies have mentioned the impact of the BET surface area of the material used on GP workability. As study by Thakur et al. [164] shows that as the percentage of MK increases in the GP formulation, the workability decreases due to MK's large BET surface area. Similarly, a study

by Al-Rawi et al. [330][331] shows that as the content of GBFS increases, the workability decreases. However, in this study, although the percentage of FCS, MK, and GBFS varies, the AR/B ratio is not constant for all formulations. Therefore, it is not very accurate to study the effect of the particles' characteristics on workability without having a constant AR/B ratio.

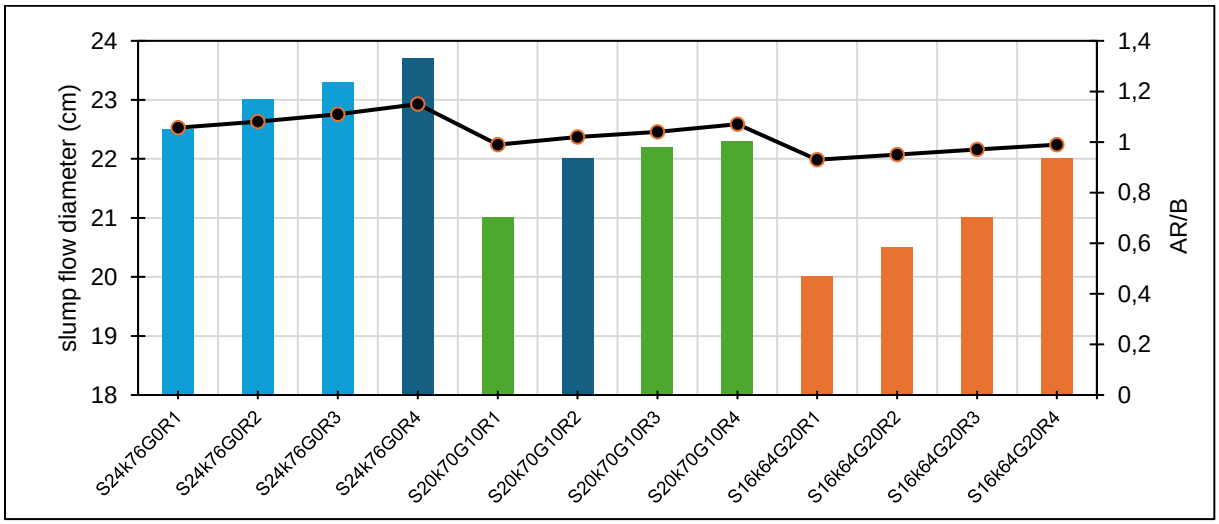

Fig. 87. Workability test results.

3.1.4. Acid attack test

Following optimization of the AR/B ratio for three distinct GP formulations (S24K76G0R1, S20K70G10R1, S16K64G20R1), a 2% sulfuric acid test was conducted to assess the durability of the formulations after 28 days of curing at ambient conditions. This study includes the evaluation of mass loss of the aforementioned GP mortar formulations at seven-day intervals during acid replenishment, as well as an assessment of compressive strength loss after 28 days of exposure. Additionally, a visual analysis of the GP formulations was conducted every seven days.

- Visual inspection

Fig. 88 illustrates the visual characteristics of the GP mortar. It appears that over time, the physical structure of the three GP mortars has altered. Days 7 and 14 didn't display significant differences compared to day 0. However, by day 28, the external layers of the GP mortars had slightly faded, and tiny pores were apparent on the surfaces and edges of the specimens. Although it is challenging to compare the mortar samples to each other, it is evident that S24K76G0R1 has deteriorated more than the other samples after 28 days.

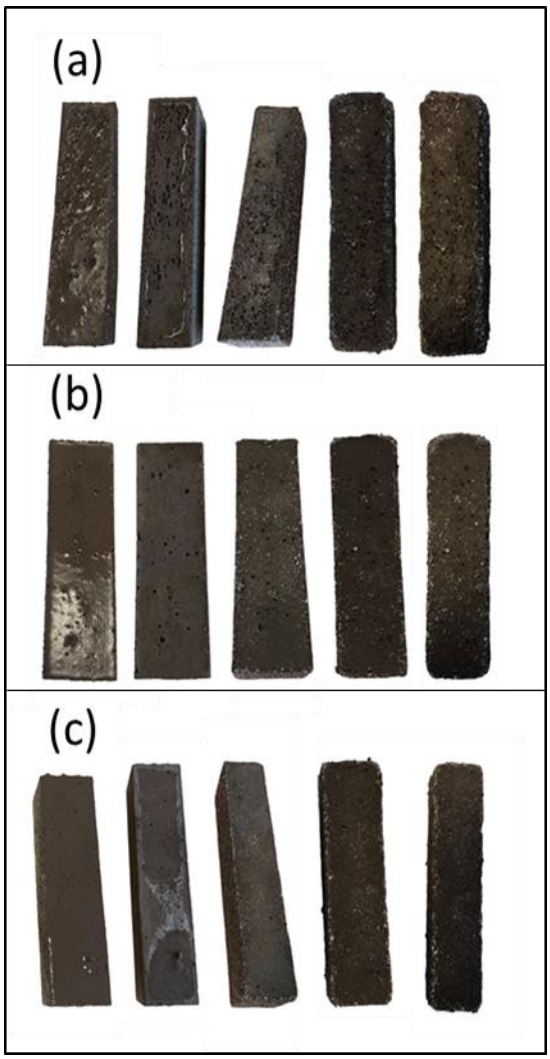

Fig. 88. (a) S24K76G0R1 exposed to 2% H_2SO_4 at days 0, 7, 14, and 28; (b) S20K70G10R1 exposed to 2% H_2SO_4 at days 0, 7, 14, and 28; (c) S16K64G20 exposed to 2% H_2SO_4 at days 0, 7, 14, and 28.

- Mass loss

The results presented in Fig. 89 demonstrate the changes in the mass of three GP formulations (S24K76G0R1, S20K70G10R1, and S16K64G20R1) over 28 days period of exposure to 2% H_2SO_4. The data displayed represents the average of two measurements from three different samples for each formulation. The graph shows a consistent linear increase in mass loss for each formulation, beginning with 1.5%, 1%, and 0.5% mass loss for S24K76G0R1, S20K70G10R1, and S16K64G20R1, respectively, on day 7. The maximum mass loss observed was 5%, 3.8%, and 2% for each respective formulation on day 28. It should be noted that acceptable mass loss values may vary depending on the application requirements. However, the mass loss observed in this

study was not deemed dangerous as visual inspection of the GP revealed no significant cracking or deformation. Notably, formulations containing 20% GBFS exhibited the lowest mass change, indicating that higher GBFS content and lower MK and FCS content resulted in greater resistance to mass change upon exposure to 2% sulfuric acid for 28 days.

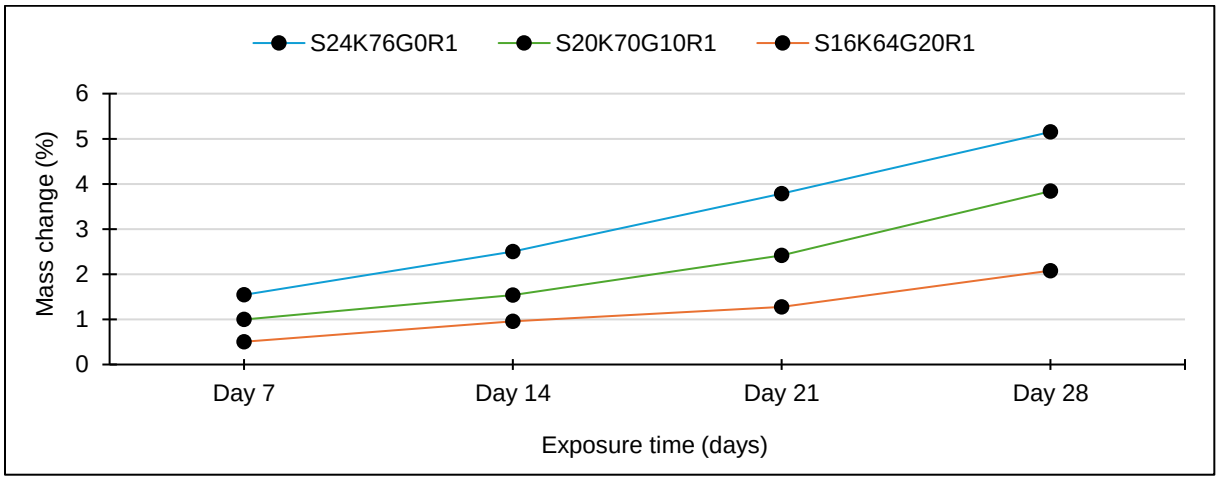

Fig. 89. Mass change % for GP mortars after exposure to acid attack test at days 7, 14, 21, and 28.

- Strength loss

The outcomes represented in Fig. 90 display the decline in compressive strength of three GP mortar compositions, namely S24K76G0R1, S20K70G10R1, and S16K64G20R1, following a 2% attack test for 28 days. The loss in strength for S24K76G0R1 was recorded at 39%, while that of S20K70G10R1 and S16K64G20R1 were found to be 26% and 11%, correspondingly. Consistent with the variation in mass, S16K64G20R1 exhibited greater durability in comparison to the other GP mortar formulations. Several studies have demonstrated the effects of incorporating GBFS in FA GP formulations. One such study conducted by Aiken et al. [310] investigated the effect of GBFS content on FA GP's mass change resistance and compressive strength after exposure to sulfuric acid. The findings of this study revealed that as the percentage of GBFS in the GP mortar increased, the mass loss decreased. Furthermore, the compressive strength of the GP mortar increased with higher GBFS content before exposure to acid, and these samples maintained their higher compressive strength even after exposure to acid with varying concentrations (1%, 3%, and 5% H_2SO_4). These findings align with the current study, which also demonstrated a reduction in mass and compressive strength loss as GBFS content increased. However, the authors [310] also

observed that as the GBFS content increased the visual appearance of the samples deteriorated due to the formation of cracks caused by the larger amounts of gypsum that led to the expansion of the samples. It is important to note that Aiken et al.'s GP formulations did not contain any MK content, and the GBFS content ranged from 20% to 70%, which is higher than the GBFS content used in this study which did not exceed 20%. But in this study, as the GBFS content increased from 0% to 10% to 20%, the visual appearance of the sample with more GBFS seemed to have less cracks especially from that with no GBFS at all, also with the formulation containing 10% of GBFS the visual appearance was similar to the sample with 20% of GBFS.

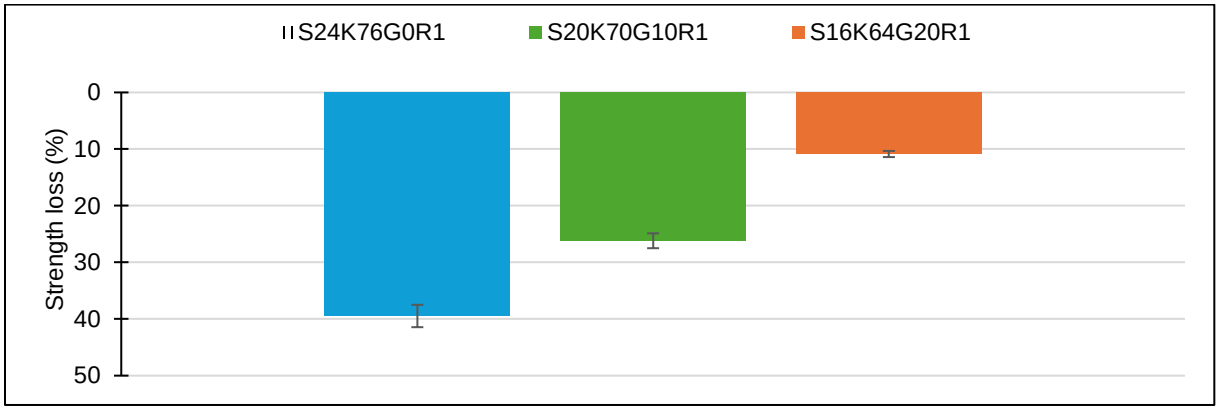

Fig. 90. Compressive strength loss (%) of GP mortars after exposure to acid attack test for 28 days.

- pH variation

The three GP formulations, S24K76G0R1, S20K70G10R1, and S16K64G20R1, all have a pH of 13 and were placed in an acidic environment with a pH of 1.11. The basic nature of the GP mortars caused the pH of the acid to increase, as shown in Fig. 91. For instance, the pH of the solution for S24K76G0R1 increased from 1.11 to 1.8 after 7 days. The acid was replaced, and on day 14, the pH was lower at 1.6 than on day 7. This pattern was consistent throughout the testing period for all three GP formulations, indicating a gradual decrease in leaching over time with each exposure. At the end of the test, the pH of the solution on day 28 was 1.25. This gradual decrease over time suggests that fewer ions were leaching from the samples into the acid solution, resulting in less impact on the samples. Additionally, S20K70G10R1 and S16K64G20R1 had less leaching of their ions in the acidic solution, as their pH increased less than S24K76G0R1. Furthermore, S16K760G10R1 recorded the lowest pH solution throughout the exposure period, with a pH of 1.19 on day 28, while S20K70G10R1 had a pH of 1.21. The ions that leached from the GP mortars were a result of the aluminosilicate network deteriorating [113][332] due to the H^+ of H_2SO_4,

which produced ($Si(OH)_4$) and $Al^{3}+$ sulfuric acid [113][333]–[335]. This indicates that S16K64G20R1 is more resistant to the acid attack test than S20K70G10R1 and S24K76G0R1 due to less leaching, as supported by the pH measurements and consistent with the mass and strength loss results.

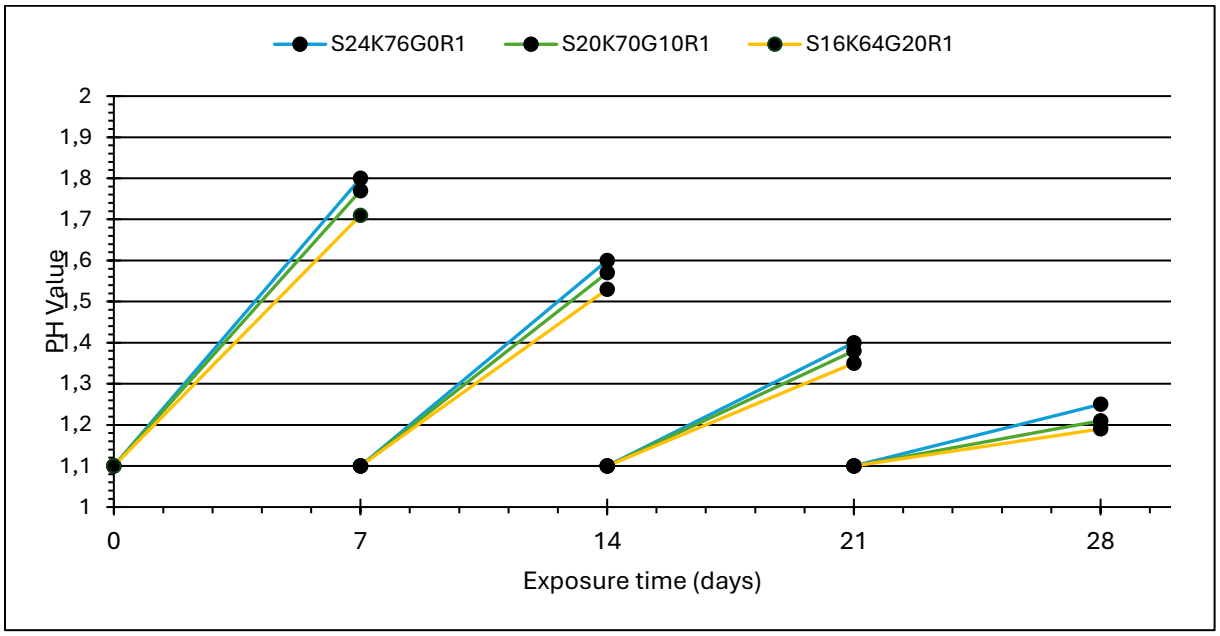

Fig. 91. pH variation with time during the sulfuric acid attack test.

3.1.5. Mercury porosity test

Following a 28-day curing period, the porosity of mortar samples was evaluated to investigate the impact of slag on mortar properties. The porosity values for S24K76G0R1, S20K70G10R1, and S16K64G20R1 were determined to be 16.21%, 15.38%, and 12.95%, respectively. Fig. 92 shows the pore size diameter distribution of the GP mortar formulations. As the percentage of GBFS is increasing in the GP formulation, the macropores exceeding 10 µm, and mesopores ranging between 100 nm and 10 µm decreased. For example, the macropores for S24K76G0R1 formulation was equivalent to 7.2% and decreased to 5.9% for S16K64G20R1. These pores tend to have a negative impact on the mechanical performance of the mortar c. On the other hand, the nanopores having a particle size diameter between 10 nm< d< 100 nm and 10 nm< d has a positive impact on the microstructure and mechanical strength [304][305]. Several studies have indicated that the addition of GBFS can decrease the porosity percentage and improve the microstructure of the GP mortar. Aiken et al. [310] reported that an increase in GBFS content led to a continuous decrease in porosity percentage, and other studies have yielded similar results

[324].Therefore, it can be inferred that higher GBFS percentages can effectively reduce porosity, strengthen GP mortar, and enhance its microstructure due to the formation of space filling C-A-S-H gel that lowers the penetration of acid into the mortar [310].

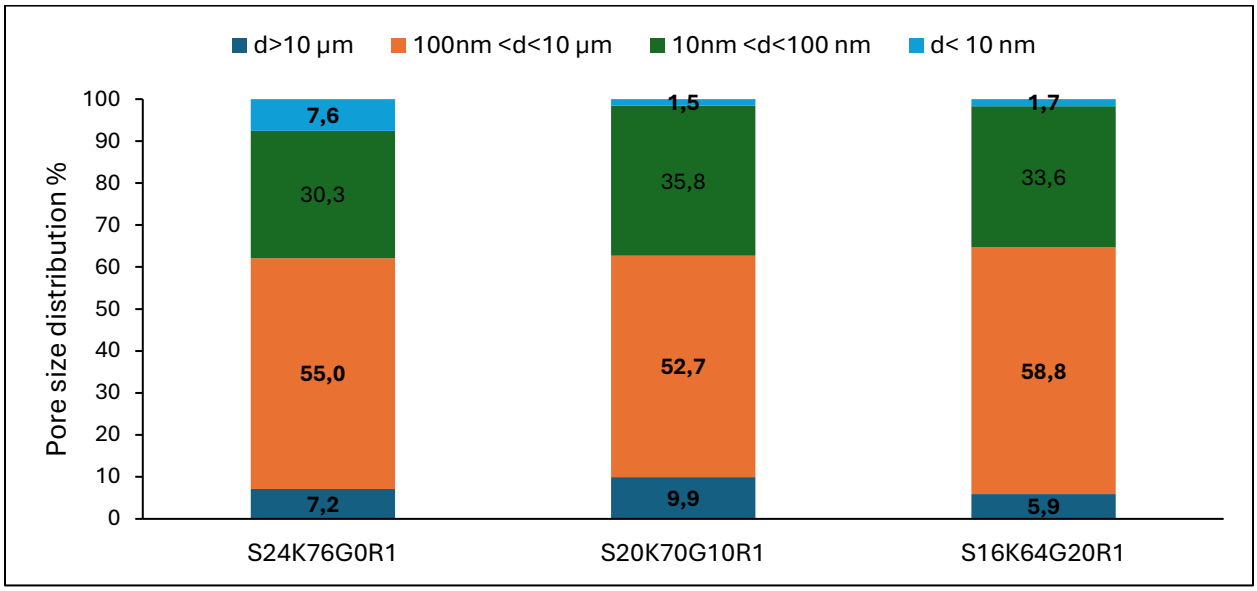

Fig. 92. Pore size diameter distribution.

3.1.6. XRD analysis on paste samples

The results of (XRD) analysis of GP paste samples not exposed and exposed to the acid attack test are presented in Fig. 93. The samples were cured for 28 days under ambient conditions and were not exposed to acid before the test. The XRD results indicate that all the GP paste formulations have the same composition, even though they contain different proportions of materials. Interestingly, there was minimal change in the peak intensities and no change in peak positions after the acid attack test, indicating the stability of the GP samples. The main composition of all GP paste samples was found to be quartz, with a small percentage of calcite present. According to Davidovits [292], geopolymers cured at room temperature are typically amorphous or glassy structures with a non-crystalline structure composed of quartz, muscovite, or hematite, depending on the materials in the precursor of the geopolymer. Since the main composition of the GP samples is MK and FCS, which have quartz as their main composition, it is logical to see quartz as the main constituent in the GP samples. The presence of calcite indicates that some particles did not react with the alkaline reagent similar to another study [336], however there is only one peak

of small intensity at 30° 2Θ. Also, all of the GP paste samples, showed a major peak at 27°-30° 2Θ, this corresponds to the presence of amorphous aluminosilicate materials [337][338][339][340].

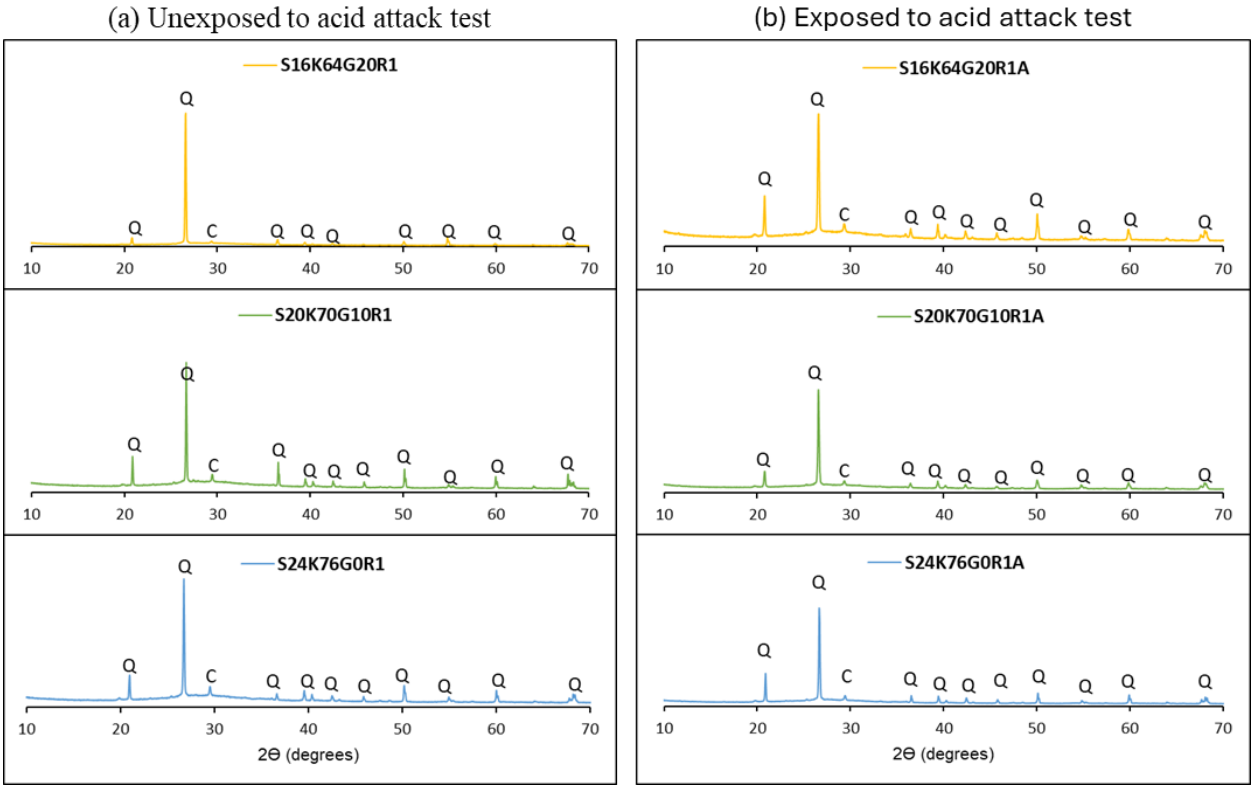

Fig. 93. XRD FOR GP samples unexposed/exposed to acid attack test.

3.1.7. FTIR analysis on paste samples

The FTIR spectra for GP paste unexposed and exposed to acid are presented in Fig. 94. The strongest vibrations for S24K760G0R1, S20K70G10R1, and S16K64G20R1 happen between 1000 cm^{-1} and 1016 cm^{-1}. These FTIR bands are important for the characterization of potassium-activated geopolymers because bands around 1000 cm^{-1} correspond to stretching vibrations of the Si-O-Si and Al-O-Si bonds in the geopolymer network [341], thus indicating a three-dimensional structure with strong Si-O and Al-O bonds. The bands present approximately at 1640 and 3440 are for the -OH groups related to the water captured in the zeolite cavities [319][342]. As indicated by [310][343] those bands corresponds to crystallization or absorption of reaction products. For bands around 690 cm^{-1} and those between 1400 and 1500 cm^{-1} are related to CO_3^{-2} of calcite mineral as indicated by [319]. The main difference between those exposed and not exposed to acid is the shifting of the main peaks. For example, the main peak of S16K64G20R1 has shifted from 1008 to 1028 cm^{-1} while that of S20K70G10R1 and S24K76G0R1 has shifted to 1028 cm^{-1}. The

shift in these peaks indicates that the acid has an effect on increasing the Si/Al ratio which is due to the dealumination of the binding gel [310][344]. The peaks at 1640 and 3440 cm^{-1} were not altered by the acid and were present at almost the same location. The shift of peaks from 1429, 1488, and 1471 cm^{-1} to 1417, 1420, and 1434 cm^{-1} for S24K76G0R1, S20K70G10R1, and S16K64G20R1, respectively indicates the release of CO_2 gas from carbonate groups, however since these peaks didn't disappear after exposure then the acid didn't have a large impact on the geopolymer matrix. A study done by Vafaei et al. [345] shows that upon acid attack test the peaks present at 1422 cm^{-1} which corresponds to O-C-O bonds disappear due to the dissolution of the carbonate compounds [345][346]. So, there was neither disappearance of some peaks nor new ones. Therefore this suggests that the acid attack test didn't alter the reaction of products of alkali activation, alike to other studies [310][344].

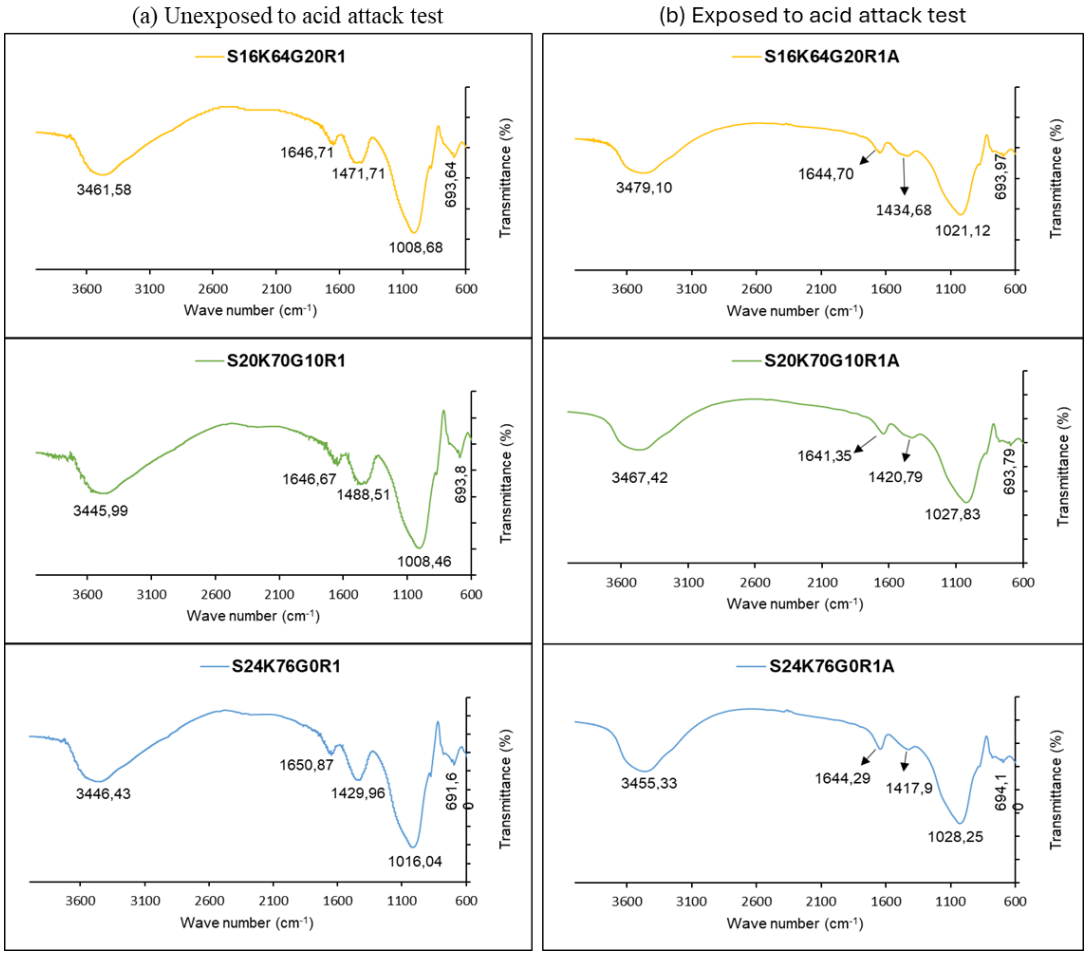

Fig. 94. FTIR spectra for GP paste samples unexposed/exposed to acid.

3.1.8. NMR test

The application of ^{29}Si NMR aims to examine the structure of Si units, categorized as Q^n (n=1 to 4), with the precursor material composition and alkali reagent employed. On the other hand, ^{27}Al NMR is employed to scrutinize the structural configurations of Al units [347]. The findings reveal that the ^{29}Si and ^{27}Al results for all the formulations are similar. Comparison of the graphs of the formulations with the model graph of MK/GBFS-based geopolymers proposed by Davidovits [292] indicates that GP binders based on MK/GBFS exhibit strong resonance within -83 to -95 ppm for ^{29}Si resonance and strong resonance at 56 ppm for ^{27}Al. The author has studied the matrix of MK/Slag based geopolymers, his investigations show that the ^{29}Si NMR shifts resonate with values at -88 and -90 ppm suggesting the formation of Q^4 3D networking elements such as Q^4(3Si,1Al), Q^4(2Si,2Al), Q^4(1Si,3Al), and Q^4(4Al), while that of ^{27}Al shifts resonate at 58 ppm suggesting three-dimensional networking of the type AlQ^4(4Si). Moreover, Klinowski [348] has identified that peaks within range -88 to -94 ppm correspond to Q^4(1Si, 3Al). Also, the authors[349][348][350] stated that four coordinated aluminum resonates at approximately 50 ± 20 ppm. The ^{29}Si and ^{27}Al NMR spectra are shown in Fig. 95 and Fig. 96. The GP formulations, namely S24K76G0R1, S20K70G10R1, and S16K64G20R1, exhibit a broad resonance at -91 ppm, -89 ppm, and -90 ppm, respectively for ^{29}Si resonance. And a resonance approximately at 60 ppm for ^{27}Al. Therefore, according to the previous explanation the GP formulations have a Q^4(1Si, 3Al) network. A study done by Ozcelikci et al. [351] has mentioned that their GP formulations have a broad resonance behavior ranging from -80 to -90 ppm indicating different Q^4(nAl) formulations and therefore this is identified by Lecomte et al. [352] as a highly polymerized structural framework. Also, Davidovits [292] has studied the ^{29}Si NMR resonance for FA geopolymer, the author has identified the peak resonating at -107 ppm corresponds to quartz. Since the GP also have FCS in their formulations that are rich in quartz as validated in the XRD test then similarly the peak found at -107 ppm corresponds to quartz as well.

A study by Duxson et al. [353] reveals that potassium geopolymer formulations with a strong resonance ratio of ^{29}Si at -90 ppm and -93 ppm have an Si/Al of 1.9 and 2.15, respectively, to confirm the design of the GP mortars having a ratio of Si/Al = 2.

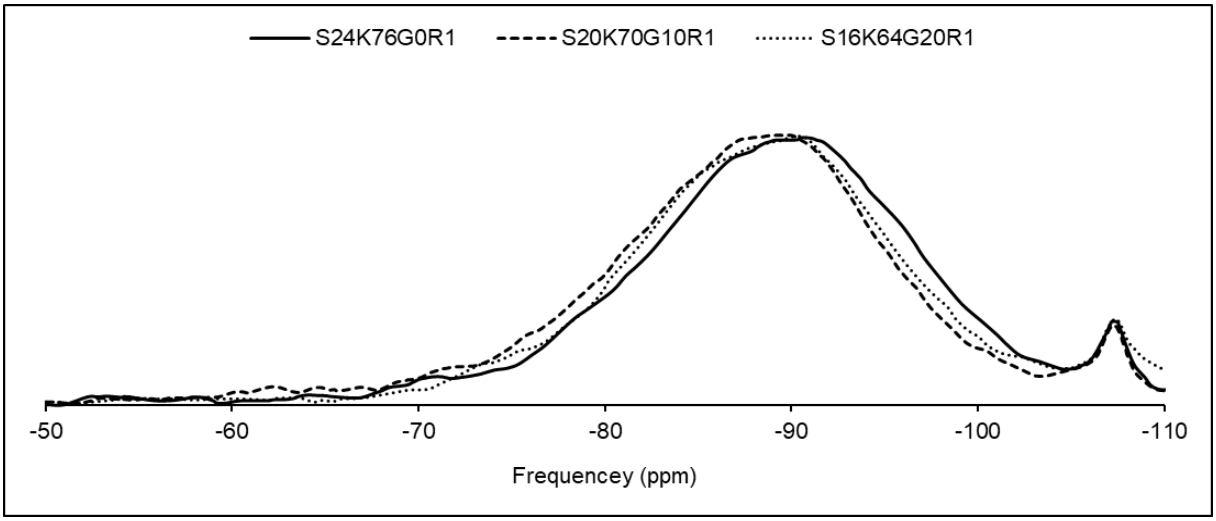

Fig. 95. ^{29}Si NMR spectra.

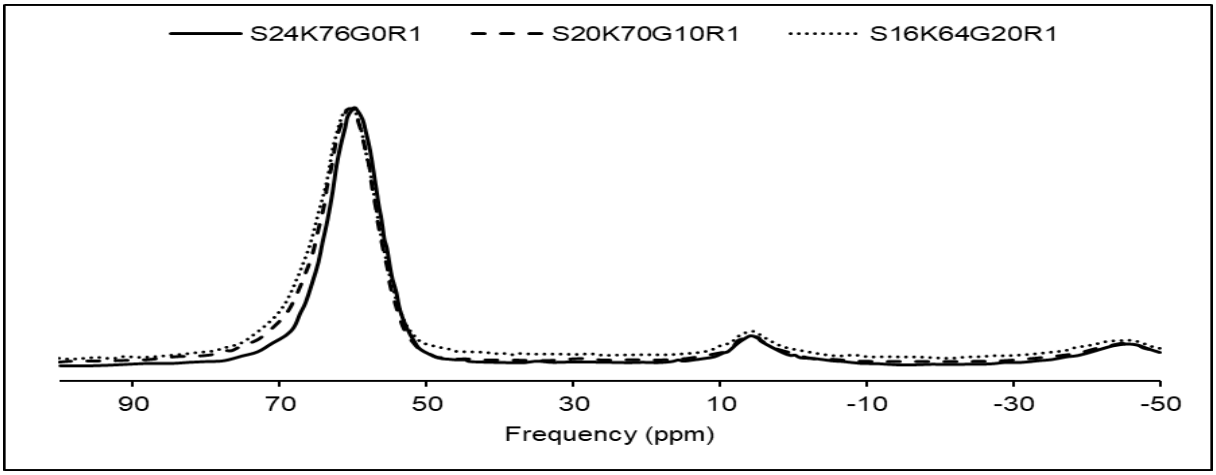

Fig. 96. ^{27}Al NMR spectra.

3.1.9. Conclusion

This part investigates the design of waste-based geopolymers. Several formulations have been prepared and have been divided into three categories based on their composition, with each category containing twelve different types. The first category comprises 24% FCS and 76% MK, with no GBFS. The second category consists of 20% FCS, 70% MK, and 10% GBFS, while the third category has 16% FCS, 64% MK, and 20% GBFS. Each category has four different AR/B ratios, determined by the percentage of Al_2O_3 reacting to the FCS. Tests were conducted on the compressive strength and boiling water resistance of each mortar to determine the best AR/B ratio for each category. Further tests were carried out on the best formulation of each category, and the results are summarized below.

- The GP formulations with the lowest AR/B ratios have demonstrated the highest compressive strength, and after being subjected to boiling water for 15 minutes, they showed no loss of strength. Consequently, as the AR/B ratio increases, the GP formulations display lower strength and durability.
- When comparing the compressive and flexural strength of the three categories, it was observed that an increase in the quantity of GBFS led to an increase in strength.
- An increase in AR/B ratio results in an increase in workability. Conversely, an increase in GBFS content in the formulations leads to a decrease in workability.
- After studying the mass and strength loss of GP mortars subjected to acid attack, it was observed that the formulation containing the highest amount of GBFS (20%) displayed the highest resistance.
- GP mortars that underwent normal curing demonstrated more porosity than those submerged in acid due to the calcium-sulphate products filling the pores. It is worth mentioning that the FCS16K64G20R1 formulation displayed fewer pores than other formulations, owing to its low AR/B ratio and high GGBFS percentage (20%).
- Microstructural tests (XRD and FTIR) conducted on paste samples that underwent normal curing and those submerged in acid displayed minimal differences, validating the fact that the GP mortar formulations were resistant to the acid attack test.
- The NMR tests confirm that the structure of the GP formulations is stable, with a 3D network. The ^{29}Si resonance indicates that the GP formulations have a $Q^4(3Al)$ network, while the ^{27}Al resonance indicates a four-coordinated aluminum structure.

3.2. Results: A comparative analysis of ambient-cured metakaolin geopolymer and flash-calcined soils geopolymer

In this section, the focus is on advancing the development of geopolymer mortar and concrete by exploring the use of alternative materials such as FCS and FCC as substitutes for MK. The same binder mix design for the binder composition is maintained as in the first section. Seven geopolymer mortar formulations are examined, varying the alkaline reagent to binder (AR/B) ratio (0.4, 0.6, 0.8) while keeping the total water-to-binder (W/B) ratio constant at 0.45. The optimal AR/B ratio, determined based on workability and compressive strength results, is found to be 0.8. To assess the reactivity of FCS and FCC and their impact on compressive strength, calorimetry tests and mercury porosity tests are conducted. The study of FCS and FCC effects on the

geopolymerization matrix involves SEM/EDS, TGA/DTG, and NMR tests. Durability assessments for geopolymer mortar formulations include acid attack, high-temperature resistance, and freeze-thaw tests. The durability of geopolymer concrete is evaluated through a water absorption test. Finally, the environmental impact is assessed by conducting a leaching test.

3.2.1. Setting optimum AR/B

The optimal ratio of AR/B is determined based on the workability and compressive strength of GP formulations at the mortar scale. Initially, when AR/B was set at 0.4, the mixture did not attain the desired consistency when using a 5 L mixer. Before the addition of sand, examination of Fig. 97 revealed inadequate interaction between binder particles, AR, and the free water in the mixture. This observation held true for formulations containing MK alone, as well as those with FCS and FCC. Consequently, GP formulations with AR/B = 0.4 were excluded from consideration, and their compressive strength was disregarded due to improper mixing of the mixture.

Fig. 97. Workability of AR/B=0.4.

In contrast to an AR/B ratio of 0.4, an AR/B ratio of 0.6 exhibited superior workability characteristics. Subsequently, compressive strength tests were performed (*Fig. 98*). All GP mortar compositions with an AR/B ratio of 0.6 demonstrated lower compressive strength compared to those with an AR/B ratio of 0.8. For instance, after 28 days, the compressive strength of MK0 with an AR/B ratio of 0.6 measured 38 MPa, whereas the counterpart with an AR/B ratio of 0.8 registered 58 MPa. Similarly, S1, S2, S3 exhibited 42%, 38%, 34% lower compressive strength, respectively, with an AR/B ratio of 0.6 compared to an AR/B ratio of 0.8. Additionally, C1, C2, C3 demonstrated 40%, 43%, 33% lower compressive strength, respectively, with an AR/B ratio of 0.6 in comparison to an AR/B ratio of 0.8. Consequently, an AR/B ratio of 0.8 is deemed the

optimal ratio. Following the establishment of this optimal ratio, various experiments were conducted to evaluate mechanical and durability properties.

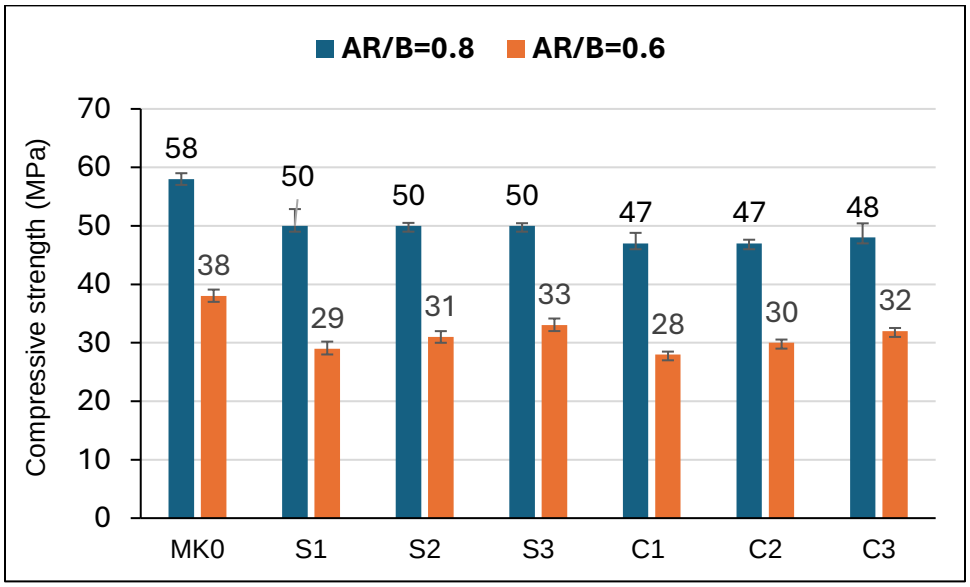

Fig. 98. Compressive strength of GP mortar formulations of AR/B=0.6, 0.8 at day 28.

3.2.2. Workability test on GP mortar formulations

The results of the workability test for GP mortar formulations with AR/B=0.8 are depicted in Fig. 99. MK0 exhibited the lowest workability, with a recorded slump flow diameter of 18 cm. In the case of GP formulations incorporating 10% GBFS into the mixture with FCS and FCC, the proportions of FCS, FCC, and MK decreased according to the mixed proportion table, resulting in an increase in the slump flow diameter. Both FCS and FCC have substantial surface areas, measuring 27.45 m^2/g and 33.01 m^2/g, respectively. The increased BET surface area negatively impacts the workability of GP [164]. For instance, S1 and C1 displayed slump flow diameters of 20 cm and 19 cm. After incorporating 10% GBFS into the mix, the slump flow diameter increased to 20.5 cm and 19.5 cm for S2 and C2, respectively. Also, with a further increase in GBFS percentage to 20%, workability increased. S3 and C3 exhibited slump flow diameters of 21 cm and 19.7 cm, respectively.

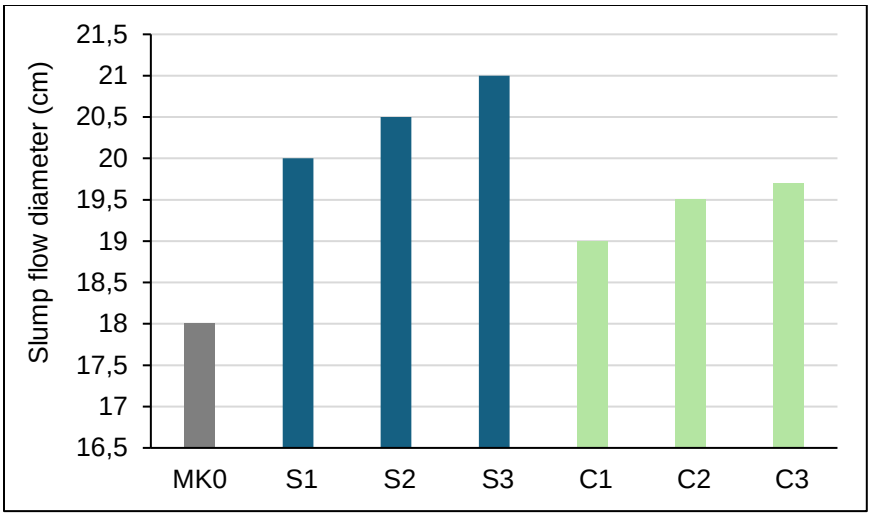

Fig. 99. Workability of GP formulations with AR/B=0.8.

3.2.3. Compressive strength test on optimized GP mortar formulations

Fig. 100 illustrates the results of the compressive strength test conducted on various GP formulations, namely MK0, S1, S2, S3, C1, C2, and C3. All these formulations exhibited a linear increase in compressive strength from day 1 to day 7. Subsequently, the compressive strength remained relatively stable during days 14 and 28, followed by another increase at day 90. For instance, the MK0 mix gained 98% of its compressive strength on day 7, amounting to 58 MPa. Similarly, S1, S2, and S3 attained 89%, 93%, and 91% of their compressive strength, corresponding to 47 MPa, 50 MPa, and 50 MPa, respectively, on day 7. In comparison, C1, C2, and C3 achieved 96%, 94%, and 89% of their compressive strength, equivalent to 47 MPa, 47 MPa, and 48 MPa, respectively, on day 7. By day 90, the compressive strength only increased by 2%, 6%, 7%, 9%, 4%, 6%, and 11% for MK0, S1, S2, S3, C1, C2, and C3, respectively. Previous research by Garcia et al. [319] discussed that geopolymer alkalized with K+ solution demonstrated an initial increase in compressive strength from days 3 to 7, followed by a plateau from days 7 to 14, and then a resumption of strength increases at day 28. Likewise, Haddad et al. [354] developed GP concrete using natural pozzolan material and categorized it as high early-strength concrete. Certainly, a prior investigation conducted by ALLOUL et al. [355] provides insights into the pozzolanic reactivity of FCS and FCC. Comparing the reference mix MK0 to the other GP formulations after 90 days of room temperature curing, MK0 exhibited higher compressive strength than S1, S2, S3, C1, C2, and C3 by 11%, 9%, 7%, 17%, 15%, and 9%, respectively. This

higher increase is explained to MK particles' better reactivity with the AR than that of FCS and FCC, thus achieving the best microstructure as evidenced by the mercury porosity test section and the SEM/EDS test results. Additionally, an interesting observation was made as the percentage of GBFS increased from 0% to 10% and 20% in the aforementioned formulations (S1, S2, S3, C1, C2, and C3), the compressive strength also increased. For instance, FCS3 showed higher compressive strength than S1 and S2 by 4% and 2%, respectively, while C3 had higher compressive strength than C1 and C2 by 9% and 7%, respectively. This increase in compressive strength is attributed to the CaO content in GBFS [33][320][321][322][323][118], which decreases the pore volume and increases the density of the GP matrix. The effect of GBFS on the pore structure is further discussed in the study.

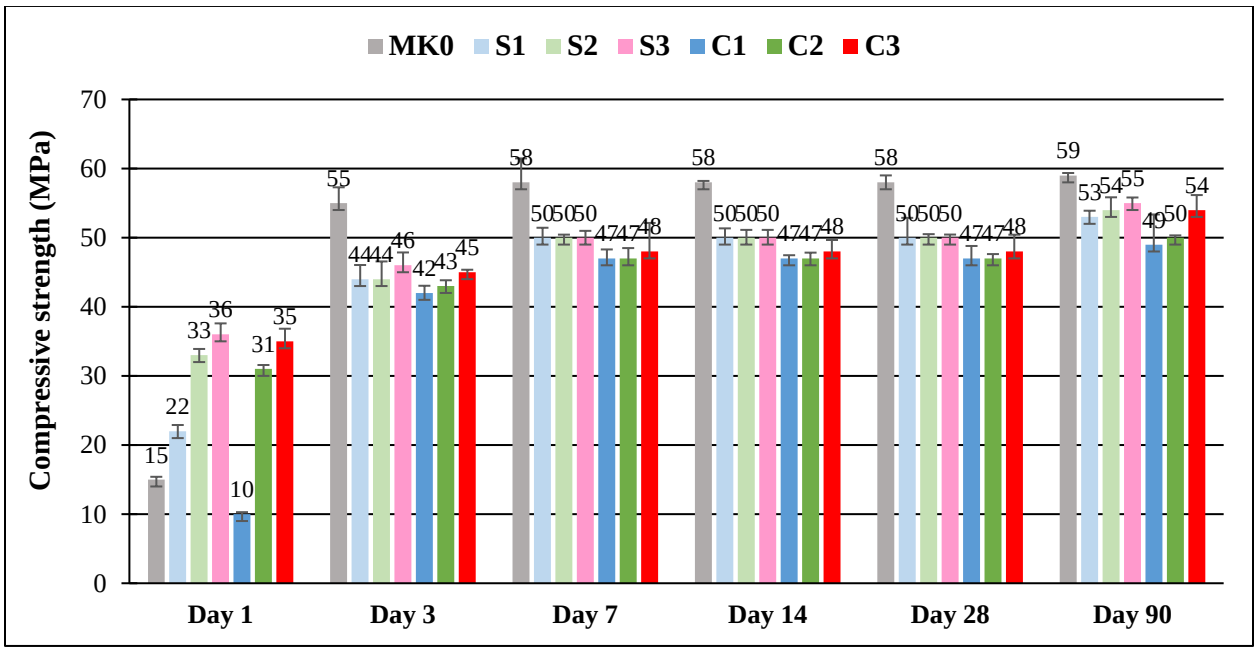

Fig. 100. Compressive strength (MPa) on days 1, 3, 7, 14, 28, and 90.

Various studies have discussed the utilization of sediments in the development of GP mortar. Hosseini et al. [3] conducted a study that examined the compressive strength of GP mortar formulations incorporating dredged sediments, distinguishing between low fractions (less than 30%) and high fractions (greater than 30%). In the present investigation, FCS was employed in the development of GP mortar, with percentages ranging from 16% to 24%, falling within the category of less than 30%. According to existing literature, GP mortar formulations with less than 30% displayed compressive strengths at day 7 ranging from 0 to 8 MPa [356], 8-24 MPa

[215][356][357], 124-32 MPa [215][229][358], and 40-56 MPa [359]. The highest reported compressive strength in previous studies was 56 MPa. Remarkably, the current study demonstrated a compressive strength of approximately 50 MPa at day 7 for GP mortar, signifying a notable advancement compared to the strengths reported in existing literature. The literature results are summarized in Fig. 101.

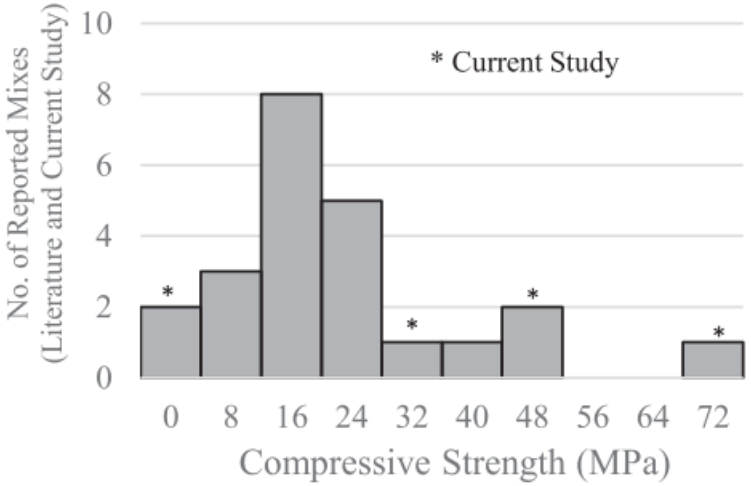

Fig. 101. Compressive strength results of GP with sediments reported by Hosseini et al. [3].

Also, different studies have mentioned the usage of clays in geopolymer binders. Similar to this study, Lekshmi et al. [360] has assessed the addition of GGBFS to clay-based GP formulations (2 types of clay). Their compressive strength results were equal to approximately 20 MPa and 25 MPa as shown in *Fig. 102*.

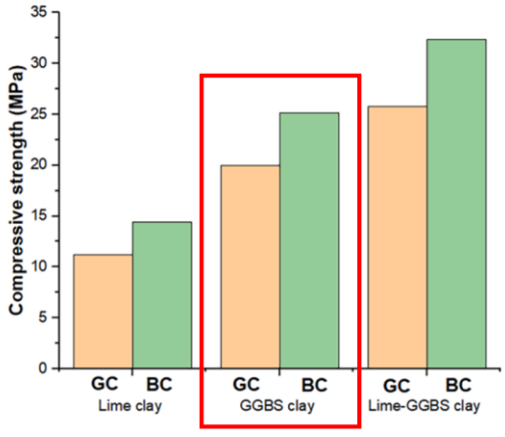

Fig. 102. Compressive strength (MPa) for GGBFS clay GP reported by Lekshmi et al. [360].

Ettahiri et al. [252] created geopolymer by utilizing four distinct varieties of Moroccan clays. The outcomes are presented in *Fig. 103* . The compressive strength on day 7 was documented for geopolymer formulations, yielding values of 8.69 MPa, 29.35 MPa, 34.5 MPa, and 63.82 MPa. The author attributed the superior strength of the geopolymer with BORJ clay due to its calcite content (26.7%), which contributes to the formation of calcium silicate hydrate (C-S-H) gel, thereby enhancing compressive strength. In this study, the FCC used has only low calcite content equal to 2.85%. However, the incorporation of GBFS to GP formulations with FCC tends to increase the compressive strength as shown in Fig. 100. Compressive strength (MPa) on days 1, 3, 7, 14, 28, and 90.. The author also mentioned that the high excess of calcium content will cause a decrease in the compressive strength [252][361][362], therefore it's important to note out that the amount of GBFS used in all GP formulations are limited to a maximum of 20% from the binder mass.

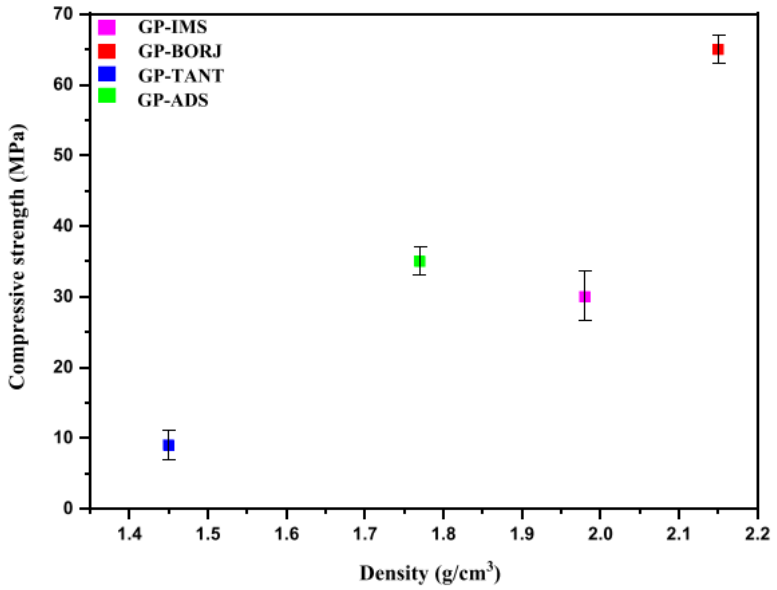

Fig. 103. Compressive strength for GP mortars using 4 clays reported by Ettahiri et al. [252].

3.2.4. Calorimetry test

Fig. 104, Fig. 105, and Fig. 106 illustrates the heat evolution of various GP mortar formulations over time in days. This investigation aimed to enhance the understanding of the early age compressive strength of GP formulations, particularly those exhibiting superior strength compared to MK0. The reference mix MK0 reaches a peak temperature of 41°C approximately

0.8 days after the addition of AR to the MK binder. This heat release is attributed to the dissolution of alumino-silicates in MK upon contact with AR. Notably, MK0 exhibits a high compressive strength of 15 MPa on day 1 on the mortar scale.

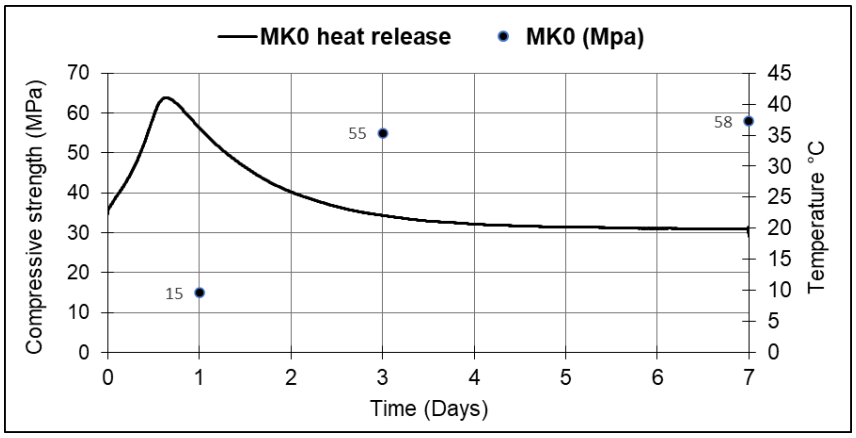

Fig. 104. Heat release of MK0 mortar for 7 days.

When comparing the heat release of the six GP mortar formulations (S1, S2, S3, C1, C2, C3) with MK0 and considering compressive strength, the following is deduced. S1, S2, S3, C2, and C3 all exhibit higher temperature releases earlier than MK0, with their compressive strength surpassing that of MK0 on day 1, except for C1. For instance, S1, S2, and S3 reach maximum heat releases of 39.5°C, 42°C, and 43°C at times of 0.6, 0.45, and 0.3 days, respectively. Correspondingly, their compressive strengths after one day are recorded as 22, 33, and 36 MPa. It's evident that the increase in the percentage of GBFS from 0% to 10% to 20% for S1, S2, and S3 results in higher compressive strength and maximum heat release at an early age of 1 day, greater than MK0.

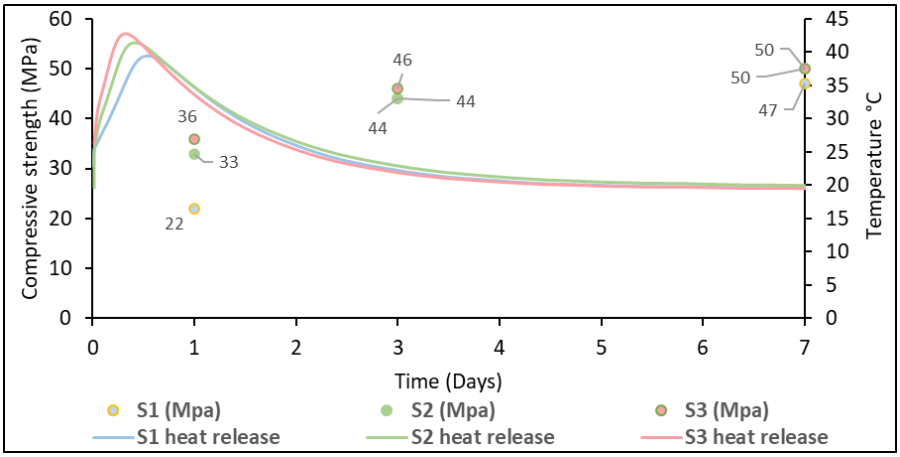

Fig. 105. Heat release of S1, S2, S3 mortar for 7 days.

Similarly, C2 and C3 show results like S1, S2, and S3, with maximum heat releases of 40-41°C after 0.45 and 0.44 days and compressive strengths of 31 and 35 MPa, respectively. On the other hand, C1 differs in that its maximum heat release of 37°C occurs at 1 day with a compressive strength of only 10 MPa. In comparison with MK0, the higher compressive strength of C2 and C3 is attributed to a faster reaction between the alumino-silicates of the binders and AR due to the incorporation of GBFS.

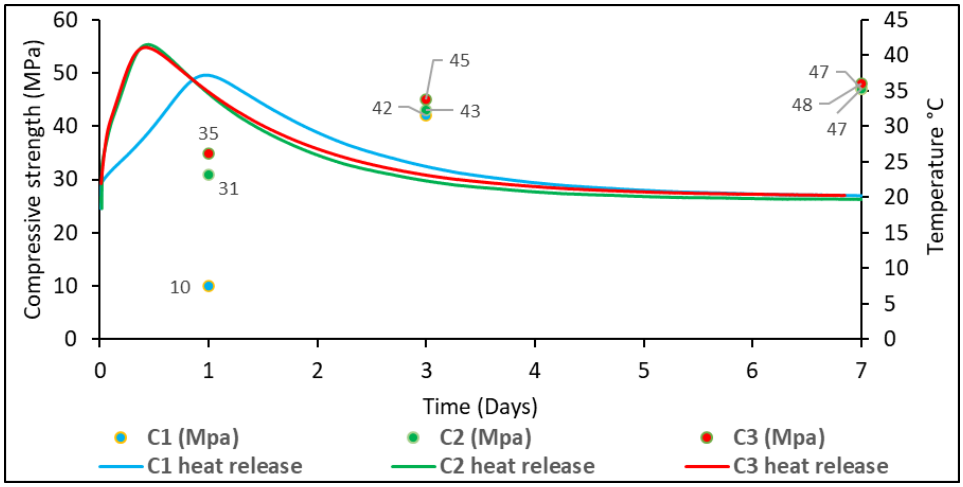

Fig. 106. Heat release of C1, C2, C3 mortar for 7 days.

In summary, the increase in the percentage of GBFS in GP mortar formulations leads to higher compressive strength due to a faster geopolymerization reaction. Previous research on the influence of ground granulated blast furnace slag (GBFS) on geopolymerization behavior and early high strength aligns with these findings. GBFS affects reaction kinetics, microstructure, and mechanical properties, promoting the development of C-S-H gel and a compact microstructure due to the presence of CaO [322][116]. It's important to mention that these trends are consistent at the concrete scale, where S1, S2, S3, C2, and C3 exhibit higher compressive strength than MK0 on day one, while C1 shows lower compressive strength.

3.2.5. Mercury porosity test

In Fig. 107, the pore size distribution of various geopolymer (GP) formulations on the mortar scale is presented. The formulations, namely MK0, S1, S2, S3, C1, C2, and C3, exhibit total porosities of 16%, 18%, 17%, 15%, 15%, 16%, and 16%, respectively. Despite MK0 sharing a similar overall porosity with other formulations, it demonstrates higher compressive strength. This distinctive strength can be attributed to MK0's remarkable feature: 45% of its porosity

comprises nanopores with diameters less than 10 nm, known to have a significant impact on the geopolymer strength [304][305]. Additionally, MK0 exhibits the least pores falling between 100 nm and 10 µm equal to 21%, which are mesopores that have a negative impact on the mortar mechanical strength as they become the source of microcracks formations [304][363].

When comparing the porosity and compressive strength between S1, S2, and S3, a trend is observed. As the percentage of GBFS increases, there is a decrease in macropores, those exceeding 10 µm, and mesopores ranging between 100 nm and 10 µm. Specifically, for S1, the macropores and mesopores constitute 32%, while for S2 and S3, these percentages are 32% and 28%, respectively. Interestingly, the proportion of beneficial pores also increases with the incorporation of GBFS in the formulations. Different studies have mentioned the positive impact of GBFS on the microstructure of the geopolymer mortar and lead to a denser matrix [364][33][324][310] .For instance, S1 has 68% of pores with diameters less than 10 nm and between 10 nm and 100 nm combined. Similarly, S2 and S3 show percentages of 69% and 7 %, respectively. Similarly, to the GP formulations with FCS, those with FCC (C1, C2, and C3) showed a similar behavior. For example, C1 showed 54% of nanopores while C2 and C3 showed 64 and 63 %, respectively. Therefore, the porosity results are compatible with the compressive strength results for the GP mortar formulations with FCS and FCC.

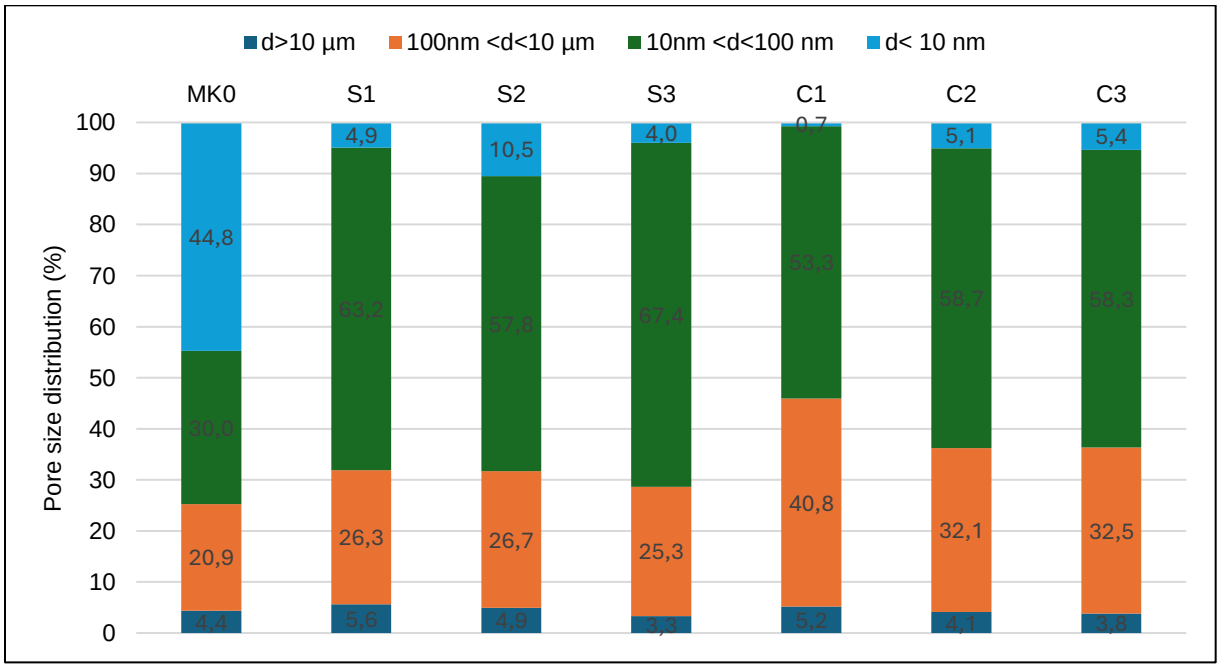

Fig. 107. Pore size diameter distribution (%).

3.2.6. Acid attack test

A 2% sulfuric acid test was performed to evaluate the formulations' durability after 28 days of curing at ambient temperatures. The mass loss of the GP mortar formulations was evaluated at seven-day intervals during acid replenishment, as well as the compressive strength loss after 28 days of exposure. A visual study of the GP formulations was also performed every seven days, with photographic evidence shown in Fig. 108.

- Visual study

Fig. 108 illustrates the tracking of GP mortar formulations' shapes, with two samples photographed for each GP formulation. It is evident that over time, all GP mortar formulations were affected, including the reference mix MK0.The most significant change in shape from day 0 to day 28 occurred in MK0, unlike the other GP formulations (S1, S2, S3, C1, C2, C3). A comparison can't be made between S1, S2, and S3 or between C1, C2, and C3 because it seems that the acid had the same impact on their visual shape. Initially, during the first 7 days, the changes in shape were not very noticeable. However, by day 14, the visual shape of the GP formulations became obvious, with noticeable color changes. MK0, C1, C2, and C3 shifted from dark orange to light orange, while S1, S2, and S3 changed from dark black to light black. These color alterations resulted from the loss of the outer layer of the GP formulations, which is caused by the acid penetration. By day 21, the impact of the acid became highly visible, particularly as it completely removed or affected the outer layer, exposing the sand particles used in developing the GP formulations. Notably, MK showed the most exposed sand particles. From day 21 onwards, there was little difference in shape observed among the mortar samples, suggesting that the acid no longer has a high impact on the physical structure of the GP mortar samples.

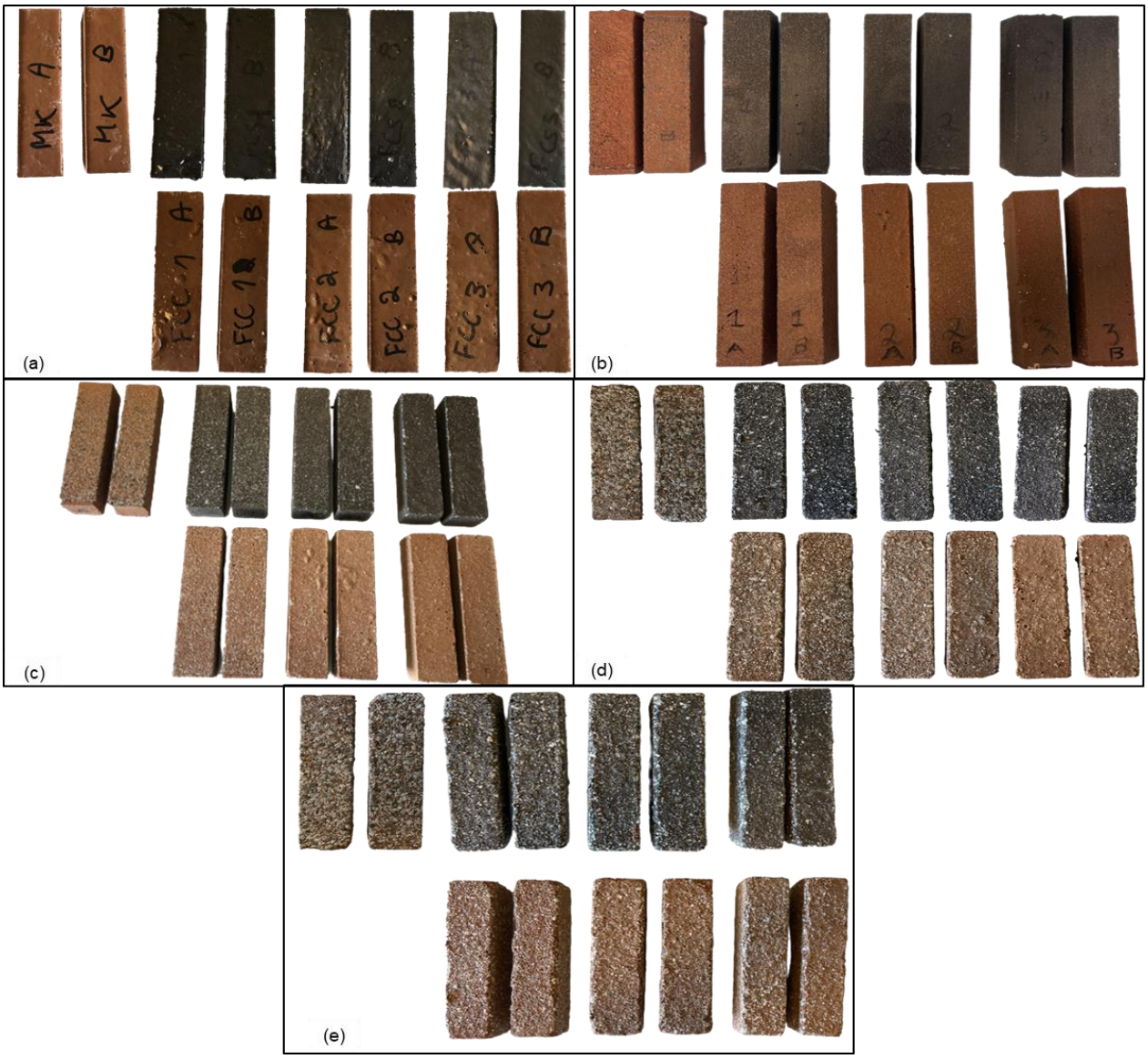

Fig. 108. Exposure of GP mortar formulations to 2% H_2SO_4 on (a) Day 0, (b) Day 7, (c) Day 14, (d) Day 21, (e) Day 28.

- Mass loss

The mass loss % change of the GP mortar formulations (MK0, S1, S2, S3, C1, C2, C3) over the 28-day acid attack test is displayed in Fig. 109. The percentage increase in mass change corresponds to a loss of mass, whereas the percentage decrease in mass change represents a gain in mass. For each formulation, the data given is the average of two measurements taken from three separate samples. Three important conclusions can be drawn from the graph. First, it is clear that MK0 has shown a linear increase in mass loss and has recorded a maximum mass loss of 13.42%

when compared to the other formulations. Second, it is also obvious when comparing S1, S2, and S3 or C1, C2, and C3 that as the GBFS content increases, the loss in mass decreases. S1, S2, S3, C1, C2, C3 recorded 1.59%, 0.61%, 0.17%, 2.81%, 1.51%, and 0.2% on day 28. Finally, it is crucial to note that, apart from MK0, the GP mortar formulations have shown a very minor increase in mass from day 21 to day 28. Aiken et al. [310] conducted the acid attack test on GP formulations and the increase in mass after the test is explained by the production of chemical compounds during the exposure time.

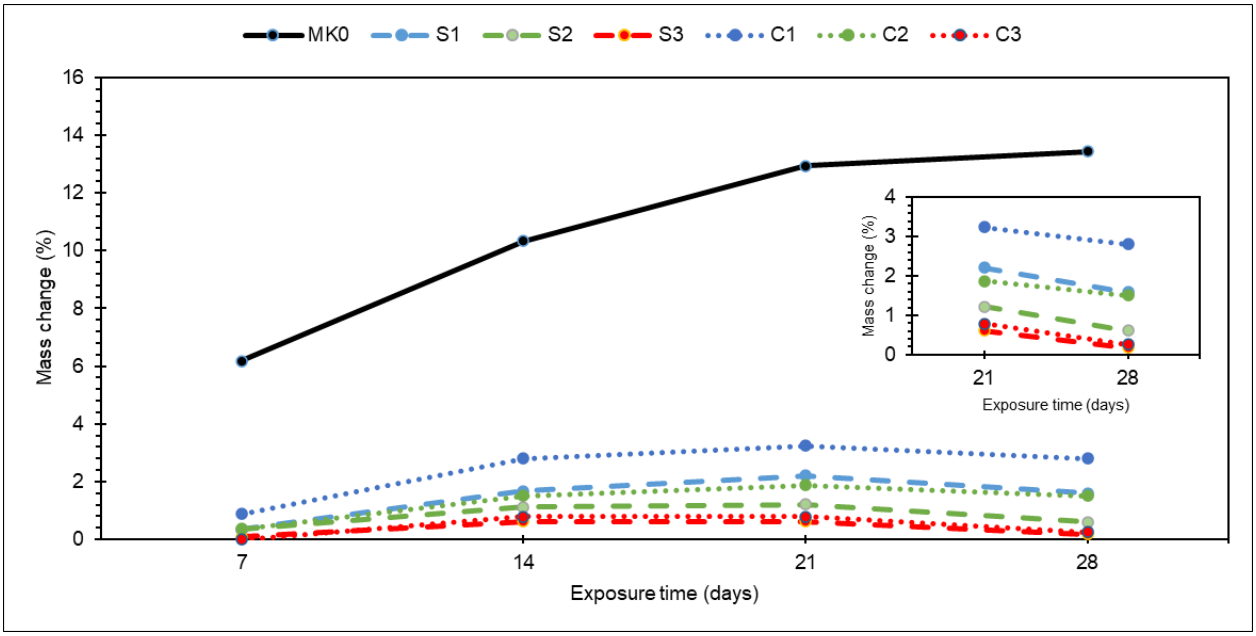

Fig. 109. Mass loss % for GP mortars after exposure to 2% H2SO4 at days 7, 14, 21, and 28.

- Strength loss

The reduction in compressive strength following exposure of the geopolymer (GP) mortar formulations to an acid attack test at day 28 is displayed in Fig. 110. In this study, all GP mortar formulations experienced a decrease in compressive strength after being subjected to 2% H_2SO_4 for 28 days. For instance, MK0 exhibited a 40% decline in compressive strength. Comparatively, S1 and C1, both lacking GBFS, displayed a slightly higher reduction in compressive strength, equal to 42 MPa. The superior performance of MK0 compared to S1 and C1 could be attributed to its higher initial compressive strength in the unexposed samples. Previous research by Aiken et al. [310] also supported the notion that formulations with higher initial compressive strength tend to sustain lower losses in compressive strength under such conditions. Moreover, S1 comprises 24% FCS and 76% MK, while C1 consists of 27% FCC and 73% MK. The substitution of MK by FCS

and FCC resulted in lower compressive strength due to MK's superior reactivity and its propensity for achieving a more rapid geopolymerization reaction with the AR. However, S2, S3, C2, and C3 experienced 35%, 35%, 40%, and 39% loss in compressive strength, respectively. Consequently, these GP formulations recorded the lowest reduction in compressive strength compared to MK0 and other GP formulations without GBFS. Additionally, other studies have also demonstrated that increasing the content of GBFS in the binder of GP leads to a decrease in compressive strength loss during acid attack testing [310][33].

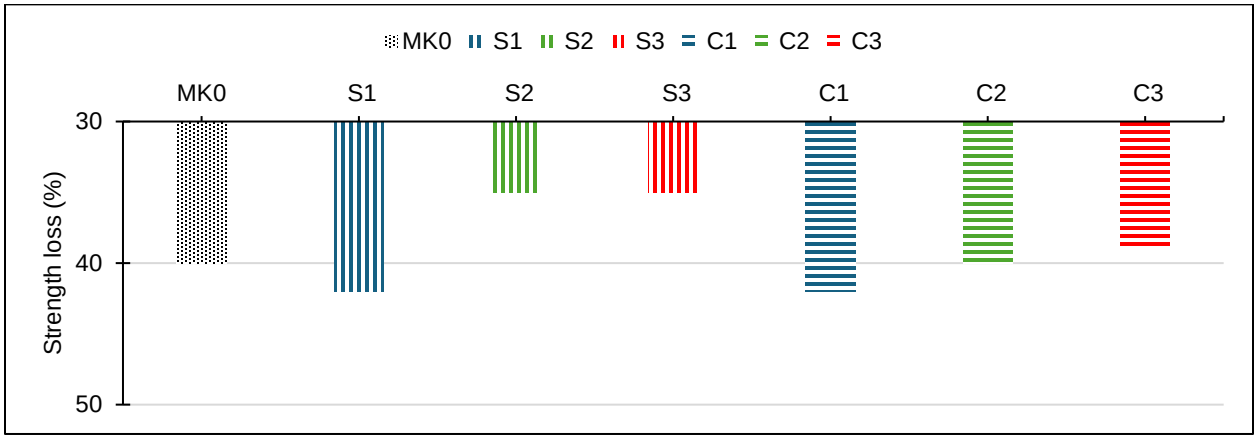

Fig. 110. Compressive strength loss (%) of GP mortars after exposure to acid attack test for 28 days.

- pH variation

Upon conducting the acid attack test, all the GP mortar formulations were tested for pH levels to examine the leaching of GP mortar samples when exposed to an acid with a pH of 1.11. The GP mortar samples initially had a pH of approximately 13 due to their basic nature. Then the pH changes upon contact with the acid as displayed in Fig. 111. On day 7, the pH values reached their highest points for all GP mortar formulations. Subsequently, as time progressed, the pH values gradually decreased, even though the acid solution was replenished every 7 days. This suggests that the leaching of ions in the GP mortar samples decreased as time went on. For instance, MK0 exhibited the highest pH change, reaching a maximum of 3.5 on day 7, but after 28 days, the pH decreased to 1.36. Similarly, the other GP formulations (S1, S2, S3, C1, C2, and C3) also recorded their highest pH values on day 7, with pH values of 2.85, 2.5, 2.3, 3.14, 2.55, and 2.29, respectively. This result corresponds to the earlier described mass loss, where MK0 showed the highest mass loss compared to other GP formulations, and as the percentage of GBFS in the

binder increased, the mass loss decreased. The change in pH followed a similar pattern, with MK0 experiencing the highest change in pH, followed by S1 and C1, S2 and C2, and finally, S3 and C3, which showed the lowest change in pH. However, after 21 to 28 days, the leaching for GP formulations, except MK0, stopped as the pH values returned to the initial pH value of 1.11. This finding aligns with the mass loss, which also stopped for these formulations after 21 days of exposure to the acid. The leaching of ions was attributed to the deterioration of the aluminosilicate networks within the samples [113][332].

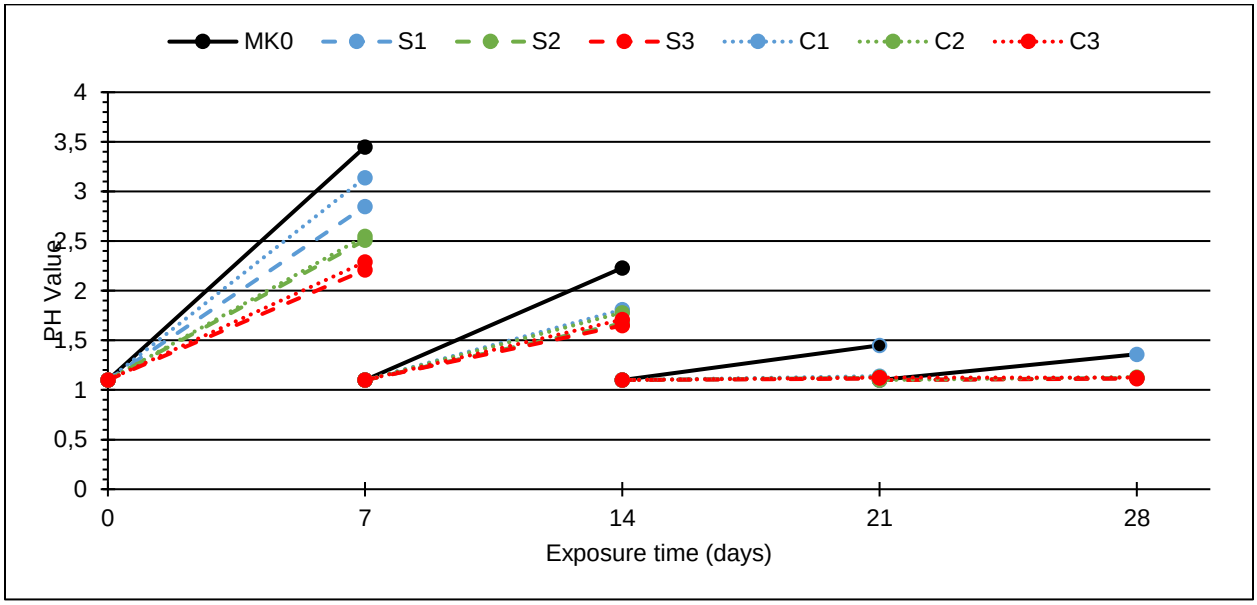

Fig. 111. pH variation with time during the acid attack test.

3.2.7. XRD analysis

The XRD analysis of GP formulations (MK0, S1, S2, S3, C1, C2, and C3) are presented in Fig. 112 while those exposed for acid attack test (AMK0, AS1, AS2, AS3, AC1, AC2, and AC3) are presented in Fig. 113. The results indicate that all samples have the same mineralogical composition with a little variation in the peak intensity. The main composition for the GP pastes samples is quartz with high-intensity peaks present at 21° 2Θ and 27° 2Θ. Also, other small intensity peaks of quartz are present at 37, 40, 50, 55, 60, and 69° 2Θ. Also, S1, S2, and S3 have small intensity of calcite at 29° 2Θ. However, calcite is not present in MK0, C1, C2, and C3, this is because neither MK nor FCC had calcite present in their mineralogical composition. Ayeni et al. [365] concluded when developing GP from MK, it doesn't alter the crystalline phases existing in the raw material. Since none of the GP formulations changed the original composition of the

GP binders' raw material, the findings of this investigation are consistent with this conclusion. After the acid attack, the GP formulations demonstrated the presence of Gypsum (G) at 11.8 and 29° 2Θ. Aiken et al. [310] have also identified the presence of G at 11.7 and 29.1 ° 2Θ and are attributed to the acid attack exposure.

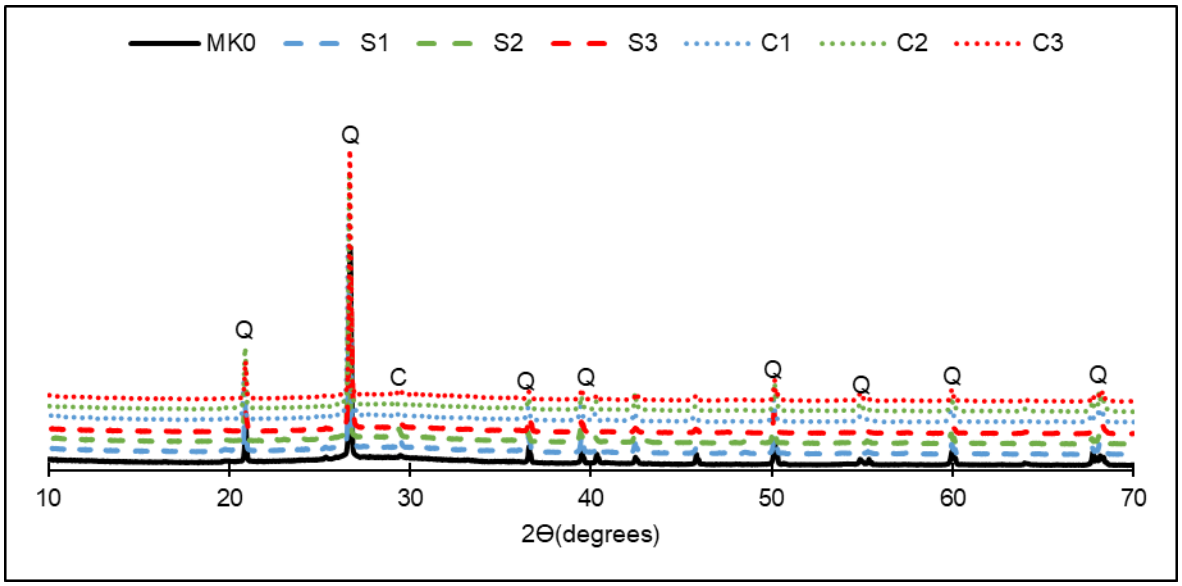

Fig. 112. XRD analysis for all GP formulations.

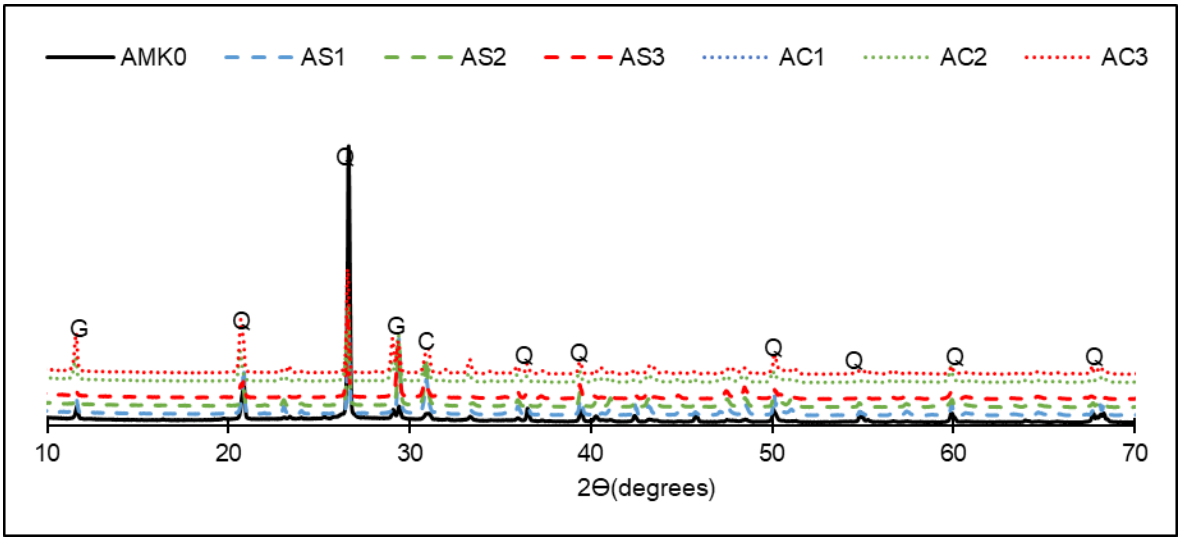

Fig. 113. XRD analysis for GP formulations exposed to acid attack test.

3.2.8. FTIR analysis

The FTIR analysis for GP formulations unexposed (MK0, S1, S2, S3, C1, C2, and C3) are illustrated in *Fig. 114* and exposed (AMK0, AS1, AS2, AS3, AC1, AC2, and AC3) to acid attack

test are illustrated in *Fig. 115*. According to the FTIR results, all GP formulations unexposed to acid have the same main and minor peaks almost at the same wavenumber (cm^{-1}). The first major peaks are found between 1000 cm^{-1} and 1020 cm^{-1}. These peaks are classified as stretching vibrations of the Si-O-Si and Al-O-Si bonds in the GP network , thus the GP formulations design indicate strong bonds of Si-O and Al-O bonds [341]. The bands found approximately between 1650 cm^{-1} and 3450 cm^{-1} are for the $^{-}$OH groups of related to water cavities [33][366]. The peaks present at 690 cm^{-1}, 1400 cm^{-1}, and 1600 cm^{-1} are for CO_3^{-2} [33]. After the acid attack, the main alteration present is shifting in the main peaks into higher wave numbers, similar to the results shown by Aiken et al. [310]. After the acid attack test, the main peaks have transformed from 1009-1024 cm^{-1} to 1090-1142 cm^{-1}. This shifting indicates a higher Si/Al ratio due to the dealumination of the binding gel resulting in a highly siliceous gel being kept behind [310][344]. For all GP formulations, the peaks present at 669 cm^{-1} correspond to gypsum [310][367][332][368]. Also, the peaks at 1622 cm^{-1} are related to gypsum as well [310][324]. The double peaks found between 3445-3480 cm^{-1} and approximately at 3550 cm^{-1} are indication for gypsum [310][342][332][369][370]. When performing the XRD analysis test, the presence of gypsum was also discovered in the GP formulations' mineralogical composition. Therefore, the formation of gypsum is due to exposure of GP formulations to acid, and indication to damage of GP matrix that might cause decrease in strength and durability.

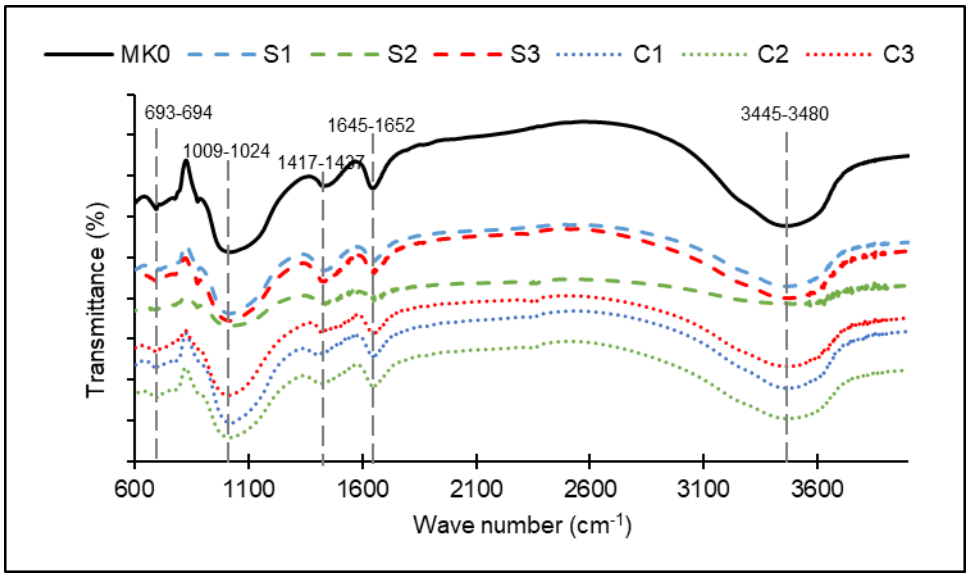

Fig. 114. FTIR analysis for all GP formulations.

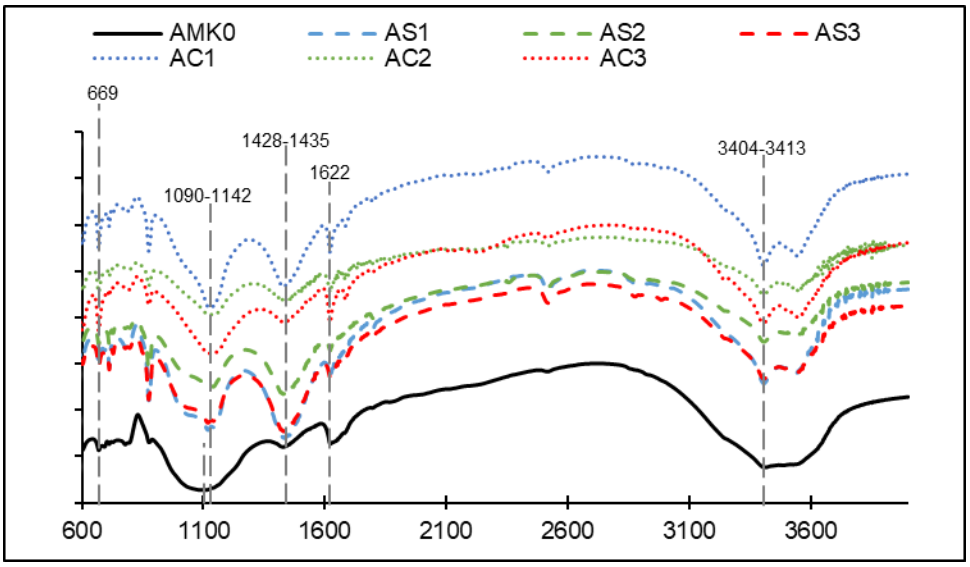

Fig. 115. FTIR analysis for GP samples exposed to acid attack test.

3.2.9. TGA/DTG test

Following a 28-day curing period, Fig. 116 shows the TGA/DTG plots of various GP paste formulations. According to the TGA and DTG graphs, weight loss is greatest between 25 and 250 °C and 400 and 750 °C, respectively. According to the ATG results, the overall mass losses for MK0, S1, S2, S3, C1, C2, and C3 were 78%, 74.6%, 74.8%, 78.17%, 76.9%, 77%, and 80.6%, respectively. It is clear from comparing the mass losses that MK0 lost more mass than S1, S2, C1, and C2, but less mass than S3 and C3. These results align with the previous section, which investigated the loss of mass and compressive strength when exposing the GP formulations to high temperatures. The dehydration process for calcium silicate hydrate (C-S-H), free water, and chemically coupled water from the GP is what causes the weight loss at 100°C [371][372]. The DTG (a) indicates that MK0 has a peak of about 532 °C, but S1, S2, S3, C1, C2, and C3 have different peaks. This peak is caused by the breakdown of free water vapor and calcium hydroxide ($Ca(OH)_2$) [373][93][374]. MK0, S1, S2, S3, C1, C2, and C3 all displayed peaks from DTG (a), DTG (b), and DTG (c) that are consistent with the amorphous decomposition of the calcium carbonate components [371][375][376]. However, S1, S2, and S3 displayed higher peaks, which is attributable to the fact that FCS contains more calcite content than MK and FCC, as demonstrated by the XRD study. Additionally, the calcium silicate hydrates (C-S-H), which result in increased strength, showed a peak in all GP formulations at roughly 200 °C [84]. It can be seen from DTG (b) that S3 exhibits a stronger peak than S2, and S2 exhibits a stronger peak than S1.

Similar to how C3 shows a stronger peak than C2, C2 exhibits a stronger peak than C1, it can be seen in DTG (c). This analysis is in line with the findings of compressive strength since it was determined that as the percentage of GBFS increased, so did compressive strength.

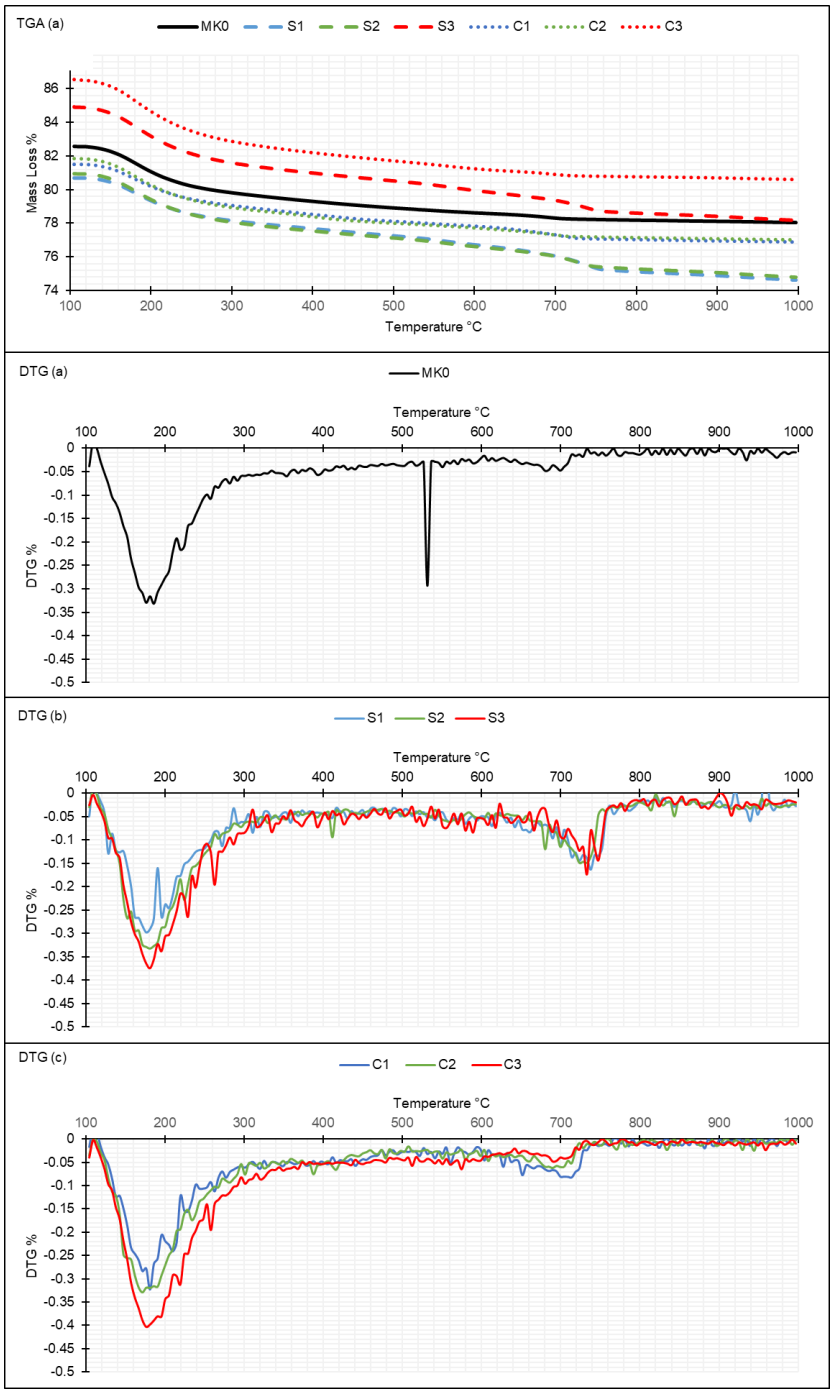

Fig. 116. TGA/DTG analysis for all GP formulations.

3.2.10. SEM/EDS test

The SEM/EDS results illustrated in Fig. 117, Fig. *149*, Fig. *118*, Fig. *150*, Fig. *151*, Fig. *119*, and Fig. 152 expose a comprehensive analysis of various GP mortar formulations, namely MK0, S1, S2, S3, C1, C2, and C3. Utilizing software, the microstructure properties of these formulations, including porosity and the presence of unreactive particles, are carefully evaluated. In the case of the reference mix, MK0, the obvious geopolymer matrix as shown in spot "1", consisting primarily of 49.96% SiO_2 and 20.22% Al_2O_3, indicates a strong geopolymerization reaction facilitated by the aluminosilicates in MK and AR. The software's examination reveals a minimal 0.37% of unreactive material and a porosity of 6.37%, with distinctive spots indicating the presence of sand as shown in spot "2".

Moving to formulation S1, which confirms MK0's characteristics, an additional observation is noticed. Spot 3 exhibits the presence of a C-S-H gel, characterized by 41% CaO, 35.93% SiO_2, and 14.64% Al_2O_3. This is due to the percentage of CaO equal to 21.89% found in FCS as identified by the chemical composition. The substitute of MK with FCS introduces an increase in the unreactive material to 0.84% and a rise in porosity to 7.22%, consequently leading to a reduction in compressive strength. Similar patterns are observed in formulations S2 and S3, where lower FCS percentages are accompanied by increased GBFS content. Both formulations display a noticeable GP matrix as shown in spot "1", with spot "2" highlighting 100% SiO_2 indicative of sand, and the presence of C-S-H gel in spot "3". Remarkably, unreactive material and porosity exhibit a decreasing trend to (0.34%, 0.11%) and (5.49%,2.44%), respectively with the elevation of GBFS content, thus having an important role in refining the microstructure of the GP formulations.

For GP mortars formulated with FCC, the SEM/EDS analysis for C1 reveals a GP matrix dominated by 52.84% SiO_2 and 23.69% Al_2O_3, indicating the main presence of Si, Al, and O elements thus forming a three-dimensional structure comparable to MK0. Spot 2, exhibiting 100% SiO_2, signifies the presence of sand. However, in contrast to FCS, the mineral composition of FCC lacks significant CaO, resulting in the absence of C-S-H bond and consequently lower compressive strength is achieved. Particularly, the C1 GP formulation displays 7.98% porosity and 0.65% unreactive material. However, formulations C2 and C3, also identifies the presence of GP matrix characterized by 48.62% SiO_2, 18.96% Al2O3, and 52.44% SiO_2, 18.56% Al_2O_3, respectively as shown in spot "1". Also, the presence of C-S-H bonds is identified by the presence of the CaO

embedded in some parts of the GP matrix such as spot "3". Therefore, the addition of GBFS yields a reduction in porosity (7.12%, 4.97%) and unreactive material (0.43%, 0.22%) in C2 and C3, confirming the beneficial impact of GBFS on refining the microstructure of the GP formulations.

Different studies have mentioned the importance of GBFS in refining the microstructure of the GP, resulting in a denser matrix and formation of C-S-H gel, which leads to increase of the compressive strength and decrease of porosity levels [116][377]. Also, the percentage of unreactive particles decreased due to the increase of GBFS content and decrease of FCS/FCC, since GBFS is known to be more reactive than FCS or FCC upon contact with the alkaline reagent. Similarly, studies have shown that GBFS is more reactive than fly ash [377][116][378].

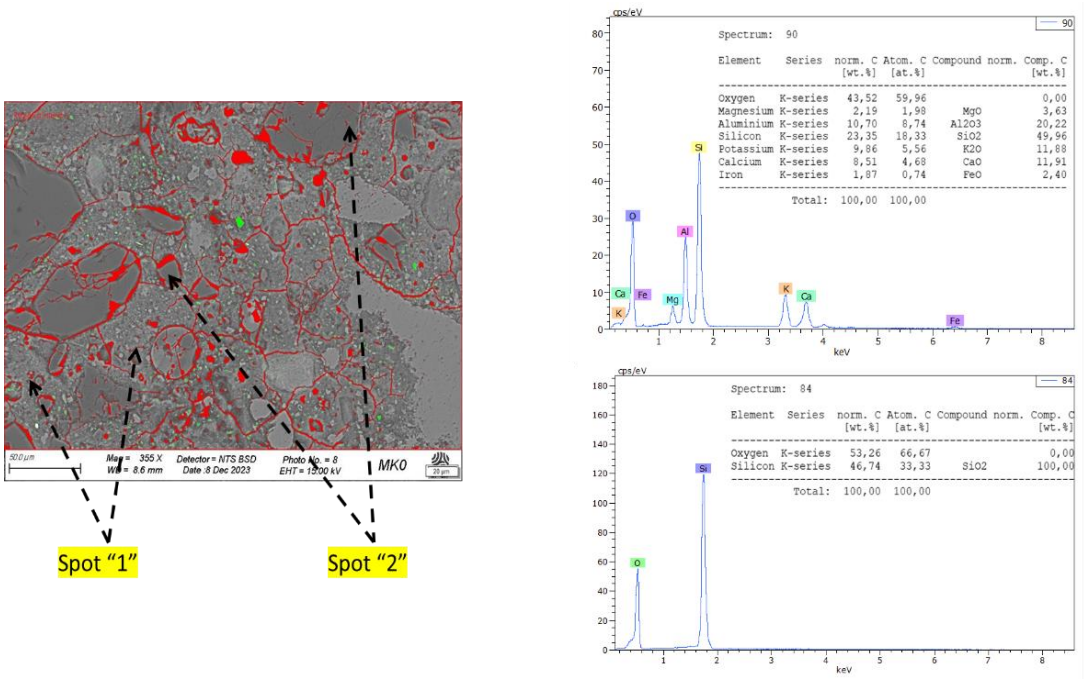

Fig. 117. SEM/EDS for MK0.

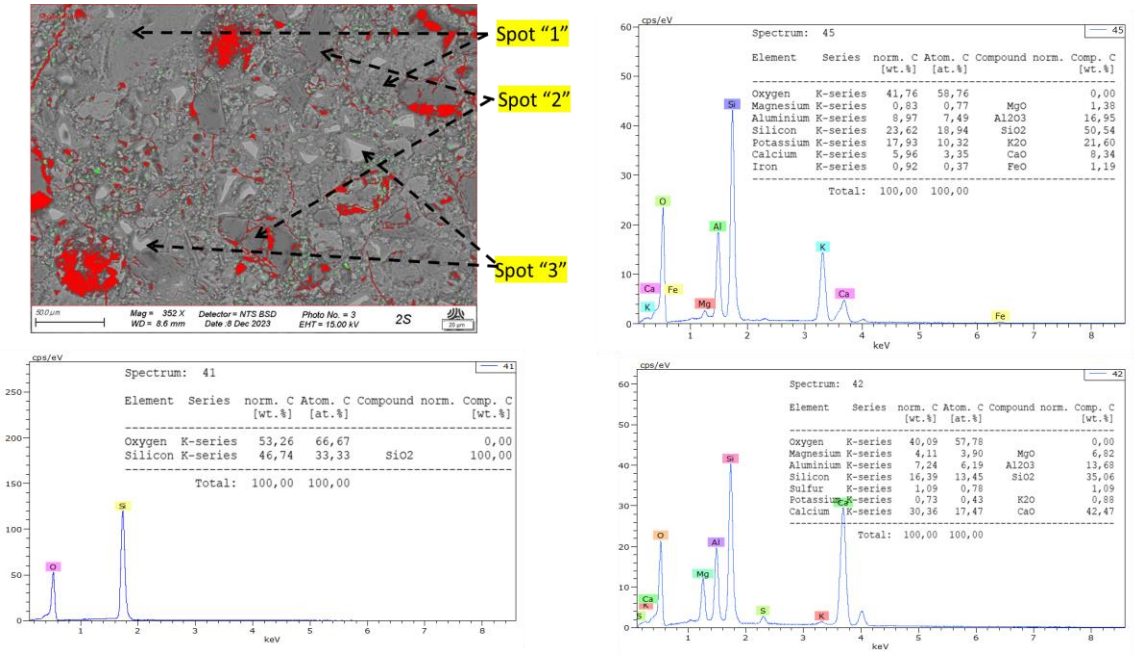

Fig. 118. SEM/EDS for S2.

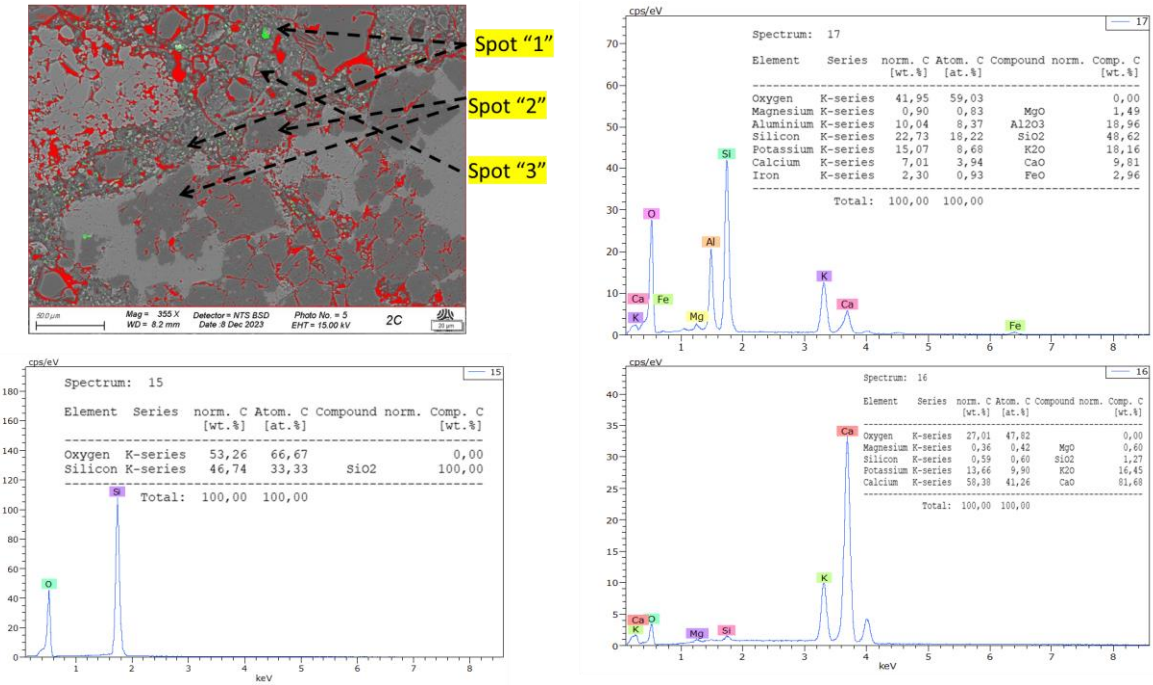

Fig. 119. SEM/EDS for C2.

3.2.11. High-temperature resistance test

The high-temperature resistance test visual inspection is illustrated in Fig. 120 involved examining various GP formulations: MK0, S1, S2, S3, C1, C2, and C3. All formulations exhibited the same behavior when exposed to a maximum temperature of 800°C. Initially, they displayed different colors, with MK0 being the first formulation, followed by S1, S2, and S3, which were black in color, and C1, C2, and C3, which were dark orange. However, during the test, a noticeable change occurred in all formulations' colors. The initial colors of MK0, C1, C2, and C3 changed to light brown, while the initial black color of S1, S2, and S3 transformed into a light orange shade. All GP formulations experienced a decrease in mass and compressive strength, as illustrated in Fig. 121. The author Fang et al. [379] provided an explanation for this phenomenon. They stated that as the temperature rose above 400 °C, the bound water evaporated, leading to the decomposition of C-S-H gel and a crystallization process within the gel. Consequently, the structure of the GP loosened, creating more pores, and resulting in a decrease in GP strength. Among the formulations, MK0 exhibited greater strength and mass loss compared to S1, S2, C1, and C2. However, S3 and C3 experienced even more strength and mass loss than MK0. Therefore, as the content of GBFS increased in the GP binder, greater losses in terms of compressive strength and mass were recorded. The increase in GBFS content also led to a decrease in porosity, as explained in section 3.2. A lower porosity caused higher mass and compressive strength at elevated temperatures (>600 °C). This is because low porosity restricts the release of water vapor from the GP network, leading to pressure buildup and potential spalling [379][380]. At a temperature of 800 °C, S3 experienced strength and mass loss equal to 47% and 12%, respectively, which was higher than S1 (25% strength loss and 10% mass loss) and S2 (26% strength loss and 11% mass loss). Similarly, C3 experienced strength and mass loss equal to 44%, and 11%, respectively, which was higher than C1 (20% strength loss and 11% mass loss) and C2 (28% strength loss and 11% mass loss). MK0 experienced strength and mass loss equal to 38% and 18%, respectively, which was higher than S1 and C1. Therefore, under the same curing conditions and AR/B ratio, GP formulations S1 and C1 demonstrated greater durability to high temperatures compared to MK0. This can be attributed to the fact that FCS and FCC have a higher BET surface area (27.45 m^2/g and 33.01 m^2/g, respectively) compared to MK (13.59 m^2/g), resulting in a denser mix for S1 and C1. Additionally, MK0 showed surface cracks indicating its lesser durability to high temperatures compared to S1 and C1.

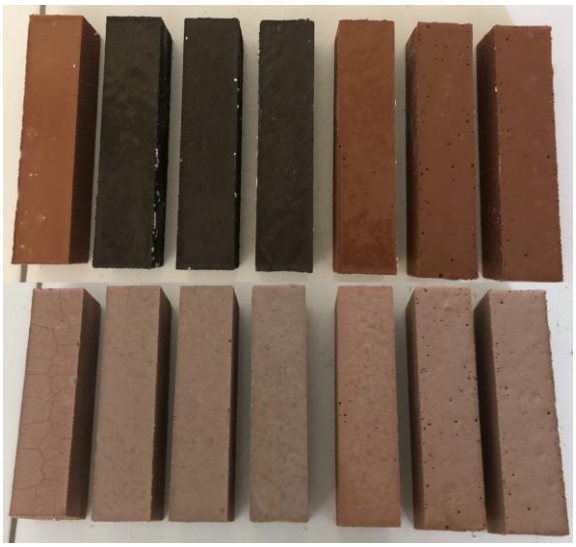

Fig. 120. Visual inspection of GP formulations before and after conducting the high-temperature resistance test.

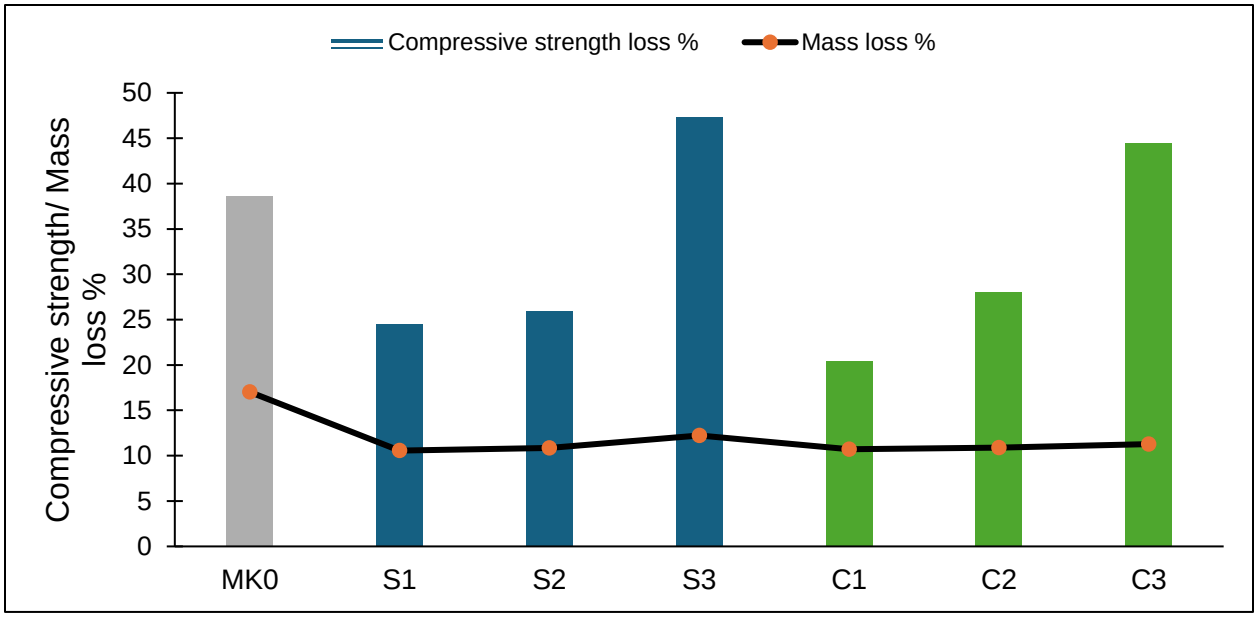

Fig. 121. Compressive strength and mass loss (%) after conducting a high-temperature resistance test.

3.2.12. Freeze-thaw test

The results of the freeze-thaw test for the geopolymer (GP) mortar samples are illustrated in *Fig. 122*, showcasing compressive strength outcomes. The compressive strength evaluations were carried out at intervals of 7, 14, 21, 28, and 35 days. Analysis of the results reveals that, up to 14 days into the test, all GP mortar formulations exhibited no decline in compressive strength.

However, after 21 days, a loss in compressive strength was observed for S1, S2, S3, C2, and C3, while MK0 and C1 showed no such loss. By day 28, all GP mortars experienced a decrease in compressive strength. MK0 exhibited a 6.77% loss, while S1, S2, and S3 showed losses of 5.66%, 11.11%, and 14.54%, respectively. Similarly, C1, C2, and C3 recorded losses of 12.25%, 16%, and 24%, respectively. This trend continued, with increased losses at day 35: MK0, S1, S2, S3, C1, C2, and C3 exhibited losses of 13.55%, 7.55%, 14.81%, 18.18%, 18.37%, 20%, and 24.07%, respectively.

At day 35, it was observed that S1 experienced a lower loss in compressive strength compared to S2 and S3 by 7.26% and 10.63%, respectively. This indicates that as the percentage of GBFS increases, resulting in higher compressive strength under normal conditions, the loss in compressive strength after the freeze-thaw test also increases. A similar trend was noted for GP formulations with FCC, C1 exhibited a lower loss than C2 and C3 by 1.63% and 5.7%, respectively. This further supports the observation that an increase in GBFS content leads to a higher loss in compressive strength.

Compared with the reference mix MK0, only S1 showed a lower loss in compressive strength by 6%. To expose the loss in compressive strength and copy comparisons, a connection between macropores and compressive strength loss was explored. In GP formulations with FCS, S1 had the highest percentage of macropores at 5.6%, followed by S2 and S3 with lower percentages at 4.9% and 3.3%, respectively. For GP formulations with FCC, C1 had the highest percentage of macropores at 5.2%, followed by lower percentages for C2 and C3 at 4.1% and 3.8%, respectively. Studies suggest that macropores have a positive impact on freeze-thaw resistance [381][304]. Additionally, Chen et al. [304] mentioned studies [382]–[384] that intentionally introduced air bubbles that enhances resistance to freeze-thaw tests, making geopolymer application viable in cold or hot conditions.

The mass loss results are compatible with the compressive strength results, in which all GP mortar formulations didn’t experience mass loss until day 35 of the test ranging only between 2.3 to 2.7% of mass loss. Therefore, the mass loss is negligible and using the compressive strength loss results are more adequate for the analysis.

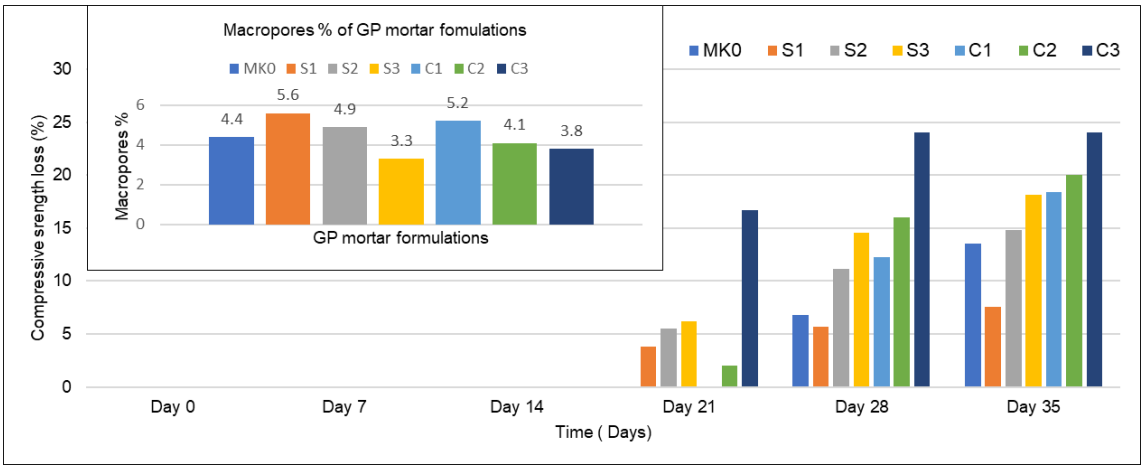

Fig. 122. Compressive strength loss (%) after conducting freeze thaw test.

3.2.13. Workability test on GP concrete

The workability of GP concrete is illustrated in Fig. 123. The results are consistent with those done on mortar scale. The reference mix MK0 showed the lowest slump flow diameter equal to 52.5 cm. S1, S2, and S3 showed slump flow diameters equal to 57.5 cm, 61 cm, and 62 cm, respectively. While C1, C2, and C3 showed slump flow diameters equal to 55.5 cm, 59 cm, and 60 cm, respectively. A similar conclusion to the workability results done on mortar scale can be drawn, as the percentages of FCS, FCC, MK, and GBFS are similar. Therefore, an increase in the FCS/FCC content has a negative impact on the workability due to their large surface area [164].

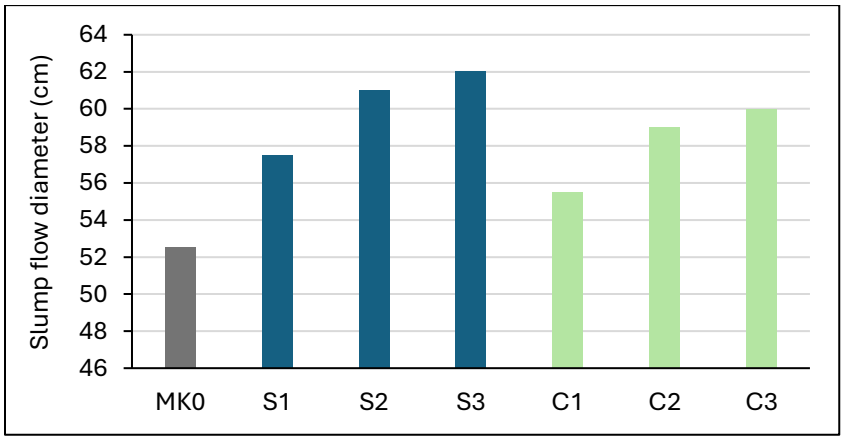

Fig. 123. Workability results on GP concrete.

3.2.14. Compressive strength test on GP concrete

Fig. 124 illustrates the compressive strength results for the GP formulations (MK0, S1, S2, S3, C1, C2, and C3). The binder for S1 GP formulations is only composed of FCS and MK, excluding GBFS. Consequently, the interference of GBFS expedites the geopolymerization reaction in the GP formulations. In contrast, S3 incorporates 20% GBFS in its formulation, while S2 contains only 10% GBFS. As a result, S3 achieves its compressive strength more rapidly than both S2 and S1. This accelerated strength gain can be attributed to the presence of CaO in GBFS within the GP formulations, promoting the formation of C-S-H gel and hastening early strength development [116]. Moreover, the positive influence of CaO on the concrete's microstructure enhances compressive strength results [18][320][321][322][323][118]. This study confirms this observation, with S3 exhibiting higher compressive strength results than S2 and S1 by 2% and 4%, respectively.

It is noteworthy that C1, C2, and C3 exhibit a similar trend to the S1, S2, and S3 formulations. Specifically, C1 achieves 48 MPa on day 28, while C2 and C3 reach 49 and 51 MPa, respectively. Consequently, C3 surpasses C2 and C1 in compressive strength by 4% and 6%, respectively. Additionally, C1 follows a trend like S1, differing from C2 and C3. The compressive strength of C1 increases by 11% from day 7 to day 28, while C2 and C3 only show a 4% increase. The noticeable impact of GBFS is evident for C1, C2, and C3, given that C1 lacks GBFS, while C2 and C3 incorporate 10% and 20% GBFS in their binder formulations, respectively.

Comparing GP concrete formulations with flash-calcined materials to the reference formulation MK0 reveals noteworthy insights. MK0 records higher strength at day 28 than S1, S2, S3, C1, C2, and C3 by 17%, 15%, 13%, 20%, 18%, and 15%, respectively. This indicates that replacing MK with FCS and FCC leads to a decrease in compressive strength. The reduction can be attributed to the presence of unreacted particles of FCS and FCC with the AR, emphasizing that the reaction with AR and MK fosters a more effective geopolymerization reaction. This is shown in SEM/EDS results.

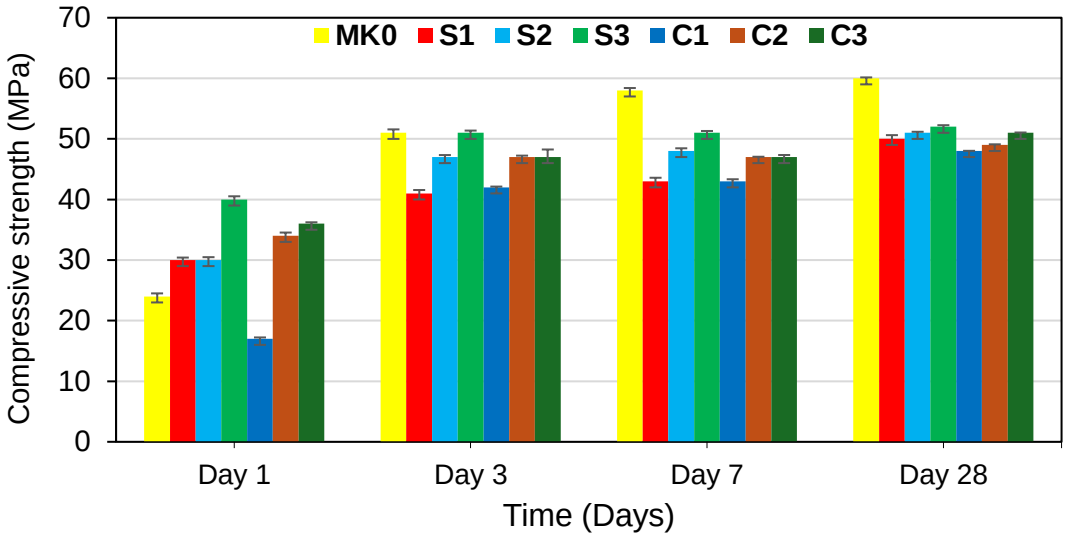

Fig. 124. Geopolymer concrete compressive strength results (MPa).

The literature review indicates limited information on utilizing sediments for the development of geopolymer concrete. However, numerous studies have explored the use of Metakaolin (MK) in geopolymer concrete. Jindal et al. [385] conducted a study that referenced various investigations on the development of geopolymer concrete using MK, presenting a summary of these findings in Table 25. Literature review on GP concrete compressive strength results [385]. In general, the cited studies predominantly employed thermal curing within the temperature range of 40-90°C. The compressive strength of MK concrete, formulated according to these studies and subjected to thermal curing, ranged from 10 MPa to 80 MPa.

In contrast, Jindal et al. [385] highlighted Yunsheng et al. [386] achievement of a compressive strength of 34.9 MPa after 28 days of curing at 20°C. Comparing these studies, the geopolymer concrete mix (MK0) developed in our study, utilizing 100% MK, reached a compressive strength of 60 MPa after 28 days of curing at room temperature. Consequently, in comparison to the previously mentioned study, MK0 exhibited a higher compressive strength by 42%.

Further comparisons with geopolymer concretes formulated with MK and cured using thermal temperatures reveal that MK0 demonstrates a compressive strength remarkably similar to those reported in the referenced studies. Thus, it is reasonable to conclude that the MK0 formulation in our study, cured under ambient conditions, exhibits commendable performance in terms of compressive strength.

Table 25. Literature review on GP concrete compressive strength results [385].

		Molar Ratios					
Type of study	Precursor Material	SiO_2/Al_2O_3	Na_2O/Al_2O_3	H_2O/Al_2O_3	H_2O/Na_2O	Compressive strength/days/curing temp	Primary findings
Silva et al. [387]	Metakaolin	3.4-3.8	0.8-1.00	-	13.6	22 MPa/3 days/40 °C	The properties of a geopolymer can be controlled by minor changes in Si and Al content during synthesis
Fletcher et al. [388]	Metakaolin	1.6	5	54	11	10.9 MPa/1 day/40-90	Geopolymer specimen get hardened at ambient temperature; high-alumina content lowers the strength, shows elastic behavior, and deformed rather than brittle failure
Rowles and O'Connor [389]	Metakaolin	2.5	1.29	18.01	-	64 MPa/7 days/75 °C for 24 h	The bonding network in the amorphous alu- minosilicate system significantly alters with Si:Al and Na:Al composition. The compressive strength depends on the Si:Al and Na:Al molar ratios
Duxson et al. [130]	Metakaolin	1.9	1	1	11	80 MPa//40 °C for 24 h	Geopolymers with a higher Si/A1 ratio exhibit reduced strength because higher silica content results in the presence of unreacted material in the specimens
Lizcano et al. [390]	Metakaolin	3	1	11	-	32 MPa/1 day/80 °C for 24 h	Geopolymer with a higher Si/Al ratio result in inhomogeneous microstructure with the presence of unreacted metakaolin particles, large pores, and some microcracks that all result in lower mechanical properties

Yunsheng et al. [386]	Metakaolin	5.5	1	-	7	34.9 MPa/28 days/20 °C	The molar ratios of Na2O/A12O3 and H2O/ Na20 had a significant effect on compressive strength. The geopolymer possesses the highest strength due to fully reacted material resulting in the largest amount of geopolymer gel
Barbosa et al. [135]	Metakaolin	3.3	0.83	10	10	49 MPa/3 days/65 °C	
Ghanbari et al. (2015)	Metakaolin	2.9	0.84	8	13.75	66 MPa/28 days/85 °C	The curing temperature and molar ratio of H2O/Na2O have the lowest and highest effect on the compressive strength of geopolymer
Kamalloo et al. [391]	Metakaolin	3.6-3.8	1-1.2	11	11	80 MPa/7 days/70 °C for 4 h	Artificial neural network optimization is in good agreement with probabilistic values
Kong et al. [392]	Metakaolin	1.54	0.42	-	-	45 MPa/3 days/80 °C for 24 h	The Si/Al ratio has a significant influence on elevated temperature exposure deterioration of metakaolin containing the potassium- based alkaline solution. Lesser strength loss

3.2.15. Water absorption test

Fig. 125 illustrates the water absorption trends in relation to the square root of time for the GP concrete formulations investigated in this research. The elevated water absorption rate in these GP concrete formulations is attributed to the aggregates constituting 60-80% of the concrete volume [393][75][76]. Initial water absorption findings encompass the period from the test commencement until 6 hours, followed by a subsequent absorption test from day 1 to day 8. Adhering to ASTM C1585 standards [313], the capillary water absorption curve of concrete was analyzed to determine the initial and secondary sorptivity, defined as the slope of the water absorption curve between water absorption per unit area and the square root of time.

Consistent with prior research [393], the initial water absorption for all specimens surpassed the secondary sorptivity in all GP concrete formulations. Krishnan et al.'s study [395] indicated

sorptivity coefficients for concrete to be 0.77, 1.16, 1.55, and 1.94 mm/min$^{0.5}$ for durability classes of excellent, good, poor, and very poor [396]. In comparison, the reference mix MK0 exhibited a sorptivity coefficient of 0.72 mm/min$^{0.5}$, signifying excellent durability based on earlier investigations.

For GP formulations incorporating FCS, S1, S2, and S3 exhibited sorptivity coefficients of 0.88 mm/min$^{0.5}$, 0.88 mm/min$^{0.5}$, and 0.80 mm/min$^{0.5}$, respectively, showing a durability comparable to MK0. Notably, S3 demonstrated a slightly superior result compared to S1 and S2. In the case of C1, C2, and C3, their sorptivity coefficients were 0.75 mm/min$^{0.5}$, 0.94 mm/min$^{0.5}$, and 0.87 mm/min$^{0.5}$, respectively, indicating good durability for all formulations. Consequently, FCS and FCC can effectively substitute MK with the incorporation of GBFS.

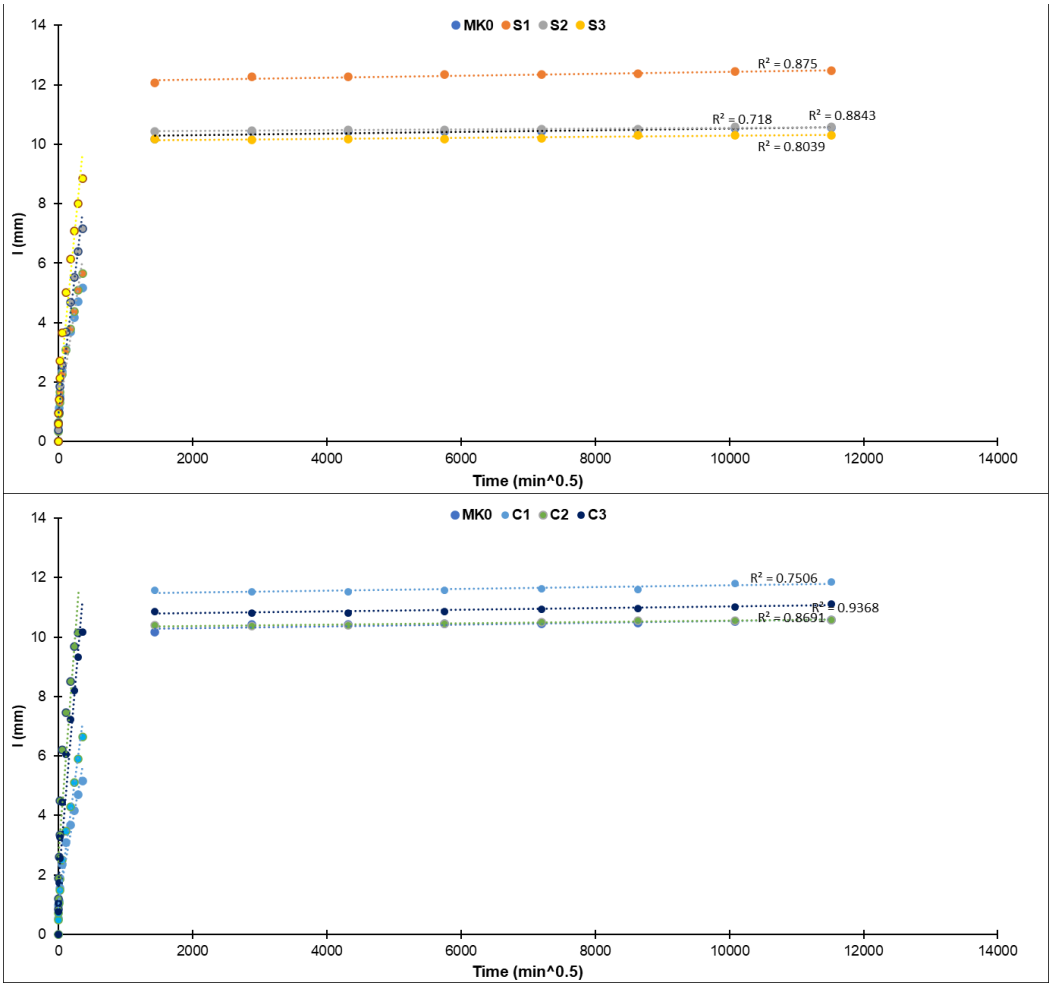

Fig. 125. Water absorption results.

3.2.16. NMR test

Using ^{29}Si and ^{27}Al NMR spectroscopy, geopolymers' structural change is investigated [397]. The resonances for various samples are displayed in the NMR spectra in Fig. 126 and Fig. 127. For ^{29}Si NMR, S1, S2, and S3 each have broad resonances at -92, -90, and -106 ppm, respectively, while MK0 has a broad resonance at -112 ppm. Broad resonances may be seen at -93 ppm, -91 ppm, and -87 ppm for C1, C2, and C3, respectively. The ^{27}Al NMR spectra demonstrate that MK0 exhibits a broad and strong resonance at 59 ppm whereas S1, S2, and S3 exhibit strong resonances at 58, 59, and 59 ppm, respectively. Broad resonances are visible for C1, C2, and C3 at 59 ppm, 59 ppm, and 60 ppm, respectively. The Si units are classified as $Q^n(mAl)$, where n denotes the Si units' coordination number and m denotes the number of Al units nearby that are coupled by oxygen (O). The resonances for the various Si units have been found by Davidovits et al. [292]; these are $Q^4(4Al)$, $Q^4(3Al)$, $Q^4(2Al)$, $Q^4(1Al)$, and $Q^4(0Al)$, which resonate at -83 to -87, -87 to -94, -92 to -99, -97 to -105, and -103 to -120 ppm, respectively. The ^{27}Al resonance at 58 ppm shows that $AlQ^4(4Si)$ is networked in three dimensions. Based on the NMR data, MK0 corresponds to $Q^4(0Al)$, S1, S2, C1, and C2 correspond to $Q^4(3Al)$, S3 corresponds to $Q^4(1Al)$, and C3 corresponds to $Q^4(4Al)$. A ^{27}Al resonance in the range of 58 ± 2 ppm is present in all GP formulations, demonstrating the three-dimensional networking of Al $Q^4(4Si)$. Therefore, a tetrahedral structure is present in all GP formulations. Despite having a constant AR/B ratio and curing circumstances, they vary in their Al adjacent units as a result of changes in their binder composition. The NMR spectra showed no resonance peaks at lower chemical shifts, ruling out the presence of Q^1 and Q^2 structures as well as monomeric or dimeric species [398]. This implies that there aren't any unreacted silicate oligomers present that aren't attached to the gel [353].

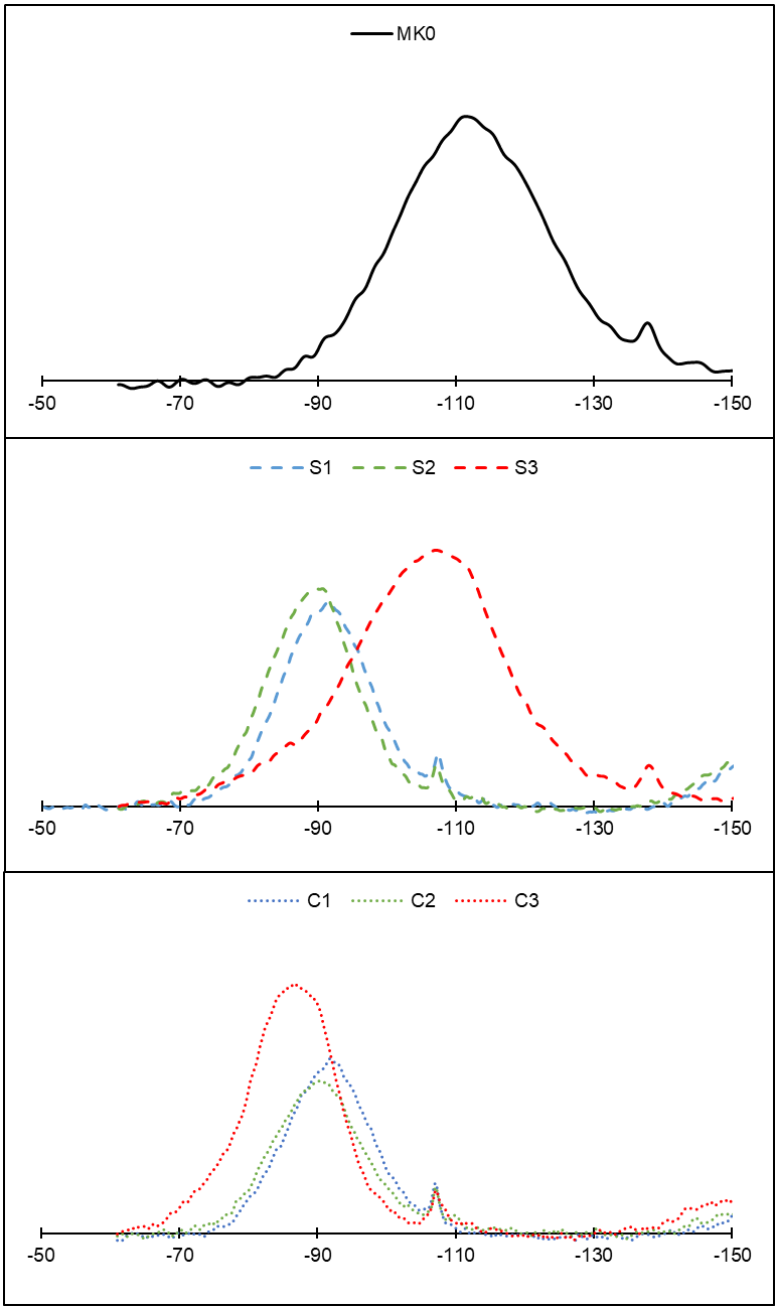

Fig. 126. ^{29}Si for all GP formulations.

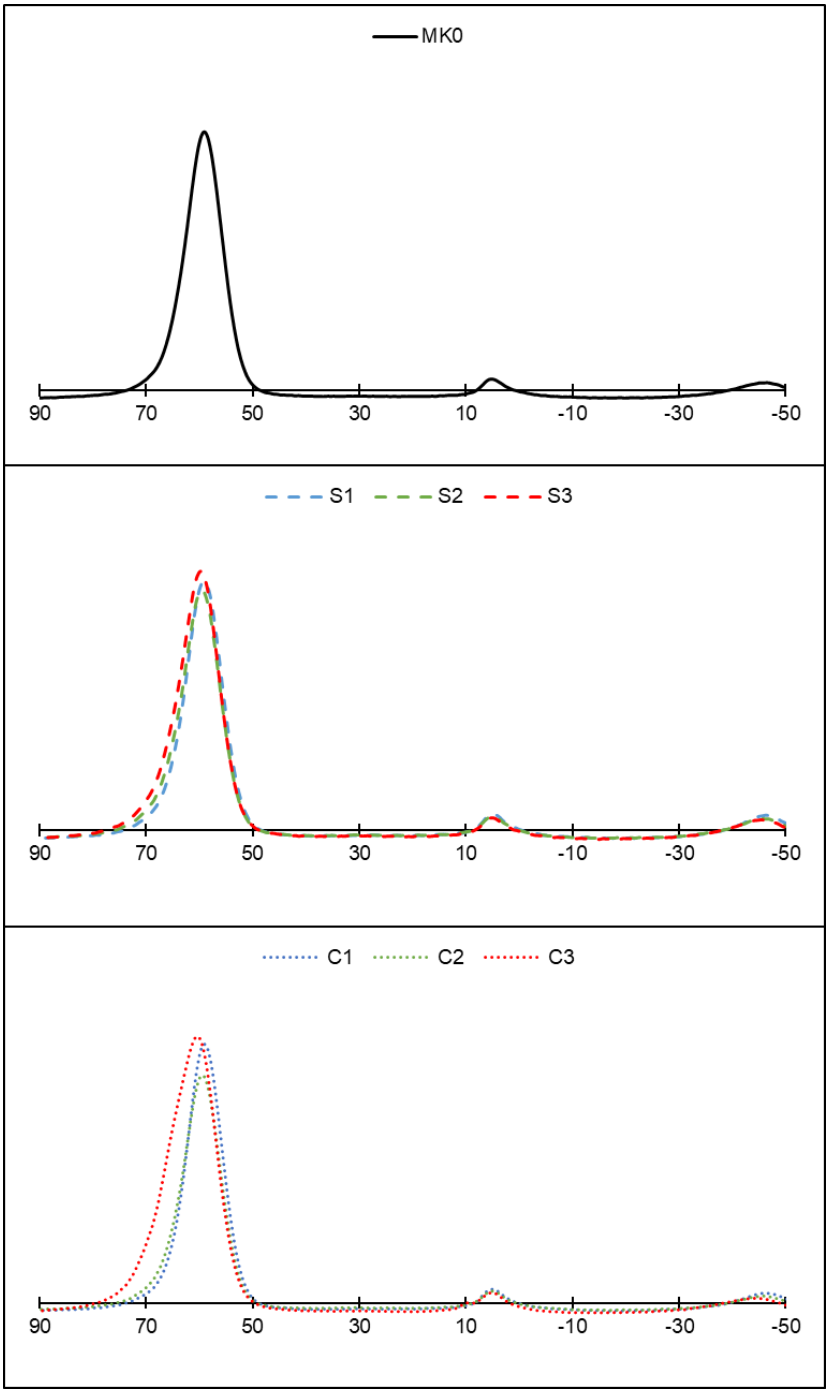

Fig. 127. 27Al for all GP formulations.

3.2.17. Leaching test

The leaching test results indicated the metallic trace element quantities present in the GP formulations listed in *Table 26*. Only elements As and Se were found to be present in higher levels in the GP formulations compared to IW, while others, including Ba, Cu, Ni, and Zn, had lower

levels than inert waste (IW). However, all the elements present in GP mortars were below the limits set by non-hazardous wastes (NHW), signifying they are not hazardous materials. In geopolymer formulations, only two elements, As and Se, exceeded the IW standards' limits.

Arsenic (As) is an inorganic species that may originate from water contamination [399] and Selenium (Se) [400] is often released by waste water into the environment by industries.

As the sediment content decreased in the samples, the concentrations of Arsenic (As) and Selenium (Se) also showed a decrease. For example, in samples S1, S2, and S3, the concentrations of As and Se decreased from 1.926 and 0.309 mg/kg to 1.542 and 0.259 mg/kg, respectively, as the sediment content dropped from 24% to 16%. The heightened levels of As and Se in the samples were likely a result of river water contamination, as the sediments from the NSL river did not undergo any treatment for inorganic elements. Similar trends were observed in the GP formulations with FCC, where decreasing substitution rates led to a reduction in the percentages of As and Se from 2.012 and 0.136 to 1.508 and 0.123, respectively. However, incorporating FCS and FCC into the GP formulations demonstrated improved leaching results compared to the reference mix MK0. Consequently, all GP formulations involving either FCS or FCC fall within acceptable limits for elemental concentrations, with only the element As showing slightly higher percentages.

Table 26. Leaching test results for GP formulations (mg/Kg).

Element	MK0	S1	S2	S3	C1	C2	C3	IW	NHW
As	2.615	1.926	1.689	1.542	2.012	1.77	1.508	0.5	2
Ba	< 0.008	< 0.008	< 0.008	< 0.008	< 0.008	< 0.008	< 0.008	20	100
Cd	< 0.009	< 0.009	< 0.009	< 0.009	< 0.009	< 0.009	< 0.009	0.04	1
Cr	0.131	0.027	0.03	0.035	0.026	0.025	0.024	0.5	10
Cu	0.083	0.131	0.22	0.145	0.096	0.084	0.052	2	50
Mo	0.11	0.219	0.205	0.179	< 0.09	< 0.09	< 0.09	0.5	10
Ni	< 0.05	< 0.05	0.1	0.101	0.073	0.152	0.15	0.4	10
Pb	< 0.03	< 0.03	0.041	< 0.03	0.042	0.044	< 0.03	0.5	10
Sb	< 0.06	< 0.06	< 0.06	< 0.06	< 0.06	< 0.06	< 0.06	0.06	0.7
Se	0.212	0.309	0.313	0.259	0.136	0.145	0.123	0.1	0.5
Zn	0.016	0.022	7.292	< 0.01	0.017	0.017	0.011	4	50

3.2.18. Conclusion

This study studies the creation of geopolymer mortar and concrete utilizing dredged sediments and thermally treated, flash-calcined, excavated clays. There have been developed a number of geopolymer formulations. First, a geopolymer mixture called MK0 that contains 100% MK. Then MK was replaced with three different GP formulations that included GBFS and flash-calcined sediment. Finally, three GP formulations that also included GBFS and flash-calcined clay were employed to replace MK. The alkaline reagent -to- binder ratio is the same throughout all GP formulations, and they are all cured in the same environment. Although the binder precursor was composed of varying amounts of MK, FCS, FCC, and GBFS, they all had the same Si/Al mole ratio of 2. Compressive strength test, calorimetry test, mercury porosity test, acid attack test, high-temperature resistance test, freeze-thaw test, water absorption test, SEM/EDS, NMR test, and leaching test were conducted. Below is a summary of the findings.

- Comparing the reference mix MK0 to the other GP formulations (S1, S2, S3, C1, C2, and C3), the reference mix MK0 displayed the maximum compressive strength. Additionally, it was shown that the compressive strength increased as the GBFS content did. Measurements on concrete show similar results.
- The mercury porosity test results validate the compressive strength results by measuring the macropores and nanopores that have a vital impact on the compressive strength.
- The calorimetry test results show the impact of GBFS on the speed reaction of the geopolymerization reaction happening when the alkaline reagent gets in contact with the aluminosilicates present in the precursor binders.
- The scanning electron microscopy (SEM) and Energy-Dispersive X-ray Spectroscopy (EDS) test results verify the presence of a geopolymer matrix in the GP formulations formulated with FCS or FCC.
- The reference mix MK0 suffered the greatest mass loss from the other GP formulations, according to the results of the acid attack test. Additionally, the MK0 demonstrated a higher compressive strength loss compared to other GP formulations, with the exception of those lacking any GBFS in the binder precursor. As a result, the resistance to the acid attack test increased as the GBFS content increased.

- Following the high-temperature resistance test, it can be said that MK0 displayed higher resistance than FCS3 and FCC3, but lower resistance than S1, S2, C1, and C2. Therefore, decreased resistance to the high-temperature test was observed as the GBFS concentration increased to 20%. When analyzing the TGA/DTG test, these findings are validated.
- The freeze-thaw test results indicate that all GP formulations didn't show loss in compressive strength until day 21 of conducting the test. The results indicate that GP formulations with lower GBFS percentages show better resistance due to the correlation between the microstructure of the GP mortar and its impact on resisting cold temperatures.
- The water absorption test results indicate that the GP formulations show similar performance to the reference mix MK0 and thus can be used in developing GP concrete.
- Finally, after performing the NMR test, it can be said that all GP formulations have a stable three-dimensional tetrahedral network, however with different numbers of nearby Al units.
- The leaching test confirms that the GP formulations with FCS and FCC are considered nonhazardous materials

Chapter 4. Results and Discussion – LFC Binders

Chapter 4. Results and Discussion – LFC Binders

4. Results: Limestone flash-calcined clay cement (LFC) binders

Only workability and compressive strength tests were done on the initial formulations while physical, mechanical, physicochemical, and durability tests were done on the developed LFC binders to determine whether the flash-calcined dredged sediments and excavated millstone clays can meet the requirements when incorporating them in LFC binders. The results are evaluated by comparing them to a reference mix made of 100% OPC and LFC binder made with MK.

4.1. Workability test of initial mortar formulations

Fig. 128 shows the workability results of the reference formulation C0 and 9 formulations done with substitution of OPC by 10, 20, and 30% of MK, FCS, and FCC. The reference mix C0 showed a slump flow diameter of 190 mm. When substituting 10, 20, and 30 % of OPC by MK, MK10, MK20, and MK30 showed a slump flow diameter of 185, 181, and 179.5 mm, respectively lower than C0. Therefore, as the percentage of MK increased the slump flow diameter decreased. The negative impact of MK on the workability is due to its irregular shape and high specific surface area whereas the friction forces between the cementitious particles cause the reduction in workability [401][161]. A study done by Brooks et al. [402] revealed as the percentage of MK increased from 5, 10, to 15%, the slump flow diameter decreased gradually. Upon the substitution of 5, 10, and 15% of OPC by FCS, FCS10, FCS20, and FCS30 showed even lower slump flow diameters equal to 175 mm, 167 mm, and 147.5 mm, respectively relative to both C0 and formulations done with MK (MK10, MK20, and MK30). A study done by Safhi et al. [403] investigates the effects of using treated marine sediments on the workability of self-consolidating concrete. The author has concluded that as the content of sediment increased when substituting OPC, the slump flow diameter decreased and could be explained by the increase in their specific surface area and fresh density of the mix. The incorporation of FCC in cement blends shows better results than those done with FCS but is not superior to MK formulations. FCC1, FCC2, and FCC3 showed a slump flow diameter of 180 mm, 170 mm, and 160 mm, respectively. Similar to FCS, FCC has a higher specific area than MK and therefore recorded lower workability results.

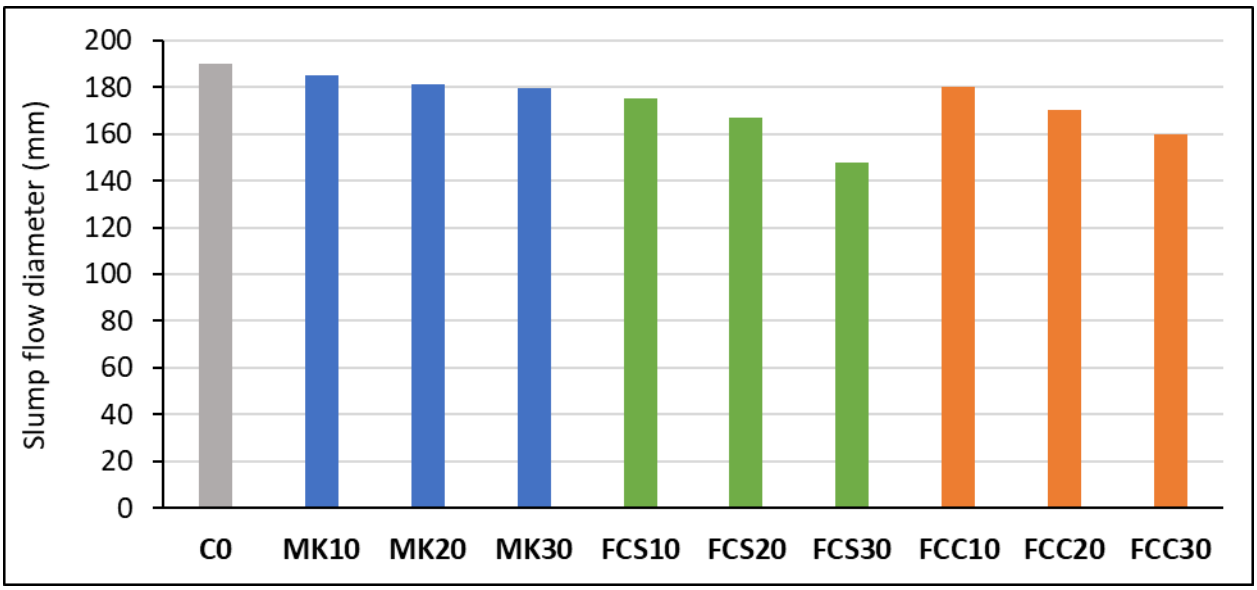

Fig. 128. Workability of initial mortar formulations.

4.2. Compressive strength test of initial mortar formulations

Fig. 129 shows the compressive strength results of the initial mortar formulations at 3, 7, and 28 days. The compressive strength at C0 is equal to 59, 62, and 78 MPa, respectively. MK10, MK20, and MK30 showed compressive strength equal to 54, 55, and 52 MPa, respectively on day 3. On day 7, the strength increased to 61, 67, and 62 MPa, respectively. On day 28, the strength increased to 80, 83, and 82 MPa, respectively. The addition of 10, 20, and 30 % of MK increased the compressive strength greater than C0 at all ages, whereas MK20 showed better results than MK10 and MK30. Mansour et al. [401] has attributed the increase of compressive strength when adding MK into cement blends due to its high surface area that fill the pores immediately and cause an increase in the early age strength. Moreover, the pozzolanic nature of MK reacts with CH and has a maximum effect at curing ages 7-14 days affecting late strength [404]. The substitution of OPC by 10, 20, and 30% of FCS showed an advantage in the compressive strength results, however only FCS10 showed better performance when compared to MK formulations. FCS10 showed a compressive strength equal to 63, 74, and 88 MPa at days 3, 7, and 28, respectively. However, FCS20 and FCS30 showed lower compressive strength results. Therefore, substituting 10% of OPC by FCS results in the optimum formulation. Safhi et al. [403] revealed that the replacement of 10% of treated sediments increased the compressive strength at early and late ages, however the substituting 20% of treated sediments decreased the compressive strength. The author concluded

that replacing more than 20% would not result in pozzolanic reaction and have a negative impact on the mechanical properties. Finally, it was noticed that the substitution of OPC by FCC showed better results than the reference mix C0 and formulations done with either MK or FCS. FCC10 showed the highest compressive strength results equal to 63, 74, and 88 MPa at ages 3, 7, and 28 days, respectively. FCC20 has also shown higher compressive strength results when compared to C0 and other formulations but FCC30 showed lower compressive strength results inferior to MK10, MK20, MK30, FCS10, and FCS20. Therefore, the substitution of OPC by FCC is limited to 10 and 20%. The high BET surface area of FCC equal to 33 m^2/g is attributed to the increase of compressive strength while its pozzolanic reactivity proven by Chapelle test and its kaolin content is in relation to the high compressive strength achieved after 28 days.

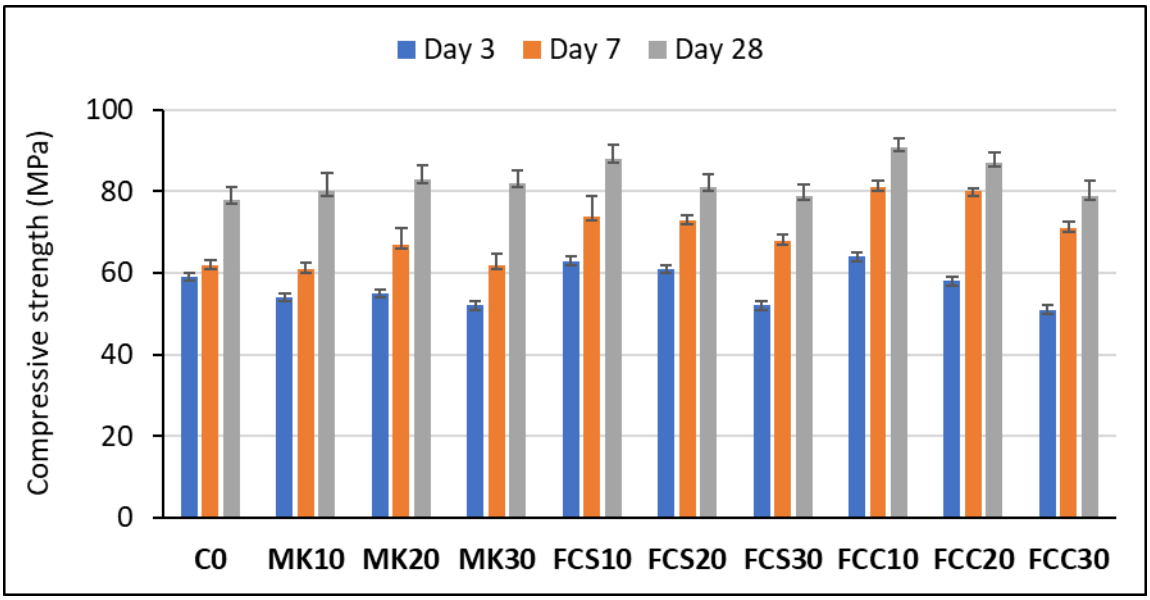

Fig. 129. Compressive strength of initial mortar formulations.

4.3. Workability test of LFC mortar formulations

The slump flow diameter of C0 was measured to be 190 mm, while C1 had the same slump flow diameter as shown in Fig. 130. However, C4 and C7 had lower values of 175 mm and 180 mm, respectively. The decrease in workability upon substituting with flash-calcined materials such as FCS and FCC is attributed to their high BET surface area, which is greater than that of MK. This increase in the specific surface area leads to an increase in water requirements to initiate the flow [405], negatively impacting workability. The fine sediments also have a high-water absorption capacity [406], which deteriorates the fresh state of the mix. Studies have shown that

at a fixed content of SP [407], the workability decreases when substituted with calcined clay. Therefore, flash-calcined materials have a similar trend to MK and have not improved workability due to their large surface area and high-water absorption capacity. When increasing the substitution of LS and decreasing the percentage of MK, FCS, and FCC, the workability increased for all formulations. For example, C2 and C3 showed higher workability than C0 and C1, equal to 195 and 197 mm, respectively. Also, C5 and C6 showed an increase in workability higher than C4, equal to 185 and 190 mm. Finally, C8 and C9 showed an increase in workability as well equal to 185 and 187 mm. The increase in workability for all formulations is attributed to an increase in LS percentages and a decrease in MK and flash-calcined materials. Different researchers have mentioned the positive effect of LS on the workability of concrete [408][409][410]. This is attributed to the fineness and spherical nature of the LS particles [409].

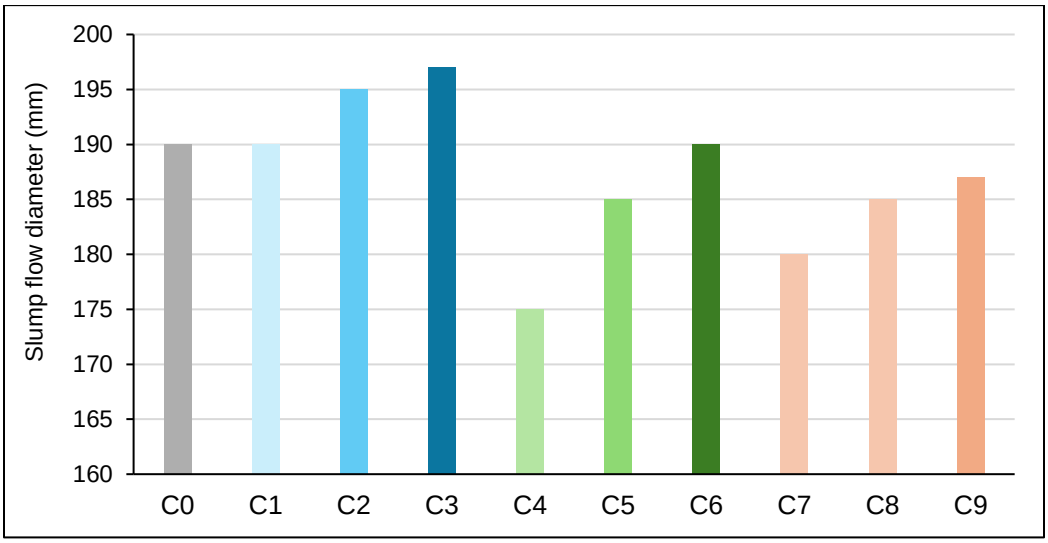

Fig. 130. Workability test results of LFC mortars.

4.4. Compressive strength test of LFC mortar formulations

The results of the compressive strength tests on various LFC formulations were compared to a reference mix called C0. The results are recorded in Fig. 131. At early age (day 3) C0 has recorded a compressive strength equal to 59 MPa higher than all LFC formulations. The LFC formulations done with MK (C1, C2, C3) have reached a compressive strength equal to 42, 45, and 43 MPa, respectively. While that done with FCS (C4, C5, C6) have recorded a compressive strength of 45, 46, and 48 MPa. Finally, those done with FCC have reached a compressive strength equal to 48, 51, and MPa, respectively. The rapid increase in compressive strength is attributed to

the CaO content in the OPC which is composed of 63.5 % CaO according to its mineral composition. The LFC formulations done with MK showed the least compressive strength at an early age while those done with FCC showed the highest. The CaO content of MK, FCS, and FCC is equal to 1.26, 21.8, and 2.86, respectively. The contribution of CaO content is explained in different research studies, specifically when GBFS is added to the cement mix. The relationship between the early age strength and the amount of added CaO content is explained by the heat liberation during the hydration reaction happening at early ages [411][412]. The hydration of the formulated formulations is explained in the results of the calorimetry section.

C0 recorded strengths of 61 MPa at 7 days and 76 MPa at 28 days. C1 had compressive strengths of 64 MPa at 7 days and 83 MPa at 28 days, and the addition of pozzolanic material MK and filler material LS in this formulation resulted in improvements in both early and late-age compressive strength. Other formulations, such as C4 and C7, also had higher compressive strengths than C0. On day 7, C4 showed improved compressive strength compared to C0 and recorded a strength of 75 MPa on day 28. Meanwhile, C7 had higher strengths than C0, recording 71 MPa on day 7 and 85 MPa on day 28. C4 had less strength than C1 by 3% and 10% on day 7 and 28, respectively. However, C7 had higher strength than C1 by 11% and 2% on day 7 and 28, respectively.

This is attributed to the pozzolanic reaction of the flash-calcined materials, which contributed to the development of strength. These results are similar to research studies. After day 7, Du et al. [284] has concluded that replacement of OPC with limestone calcined clay cement can increase the compressive strength in comparison with the reference mix. The author has explained that this increase is due to the reaction of portlandite, calcined clay, and LS which cause densification to the microstructure and the pore connectivity could decrease [9][284]. When the formulations were modified by increasing the percentage of LS and decreasing the percentage of MK, FCS, and FCC, a gradual decrease in compressive strength was observed. For instance, on day 28, C2 and C3 exhibited a reduction of 4% and 5% in compressive strength, respectively. Similarly, C5 and C6 showed a decrease of 3% and 4% in compressive strength. The compressive strength of C8 and C9 formulations followed a similar trend, with a decrease of 14% and 15% on day 28. Therefore, as the percentage of LS increased from 10% to 14% and 18%, while simultaneously decreasing the percentage of MK and flash-calcined materials, the compressive strength decreased. Literature studies have demonstrated that the combination of limestone and calcined clays can enhance the mechanical and physical properties of materials and allow for higher substitution of OPC [413].

However, the highest compressive strength is achieved when using a 1:2 ratio of calcined clay to limestone [413]. In this study, three different ratios of MK or flash-calcined materials to limestone, namely 2.6, 1.6, and 1, were examined. The results indicate that the ratio of 2.6 yields the highest compressive strength, while the ratio of 1 exhibits the lowest compressive strength. Another study conducted by Parsompech et al. [414] on LC3 mixes reveals that as the percentage of calcined clay exceeds that of LS, the compressive strength increases linearly. This increase can be attributed to the pozzolanic reactivity of the calcined clay, where the amorphous $Al_2O_3.2SiO_2$ in the calcined clay reacts with calcium hydroxide from OPC, forming a calcium aluminum silicate hydrated gel that refines the pore structure and improves compressive strength [414].

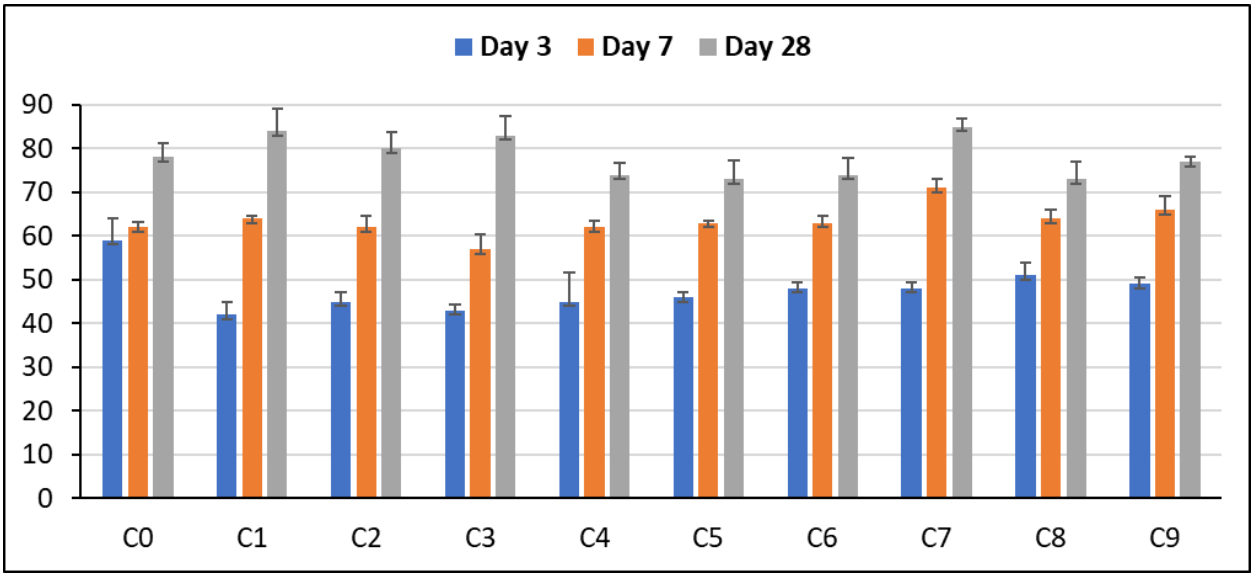

Fig. 131. Compressive strength (MPa) results on LFC mortars.

Du et al. [415] did a study on high-performance concrete incorporating calcined kaolin clay and limestone as cement substitute. The author did various formulations using two types of clay and different percentages of clay and limestone. The author used a W/B ratio equal to 0.3 and resulted in high strength concrete. On day 3, the author has reported compressive strength of 34, 46, 50, and 60 MPa. On day 7 and 28, the maximum strength achieved is equal to 79 MPa and 85 MPa, respectively. In comparison to the LFC done in this study with a W/B ratio equal to 0.33, after 28 days the compressive strength results were ranging from 79 to 91 MPa, depending on the type of clay used and its percentage, thus recording higher strength than the high-performance binder reported by the previous study.

4.5. Mercury porosity test

Fig. 132 illustrates the distribution of pore sizes in LFC mortar formulations after a 28-day curing period. The porosity percentages for C1, C4, and C7 are 5.65%, 7.52%, and 4.54%, respectively. Maintaining low porosity is crucial for enhancing the strength of cement-based materials, as emphasized in various studies [414][416][417][418]. To establish a correlation between porosity and compressive strength results, an examination of their respective pore size distributions is essential.

The compressive strength values for C1, C4, and C7 are 83 MPa, 75 MPa, and 85 MPa, respectively. Pores are categorized into four groups: (d< 10 nm), (10 nm < d < 100 nm), (100 nm < d < 10 μm), and (d > 10 μm), as discussed in section 2.5.4. Mortar specimens with diameters ranging between 100 nm and 10 μm negatively impact compressive strength, unlike those falling between 10 nm and 100 nm [304][305] . Notably, C4 exhibits lower compressive strength than C1 and C7, attributed to its higher macropore percentage (8.7%), exceeding that of C1 (8%) and C7 (6.7%).

The study concludes that porosity measurements validate compressive strength for LFC, as higher porosity corresponds to lower compressive strength, consistent with findings in various studies [418][414][419]. Despite the identical water-to-binder and sand-to-binder ratios, as well as similar mixing and molding procedures for all three formulations, the variation in porosity and compressive strength results arises from the distinct nature of FCS compared to FCC and MK.

The TGA test reveals that C4 experiences a more significant mass decrease than C1 and C7 between 230 °C and 420 °C, aligning with the decomposition of calcium carbonate (CaCO3). This indicates differences in the hydration process between the materials, emphasizing that the compressive strength duration may not fully reflect the long-term characteristics of the mortar samples. The mortar mix C0 composed of 100% OPC has recorded a porosity of 6.55 % and compressive strength of 76 MPa, whereas 68.9% of the pore size distribution are within a range between 10nm<d<100 nm. C1, C4, and C7 formulations are composed of either MK, FCS, or FCC and LS in addition to OPC, therefore it’s hard to correlate a reasonable relationship between C0 and the LFC mortars due to their different composition nature and hydration reaction.

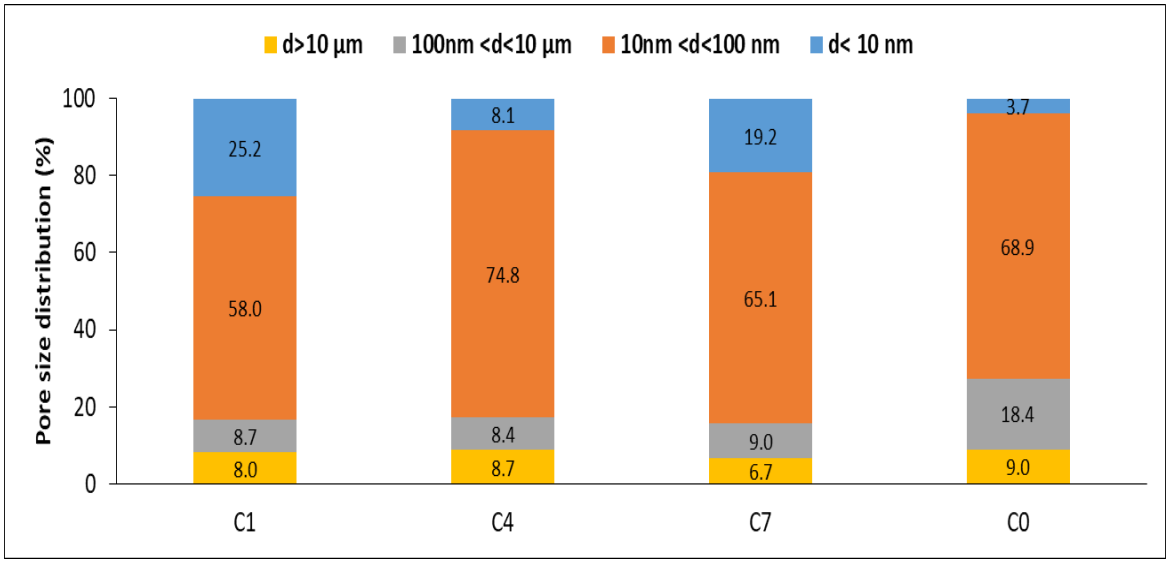

Fig. 132. Pore size diameter (%).

4.6. TGA/ DTG test

TGA is a thermal analysis technique used to determine the changes in the mass of a material as it is heated, and it can provide information about the thermal stability and decomposition behavior of the material. LFC formulations have been demonstrated from the TGA curves 4 major transformation phases. The first phase occurs between 40 °C to 230 °C, which corresponds to the evaporation of water at 105 °C and then the decomposition of ettringite and the dehydration of hydration products [420]. The hydration products identified in the research for LC3 powder are C-S-H, ettringite, monocarboaluminate, and hemicarboaluminate, and portlandite [7][421]. The second phase of mass loss is between 230 °C and 420 °C which is C-S-H dehydration and the beginning of portlandite decomposition [420][422]. The portlandite decomposition is between 420 °C and 500 °C. Finally, the de-carbonation reaction takes place between 500 °C and 1000 °C which corresponds to the decomposition of calcite ($CaCO_3$).

On day 28, the TGA curve demonstrated in Fig. 133 a similar trend of mass loss (%) and temperature (°C) for the LFC formulations with MK and flash-calcined materials, indicating that these formulations may have undergone a comparable hydration reaction during curing.

The three mortar formulations experienced mass loss at different temperature ranges. C1, C4, and C7 all lost water between 40°C and 105°C, with a loss of 1.26%, 1.18%, and 1.22%, respectively. Between 105°C and 230°C, the samples lost mass due to the decomposition of calcium hydroxide

($Ca(OH)_2$). The amount of mass loss for C1, C4, and C7 was 4.79%, 4.68%, and 5.14%, respectively.

The temperature range of 230°C to 420°C has a mass loss of 2.77%, 2.84%, and 2.88%, respectively. Any remaining organic compounds in the samples began to decompose between 420°C and 500°C, causing them to lose 1.83%, 1.59%, and 2% of their mass.

Between 500°C and 1000°C, the samples experienced a significant loss of mass, with C1, C4, and C7 losing 7.05%, 6.18%, and 7.99% of their mass, respectively. The total loss for the mortar samples C1, C4, and C7 was 25.74%, 22.28%, and 24.33%, respectively.

Notably, the mass loss between the three formulations was very similar at all stages, especially for C1 and C7, which had almost identical trends.

The DTG curve reveals three distinct temperature zones of mass loss, approximately occurring at 200 °C, 470 °C, and 800 °C. The initial peak is associated with the hydration products of ettringite, carboaluminates (Mc and Hc), and C-S-H [423]. The second peak corresponds to the hydration product of portlandite (CH) [424], while the third peak aligns with that of calcite ($CaCO_3$) [425]. Variations in the composition of MK, FCS, and FCC contribute to differing intensities of hydration products, influencing the mechanical characteristics of LFC formulations. Examining the DTG, it becomes evident that C4 has the highest portlandite content and C1 the lowest, indicating a lower pozzolanic content for C4 compared to C1 and C7. The Chapelle test further validates this, highlighting MK's higher pozzolanic reactivity compared to FCS and FCC. Similarly, in terms of $CaCO_3$ content, C1 displays the lowest mass loss, while C4 exhibits the highest. This is attributed to MK's higher pozzolanic reactivity, leading to reduced portlandite consumption and lower calcite content. Analyzing compressive strength at 28 days, C1, C4, and C7 demonstrate strengths of 83 MPa, 75 MPa, and 85 MPa, respectively. The lower strength of C4 is attributed to FCS's lower pozzolanic reactivity, as reflected in the DTG curve, indicating lower consumption of portlandite and calcite, resulting in higher mass loss values. A study done by Blouch et al. [426] shows similar results. The author has conducted a study between LC3 formulations using two clays and compared them to OPC binder. The last has concluded that the OPC formulation has no pozzolanic reactivity and thus has the highest portlandite content. For the LC3 formulations, the one with higher clay pozzolanic reactivity showed lower portlandite and calcite content. Therefore, a higher pozzolanic reactivity for MK in C1 is associated with more efficient consumption of portlandite and calcite,

resulting in lower peaks on the DTG curve. Conversely, lower pozzolanic reactivity for FCS as for C4 would lead to less effective consumption of portlandite and calcite and result in higher peaks.

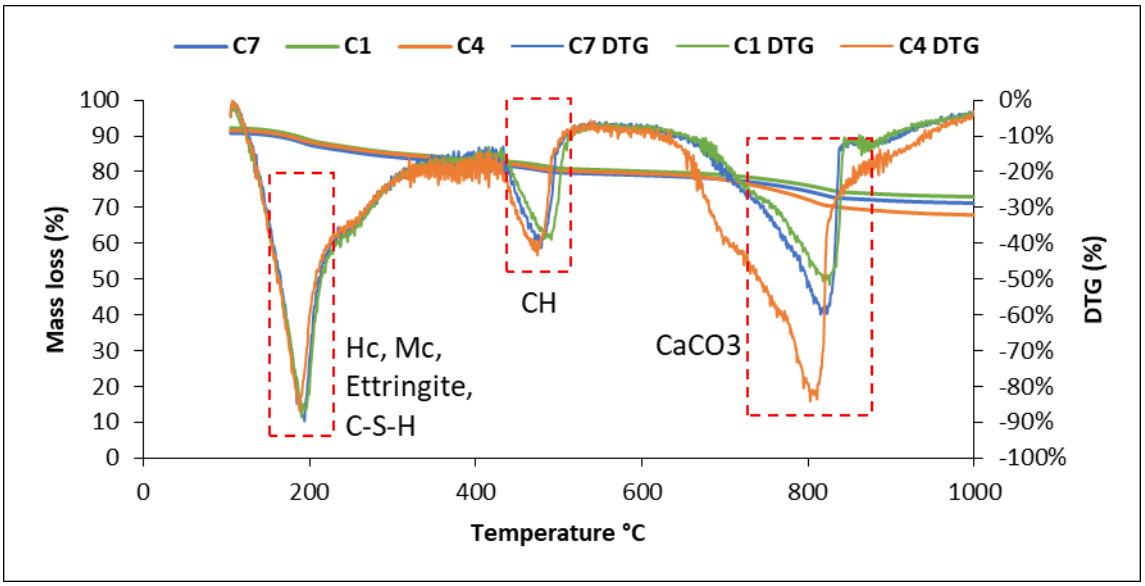

Fig. 133. TGA/DTG on LFC paste formulations (C1, C4, C7).

4.7. XRD analysis

Fig. 134 and Fig. 135 displays the XRD results for C0 and the three LFC pastes (C1, C4, C7), respectively after 28 days of curing. The XRD for C0 shows the expected hydrates ettringite (Et), portlandite (P), calcite (C), alite (A), and belite (B). The LFC paste samples which have ettringite (ET), calcium hydroxide (CH), calcite ($CaCO_3$), calcium monocarboaluminate (Mc), hemicarbolauminate (Hc), and calcium silicate hydrate (CSH) as their main components. Notably, a small variation in peak intensity is the only difference observed among the XRD results for the three paste samples.

Drissi et al. [427]conducted a study that examined the hydration process of a binder that consisted of OPC+ MK+ LS. The last examined various samples using XRD at different time periods. On the 28th day, the XRD outcomes were comparable to the current ones. Specifically, they detected Et at around 16° and 35°, and CH at 18°, 29°, and 34°. Moreover, the author identified the peaks at 12° as Hc and Mc, which exist in LS-binary and ternary binders. Another study done by Zadeh et al. [428] shows that LC3 binder has CH at 18° and 34°, $CaCO_3$ at 30°, and Mc at 12°.

Cao et al. [7] indicated that in LC3 blends replacing 50% cement, calcined clays have strong pozzolanic reactivity and work together with limestone to use up the portlandite generated during cement hydration. As a result, lower levels of C2S and C3S are observed when compared to OPC

mixtures. The XRD findings from this study indicate that the quantities of C2S and C3S are the same for all three formulations, implying that the reaction between MK and LS is comparable to that of FCS and LS, as well as FCC and LS.

Therefore, the XRD findings for C1, C4, and C7 are similar to those in their prior study. Thus, both FCS and FCC can be used to replace MK to form LFC binder.

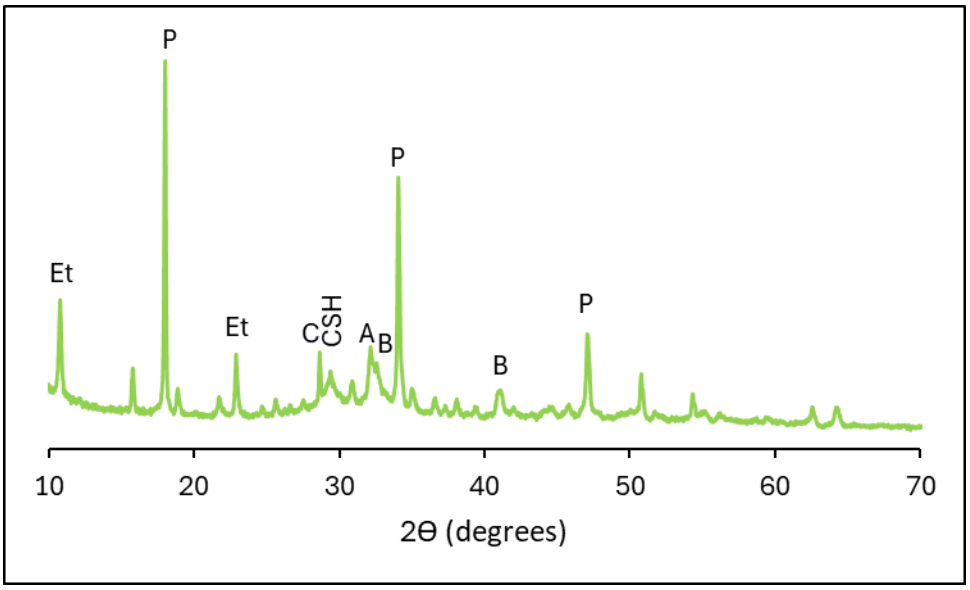

Fig. 134. XRD on C0 paste.

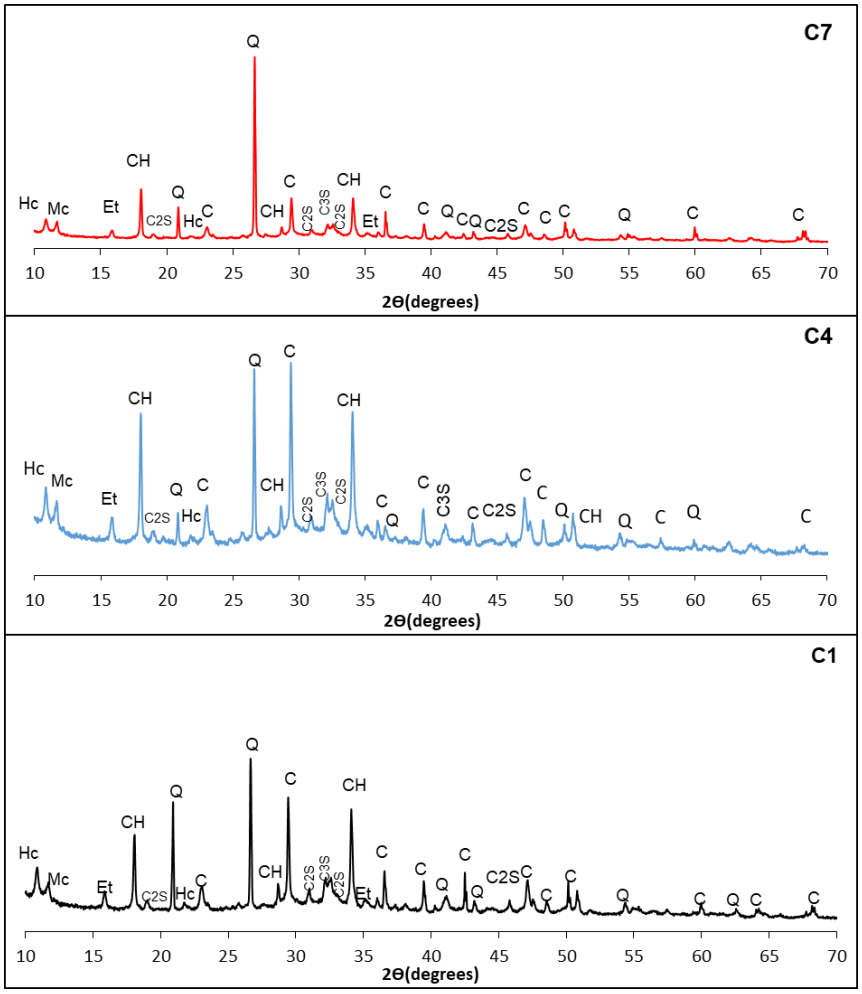

Fig. 135. XRD on LFC paste samples.

4.8. FTIR analysis

The FTIR Spectra are utilized to identify the structural bonds present in the designed mortars. The FTIR results for C0 is shown in Fig. 136 while that of the LFC samples (C1, C4, C7) are shown in Fig. 137. For C0, the bands at 3640 and 1412 cm^{-1} correspond to the presence of CH [429]. The bands at 1650 cm^{-1} are related to the formation of Et [430]. Whereas the bands at 950 cm^{-1} and 880 cm^{-1} were attributed to CSH and $CaCO_3$, respectively [430].

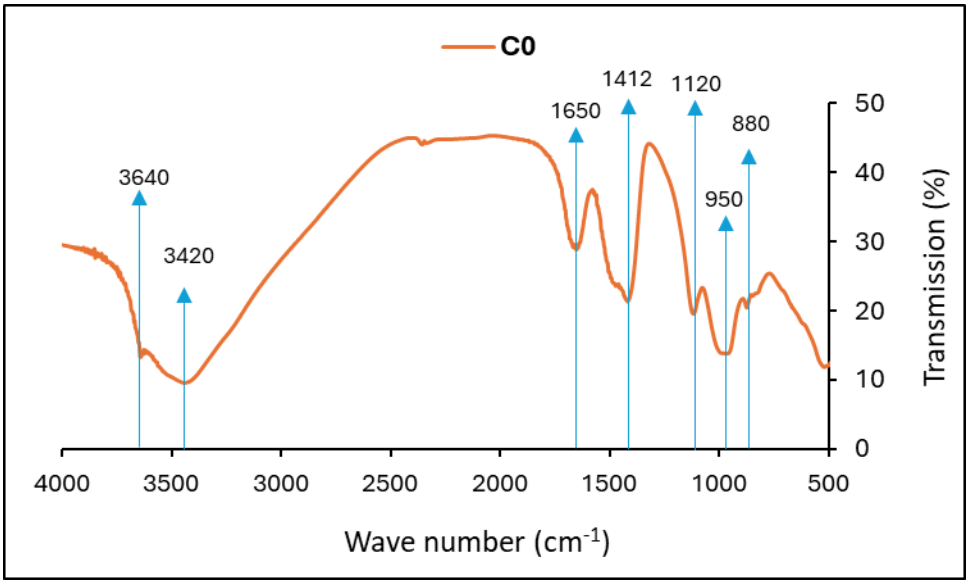

Fig. 136. FTIR on C0 paste sample.

For the LFC formulations the results indicate that the three formulations exhibit a similar structure, as evidenced by the presence of identical peaks at 3644 $cm^{-1,}$ 3522 cm^{-1}, 1651 cm^{-1}, 1422 cm^{-1}, 874 cm^{-1}, and 712 cm^{-1}. Furthermore, C1, C4, and C7 display peaks approximately at 980 cm^{1}, respectively. The peak observed at 3644 cm^{-1} is attributed to portlandite and corresponds to the symmetric stretching vibration of the -OH bond [7][431]. The broad-centered peaks at 3522 cm^{-1} and 1651 cm^{-1} are caused by symmetric and asymmetric stretching vibrations and bending vibrations of -OH in free or chemically bound water [7][432]. Additionally, the peaks centered at 1422 cm^{-1}, 874 cm^{-1}, and 712 cm^{-1} correspond to the asymmetric stretching vibration and plane vibration of calcium carbonate [7][433]. The peaks at 980 cm^{-1} represent the Si-O-T asymmetric vibration which indicates the C-S-H structure [7]. Given that all three formulations possess the same structural bonds on day 28 of the test, FCS and FCC can both be used as substitutes for MK in producing LFC.

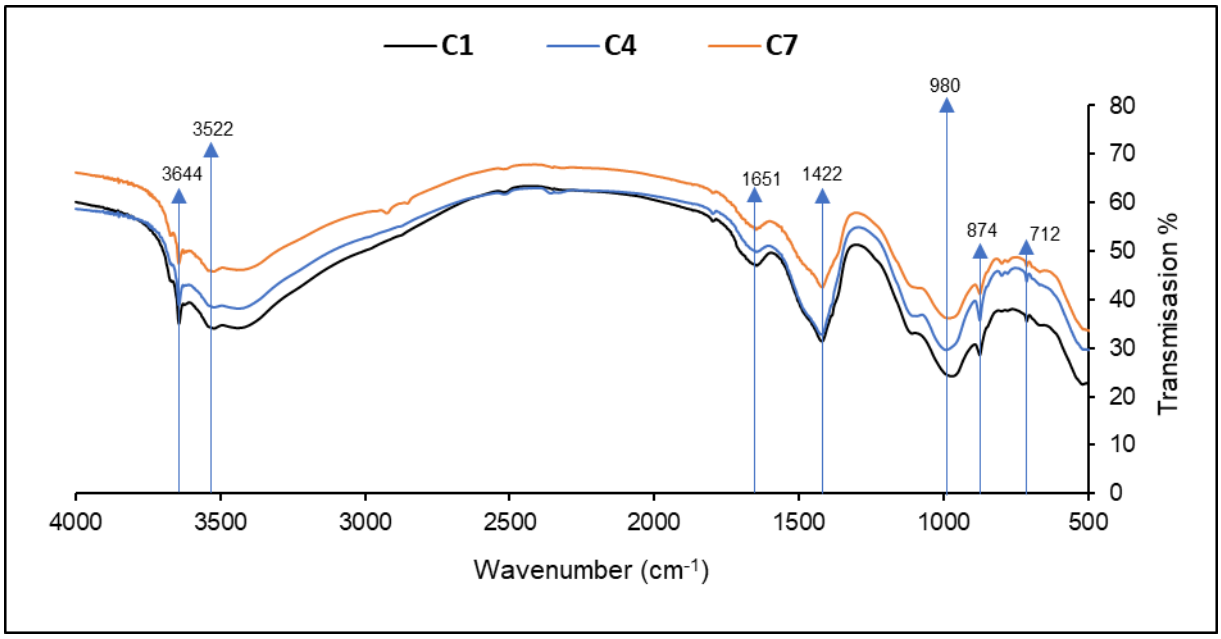

Fig. 137. FTIR on LFC paste samples.

4.9. Calorimetry test

The calorimetry test results for C0, C1, C4, and C7 are illustrated in Fig. 138, illustrating their significance in elucidating the relationship between early-age compressive strength and the hydration reaction of the binder formulations. As indicated in the compressive strength section, C0, C1, C4, and C7 achieved strength levels of 59 MPa, 42 MPa, 45 MPa, and 48 MPa, respectively. The mortar formulations exhibited maximum heat release at ages of 0.8, 1.08, 0.97, and 1.43 days, respectively. Consequently, C0 demonstrated the highest hydration rate among the LFC formulations, as anticipated due to its elevated CaO content (62.5 %), consequently attaining the highest compressive strength on day 3.

Comparatively, C4 exhibited a faster hydration rate than C1 and C7, resulting in higher strength than C1 but lower than C7. This can be attributed to the notably higher CaO content in FCS, amounting to 21.80 %. Nonetheless, at day 3, C7 still managed to achieve greater compressive strength than C4, possibly due to the superior reactivity of FCC compared to FCS, inherent to its reactive clayey nature. Additionally, the higher BET surface area of FCC compared to FCS and MK may explain the increased compressive strength attained, as it contributes to a denser mixture. The BET surface area values for MK, FCS, and FCC are 13.59, 27.45, and 33.01 m^2/g, respectively.

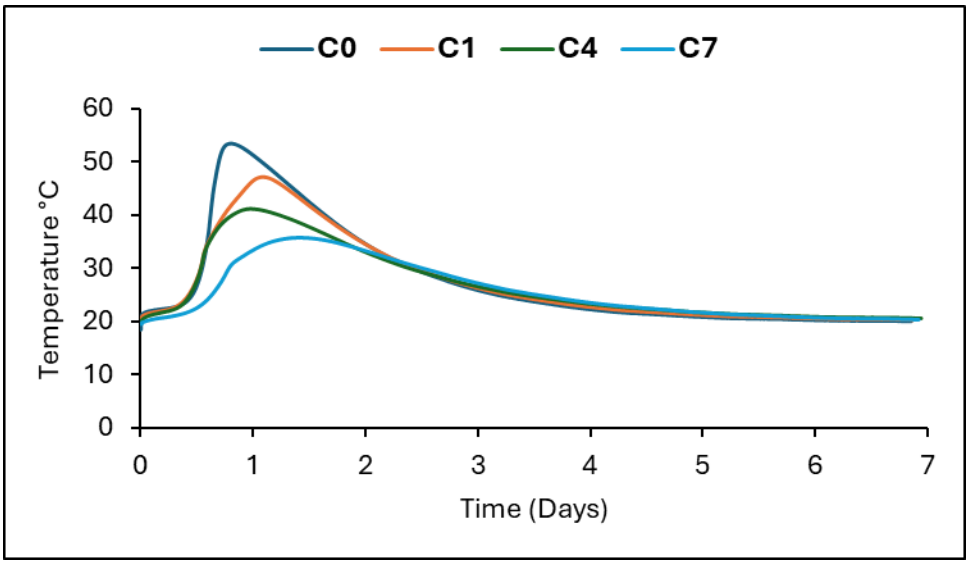

Fig. 138. Calorimetry results for C0, C1, C4, and C7.

4.10. Acid attack test

A 2% sulfuric acid test was performed to evaluate the formulations' durability after 28 days of curing at ambient temperatures. The mass loss of the GP mortar formulations was evaluated at seven-day intervals during acid replenishment, as well as the compressive strength loss after 28 days of exposure. A visual study of the GP formulations was also performed every seven days, with photographic evidence. Afterwards, the XRD and FTIR analysis were done on the samples exposed to acid attack test to study the impact of the test on their mineralogical composition.

- Visual study

Fig. 139Fig. *108* illustrates the monitoring of the visual evolution of LFC mortar formulations (C1, C4, C7) and a reference mix (C0) comprising 100% OPC over a 28-day acid attack period, with measurements taken at 7-day intervals. All mortar formulations exhibited changes in their appearances, with sand particles becoming visible. However, evaluating the impact of the acid attack test on the structural integrity of the mortar formulations is challenging due to their similar shapes but differing colors. This color variation is attributed to the distinct colors of MK, FCS, and FCC. Despite observable degradation in the outer layer of the mortar samples, the conducted test revealed that the samples remained resilient, indicating the feasibility of studying their compressive strength at the conclusion of the test.

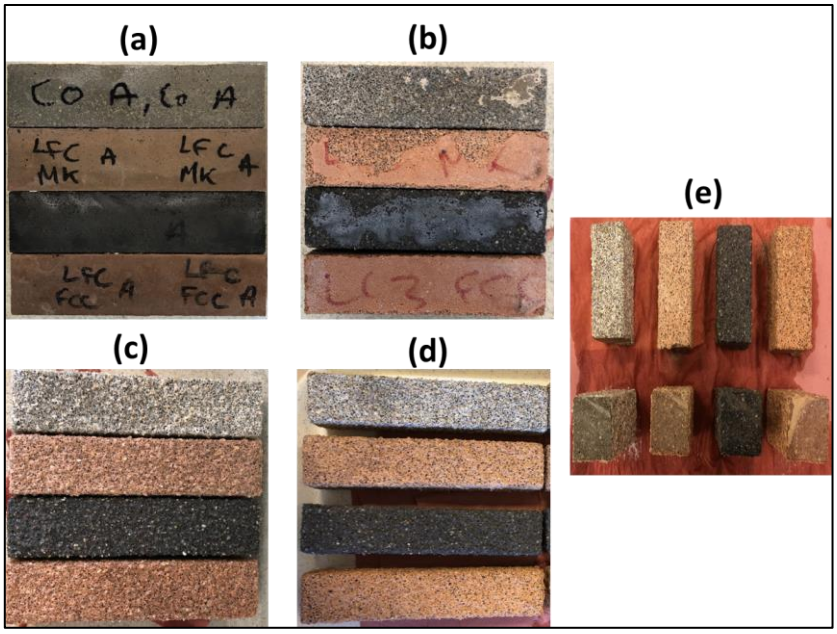

Fig. 139. Visual study of the LFC mortar formulation undergone acid attack test at (a) day 0, (b) day 7, (c) day 14, (d) day 21, (e) day 28.

- Mass loss

Fig. 140 illustrates the influence of the acid attack test on the mass alteration in both the reference mix C0 and various formulations of LFC mortar. While all samples exhibit a similar trend in mass change, there are variations in the percentage of mass loss. Notably, C0 exhibits the highest percentage of mass change at days 7, 14, 21, and 28, registering values of 5.36%, 14.36%, 17.29%, and 18%, respectively. The most substantial mass change occurs at days 7 and 14, with minimal change at day 21 and 28, a pattern observed across all formulations. Evaluating the mass change among LFC mortar formulations, the one formulated with FCS, labeled as C4, demonstrates the highest mass loss throughout the acid attack test, reaching 16.69% after 28 days. In contrast, the formulation with FCC (C7) experiences the lowest mass loss, recording 15.28% after 28 days, while the one with MK (C4) follows closely with a mass loss of 17% after the same period. It is worth noting that C1 exhibits the lowest compressive strength among the LFC formulations at 75 MPa similar to C0 (76 MPa), whereas C7 attains the highest compressive strength at 85 MPa, closely followed by C4 at 83 MPa. Consequently, substituting MK with FCS and FCC proves effective, especially with FCC, as C7 demonstrates the least mass loss. Despite C4 exhibiting the highest mass loss among LFC mortar formulations, the difference in mass loss

compared to C7 is only 2%, suggesting that the use of FCS in LFC can still be considered efficient as the mass loss is not significantly different between the formulations.

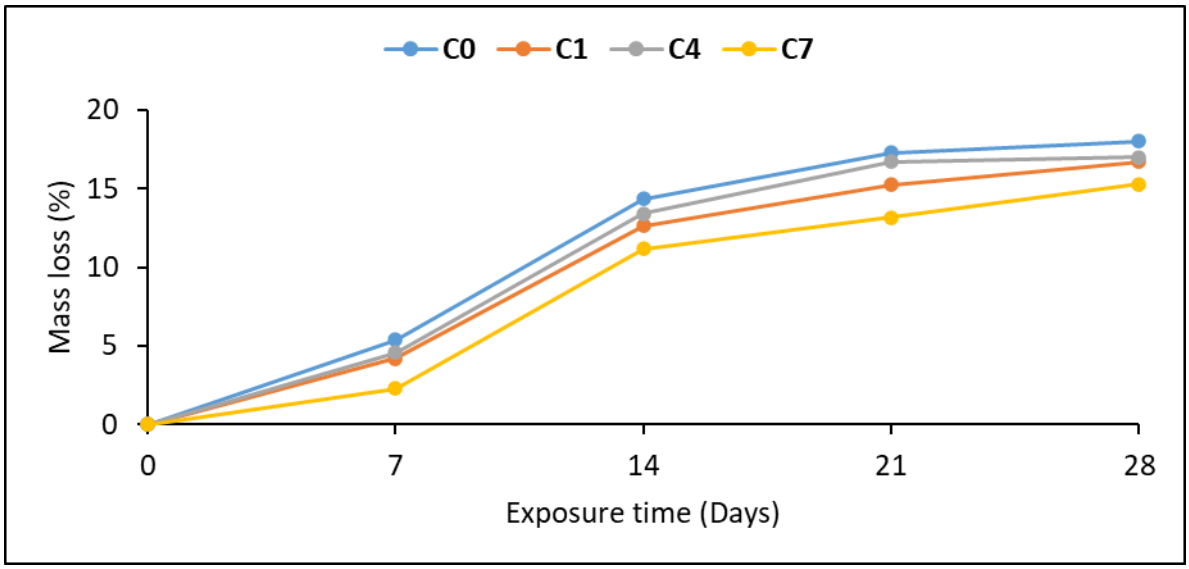

Fig. 140. Mass loss of LFC mortar formulations upon conducting acid attack test.

- Strength loss

Fig. 141 illustrates the reduction in strength for both C0 and LFC mortar formulations following a 28-day acid attack test. The strength loss outcomes align with those observed in mass loss. Similar to the mass loss findings, C0 exhibits the highest mass loss at 59%, correlating with a compressive strength of 31 MPa.

Comparing the strength loss in LFC formulations, C1, C4, and C7 experienced compressive strength reductions of 58%, 59%, and 56%, respectively, with corresponding compressive strengths of 35 MPa, 31 MPa, and 37 MPa. Consequently, C7 emerges as the most resistant LFC mortar formulation to the acid attack test, while C4 exhibits the lowest resistance, although still more resistant than C0. This underscores the effectiveness of FCC and FCS in enhancing the resilience of limestone calcined clay formulations when subjected to acid attack tests.

Both strength loss and mass loss are attributed to the sulfuric acid attack test on CSH and CH phases present in LC3 [434][435][436][437]. Marangu [434] has explained this depletion by the $SO4^{2-}$ and H^{+} into the pore water which contributes to sulfate attack. Ettringite, characterized by the presence of SO_4^{2-} ions, leads to expansive reactions. Conversely, H^{+} ions can directly target CH and CSH phases or indirectly lower the pH of pore water. The exposure of mortar specimens to acidic environments typically triggers a neutralization reaction between hydrogen ions and

$Ca(OH)_2$ in cementitious materials, resulting in decreased mortar alkalinity. This, in turn, leads to the dissolution of hydration products, primarily CSH and CH, causing the deterioration of mortar. The consequences include a reduction in compressive strength and mass loss.

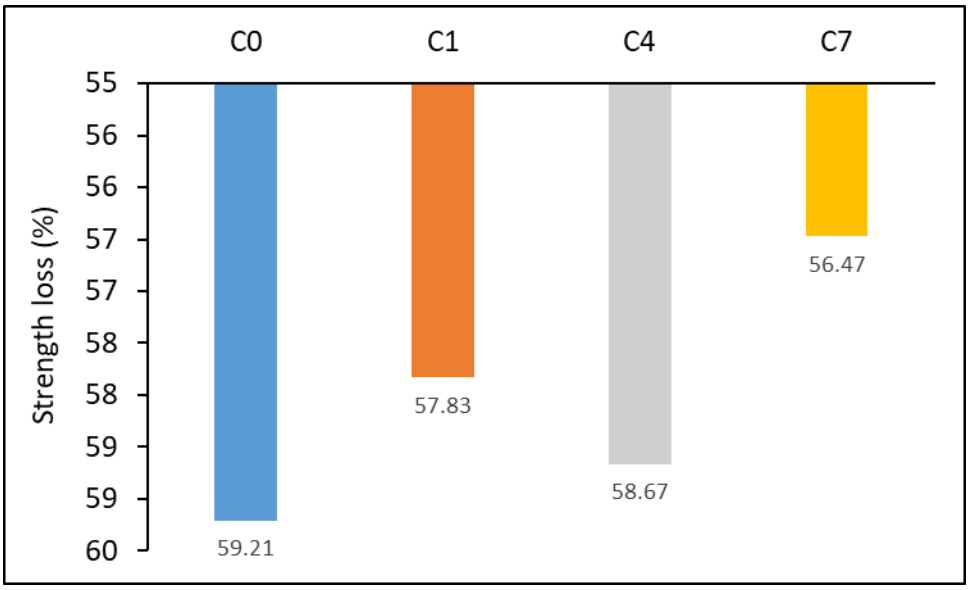

Fig. 141. Strength loss (%) of LFC formulations after acid attack test.

- pH variation

Upon conducting the acid attack test, all the LFC mortar formulations were tested for pH levels to examine the leaching of GP mortar samples when exposed to an acid with a pH of 1.11. The LFC mortar samples initially had a pH of approximately 13 due to their basic nature. Then the pH changes upon contact with the acid as displayed in Fig. 142. On day 7, the pH values reached their highest points for all LFC mortar formulations. Subsequently, as time progressed, the pH values gradually decreased, even though the acid solution was replenished every 7 days. This suggests that the leaching of ions in the LFC mortar samples decreased as exposure time increased. The reference formulation C0 exhibited the highest pH change, reaching a maximum of 3.8 on day 7, but after 28 days, the pH decreased to 1.75. Similarly, the LFC formulations (C1, C4, C7) also recorded their highest pH values on day 7, with pH values of 2.63, 3.5, and 2.55, respectively. This result corresponds to the earlier described mass loss, where C0 showed the highest mass loss compared to the LFC formulations. The change in pH followed a similar pattern, with C0 experiencing the highest change in pH, followed by C4, C1, and C7. This trend was constant through all the acid attack test exposure time. However, from day 21 to day 28, the leaching has

decreased where the change of pH wasn't significant. For example, on day 21 the pH of C0, C1, C4, and C7 were equal to 1.86, 1.29, 1.71, and 1.25, respectively. Afterwards, on day 28 the pH of C0, C1, C4, and C7 almost kept constant and were closet to the initial pH of the acid. This finding aligns with the mass loss, which also decreased partially for these formulations after 21 days of exposure to the acid.

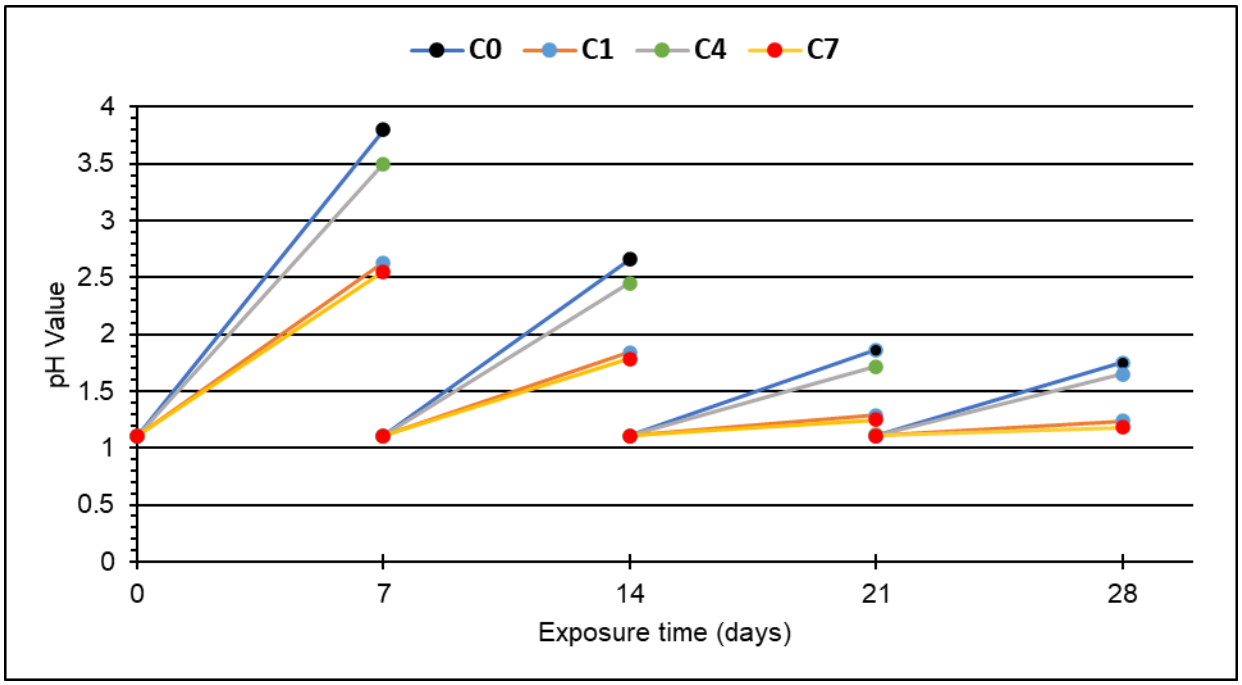

Fig. 142. pH variation of the LFC mortar formulations when conducting acid attack test.

- XRD analysis

Fig. 143 presents the XRD analysis for C0 following exposure to an acid attack test, while Fig. 144 illustrates the XRD results for C1, C4, and C7. This analysis aims to examine the mineralogical composition of samples subjected to the acid attack test and assess the impact on the integrity of their mineral composition. A comparative study is conducted by analyzing the mineralogical composition before and after exposure to the acid attack test. The mineralogical composition of the unexposed samples is detailed in Section 3.3.5 for all samples.

It is crucial to note that the XRD results presented in the figures below pertain to mortar samples rather than paste samples, explaining the presence of quartz corresponding to sand. Examining the XRD of C0 post acid attack test reveals a compromised mineralogical composition, with most of the primary elements, including C-S-H, C-A-H, and Ca $(OH)_2$, eliminated. After the acid attack test, only Calcite remains.

Similarly, for C1, C4, and C7, the main mineralogical elements are eliminated. Prior to acid exposure, the LFC samples exhibit Hc, Mc, Et, CH, C2S, and C3S, as discussed in Section 3.3.5. However, post-acid attack test, most of these elements are eliminated, leaving only C3S and C2S at 42 and 46 °C. Additionally, it's noteworthy that all LFC mortar formulations exhibit similar behavior, indicating that FCS and FCC are affected equally compared to MK in the LFC formulations.

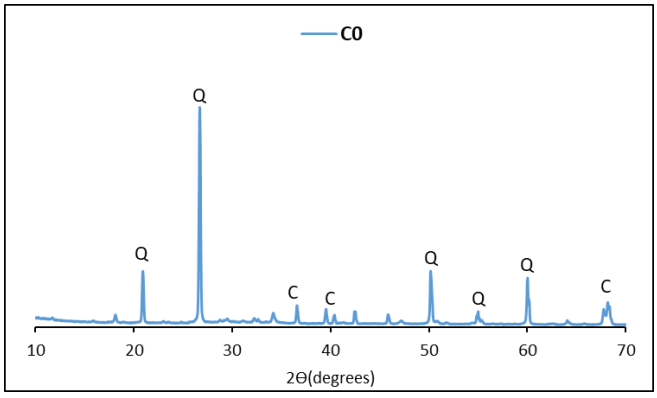

Fig. 143. XRD for C0 after exposure to acid attack test.

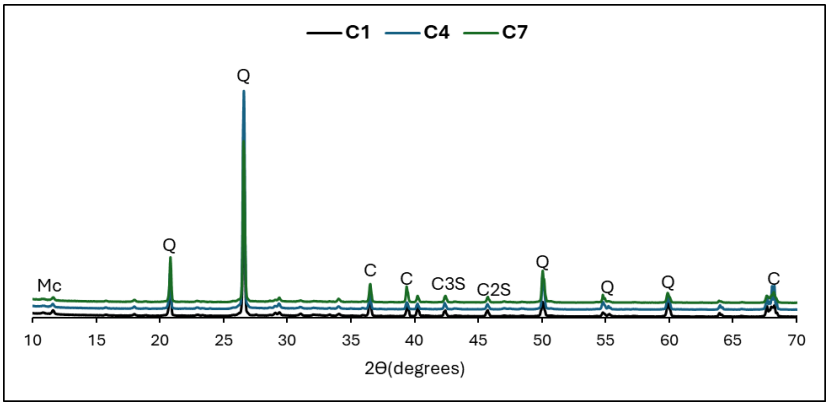

Fig. 144. XRD for C1, C4, and C7 after exposure to acid attack test.

- FTIR analysis

Fig. 145 shows the FTIR analysis of the reference mix C0 subjected to acid attack test. For C0 not subjected to acid attack test, show various peaks as identified in section 4.8 while that subjected to acid attack test only show peaks at 3643 cm^{-1}, 1384 cm^{-1}, 778 cm^{-1}, and 693 cm^{-1}. This indicates potential changes in chemical bonds especially ettringite, CSH, and $CaCO_3$ which have large negative impact on the loss of mass and strength.

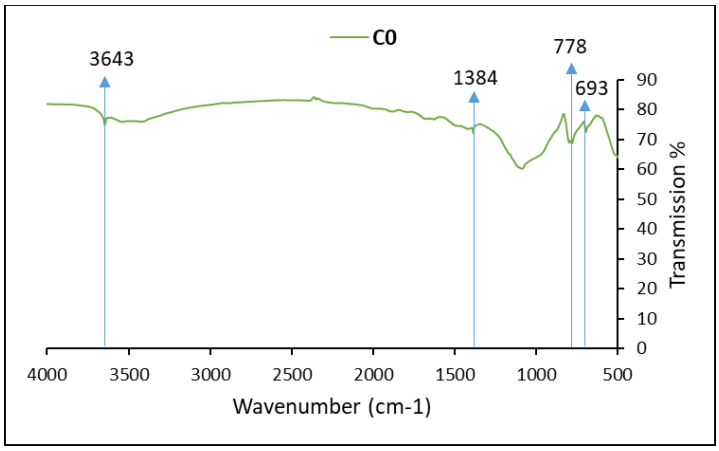

Fig. 145. FTIR analysis of C0 after acid attack test.

Fig. 146 shows the FTIR analysis of the samples subjected to acid attack test. The main peaks before subjecting the samples to acid attack test are identified in section 3.3.6. The peak attributed to H-O bonds in free water at 3542-3644 cm^{-1} -OH bond [7][431] is still available after subjecting them to acid. Also, the peaks present at 1650 cm^{-1} before the acid attack test are still available but with shifting of peak to 1621 cm^{-1}. These peaks correspond to the asymmetric stretching vibrations and bending vibrations of -OH in free or chemically bound water [7][432]. However, for the peaks centered at 1422 cm^{-1}, 874 cm^{-1}, and 712 cm^{-1} and represent calcium carbonate [7][433] are shifted to 1417 cm^{-1}, 1117 cm^{-1}, and 778 cm^{-1}, respectively. Therefore, as explained behind the impact of acid attack on the strength and mass, the sulfuric acid attacks the CSH and CH bonds. Moreover, comparing the intensity of the peaks, most of the peaks have changed their original format into narrow peaks without symmetric vibrations. Also, it is important to mention that upon conducting the FTIR all LFC samples subjected to acid show similar results and therefore it can be concluded that MK, FCS, and FCC show a similar performance on the durability of the LFC formulations.

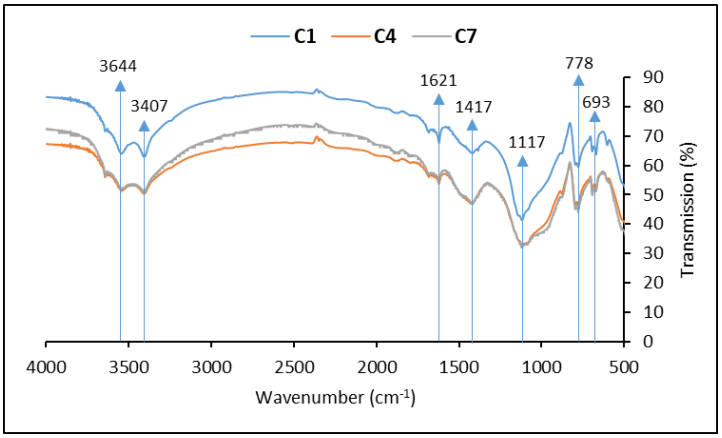

Fig. 146. FTIR analysis on LFC mortar exposed to acid attack test.

4.11. Workability test of LFC concrete

Fig. 147 shows the slump flow diameter of the reference mix C0 and LFC concrete formulations (C0, C1, C4, and C7). Similar to the workability results done on mortar scale, the reference mix C0 shows better results than C4 and C7, while C1 shows better results than. C0 has a slump flow diameter equal to 540 mm while that of C1, C4, and C7 show slump flow diameter results equal to 600 mm, 480 mm, and 520 mm, respectively. The increase in workability for C1 can be attributed to the addition of LS which has a positive impact on the workability of concrete [408][409][410], while the decrease in the workability of C4 and C7 can be explained by the high surface area of both FCS and FCC that affects the water requirement for initiating the flow [405].

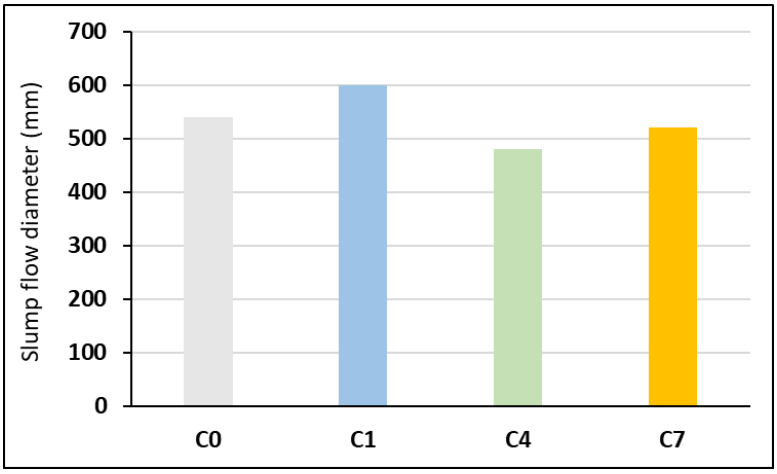

Fig. 147. Workability results on LFC concrete (mm).

4.12. Compressive strength test of LFC concrete

Fig. 148 shows the compressive strength results done on LFC concrete samples (C0, C1, C4, C7). On day 7, the reference mix C0 showed a compressive strength equal to 68 MPa greater than the LFC binder done with sediment (C4) equal to 60 MPa. The LFC binders done with MK (C1) and FCC (C7) showed a higher compressive strength than C0 equal to 80 MPa and 77 MPa, respectively. On day 28, the compressive strength for C0, C1, C4, and C7 increased to 85 MPa, 104 MPa, 72 MPa, and 92 MPa, respectively. Similar to the mortar formulations, the compressive strength was higher for formulations done with MK and FCC than done with FCS. However, the compressive strength for C0 was only higher than C4 by 14.8 %. Therefore, both flash-calcined materials FCS and FCC were able to achieve a concrete classified as high strength binder.

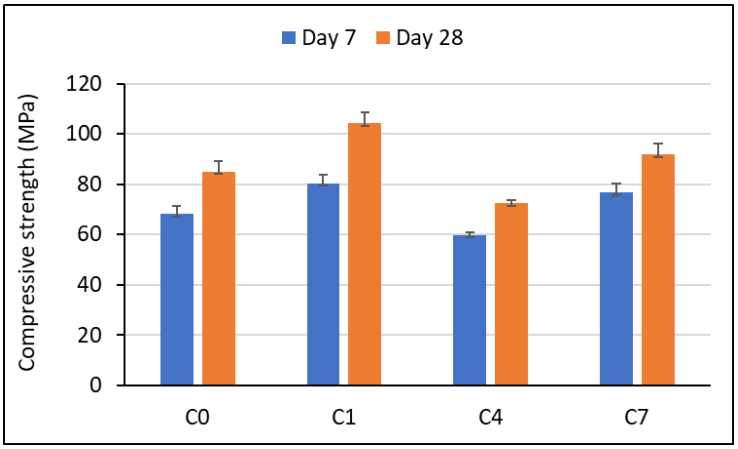

Fig. 148. Compressive strength of LFC concrete

4.13. Leaching test

Table 27 displays the results of leaching tests conducted on mortar scale for C0 and LFC binders. Compared to the reference mix C0, all LFC binders (C1, C4, and C7) exhibited similar traces of elements with nearly identical concentrations across all elements. However, for Barium (Ba), C0 showed the highest concentration at 7.67 mg/kg. In contrast, C1 had the lowest concentration of Ba at 1.53 mg/kg, while C4 had the highest at 6.81 mg/kg. Additionally, it is noteworthy that for Zinc (Zn), C0 had the highest concentration at 0.03 mg/kg, whereas for the LFC binders, the concentration of Zn was below 0.01 for all samples. In terms of waste classification, all tested samples were classified as inert and nonhazardous waste, indicating that the use of flash-calcined materials (FCS and FCC) in limestone calcined clay cement binders complies with environmental safety requirements based on the recorded element concentrations.

Table 27. Leaching test results for C0 and LFC binders (mg/kg).

Element	C0	C1	C4	C7	IW	NHW
As	< 0.1	< 0.1	< 0.1	< 0.1	0.5	2
Ba	7.667	1.535	6.809	4.867	20	100
Cd	< 0.009	< 0.009	< 0.009	< 0.009	0.04	1
Cr	< 0.004	0.007	< 0.004	< 0.004	0.5	10
Cu	< 0.02	< 0.02	< 0.02	< 0.02	2	50
Mo	< 0.09	< 0.09	< 0.09	< 0.09	0.5	10
Ni	< 0.05	< 0.05	< 0.05	< 0.05	0.4	10
Pb	< 0.03	< 0.03	0.066	< 0.03	0.5	10
Sb	< 0.06	< 0.06	< 0.06	< 0.06	0.06	0.7

Se	< 0.08	< 0.08	< 0.08	< 0.08	0.1	0.5
Zn	0.03	< 0.01	< 0.01	< 0.01	4	50

4.14. Conclusion

The purpose of this research is to create limestone calcined clay cement using flash-calcined dredged sediments (FCS) and flash-calcined excavated clays (FCC). These formulations are referred to as LFC binders. The study investigates the effects of replacing 10%, 20%, and 30% of ordinary Portland cement (OPC) with FCS and FCC. Additionally, for comparison, 10%, 20%, and 30% of OPC are replaced with metakaolin (MK). A control mix consisting of 100% OPC is also prepared. The findings indicate that substituting OPC with MK, FCS, or FCC adversely affects the workability of the mortar mix due to their high specific surface area. However, substituting 10%, 20%, and 30% of OPC with MK, FCS, or FCC has a positive impact on compressive strength at all ages beyond C0. Among the MK substitutions, MK20 exhibits the highest compressive strength compared to MK10 and MK30. Similarly, FCS10 demonstrates superior compressive strength compared to FCS20 and FCS30 when substituting 10% of OPC with FCS. Likewise, FCC10 is identified as the optimal formulation among the tested substitutions.
For LFC formulations, the study highlights the impact of using FCS and FCC in limestone calcined clay cement formulations.

- The findings indicate a decrease in workability due to the high surface area and water absorption capacity of flash-calcined materials, similar to MK. However, increasing the substitution of limestone (LS) while decreasing the percentage of MK and flash-calcined materials resulted in improved workability across all formulations. This underscores the importance of carefully balancing the constituents to optimize the workability of cementitious mixes for various applications.
- In conclusion, the compressive strength tests conducted on various LFC formulations compared to the reference mix C0 revealed significant insights. While C0 exhibited higher compressive strength at early ages, formulations incorporating pozzolanic materials such as MK and flash-calcined materials like FCS and FCC displayed notable improvements over time. The rapid increase in strength was attributed to the CaO content present in OPC, influencing early-age hydration reactions as shown from the calorimetry test. Additionally, formulations

like C1, C4, and C7 showcased enhanced strengths at both early and late ages due to the pozzolanic reactions of the added materials. However, adjustments in the formulations, such as increasing limestone content while reducing MK and flash-calcined materials, led to a gradual decrease in compressive strength. Literature supports the enhancement of mechanical properties with the combination of limestone and calcined clays, with optimal ratios yielding the highest compressive strengths. The porosity test results validate the compressive strength results.

- The physicochemical tests TGA, XRD, and FTIR done on the LFC formulations with FCS and FCC revealed similar results to those done with MK.
- The LFC concrete formulations showed similar results to the mortar formulations.
- When conducting the durability test, the acid attack test results revealed that LFC formulation done with FCS was the least resistance whereas that done with FCC showed the higher resistance.
- The leching test results for LFC binders done with FCS and FCC are classified as inert waste and nonhazardous materials.

General Conclusion and Perspectives

Chapter 5. General Conclusion and Perspectives

General Conclusion

The experimental investigation involved the utilization of flash-calcined dredged sediments (FCS) and flash-calcined excavated clays (FCC) in geopolymer binders and limestone flash-calcined-clay cement (LFC) binders to enhance strength and durability properties. The impact of flash calcination at 750 °C on the materials' properties was assessed by examining their physical, chemical, and mineralogical characteristics pre- and post-flash calcination. The study revealed the following outcomes:

- Flash calcination effectively removed water and organic content from both raw sediment and raw millstone clay.
- It increased the density of raw sediment and raw clays due to organic content elimination.
- Chemical analysis showed no change in the percentage of major oxides post-flash calcination.
- Flash calcination led to an increase in particle size distribution due to agglomeration phenomenon.
- Scanning electron microscopy (SEM) analysis revealed a transformation from irregular to spherical particle shapes post-flash calcination, along with observed agglomeration.
- XRD analysis indicated a decrease in calcite intensity post-flash calcination, while quartz remained unchanged. Anhydrite formation was observed in flash-calcined sediments due to CaO from $CaCO_3$ decomposition reacting with sulfate from $CaSO_4$. Kaolin peaks decreased, indicating the transition to metakaolin.
- The Chapelle test showed positive indications of pozzolanic reactivity of FCS and FCC, though not surpassing that of metakaolin.

The incorporation of FCS and FCC in geopolymer binders, alongside metakaolin (MK) and granulated blast furnace slag (GBFS), resulted in high-strength binders with good durability. Three formulations each were prepared with FCS and FCC while maintaining a Si/Al ratio of 2.

- As the percentage of FCS and FCC decreased, and GBFS percentage increased, workability improved compared to the reference mix.

- Compressive strength increased with higher GBFS content, with GP formulations showing significant strength comparable to the MK reference mix.
- Physicochemical analyses indicated the presence of stable geopolymer, supported by NMR and SEM/EDX tests showing a well-structured GP matrix.
- Increased GBFS content accelerated geopolymerization reaction and enhanced compressive strength at early ages.
- Higher GBFS content resulted in denser structures with increased resistance to acid attack.
- Resistance to high temperatures and freeze-thaw cycles varied with GBFS content, while water absorption tests were consistent with porosity results.
- The Leaching test classified GP mortar formulations as non-hazardous.

The inclusion of FCS and FCC in LCF formulations yielded favorable results in terms of physical, mechanical, microstructural, and durability properties. Comparative physicochemical analysis of LFC formulations using TGA/DTG, XRD, and FTIR was conducted to assess the behavior of FCS and FCC against MK. The study yielded the following observations:

- Addition of FCS and FCC in LFC formulations resulted in decreased workability compared to those with MK and to the reference mix using 100% OPC.
- Both LFC formulations with FCS and FCC exhibited enhanced mechanical strength compared to those with MK and the reference mix.
- Regarding resistance to acid attack, formulations with FCS showed lower resistance but still outperformed the reference mix.
- TGA/DTG, XRD, and FTIR analysis indicated similar behavior among FCS, FCC, and MK, suggesting that both FCS and FCC can serve as substitutes for MK in LFC formulations.
- The leaching test classified the LFC formulations as inert and non-hazardous materials.

Perspectives

This thesis was divided into two main parts. The first part discussed the utilization of flash-calcined sediments and flash-calcined excavated clays in geopolymer binders. The second part of the thesis discussed the utilization of the flash-calcined sediments and flash-calcined excavated clays in limestone calcined clay cement binders. Both binders were able to achieve high strength in accordance with high performance standards and comparable results to literature examples.

The binders were assessed on both mortar scale and concrete scale in terms of rheological properties, mechanical properties, durability properties, and their impact on the environment.
However, more work can be done on these binders to have a better evaluation of their performance and their ability to be used by researchers interested in the valorization of waste materials in geopolymer and cementitious formulations.
This can be done by performing more variations in the percentages of flash-calcined sediments and flash-calcined excavated clay and by conducting more lab experiments. On a concrete scale, more durability tests could be done to evaluate the durability of the binders. For example, acid attack tests, chloride penetration test, freeze-thaw test could be done on concrete scale.
Finally, to ensure that a proper design was adopted, dredged sediments and excavated clays of different physical, physico-chemical, and mineralogical properties could be used to consolidate the results obtained.

References

References

[1] C. M. Moundounga, “Contribution to the high temperature thermodynamics of OPC clinker phases Chancel Mawalala Moundounga To cite this version : HAL Id : tel-04048643 Contribution à la thermodynamique à haute température des phases d ’ un clinker OPC Contribution to the high,” 2023.

[2] F. Preston and J. Lehne, “Making Concrete Change Innovation in Low-carbon Cement and Concrete,” 2018. [Online]. Available: https://api.semanticscholar.org/CorpusID:139317858

[3] S. Hosseini, N. A. Brake, M. Nikookar, Ö. Günaydın-Şen, and H. A. Snyder, “Enhanced strength and microstructure of dredged clay sediment-fly ash geopolymer by mechanochemical activation,” *Constr. Build. Mater.*, vol. 301, p. 123984, 2021, doi: 10.1016/j.conbuildmat.2021.123984.

[4] A. Z. Khalifa *et al.*, “Advances in alkali-activation of clay minerals,” *Cem. Concr. Res.*, vol. 132, no. March, p. 106050, 2020, doi: 10.1016/j.cemconres.2020.106050.

[5] R. S. Lin, S. Oh, W. Du, and X. Y. Wang, “Strengthening the performance of limestone-calcined clay cement (LC3) using nano silica,” *Constr. Build. Mater.*, vol. 340, no. April, 2022, doi: 10.1016/j.conbuildmat.2022.127723.

[6] F. Bahman-Zadeh, A. A. Ramezanianpour, and A. Zolfagharnasab, “Effect of carbonation on chloride binding capacity of limestone calcined clay cement (LC3) and binary pastes,” *J. Build. Eng.*, vol. 52, no. August 2021, p. 104447, 2022, doi: 10.1016/j.jobe.2022.104447.

[7] Y. Cao, Y. Wang, Z. Zhang, Y. Ma, and H. Wang, “Thermal stability of limestone calcined clay cement (LC3) at moderate temperatures 100–400 °C,” *Cem. Concr. Compos.*, vol. 135, no. August 2022, p. 104832, 2023, doi: 10.1016/j.cemconcomp.2022.104832.

[8] S. Karkhaneh, A. Tarighat, and S. Ghaffarpour Jahromi, “Kinetics behavior of delayed ettringite in limestone calcined clay cement (LC3) by thermodynamic approach and consideration of the time factor,” *Constr. Build. Mater.*, vol. 367, no. September 2022, p.

129143, 2023, doi: 10.1016/j.conbuildmat.2022.129143.

[9] F. Avet and K. Scrivener, “Investigation of the calcined kaolinite content on the hydration of Limestone Calcined Clay Cement (LC3),” *Cem. Concr. Res.*, vol. 107, no. August 2017, pp. 124–135, 2018, doi: 10.1016/j.cemconres.2018.02.016.

[10] P.-C. Aitcin, *Binders for Durable and Sustainable Concrete*. 2008.

[11] M. C. G. Juenger and R. Siddique, “Recent advances in understanding the role of supplementary cementitious materials in concrete,” *Cem. Concr. Res.*, vol. 78, pp. 71–80, 2015, doi: 10.1016/j.cemconres.2015.03.018.

[12] R. P. Khatri, V. Sirivivatnanon, and W. Gross, “Effect of different supplementary cementitious materials on mechanical properties of high performance concrete,” *Cem. Concr. Res.*, vol. 25, no. 1, pp. 209–220, 1995, doi: https://doi.org/10.1016/0008-8846(94)00128-L.

[13] D. Wang, “Solidification et valorisation de sédiments du port de Dunkerque en travaux routiers,” 2011. [Online]. Available: http://www.theses.fr/2011LIL10086/document

[14] “Ministère de l’environnement et du developpement durable : Groupe de travail numéro 11 – sédiments de dragag,” 2011. doi: http://www.developpement-durable.gouv.fr/IMG/pdf/G11-2.pdf.

[15] H. Slimanou, K. Bouguermouh, and N. Bouzidi, “Synthesis of geopolymers based on dredged sediment in calcined and uncalcined states,” *Mater. Lett.*, vol. 251, pp. 188–191, 2019, doi: 10.1016/j.matlet.2019.05.070.

[16] C. Ferone, F. Colangelo, R. Cioffi, F. Montagnaro, and L. Santoro, “Use of reservoir clay sediments as raw materials for geopolymer binders,” *Adv. Appl. Ceram.*, vol. 112, no. 4, pp. 184–189, 2013, doi: 10.1179/1743676112Y.0000000064.

[17] C. Ferone *et al.*, “Thermally treated clay sediments as geopolymer source material,” *Appl. Clay Sci.*, vol. 107, pp. 195–204, 2015, doi: 10.1016/j.clay.2015.01.027.

[18] A. Alloul, M. Amar, M. Benzerzour, and N. E. Abriak, “Geopolymer mortar with flash-calcined sediments cured under ambient conditions,” *Constr. Build. Mater.*, vol. 391, no. May, p. 131809, 2023, doi: 10.1016/j.conbuildmat.2023.131809.

[19] R. Snellings, L. Horckmans, C. Van Bunderen, L. Vandewalle, and Ö. Cizer, “Flash-calcined dredging sediment blended cements: effect on cement hydration and properties,” *Mater. Struct. Constr.*, vol. 50, no. 6, Dec. 2017, doi: 10.1617/s11527-017-1108-5.

[20] M. Amar, M. Benzerzour, J. Kleib, and N. E. Abriak, “From dredged sediment to supplementary cementitious material: characterization, treatment, and reuse,” *International Journal of Sediment Research*, vol. 36, no. 1. Elsevier B.V., pp. 92–109, Feb. 01, 2021. doi: 10.1016/j.ijsrc.2020.06.002.

[21] G. Aouad, A. Laboudigue, N. Gineys, and N. E. Abriak, “Dredged sediments used as novel supply of raw material to produce Portland cement clinker,” *Cem. Concr. Compos.*, vol. 34, no. 6, pp. 788–793, 2012, doi: 10.1016/j.cemconcomp.2012.02.008.

[22] S. Coussy, G. Boissard, S. Belbèze, and D. Guyonnet, “French Feedback on the Use of Inert Waste Landfill Criteria for Managing Excavated Soils,” 2019.

[23] H. Yanguatin, J. H. Ramírez, A. Tironi, and J. I. Tobón, “Effect of thermal treatment on pozzolanic activity of excavated waste clays,” *Constr. Build. Mater.*, vol. 211, pp. 814–823, 2019, doi: 10.1016/j.conbuildmat.2019.03.300.

[24] P. Priyadharshini, K. Ramamurthy, and R. G. Robinson, “Reuse potential of stabilized excavation soil as fine aggregate in cement mortar,” *Constr. Build. Mater.*, vol. 192, pp. 141–152, Dec. 2018, doi: 10.1016/J.CONBUILDMAT.2018.10.141.

[25] Y. Cao, Y. Wang, Z. Zhang, Y. Ma, and H. Wang, “Turning sandstone clay into supplementary cementitious material: activation and pozzolanic reactivity evaluation,” *Compos. Part B Eng.*, vol. 223, no. April, p. 109137, 2021, doi: 10.1016/j.compositesb.2021.109137.

[26] J. Skibsted and R. Snellings, “Reactivity of supplementary cementitious materials (SCMs) in cement blends,” *Cement and Concrete Research*, vol. 124. Elsevier Ltd, Oct. 01, 2019.

doi: 10.1016/j.cemconres.2019.105799.

[27] S. Salvador, “Pozzolanic properties of flash-calcined kaolinite: A comparative study with soak-calcined products,” *Cem. Concr. Res.*, vol. 25, no. 1, pp. 102–112, 1995, doi: 10.1016/0008-8846(94)00118-I.

[28] S. Salvador and O. Pons, “A semi-mobile flash dryer / calciner unit to manufacture pozzolana from raw clay soils - application to soil stabilisation To cite this version : HAL Id : hal-01697286 A semi-mobile flash dryer r calciner unit to manufacture pozzolana from raw clay soils ,” 2018.

[29] R. S. Nicolas, “Approche performantielle des bétons avec métakaolins obtenus par calcination flash,” Université Paul Sabatier-Toulouse III, 2011.

[30] C. Bich, “Contribution à l’étude de l’activation thermique du kaolin : évolution de la structure cristallographique et activité pouzzolanique,” NSA,Villeurbanne, 2005.

[31] M. A. A. Amar, “Traitement des sédiments de dragage pour une valorisation dans les matrices cimentaires,” *Http://Www.Theses.Fr*, 2017, [Online]. Available: http://www.theses.fr/2017LIL10154

[32] J. Davidovits, “Geopolymers,” *J. Therm. Anal.*, vol. 37, no. 8, pp. 1633–1656, 1991, doi: 10.1007/BF01912193.

[33] A. Alloul, M. Amar, M. Benzerzour, and N. E. Abriak, “Geopolymer mortar with flash-calcined sediments cured under ambient conditions,” *Constr. Build. Mater.*, vol. 391, no. March, p. 131809, 2023, doi: 10.1016/j.conbuildmat.2023.131809.

[34] M. Izquierdo, X. Querol, J. Davidovits, D. Antenucci, H. Nugteren, and C. Fernández-Pereira, “Coal fly ash-slag-based geopolymers: Microstructure and metal leaching,” *J. Hazard. Mater.*, vol. 166, no. 1, pp. 561–566, 2009, doi: 10.1016/j.jhazmat.2008.11.063.

[35] J. Davidovits and G. Resins, “Geopolymer chem istry and sustain able Dev elopment . The Poly (s ialate) term inolog y : a v ery useful and simp le model for th e p rom otion and understanding of green-chemistr y .,” *Geopolymer 2005 Conf.*, no. July 2005, pp. 9–16,

1980.

[36] A. Alloul, M. Amar, M. Benzerzour, and N. Abriak, “A comparative analysis of ambient-cured metakaolin geopolymer mortar and flash-calcined soil geopolymer,” *Constr. Build. Mater.*, vol. 409, no. October, p. 134085, 2023, doi: 10.1016/j.conbuildmat.2023.134085.

[37] F. Avet, R. Snellings, A. Alujas Diaz, M. Ben Haha, and K. Scrivener, “Development of a new rapid, relevant and reliable (R3) test method to evaluate the pozzolanic reactivity of calcined kaolinitic clays,” *Cem. Concr. Res.*, vol. 85, pp. 1–11, 2016, doi: https://doi.org/10.1016/j.cemconres.2016.02.015.

[38] S. Sánchez Berriel *et al.*, “Assessing the environmental and economic potential of Limestone Calcined Clay Cement in Cuba,” *J. Clean. Prod.*, vol. 124, pp. 361–369, 2016, doi: https://doi.org/10.1016/j.jclepro.2016.02.125.

[39] “low clinker.pdf.”

[40] F. Avet, R. Snellings, A. Alujas Diaz, M. Ben Haha, and K. Scrivener, “Development of a new rapid, relevant and reliable (R3) test method to evaluate the pozzolanic reactivity of calcined kaolinitic clays,” *Cem. Concr. Res.*, vol. 85, pp. 1–11, 2016, doi: 10.1016/j.cemconres.2016.02.015.

[41] A. I. Gabitov, R. R. Muhamedzjanov, A. S. Salov, and V. A. Rjazanova, “Concrete: Previous and Future Technologies,” *IOP Conf. Ser. Mater. Sci. Eng.*, vol. 1079, no. 2, p. 022036, 2021, doi: 10.1088/1757-899x/1079/2/022036.

[42] J. Davidovits, *Geopolymer Chemistry and Applications*, vol. 171. 2008.

[43] E. Güneyisi, M. Gesoğlu, S. Karaoğlu, and K. Mermerdaş, “Strength, permeability and shrinkage cracking of silica fume and metakaolin concretes,” *Constr. Build. Mater.*, vol. 34, pp. 120–130, 2012, doi: https://doi.org/10.1016/j.conbuildmat.2012.02.017.

[44] A. Dushimimana, A. A. Niyonsenga, and F. Nzamurambaho, “A review on strength development of high performance concrete,” *Construction and Building Materials*, vol. 307. Elsevier Ltd, Nov. 08, 2021. doi: 10.1016/j.conbuildmat.2021.124865.

[45] L. Moreillon, “Shear strength of structural elements in high performance fibre reinforced concrete (HPFRC),” 2013. [Online]. Available: http://www.theses.fr/2013PEST1033/document

[46] O. Büyüköztürk and D. Lau, “High performance concrete: fundamentals and application,” *Massachusetts Inst. Technol. Cambridge, Massachusetts, US*, 2002.

[47] S.-J. Guo and T.-H. Tsai, “Application of high performance concrete on a 85-story high rise building in Taiwan,” in *The 30th International Symposium on Automation and Robotics in Construction and Mining*, 2013, pp. 933–940.

[48] P.-K. Chang, C.-L. Hwang, and Y.-N. Peng, “Application of high-performance concrete to high-rise building in Taiwan,” *Adv. Struct. Eng.*, vol. 4, no. 2, pp. 65–73, 2001.

[49] C.-T. Tsai, G. T.-C. Kung, and C.-L. Hwang, “Use of high performance concrete on rigid pavement construction for exclusive bus lanes,” *Constr. Build. Mater.*, vol. 24, no. 5, pp. 732–740, 2010, doi: https://doi.org/10.1016/j.conbuildmat.2009.10.035.

[50] M. Zhou, W. Lu, J. Song, and G. C. Lee, “Application of Ultra-High Performance Concrete in bridge engineering,” *Constr. Build. Mater.*, vol. 186, pp. 1256–1267, 2018, doi: https://doi.org/10.1016/j.conbuildmat.2018.08.036.

[51] F. de Larrard, “Structures granulaires et formulation des bétons,” *Etudes Rech. des Lab. des ponts chaussées*, p. 591, 1999.

[52] F. Toutlemonde, F. Légeron, and A. Piquet, “Valorisation des betons a hautes et tres hautes performances dans les structures d’ouvrages d’art,” 2004. [Online]. Available: https://api.semanticscholar.org/CorpusID:190368037

[53] R. Le Roy, “Déformations instantanées et différées des bétons à hautes performances,” 1995. [Online]. Available: http://www.theses.fr/1995ENPC9534

[54] A. Loukili, “Etude du retrait et du fluage de bétons à ultra-hautes performances,” 1996. [Online]. Available: http://www.theses.fr/1996NANT2080

[55] Comité Euro-international du Béton., “CEB-FIP Model Code 90. , Bulletin d’information N°213 - 214, Lausanne,” Switzerland, 1993.

[56] AMERICAN CONCRETE INSTITUTE, “State-of-the-art Report on high strength concrete,” Detroit, MI, 1992.

[57] I. Standard, “AH Price Code EUROCODE 2: DESIGN OF CONCRETE STRUCTURES - PART 1-1: GENERAL RULES AND RULES FOR BUILDINGS NO COPYING WITHOUT NSAI PERMISSION EXCEPT AS PERMITTED BY COPYRIGHT LAW,” *Natl. Stand. Autority*, 2005, [Online]. Available: www.saiglobal.com/shop

[58] Swiss Society of Engineers and Architects, “SN 505 262, Concrete Structures, Standard,” Zürich, 2003.

[59] A. Alsalman, C. N. Dang, J. R. Martí-Vargas, and W. Micah Hale, “Mixture-proportioning of economical UHPC mixtures,” *J. Build. Eng.*, vol. 27, p. 100970, 2020, doi: https://doi.org/10.1016/j.jobe.2019.100970.

[60] S. Moula, A. Ben Fraj, T. Wattez, M. Bouasker, and N. B. Hadj Ali, “Mechanical properties, carbon footprint and cost of ultra-high performance concrete containing ground granulated blast furnace slag,” *J. Build. Eng.*, vol. 79, no. June, p. 107796, 2023, doi: 10.1016/j.jobe.2023.107796.

[61] A. Tafraoui, G. Escadeillas, and T. Vidal, “Durability of the Ultra High Performances Concrete containing metakaolin,” *Constr. Build. Mater.*, vol. 112, pp. 980–987, 2016, doi: https://doi.org/10.1016/j.conbuildmat.2016.02.169.

[62] Y. Sun, Z. Wang, Q. Gao, and C. Liu, “A new mixture design methodology based on the Packing Density Theory for high performance concrete in bridge engineering,” *Constr. Build. Mater.*, vol. 182, 2018, doi: 10.1016/j.conbuildmat.2018.06.062.

[63] S. Moula, A. Ben Fraj, T. Wattez, M. Bouasker, and N. B. Hadj Ali, “Mechanical properties, carbon footprint and cost of ultra-high performance concrete containing ground granulated blast furnace slag,” *J. Build. Eng.*, vol. 79, p. 107796, 2023, doi: https://doi.org/10.1016/j.jobe.2023.107796.

[64] H. Yazıcı, M. Y. Yardımcı, S. Aydın, and A. Ş. Karabulut, “Mechanical properties of reactive powder concrete containing mineral admixtures under different curing regimes,” *Constr. Build. Mater.*, vol. 23, no. 3, pp. 1223–1231, 2009, doi: https://doi.org/10.1016/j.conbuildmat.2008.08.003.

[65] S. Pyo and H.-K. Kim, “Fresh and hardened properties of ultra-high performance concrete incorporating coal bottom ash and slag powder,” *Constr. Build. Mater.*, vol. 131, pp. 459–466, 2017, doi: https://doi.org/10.1016/j.conbuildmat.2016.10.109.

[66] R. Yu, P. Spiesz, and H. J. H. Brouwers, “Development of an eco-friendly Ultra-High Performance Concrete (UHPC) with efficient cement and mineral admixtures uses,” *Cem. Concr. Compos.*, vol. 55, pp. 383–394, 2015, doi: https://doi.org/10.1016/j.cemconcomp.2014.09.024.

[67] Z. Liu, S. El-Tawil, W. Hansen, and F. Wang, “Effect of slag cement on the properties of ultra-high performance concrete,” *Constr. Build. Mater.*, vol. 190, pp. 830–837, 2018, doi: https://doi.org/10.1016/j.conbuildmat.2018.09.173.

[68] O. M. Abdulkareem, A. Ben Fraj, M. Bouasker, and A. Khelidj, “Mixture design and early age investigations of more sustainable UHPC,” *Constr. Build. Mater.*, vol. 163, pp. 235–246, 2018, doi: https://doi.org/10.1016/j.conbuildmat.2017.12.107.

[69] S. B. Duraman and I. G. Richardson, “Microstructure & properties of steel-reinforced concrete incorporating Portland cement and ground granulated blast furnace slag hydrated at 20 °C,” *Cem. Concr. Res.*, vol. 137, p. 106193, 2020, doi: https://doi.org/10.1016/j.cemconres.2020.106193.

[70] Ç. Yalçınkaya and O. Çopuroğlu, “Hydration heat, strength and microstructure characteristics of UHPC containing blast furnace slag,” *J. Build. Eng.*, vol. 34, p. 101915, 2021, doi: https://doi.org/10.1016/j.jobe.2020.101915.

[71] O. M. Abdulkareem, A. Ben Fraj, M. Bouasker, L. Khouchaf, and A. Khelidj, “Microstructural investigation of slag-blended UHPC: The effects of slag content and chemical/thermal activation,” *Constr. Build. Mater.*, vol. 292, p. 123455, 2021, doi:

https://doi.org/10.1016/j.conbuildmat.2021.123455.

[72] T. Ahmed, M. Elchalakani, A. Karrech, M. S. Mohamed Ali, and L. Guo, “Development of ECO-UHPC with very-low-C3A cement and ground granulated blast-furnace slag,” *Constr. Build. Mater.*, vol. 284, p. 122787, 2021, doi: https://doi.org/10.1016/j.conbuildmat.2021.122787.

[73] D. K. Ashish and S. K. Verma, “Cementing Efficiency of Flash and Rotary-Calcined Metakaolin in Concrete,” *J. Mater. Civ. Eng.*, vol. 31, no. 12, 2019, doi: 10.1061/(ASCE)MT.1943-5533.0002953.

[74] M. Sarıdemir, M. Çiflikli, and F. Soysat, “Mechanical and microstructural properties of HFRHSCs containing metakaolin subjected to elevated temperatures and freezing-thawing cycles,” *Constr. Build. Mater.*, vol. 158, pp. 11–23, 2018, doi: https://doi.org/10.1016/j.conbuildmat.2017.10.014.

[75] R. Siddique and J. Klaus, “Influence of metakaolin on the properties of mortar and concrete: A review,” *Appl. Clay Sci.*, vol. 43, no. 3–4, pp. 392–400, 2009, doi: 10.1016/j.clay.2008.11.007.

[76] E. H. Kadri, S. Kenai, K. Ezziane, R. Siddique, and G. De Schutter, “Influence of metakaolin and silica fume on the heat of hydration and compressive strength development of mortar,” *Appl. Clay Sci.*, vol. 53, no. 4, pp. 704–708, 2011, doi: 10.1016/j.clay.2011.06.008.

[77] K. G. Sobolev and S. V. Soboleva, “High-performance concrete mixture proportioning,” *Am. Concr. Institute, ACI Spec. Publ.*, vol. SP179, pp. 421–438, 1998, doi: 10.14359/6053.

[78] B. Ye, Y. Zhang, J. Han, and P. Pan, “Effect of water to binder ratio and sand to binder ratio on shrinkage and mechanical properties of High-strength Engineered Cementitious Composite,” *Constr. Build. Mater.*, vol. 226, pp. 899–909, 2019, doi: https://doi.org/10.1016/j.conbuildmat.2019.07.303.

[79] UNSTATS, “Greenhouse Gas Emissions by Sector (Absolute Values),” *United Nation Statistical Division, New York, USA.*, 2010.

[80] G. Habert and N. Roussel, “Study of two concrete mix-design strategies to reach carbon mitigation objectives,” *Cem. Concr. Compos.*, vol. 31, no. 6, pp. 397–402, 2009, doi: https://doi.org/10.1016/j.cemconcomp.2009.04.001.

[81] G. Habert, D. Arribe, T. Dehove, L. Espinasse, and R. Le Roy, “Reducing environmental impact by increasing the strength of concrete: Quantification of the improvement to concrete bridges,” *J. Clean. Prod.*, vol. 35, pp. 250–262, 2012, doi: 10.1016/j.jclepro.2012.05.028.

[82] A. Faure, “Capacité d’un sédiment à se substituer à la fraction argileuse de la matière première de l’industrie des liants hydrauliques,” 2017. [Online]. Available: http://www.theses.fr/2017LIMO0079/document

[83] A. F. de N. (AFNOR), “NF EN 197-1: Composition, spécifications et critères de conformité des ciment courant.”

[84] M. RENAUT, “Calcination des déchets industriels : synthèse de ciment et stabilisation / solidification des résidus de combustion,” vol. 072, p. 183, 2017.

[85] M. Gani, *Cement and Concrete. Londres: Chapman & Hall. 224 p. ISBN : 978-0412790508.* 1997.

[86] D. C. Chu, D. Chinh, and C. Valorisation, “Valorisation des sédiments de dragage dans l ’ industrie cimentaire To cite this version : Thèse de Doctorat,” 2022.

[87] H. F. W. Taylor, *Cement chemistry*, 3rd ed. London [U.K.] SE - xviii, 459 pages : illustrations, maps ; 25 cm: T. Telford London [U.K.], 2013. doi: LK - https://worldcat.org/title/1067143195.

[88] I. Maki and K. Goto, “Factors influencing the phase constitution of alite in portland cement clinker,” *Cem. Concr. Res.*, vol. 12, no. 3, pp. 301–308, 1982, doi: https://doi.org/10.1016/0008-8846(82)90078-3.

[89] W. Kurdowski, *Cement and Concrete chemistry*, 1st ed. Springer Dordrecht, 2016. doi: https://doi.org/10.1007/978-94-007-7945-7.

[90] N. Gineys, “Influence de la teneur en éléments métalliques sur les propriétés techniques et environnementales du ciment Portland,” 2011. [Online]. Available: http://www.theses.fr/2011LIL10111/document

[91] G. C. Bye, *Portland Cement: Composition, Production and Properties*. Thomas Telford, 1999. [Online]. Available: https://books.google.fr/books?id=6sRmAQAACAAJ

[92] R. H. Bogue and W. Lerch, “Hydration of Portland Cement Compounds,” *Ind. Eng. Chem.*, vol. 26, no. 8, pp. 837–847, Aug. 1934, doi: 10.1021/ie50296a007.

[93] E. Hewlett, Peter, and Martin Liska, *Lea’s chemistry of cement and concrete, Butterworth-Heinemann*. 2019. doi: 10.1016/C2013-0-19325-7.

[94] E. Gartner, J. Young, D. Damidot, and I. Jawed, “Hydration of Portland Cement,” 2001, pp. 57–113.

[95] J. Bullard *et al.*, “Mechanisms of Cement Hydration,” *Cem. Concr. Res.*, vol. 41, pp. 1208–1223, 2011, doi: 10.1016/j.cemconres.2010.09.011.

[96] D. Jansen, F. Goetz-Neunhoeffer, B. Lothenbach, and J. Neubauer, “The early hydration of Ordinary Portland Cement (OPC): An approach comparing measured heat flow with calculated heat flow from QXRD,” *Cem. Concr. Res.*, vol. 42, no. 1, pp. 134–138, 2012, doi: https://doi.org/10.1016/j.cemconres.2011.09.001.

[97] W. Lerch, “The Influence of Gypsum on the Hydration and Properties of Portland Cement Pastes,” 2008. [Online]. Available: https://api.semanticscholar.org/CorpusID:210731290

[98] A. BENTUR, “Effect of Gypsum on the Hydration and Strength of C3S Pastes,” *J. Am. Ceram. Soc.*, vol. 59, pp. 210–213, 2006, doi: 10.1111/j.1151-2916.1976.tb10935.x.

[99] S. Aydin Gunay (Aydin), “Influence de la cinétique d’hydratation des phases aluminates en présence de sulfate de calcium sur celles des phases silicates : conséquences sur l’optimum de sulfatage des ciments,” 2012. [Online]. Available: http://www.theses.fr/2012DIJOS007/document

[100] E. Gartner, “Industrially interesting approaches to ‘low-CO2’ cements,” *Cem. Concr. Res.*, vol. 34, no. 9, pp. 1489–1498, 2004, doi: https://doi.org/10.1016/j.cemconres.2004.01.021.

[101] J. Davidovits, “PROPERTIES OF GEOPOLYMER CEMENTS, Proceedings First,” in *International Conference on Alkaline Cements*, 1994, pp. 131–149.

[102] P. Duxson, A. Fernández-Jiménez, J. L. Provis, G. C. Lukey, A. Palomo, and J. S. J. Van Deventer, “Geopolymer technology: The current state of the art,” *J. Mater. Sci.*, vol. 42, no. 9, pp. 2917–2933, 2007, doi: 10.1007/s10853-006-0637-z.

[103] Geopolymer Institute, “Why Alkali-Activated Materials are NOT Geopolymers ? – Geopolymer Institute,” *Geopolymer Camp*, no. November, 2017, doi: 10.13140/RG.2.2.34337.25441.

[104] G. VD, “Soil silicates,” Gosstroyizdat, Kiev, 1959.

[105] C. M. C. Fernandez-Jimenez A, Palomo A, “No Title,” *Conc Res*, vol. 35:1204, 2005.

[106] A. Fernández-Jiménez, A. Palomo, I. Sobrados, and J. Sanz, “The role played by the reactive alumina content in the alkaline activation of fly ashes,” *Microporous Mesoporous Mater.*, vol. 91, no. 1, pp. 111–119, 2006, doi: https://doi.org/10.1016/j.micromeso.2005.11.015.

[107] J. L. Provis, G. C. Lukey, and J. S. J. van Deventer, “Do Geopolymers Actually Contain Nanocrystalline Zeolites? A Reexamination of Existing Results,” *Chem. Mater.*, vol. 17, no. 12, pp. 3075–3085, Jun. 2005, doi: 10.1021/cm050230i.

[108] J. Davidovits, “Geopolymers based on natural and synthetic metakaolin a critical review,” *Ceram. Eng. Sci. Proc.*, vol. 38, no. 3, pp. 201–214, 2018, doi: 10.1002/9781119474746.ch19.

[109] B. V. Rangan, “SPECIAL ISSUE -Future Concrete,” *Indian Concr. J.*, vol. 88, no. 4, pp. 41–48, 50–59, 2014, [Online]. Available: https://www.geopolymer.org/fichiers_pdf/FA-GP-Concrete.pdf

[110] J. T. Gourley, "'Geopolymers; Opportunities for Environmentally Friendly Construction Materials,'" 2003.

[111] S. E. Wallah and B. V. Rangan, "Low-calcium fly ash-based geopolymer concrete: Long-term properties," *Res. Rep. GC*, 2006, [Online]. Available: http://www.geopolymer.org/fichiers_pdf/curtin_flyash_GC-2.pdf

[112] G. B. Gourley, J. T., & Johnson, "Developments in Geopolymer Precast Concrete," 2005.

[113] J. C. Kuri, P. K. Sarker, and F. U. A. Shaikh, "Sulphuric acid resistance of ground ferronickel slag blended fly ash geopolymer mortar," *Constr. Build. Mater.*, vol. 313, no. July, p. 125505, 2021, doi: 10.1016/j.conbuildmat.2021.125505.

[114] M. Guerrieri and J. G. Sanjayan, "Behavior of combined fly ash/slag-based geopolymers when exposed to high temperatures," *Fire Mater.*, vol. 34, no. 4, pp. 163 – 175, 2010, doi: 10.1002/fam.1014.

[115] P. Kumar, C. Pankar, D. Manish, and A. S. Santhi, "Study of mechanical and microstructural properties of geopolymer concrete with GGBS and Metakaolin," *Mater. Today Proc.*, vol. 5, no. 14, pp. 28127–28135, 2018, doi: 10.1016/J.MATPR.2018.10.054.

[116] X. Yang *et al.*, "Effects of GBFS content and curing methods on the working performance and microstructure of ternary geopolymers based on high-content steel slag," *Constr. Build. Mater.*, vol. 410, no. September 2023, p. 134128, 2024, doi: 10.1016/j.conbuildmat.2023.134128.

[117] A. Saludung, Y. Ogawa, and K. Kawai, "Microstructure and mechanical properties of FA/GGBS-based geopolymer," *MATEC Web Conf.*, vol. 195, Aug. 2018, doi: 10.1051/MATECCONF/201819501013.

[118] N. Ismail and H. El-Hassan, "Development and Characterization of Fly Ash–Slag Blended Geopolymer Mortar and Lightweight Concrete," *J. Mater. Civ. Eng.*, vol. 30, no. 4, p. 5533, 2018, doi: 10.1061/(asce)mt.1943-5533.0002209.

[119] N. Poornima, D. Katyal, T. Revathi, M. Sivasakthi, and R. Jeyalakshmi, "Effect of curing

on mechanical strength and microstructure of fly ash blend GGBS geopolymer, Portland cement mortar and its behavior at elevated temperature," *Mater. Today Proc.*, vol. 47, pp. 863–870, 2021, doi: 10.1016/J.MATPR.2021.04.087.

[120] R. Zhao *et al.*, "Freeze-thaw resistance of Class F fly ash-based geopolymer concrete," *Constr. Build. Mater.*, vol. 222, pp. 474–483, 2019, doi: 10.1016/j.conbuildmat.2019.06.166.

[121] R. R. Bellum, M. Al Khazaleh, R. K. Pilla, S. Choudhary, and C. Venkatesh, "Effect of slag on strength, durability and microstructural characteristics of fly ash-based geopolymer concrete," *J. Build. Pathol. Rehabil.*, vol. 7, no. 1, p. 41024, 2022, doi: 10.1007/s41024-022-00163-4.

[122] B. Lothenbach, K. Scrivener, and R. D. Hooton, "Supplementary cementitious materials," *Cem. Concr. Res.*, vol. 41, no. 12, pp. 1244–1256, 2011, doi: 10.1016/j.cemconres.2010.12.001.

[123] F. Chupin, F. Chupin, and C. De, "Caractérisation de l ' effet des irradiations sur les géopolymères To cite this version : HAL Id : tel-01380683 Université Pierre et Marie Curie Caractérisation de l ' effet des irradiations sur les Par Frédéric Chupin," 2017.

[124] J. S. J. van Deventer, J. L. Provis, P. Duxson, and G. C. Lukey, "Reaction mechanisms in the geopolymeric conversion of inorganic waste to useful products," *J. Hazard. Mater.*, vol. 139, no. 3, pp. 506–513, 2007, doi: https://doi.org/10.1016/j.jhazmat.2006.02.044.

[125] O. M. Abdulkareem and A. Lecomte, "Microstructure and Durability Properties of Environmentally Friendly Ultra-High Performance Concrete (UHPC) JURY."

[126] P. Duxson, G. C. Lukey, and J. S. J. Van Deventer, "Physical evolution of Na-geopolymer derived from metakaolin up to 1000 °c," *J. Mater. Sci.*, vol. 42, no. 9, pp. 3044–3054, May 2007, doi: 10.1007/S10853-006-0535-4/FIGURES/12.

[127] P. Duxson, S. W. Mallicoat, G. C. Lukey, W. M. Kriven, and J. S. J. van Deventer, "The effect of alkali and Si/Al ratio on the development of mechanical properties of metakaolin-based geopolymers," *Colloids Surfaces A Physicochem. Eng. Asp.*, vol. 292, no. 1, pp. 8–

20, 2007, doi: https://doi.org/10.1016/j.colsurfa.2006.05.044.

[128] D. E. Day, “Mixed alkali glasses — Their properties and uses,” *J. Non. Cryst. Solids*, vol. 21, no. 3, pp. 343–372, 1976, doi: https://doi.org/10.1016/0022-3093(76)90026-0.

[129] S. O. Sore, A. Messan, E. Prud’Homme, G. Escadeillas, and F. Tsobnang, “Comparative Study on Geopolymer Binders Based on Two Alkaline Solutions (NaOH and KOH),” *J. Miner. Mater. Charact. Eng.*, vol. 08, no. 06, pp. 407–420, 2020, doi: 10.4236/JMMCE.2020.86026.

[130] P. Duxson, J. L. Provis, G. C. Lukey, S. W. Mallicoat, W. M. Kriven, and J. S. J. van Deventer, “Understanding the relationship between geopolymer composition, microstructure and mechanical properties,” *Colloids Surfaces A Physicochem. Eng. Asp.*, vol. 269, no. 1, pp. 47–58, 2005, doi: https://doi.org/10.1016/j.colsurfa.2005.06.060.

[131] H. Xu and J. S. J. Van Deventer, “The geopolymerisation of alumino-silicate minerals,” *Int. J. Miner. Process.*, vol. 59, no. 3, pp. 247–266, 2000, doi: https://doi.org/10.1016/S0301-7516(99)00074-5.

[132] S. Alonso and A. Palomo, “Alkaline activation of metakaolin and calcium hydroxide mixtures: influence of temperature, activator concentration and solids ratio,” *Mater. Lett.*, vol. 47, no. 1, pp. 55–62, 2001, doi: https://doi.org/10.1016/S0167-577X(00)00212-3.

[133] D. J, “Properties of Geopolymer Cements,” *First Int. Conf. Alkaline Cem. Concr.*, no. October 1994, pp. 131–149, 1994.

[134] D. Khale and R. Chaudhary, “Mechanism of geopolymerization and factors influencing its development: A review,” *J. Mater. Sci.*, vol. 42, no. 3, pp. 729–746, Feb. 2007, doi: 10.1007/S10853-006-0401-4.

[135] V. F. F. Barbosa, K. J. D. MacKenzie, and C. Thaumaturgo, “Synthesis and characterisation of materials based on inorganic polymers of alumina and silica: sodium polysialate polymers,” *Int. J. Inorg. Mater.*, vol. 2, no. 4, pp. 309–317, Sep. 2000, doi: 10.1016/S1466-6049(00)00041-6.

[136] M. Steveson and K. Sagoe-Crentsil, “Relationships between composition, structure and strength of inorganic polymers,” *J. Mater. Sci.*, vol. 40, no. 8, pp. 2023–2036, 2005, doi: 10.1007/s10853-005-1226-2.

[137] A. Palomo, M. W. Grutzeck, and M. T. Blanco, “Alkali-activated fly ashes: A cement for the future,” *Cem. Concr. Res.*, vol. 29, no. 8, pp. 1323–1329, 1999, doi: 10.1016/S0008-8846(98)00243-9.

[138] T. Bakharev, “Geopolymeric materials prepared using Class F fly ash and elevated temperature curing,” *Cem. Concr. Res.*, vol. 35, no. 6, pp. 1224–1232, 2005, doi: https://doi.org/10.1016/j.cemconres.2004.06.031.

[139] J. G. S. van Jaarsveld, J. S. J. van Deventer, and G. C. Lukey, “The effect of composition and temperature on the properties of fly ash- and kaolinite-based geopolymers,” *Chem. Eng. J.*, vol. 89, no. 1, pp. 63–73, 2002, doi: https://doi.org/10.1016/S1385-8947(02)00025-6.

[140] D. S. Perera, O. Uchida, E. R. Vance, and K. S. Finnie, “Influence of curing schedule on the integrity of geopolymers,” *J. Mater. Sci.*, vol. 42, no. 9, pp. 3099–3106, 2007, doi: 10.1007/s10853-006-0533-6.

[141] P. Rovnaník, “Effect of curing temperature on the development of hard structure of metakaolin-based geopolymer,” *Constr. Build. Mater.*, vol. 24, no. 7, pp. 1176–1183, 2010, doi: https://doi.org/10.1016/j.conbuildmat.2009.12.023.

[142] A. Fernandez-Jimenez, D. E. Macphee, E. E. Lachowski, and A. Palomo, “Immobilization of cesium in alkaline activated fly ash matrix,” *J. Nucl. Mater.*, vol. 346, no. 2, pp. 185–193, 2005, doi: https://doi.org/10.1016/j.jnucmat.2005.06.006.

[143] P. Steins *et al.*, “Effect of aging and alkali activator on the porous structure of a geopolymer,” *J. Appl. Crystallogr.*, vol. 47, no. 1, pp. 316–324, 2014, doi: 10.1107/S160057671303197X.

[144] J. Davidovits, “Global Warming Impact on the Cement and Aggregates Industries,” *World Resour. Rev.*, vol. 6, no. 2, pp. 263–278, 1994, [Online]. Available: http://www.osti.gov/energycitations/product.biblio.jsp?osti_id=6593603

[145] L. K. Turner and F. G. Collins, “Carbon dioxide equivalent (CO2-e) emissions: A comparison between geopolymer and OPC cement concrete,” *Constr. Build. Mater.*, vol. 43, pp. 125–130, 2013, doi: 10.1016/j.conbuildmat.2013.01.023.

[146] J. S. J. Van Deventer, J. L. Provis, P. Duxson, and D. G. Brice, “Chemical research and climate change as drivers in the commercial adoption of alkali activated materials,” *Waste and Biomass Valorization*, vol. 1, no. 1, pp. 145–155, 2010, doi: 10.1007/s12649-010-9015-9.

[147] P. Duxson, J. L. Provis, G. C. Lukey, and J. S. J. van Deventer, “The role of inorganic polymer technology in the development of ‘green concrete,’” *Cem. Concr. Res.*, vol. 37, no. 12, pp. 1590–1597, 2007, doi: https://doi.org/10.1016/j.cemconres.2007.08.018.

[148] J. Davidovits, “False Values on CO2 Emission for Geopolymer Cement/Concrete published In Scientific Papers,” *Geopolymer Inst. Libr. Tech. Pap.*, vol. 24, pp. 1–9, 2015, [Online]. Available: http://www.materialstoday.com/polymers-soft-materials/features/environmental-implications-of-geopolymers/,

[149] AFNOR, “NF EN 197-5, Cement- Part 5 : portland-composite cement CEM II/C-M and Composite cement CEM VI,” 2021.

[150] P. R. Suzanne Le Thierry, François Jacquemot, “RESSOURCES MINÉRALES POUR LES LIANTS DES BÉTONS DÉCARBONÉS : DISPONIBILITÉ, PERSPECTIVES D’ÉVOLUTION ET INNOVATIONS,” 2022.

[151] L. Mosser, “Formulation de bétons décarbonés à base de clinker , métakaolin et d ’ addition calcaire pour une application aux produits préfabriqués To cite this version : HAL Id : tel-04233378 THÈSE POUR OBTENIR LE GRADE DE DOCTEUR DE L ’ INSTITUT MINES -TELECOM (IM,” 2023.

[152] K. Scrivener, F. Martirena, S. Bishnoi, and S. Maity, “Calcined clay limestone cements (LC3),” *Cem. Concr. Res.*, vol. 114, pp. 49–56, 2018, doi: https://doi.org/10.1016/j.cemconres.2017.08.017.

[153] A. F. de N. (AFNOR), “Comité Européen de Normalisation, «NF P 18-508 - Additions pour

béton hydraulique - Additions calcaires - Spécifications et critères de conformité,»," 1995.

[154] S. et G. L. N. Charles, Colin, "Carbonates calciques et magnésiens - Mémento - Rapport final," 2017.

[155] CEN-CENELEC and B. Management Centre, "Comité Européen de Normalisation, «EN 12620 Granulats pour béton»," 2017.

[156] A. Française and L. P. S.-D. de Normalisation (AFNOR), "Comité Européen de Normalisation, NF EN 206/CN - Béton - Spécification, Performance 206, production et conformité - Complément national à la norme NF EN 206," 2014.

[157] A. F. De and N. (AFNOR), "Comité Européen de Normalisation, «NF P 18-508 - Additions pour béton hydraulique - Additions calcaires - Spécifications et critères de conformité,»," 1995.

[158] L. G. Charles N., Colin S., Gutierrez T., "Kaolin et argiles kaoliniques Mémento Rapport final," -*Mémento*, no. May, pp. 17–93, 2018.

[159] A. Léonard, B. Delmon, and J. Lemaitre, "Le mécanisme de la transformation thermique de la métakaolinite," 1982. [Online]. Available: https://www.persee.fr/doc/bulmi_0180-9210_1982_act_105_5_7572

[160] M. Murat and A. Bachiorrini, "Corrélation entre l'état d'amorphisation et l'hydraulicité du métakaolin," 1982. [Online]. Available: https://www.persee.fr/doc/bulmi_0180-9210_1982_act_105_5_7577

[161] F. Cassagnabère, P. Diederich, M. Mouret, G. Escadeillas, and M. Lachemi, "Impact of metakaolin characteristics on the rheological properties of mortar in the fresh state," *Cem. Concr. Compos.*, vol. 37, pp. 95–107, 2013, doi: https://doi.org/10.1016/j.cemconcomp.2012.12.001.

[162] AFNOR, "NF P 18-513- Additions pour béton hydraulique- Métakaolin." 2012.

[163] T. Muzenda, S. Kawashima, T. Sui, and X. Cheng, "The role of limestone and calcined clay

on the rheological properties of LC3," *Cem. Concr. Compos.*, vol. 107, p. 103516, 2020, doi: 10.1016/j.cemconcomp.2020.103516.

[164] M. Thakur and S. Bawa, "Self-Compacting geopolymer Concrete: A review," *Mater. Today Proc.*, vol. 59, pp. 1683–1693, 2022, doi: 10.1016/j.matpr.2022.03.400.

[165] F. Avet and K. Scrivener, "Study of Concrete Made of Limestone Calcined Clay Cements (LC3)," 2020, pp. 257–261. doi: 10.1007/978-981-15-2806-4_29.

[166] N. Nair, M. Kolakkadan, M. Santhanam, and R. Gettu, "A study on fresh properties of limestone calcined clay blended cementitious systems," *Constr. Build. Mater.*, vol. 254, p. 119326, 2020, doi: 10.1016/j.conbuildmat.2020.119326.

[167] S. Ferreiro, D. Herfort, and J. S. Damtoft, "Effect of raw clay type, fineness, water-to-cement ratio and fly ash addition on workability and strength performance of calcined clay – Limestone Portland cements," *Cem. Concr. Res.*, vol. 101, no. August, pp. 1–12, 2017, doi: 10.1016/j.cemconres.2017.08.003.

[168] M. Antoni, J. Rossen, F. Martirena, and K. Scrivener, "Cement substitution by a combination of metakaolin and limestone," *Cem. Concr. Res.*, vol. 42, no. 12, pp. 1579–1589, 2012, doi: 10.1016/j.cemconres.2012.09.006.

[169] Y. Dhandapani, S. T., M. Santhanam, R. Gettu, and R. Pillai, "Mechanical properties and durability performance of concretes with Limestone Calcined Clay Cement (LC3)," *Cem. Concr. Res.*, vol. 107, pp. 136–151, 2018, doi: 10.1016/j.cemconres.2018.02.005.

[170] Y. Mamindy-Pajany, "Traitement de sédiments portuaires méditerranéens contaminés en arsenic et en métaux : géochimie et écotoxicologie," 2010. [Online]. Available: http://www.theses.fr/2010NICE4060

[171] H. Oh, J. Lee, N. Banthia, and S. Talukdar, "An Experimental Study of the Physicochemical Properties of a Cement Matrix Containing Dredged Materials," *Mater. Sci. Appl.*, vol. 02, no. 07, pp. 847–857, 2011, doi: 10.4236/msa.2011.27115.

[172] "Present Situation of Dredged Materials Dumping and the Study of Transforming Dredged

Mud into Regenerative Resources."

[173] R. Zentar, H. Wang, and D. Wang, "Comparative study of stabilization/solidification of dredged sediments with ordinary Portland cement and calcium sulfo-aluminate cement in the framework of valorization in road construction material," *Constr. Build. Mater.*, vol. 279, Apr. 2021, doi: 10.1016/j.conbuildmat.2021.122447.

[174] Y. Z. D.-S. Xu, M. Huang, "One-Dimensional Compression Behavior of Calcareous Sand and Marine Clay Mixtures," *Int. J. Geomech.*, vol. 20 (9), 2020.

[175] M. Amar, M. Benzerzour, and N. E. Abriak, "Designing Efficient Flash-Calcined Sediment-Based Ecobinders.," *Mater. (Basel, Switzerland)*, vol. 15, no. 20, pp. 7107–7107, Oct. 2022, doi: 10.3390/MA15207107.

[176] M. Brahim, "Valorisation des sédiments de dragage dans la fabrication de blocs de terre comprimée stabilisée par des liants géopolymères," 2022. [Online]. Available: http://www.theses.fr/2022CYUN1135/document

[177] D. Université *et al.*, "Thèse de doctorat Thèse de doctorat," no. Paris VI, 2006.

[178] C. Julien, "Gestion d'un sédiment de dragage marin contaminé : Caractérisation de la réactivité biogéochimique, valorisation en mortier et évaluation environnementale," p. 248, 2016, [Online]. Available: https://tel.archives-ouvertes.fr/tel-01368438

[179] Cerema, "Marine and river sediment sampling," *Cerema*, 2018.

[180] G. Schneider, "Boue de curage des cours d'eau.," *Le Courr. l'environnement l'INRA.*, 2001.

[181] J. . « Beauchamp, "Sédiments et roches sédimentaires, cours de sédimentologie".

[182] K. Hamer and V. Karius, "Brick production with dredged harbour sediments. An industrial-scale experiment," *Waste Manag.*, vol. 22, no. 5, pp. 521–530, 2002, doi: 10.1016/S0956-053X(01)00048-4.

[183] M. Ali, M. Seeger, G. Sterk, and D. Moore, "A unit stream power based sediment transport function for overland flow," *CATENA*, vol. 101, pp. 197–204, 2013, doi:

https://doi.org/10.1016/j.catena.2012.09.006.

[184] M. A. A. Amar, “Traitement des sédiments de dragage pour une valorisation dans les matrices cimentaires,” 2017. [Online]. Available: https://api.semanticscholar.org/CorpusID:133701221

[185] A. D. E. L. A. PICARDIE, *Méthodes de gestion et de réutilisation des sédiments pollués*. AGENCE DE L’EAU ARTOIS-PICARDIE CN - 4306. [Online]. Available: https://side.developpement-durable.gouv.fr/GUAD/doc/SYRACUSE/81554/methodes-de-gestion-et-de-reutilisation-des-sediments-pollues

[186] I. Ujević, N. Odžak, and A. Barić, “Trace metal accumulation in different grain size fractions of the sediments from a semi-enclosed bay heavily contaminated by urban and industrial wastewaters,” *Water Res.*, vol. 34, no. 11, pp. 3055–3061, 2000, doi: https://doi.org/10.1016/S0043-1354(99)00376-0.

[187] J.-G. Lin and S.-Y. Chen, “The relationship between adsorption of heavy metal and organic matter in river sediments,” *Environ. Int.*, vol. 24, no. 3, pp. 345–352, 1998, doi: https://doi.org/10.1016/S0160-4120(98)00012-9.

[188] A. Gosselin, *Protocole d’évaluation de la traitabilité des sediments, des sols et des boues à l’aide des technologies minéralurgiques*. 1999. [Online]. Available: http://publications.gc.ca/collections/Collection/En40-542-5-1997F.pdf

[189] F. Marot, “Caractérisation et traitement de sédiments de dragage contenant des polluants métalliques,” 1997. [Online]. Available: http://www.theses.fr/1997LEHA0009

[190] M. Loustau Cazalet, “Caractérisation physico-chimique d’un sédiment marin traité aux liants hydrauliques : Évaluation de la mobilité potentielle des polluants inorganiques,” 2012. [Online]. Available: http://www.theses.fr/2012ISAL0012/document

[191] S. M. Nedrich and G. A. Burton, “Sediment Zn-release during post-drought re-flooding: Assessing environmental risk to Hyalella azteca and Daphnia magna,” *Environ. Pollut.*, vol. 230, pp. 1116–1124, 2017, doi: 10.1016/j.envpol.2017.07.073.

[192] D. Grosdemange, “Guide pour la gestion des opérations de dragage,” *Fédération Française des Ports Plaisance*, pp. 1–83, 2005.

[193] P. Hlaváčková, “Evaluation du comportement du cuivre et du zinc dans une matrice de type sol à l’aide de différentes méthodologies,” 2005. [Online]. Available: http://www.theses.fr/2005ISAL0066/document

[194] C. Alzieu, “Dragages et environnement marin,” *Rapp. IFREMER*, p. 223, 1999.

[195] F. Mac FARLANE, “Methodologie de gestion des materiaux de dragage maritime-Application au Port Autonome de Dunkerque,” Universite d’ Artois, 2004.

[196] O. Geffard, “Potential Toxicity of Contaminated Marine and Estuarine Sediments: Chemical and Biological Assessment, Bioavailability of Sediment Contaminants,” Bordeaux 1, 2001. [Online]. Available: https://archimer.ifremer.fr/doc/00000/1482/

[197] ouedragogo Celia, “La contamination chimique des espèces halieutiques marines,” pp. 1–46, 2020.

[198] T. Minister *et al.*, “Order of December 12 , 2014 relating to the conditions for admitting inert waste into installations falling under headings 2515 , 2516 , 2517 and into inert waste storage facilities falling under heading 2760 of the nomenclature of classified installation,” pp. 5–9, 2024, [Online]. Available: https://www.legifrance.gouv.fr/loda/id/JORFTEXT000029893828/

[199] Y. B. Pierre MISKO, Didier GROSDEMANGE, “Guide pour la gestion durable des déblais de dragage ... - In Vivo,” *Yumpu.com*, 2021. https://www.yumpu.com/fr/document/read/17376012/guide-pour-la-gestion-durable-des-deblais-de-dragage-in-vivo

[200] S. Murphy, W F., Ward, W P., Boyd, B., Fleming, G., Nolen-Hoeksema, R., Tetrault, I., Art, M., Rosales-R, D A., Baker, B., Sulayman, J A., & Weinberg, SMurphy, W F., Ward, W P., Boyd, B., Fleming, G., Nolen-Hoeksema, R., Tetrault, I., Art, M., Rosales-R, D A, “Geophysics and Dredging in the Giant New York Harbor Deepening Project,” in *Building on the Past, Respecting the Future*, 2010. [Online]. Available:

https://doi.org/10.1061/41098(368)79

[201] N. R. Council, *Sedimentation Control to Reduce Maintenance Dredging of Navigational Facilities in Estuaries: Report and Symposium Proceedings*. Washington, DC: The National Academies Press, 1987. doi: 10.17226/1023.

[202] H. Q. Zhang, J. Xie, W.Zhu, Y. Z. Huang, and P. Shi, "Present Situation of Dredged Materials Dumping and the Study of Transforming Dredged Mud into Regenerative Resources," *Mar. Sci. Bull.*, vol. 23, no. 6, pp. 54–60, 2004.

[203] Z. Lafhaj, M. Samara, F. Agostini, L. Boucard, F. Skoczylas, and G. Depelsenaire, "Polluted river sediments from the North region of France: Treatment with Novosol® process and valorization in clay bricks," *Constr. Build. Mater.*, vol. 22, no. 5, pp. 755–762, 2008, doi: 10.1016/j.conbuildmat.2007.01.023.

[204] C. Van Bunderen, F. Benboudjema, R. Snellings, L. Vandewalle, and Ö. Cizer, "Experimental analysis and modelling of mechanical properties and shrinkage of concrete recycling flash calcined dredging sediments," *Cem. Concr. Compos.*, vol. 115, no. September 2019, 2021, doi: 10.1016/j.cemconcomp.2020.103787.

[205] C. Van Bunderen, R. Snellings, L. Vandewalle, and Ö. Cizer, "Early-age hydration and autogenous deformation of cement paste containing flash calcined dredging sediments," *Constr. Build. Mater.*, vol. 200, pp. 104–115, 2019, doi: 10.1016/j.conbuildmat.2018.12.090.

[206] D. E. F. S. Ecobinders, "Designing Efficient Flash-Calcined Sediment-Based Ecobinders," 2022.

[207] N.-E. A. Amar, Mouhamadou, Mahfoud Benzerzour, "Designing Efficient Flash-Calcined Sediment-Based Ecobinders," *Materials (Basel).*, 2022.

[208] L. Monteiro, A. Feraille, J. Saliba, H. yanez-Godoy, and N. Saiyouri, "Life cycle analysis of sediment valorization by means of geopolymerization from laboratory to industrial scale," *Constr. Build. Mater.*, vol. 411, p. 134598, 2024, doi: https://doi.org/10.1016/j.conbuildmat.2023.134598.

[209] L. N. Assi, K. Carter, E. Deaver, and P. Ziehl, “Review of availability of source materials for geopolymer/sustainable concrete,” *J. Clean. Prod.*, vol. 263, p. 121477, 2020, doi: https://doi.org/10.1016/j.jclepro.2020.121477.

[210] S. Maitenaz, “Optimisation and Digital Fabrication of Concrete Structures,” 2022. [Online]. Available: http://www.theses.fr/2022ENPC0021/document

[211] T. Hemalatha and A. Ramaswamy, “A review on fly ash characteristics – Towards promoting high volume utilization in developing sustainable concrete,” *J. Clean. Prod.*, vol. 147, pp. 546–559, 2017, doi: 10.1016/j.jclepro.2017.01.114.

[212] M. Amran, S. Debbarma, and T. Ozbakkaloglu, “Fly ash-based eco-friendly geopolymer concrete: A critical review of the long-term durability properties,” *Constr. Build. Mater.*, vol. 270, p. 121857, 2021, doi: 10.1016/j.conbuildmat.2020.121857.

[213] P. Nuaklong, P. Jongvivatsakul, T. Pothisiri, V. Sata, and P. Chindaprasirt, “Influence of rice husk ash on mechanical properties and fire resistance of recycled aggregate high-calcium fly ash geopolymer concrete,” *J. Clean. Prod.*, vol. 252, p. 119797, 2020, doi: 10.1016/j.jclepro.2019.119797.

[214] P. Chindaprasirt, P. De Silva, K. Sagoe-Crentsil, and S. Hanjitsuwan, “Effect of SiO 2 and Al 2O 3on the setting and hardening of high calcium fly ash-based geopolymer systems,” *J. Mater. Sci.*, vol. 47, no. 12, pp. 4876–4883, 2012, doi: 10.1007/s10853-012-6353-y.

[215] S. Lirer, B. Liguori, I. Capasso, A. Flora, and D. Caputo, “Mechanical and chemical properties of composite materials made of dredged sediments in a fly-ash based geopolymer,” *J. Environ. Manage.*, vol. 191, pp. 1–7, 2017, doi: https://doi.org/10.1016/j.jenvman.2017.01.001.

[216] E. Mahfoud, W. Maherzi, K. Ndiaye, M. Benzerzour, S. Aggoun, and N.-E. Abriak, “Mechanical and microstructural properties of just add water geopolymer cement comprised of Thermo-Mechanicalsynthesis Sediments-Fly ash mix,” *Constr. Build. Mater.*, vol. 400, p. 132626, 2023, doi: https://doi.org/10.1016/j.conbuildmat.2023.132626.

[217] R. Achour, R. Zentar, N.-E. Abriak, P. Rivard, and P. Gregoire, “Durability study of

concrete incorporating dredged sediments," *Case Stud. Constr. Mater.*, vol. 11, p. e00244, 2019, doi: https://doi.org/10.1016/j.cscm.2019.e00244.

[218] Z. Zhao, M. Benzerzour, N.-E. Abriak, D. Damidot, L. Courard, and D. Wang, "Use of uncontaminated marine sediments in mortar and concrete by partial substitution of cement," *Cem. Concr. Compos.*, vol. 93, pp. 155–162, 2018, doi: 10.1016/j.cemconcomp.2018.07.010.

[219] J. Limeira, L. Agullo, and M. Etxeberria, "Dredged marine sand in concrete: An experimental section of a harbor pavement," *Constr. Build. Mater.*, vol. 24, no. 6, pp. 863–870, 2010, doi: https://doi.org/10.1016/j.conbuildmat.2009.12.011.

[220] P. Ozer-Erdogan, H. M. Basar, I. Erden, and L. Tolun, "Beneficial use of marine dredged materials as a fine aggregate in ready-mixed concrete: Turkey example," *Constr. Build. Mater.*, vol. 124, pp. 690–704, 2016, doi: https://doi.org/10.1016/j.conbuildmat.2016.07.144.

[221] W. Maherzi, I. Ennahal, M. Benzerzour, Y. Mammindy-Pajany, and N.-E. Abriak, "Study of the polymer mortar based on dredged sediments and epoxy resin: Effect of the sediments on the behavior of the polymer mortar," *Powder Technol.*, vol. 361, pp. 968–982, 2020, doi: https://doi.org/10.1016/j.powtec.2019.10.104.

[222] Y. Xu, C. Yan, B. Xu, X. Ruan, and Z. Wei, "The use of urban river sediments as a primary raw material in the production of highly insulating brick," *Ceram. Int.*, vol. 40, no. 6, pp. 8833–8840, 2014, doi: https://doi.org/10.1016/j.ceramint.2014.01.105.

[223] J. X. Liu, R. Hai, and L. Zhang, "Modification of yellow river sediment based stabilized earth bricks," *Kem. u Ind. Chem. Chem. Eng.*, vol. 65, no. 11–12, pp. 613–618, 2016, doi: 10.15255/KUI.2016.023.

[224] N. Junakova and J. Junak, "Sustainable Use of Reservoir Sediment through Partial Application in Building Material," *Sustainability*, vol. 9, no. 5, 2017, doi: 10.3390/su9050852.

[225] C.-W. Tang, H.-J. Chen, S.-Y. Wang, and J. Spaulding, "Production of synthetic lightweight

aggregate using reservoir sediments for concrete and masonry," *Cem. Concr. Compos.*, vol. 33, no. 2, pp. 292–300, 2011, doi: https://doi.org/10.1016/j.cemconcomp.2010.10.008.

[226] E. Ilyas, W. MAHERZI, M. Benzerzour, Y. Mamindy-Pajany, and N.-E. Abriak, "Performance of Lightweight Aggregates Comprised of Sediments and Thermoplastic Waste," *Waste and Biomass Valorization*, vol. 12, 2021, doi: 10.1007/s12649-020-00970-1.

[227] V. Mymrin *et al.*, "Utilization of sediments dredged from marine ports as a principal component of composite material," *J. Clean. Prod.*, vol. 142, pp. 4041–4049, 2017, doi: https://doi.org/10.1016/j.jclepro.2016.10.035.

[228] A. Mezencevova, N. N. Yeboah, S. E. Burns, L. F. Kahn, and K. E. Kurtis, "Utilization of Savannah Harbor river sediment as the primary raw material in production of fired brick," *J. Environ. Manage.*, vol. 113, pp. 128–136, 2012, doi: https://doi.org/10.1016/j.jenvman.2012.08.030.

[229] K. Komnitsas, "Co-valorization of marine sediments and construction & demolition wastes through alkali activation," *J. Environ. Chem. Eng.*, vol. 4, no. 4, Part A, pp. 4661–4669, 2016, doi: https://doi.org/10.1016/j.jece.2016.11.003.

[230] Y.-L. Wei, P.-J. Kuo, Y.-Z. Yin, Y.-T. Huang, T.-H. Chung, and X.-Q. Xie, "Co-sintering oyster shell with hazardous steel fly ash and harbor sediment into construction materials," *Constr. Build. Mater.*, vol. 172, pp. 224–232, 2018, doi: 10.1016/j.conbuildmat.2018.03.242.

[231] A. El Khomsi, "Préparation de géopolymères à partir de quelques types d'argiles Marocaines, étude, faisabilité et tests de revêtements," 2021. [Online]. Available: http://www.theses.fr/2021LIMO0096

[232] S. W. Bailey, "Summary of recommendations of AIPEA nomenclature committee," *Clay Miner.*, vol. 15, no. 1, pp. 85–93, 1980, doi: 10.1180/claymin.1980.015.1.07.

[233] G. Cardinaud, "Liants ternaires à base d'argile calcinée : Etude des mécanismes de structuration, optimisation mécanique et durabilité," 2021. [Online]. Available:

http://www.theses.fr/2021ECDN0018/document

[234] E. Gianni, K. Avgoustakis, and D. Papoulis, “Kaolinite group minerals: Applications in cancer diagnosis and treatment,” *Eur. J. Pharm. Biopharm.*, vol. 154, pp. 359–376, 2020, doi: https://doi.org/10.1016/j.ejpb.2020.07.030.

[235] J. S. Moya, B. Cabal, S. Lopez-Esteban, J. F. Bartolomé, and J. Sanz, “Significance of the formation of pentahedral aluminum in the reactivity of calcined kaolin/metakaolin and its applications,” *Ceram. Int.*, vol. 50, no. 1, Part B, pp. 1329–1340, 2024, doi: https://doi.org/10.1016/j.ceramint.2023.10.304.

[236] P. A. Alaba, Y. M. Sani, and W. M. Ashri Wan Daud, “Kaolinite properties and advances for solid acid and basic catalyst synthesis,” *RSC Adv.*, vol. 5, no. 122, pp. 101127–101147, 2015, doi: 10.1039/C5RA18884A.

[237] M. Bartolomé, “Panorámica general de la investigación sobre educación intercultural en Europa,” *Rev. Investig. Educ.*, vol. 15, no. 1, pp. 7 – 30, 1997, [Online]. Available: https://www.scopus.com/inward/record.uri?eid=2-s2.0-79954837219&partnerID=40&md5=a6862c2511f85acd01763e7a228a34bc

[238] M. M. H. Suzanne Christine Aboudi Mana and A. J. K. Chowdhury, “Environmental characteristics of clay and clay-based minerals,” *Geol. Ecol. Landscapes*, vol. 1, no. 3, pp. 155–161, 2017, doi: 10.1080/24749508.2017.1361128.

[239] P. Wei, S. Zhou, Y. Y. Zheng, Z. Y. Yin, and W. Xu, “Nanoscale Stick-Slip Behavior and Hydration of Hydrated Illite Clay,” *Comput. Geotech.*, vol. 166, no. December 2023, p. 105976, 2024, doi: 10.1016/j.compgeo.2023.105976.

[240] J. Sanz, A. Madani, J. Serratosa, J. Moya, and P. De Aza, “Aluminum-27 and Silicon-29 Magic-Angle Spinning Nuclear Magnetic Resonance Study of the Kaolinite-Mullite Transformation,” *J. Am. Ceram. Soc.*, vol. 71, pp. C418–C421, 2005, doi: 10.1111/j.1151-2916.1988.tb07513.x.

[241] J. Rocha and J. Klinowski, “29Si and 27Al magic-angle-spinning NMR studies of the thermal transformation of kaolinite,” *Phys. Chem. Miner.*, vol. 17, pp. 179–186, 1990, doi:

10.1007/BF00199671.

[242] A. Shvarzman, K. Kovler, G. S. Grader, and G. E. Shter, “The effect of dehydroxylation/amorphization degree on pozzolanic activity of kaolinite,” *Cem. Concr. Res.*, vol. 33, no. 3, pp. 405–416, 2003, doi: https://doi.org/10.1016/S0008-8846(02)00975-4.

[243] F. H. Avet, “Investigation of the grade of calcined clays used as clinker substitute in Limestone Calcined Clay Cement (LC3),” p. 169, 2017, doi: https://doi.org/10.5075/epfl-thesis-8143.

[244] K. L. Konan, C. Peyratout, A. Smith, J.-P. Bonnet, S. Rossignol, and S. Oyetola, “Comparison of surface properties between kaolin and metakaolin in concentrated lime solutions,” *J. Colloid Interface Sci.*, vol. 339, no. 1, pp. 103–109, 2009, doi: https://doi.org/10.1016/j.jcis.2009.07.019.

[245] G. BRINDLEY and M. NAKAHIRA, “The Kaolinite-Mullite Reaction Series: II, Metakaolin,” *J. Am. Ceram. Soc.*, vol. 42, pp. 314–318, 2006, doi: 10.1111/j.1151-2916.1959.tb14315.x.

[246] A. Gualtieri and S. Ferrari, “Kinetics of Illite Dehydroxylation,” *Phys. Chem. Miner.*, vol. 33, pp. 490–501, 2006, doi: 10.1007/s00269-006-0092-z.

[247] C. He, E. Makovicky, and B. Osbæck, “Thermal stability and pozzolanic activity of raw and calcined mixed-layer mica/smectite,” *Appl. Clay Sci. - APPL CLAY SCI*, vol. 17, pp. 141–161, 2000, doi: 10.1016/S0169-1317(00)00011-9.

[248] A. Alujas, R. Fernández, R. Quintana, K. L. Scrivener, and F. Martirena, “Pozzolanic reactivity of low grade kaolinitic clays: Influence of calcination temperature and impact of calcination products on OPC hydration,” *Appl. Clay Sci.*, vol. 108, pp. 94–101, 2015, doi: https://doi.org/10.1016/j.clay.2015.01.028.

[249] R. Fernandez, F. Martirena, and K. L. Scrivener, “The origin of the pozzolanic activity of calcined clay minerals: A comparison between kaolinite, illite and montmorillonite,” *Cem. Concr. Res.*, vol. 41, no. 1, pp. 113–122, Jan. 2011, doi: 10.1016/j.cemconres.2010.09.013.

[250] “Bilan des émissions de gaz à effet de serre de la Société du Grand Paris et du Grand Paris Express,” 2021.

[251] J. Davidovits, “Geopolymers Based on Natural and Synthetic Metakaolin a Critical Review: Ceramic Engineering and Science Proceedings, Volume 38, Issue 3,” 2018, pp. 201–214. doi: 10.1002/9781119474746.ch19.

[252] Y. Ettahiri *et al.*, “Comparative study of physicochemical properties of geopolymers prepared by four Moroccan natural clays,” *J. Build. Eng.*, vol. 80, p. 108021, 2023, doi: https://doi.org/10.1016/j.jobe.2023.108021.

[253] A. S. Bature, M. Khorami, E. Ganjian, and M. Tyrer, “Influence of alkali activator type and proportion on strength performance of calcined clay geopolymer mortar,” *Constr. Build. Mater.*, vol. 267, p. 120446, 2021, doi: https://doi.org/10.1016/j.conbuildmat.2020.120446.

[254] R. Lopez, “Calcined clayey soils as a potential replacement for cement in developing countries,” 2009, doi: 10.5075/epfl-thesis-4302.

[255] F. Avet and K. Scrivener, “Investigation of the calcined kaolinite content on the hydration of Limestone Calcined Clay Cement (LC3),” *Cem. Concr. Res.*, vol. 107, pp. 124–135, 2018, doi: https://doi.org/10.1016/j.cemconres.2018.02.016.

[256] J. Ambroise, S. Maximilien, and J. Pera, “Properties of Metakaolin blended cements,” *Adv. Cem. Based Mater.*, vol. 1, no. 4, pp. 161–168, 1994, doi: https://doi.org/10.1016/1065-7355(94)90007-8.

[257] F. Cassagnabère, M. Mouret, G. Escadeillas, P. Broilliard, and A. Bertrand, “Metakaolin, a solution for the precast industry to limit the clinker content in concrete: Mechanical aspects,” *Constr. Build. Mater.*, vol. 24, no. 7, pp. 1109–1118, 2010, doi: https://doi.org/10.1016/j.conbuildmat.2009.12.032.

[258] M. Antoni, J. Rossen, F. Martirena, and K. Scrivener, “Cement substitution by a combination of metakaolin and limestone,” *Cem. Concr. Res.*, vol. 42, no. 12, pp. 1579–1589, 2012, doi: https://doi.org/10.1016/j.cemconres.2012.09.006.

[259] S. Barbhuiya, J. Nepal, and B. B. Das, “Properties, compatibility, environmental benefits and future directions of limestone calcined clay cement (LC3) concrete: A review,” *J. Build. Eng.*, vol. 79, p. 107794, 2023, doi: https://doi.org/10.1016/j.jobe.2023.107794.

[260] F. Avet and K. Scrivener, “Influence of pH on the chloride binding capacity of Limestone Calcined Clay Cements (LC3),” *Cem. Concr. Res.*, vol. 131, p. 106031, 2020, doi: https://doi.org/10.1016/j.cemconres.2020.106031.

[261] W. Agency, “Method of management and reuse of polluted sediments - detailed inventory of cleaning techniques, transport, treatment and use of sediments,” 2002. [Online]. Available: http://www.eauartois-picardie.fr/.

[262] R. San Nicolas, “Approche performantielle des bétons avec métakaolins obtenus par calcination flash,” 2011. [Online]. Available: http://www.theses.fr/2011TOU30148/document

[263] AFNOR, “prEN 17685-1, Earthworks- Chemical tests- Part 1: Determination of organic matter content by loss on ignition,” 2021.

[264] M. S. Sullivan, M. G. Chorzepa, H. Hamid, S. A. Durham, and S. S. Kim, “Sustainable Materials for Transportation Infrastructures: Comparison of Three Commercially-Available Metakaolin Products in Binary Cementitious Systems,” *Infrastructures*, vol. 3, no. 3, 2018, doi: 10.3390/infrastructures3030017.

[265] B. George, P. Pantazopoulou, S. Tsivilis, and E. Badogiannis, “The effect of metakaolin on the corrosion behavior of cement mortars,” *Cem. Concr. Compos.*, vol. 27, pp. 125–130, 2005, doi: 10.1016/j.cemconcomp.2004.02.041.

[266] E. Badogiannis, G. Kakali, G. Dimopoulou, E. Chaniotakis, and S. Tsivilis, “Metakaolin as a main cement constituent. Exploitation of poor Greek kaolins,” *Cem. Concr. Compos.*, vol. 27, no. 2, pp. 197–203, 2005, doi: https://doi.org/10.1016/j.cemconcomp.2004.02.007.

[267] D. C. Chu *et al.*, “The Pozzolanic Activity of Sediments Treated by the Flash Calcination Method,” *Waste and Biomass Valorization*, vol. 13, no. 12, pp. 4963–4982, 2022, doi: 10.1007/s12649-022-01789-8.

[268] R. Snellings *et al.*, "Properties and pozzolanic reactivity of flash calcined dredging sediments," *Appl. Clay Sci.*, vol. 129, pp. 35–39, 2016, doi: 10.1016/j.clay.2016.04.019.

[269] N. Essaidi, B. Samet, S. Baklouti, and S. Rossignol, "Effect of calcination temperature of tunisian clays on the properties of geopolymers," *Ceram. - Silikaty*, vol. 57, no. 3, pp. 251–257, 2013.

[270] A. Nmiri, N. Hamdi, O. Yazoghli-Marzouk, M. Duc, and E. Srasra, "Synthesis and characterization of kaolinite-based geopolymer: Alkaline activation effect on calcined kaolinitic clay at different temperatures," *J. Mater. Environ. Sci.*, vol. 8, no. 2, pp. 276–290, 2017.

[271] AFNOR, "NF P18-545, Granulats - Éléments de définition, conformité et codification," 2011.

[272] AFNOR, "NF P94-050 'Sols : reconnaissance et essais - Détermination de la teneur en eau pondérale des sols - Méthode par étuvage'.," 1991.

[273] AFNOR, "NF EN 1097-7 'Essais pour déterminer les caractéristiques mécaniques et physiques des granulats - Partie 7 : détermination de la masse volumique absolue du filler - Méthode au pycnomètre,'" 2008.

[274] AFNOR, "NF ISO 9277 'Détermination de l'aire massique (surface spécifique) des solides par adsorption de gaz à l'aide de la méthode BET,'" 1996.

[275] F. Hamouche and R. Zentar, "Effects of Organic Matter on Physical Properties of Dredged Marine Sediments," *Waste and Biomass Valorization*, vol. 11, 2020, doi: 10.1007/s12649-018-0387-6.

[276] F. Zander, T. Heimovaara, and J. Gebert, "Spatial variability of organic matter degradability in tidal Elbe sediments," *J. Soils Sediments*, vol. 20, 2020, doi: 10.1007/s11368-020-02569-4.

[277] H. Beddaa, I. Ouazi, A. Ben Fraj, F. Lavergne, and J. M. Torrenti, "Reuse potential of dredged river sediments in concrete: Effect of sediment variability," *J. Clean. Prod.*, vol.

265, p. 121665, Aug. 2020, doi: 10.1016/J.JCLEPRO.2020.121665.

[278] AFNOR, “NF EN 15169:12 ‘Caractérisation des déchets - Détermination de la perte au feu des déchets, des boues et des sédiments’.,” 2007.

[279] V. Nozahic, “Vers une nouvelle démarche de conception des bétons de végétaux lignocellulosiques basée sur la compréhension et l’amélioration de l’interface liant / végétal : application à des granulats de chenevotte et de tige de tournesol associés à un liant ponce / ,” 2012, [Online]. Available: http://tel.archives-ouvertes.fr/tel-00822142

[280] E. Yaşar, Y. Erdogan, and A. Kiliç, “Effect of limestone aggregate type and water-cement ratio on concrete strength,” *Mater. Lett.*, vol. 58, no. 5, pp. 772–777, 2004, doi: 10.1016/j.matlet.2003.06.004.

[281] J. Ramaroson, J. L. Dirion, A. Nzihou, and G. Depelsenaire, “Characterization and kinetics of surface area reduction during the calcination of dredged sediments,” *Powder Technol.*, vol. 190, no. 1–2, pp. 59–64, 2009, doi: 10.1016/j.powtec.2008.04.094.

[282] D. R. Vollet, J. D. Macedo, and Y. P. Mascarenhas, “Pore structure characterization of kaolin, metakaolin, and their acid-treated products using small-angle X-ray scattering,” *Appl. Clay Sci.*, vol. 8, no. 6, pp. 397–404, 1994, doi: 10.1016/0169-1317(94)90035-3.

[283] R. San Nicolas, M. Cyr, and G. Escadeillas, “Characteristics and applications of flash metakaolins,” *Appl. Clay Sci.*, vol. 83–84, pp. 253–262, 2013, doi: 10.1016/j.clay.2013.08.036.

[284] H. Du and S. D. Pang, “High-performance concrete incorporating calcined kaolin clay and limestone as cement substitute,” *Constr. Build. Mater.*, vol. 264, Dec. 2020, doi: 10.1016/j.conbuildmat.2020.120152.

[285] N. S. Msinjili, G. J. G. Gluth, P. Sturm, N. Vogler, and H.-C. Kühne, “Comparison of calcined illitic clays (brick clays) and low-grade kaolinitic clays as supplementary cementitious materials,” *Mater. Struct.*, vol. 52, no. 5, p. 94, 2019, doi: 10.1617/s11527-019-1393-2.

[286] A. Teklay, C. Yin, and L. Rosendahl, “Flash calcination of kaolinite rich clay and impact of process conditions on the quality of the calcines: A way to reduce CO2 footprint from cement industry,” *Appl. Energy*, vol. 162, pp. 1218–1224, 2016, doi: 10.1016/j.apenergy.2015.04.127.

[287] S. Ferreiro, D. Herfort, and J. S. Damtoft, “Effect of raw clay type, fineness, water-to-cement ratio and fly ash addition on workability and strength performance of calcined clay – Limestone Portland cements,” *Cem. Concr. Res.*, vol. 101, 2017, doi: 10.1016/j.cemconres.2017.08.003.

[288] M. Claverie *et al.*, “Structural and chemical changes in kaolinite caused by flash calcination: Formation of spherical particles,” *Appl. Clay Sci.*, vol. 114, pp. 247–255, 2015, doi: 10.1016/j.clay.2015.05.031.

[289] S. Ferreiro, M. M. C. Canut, J. Lund, and D. Herfort, “Influence of fineness of raw clay and calcination temperature on the performance of calcined clay-limestone blended cements,” *Appl. Clay Sci.*, vol. 169, no. December 2018, pp. 81–90, 2019, doi: 10.1016/j.clay.2018.12.021.

[290] I. Mehdipour and K. H. Khayat, “Effect of particle-size distribution and specific surface area of different binder systems on packing density and flow characteristics of cement paste,” *Cem. Concr. Compos.*, vol. 78, pp. 120–131, 2017, doi: 10.1016/j.cemconcomp.2017.01.005.

[291] M. Meraz *et al.*, “Performance evaluation of high-performance self-compacting concrete with waste glass aggregate and metakaolin,” *J. Build. Eng.*, vol. 67, no. November 2022, p. 105976, 2023, doi: 10.1016/j.jobe.2023.105976.

[292] Joesph DAVIDOVITS, *Geopolymer chemistry &Applications*, 5th ed. Institute Geopolymere, 2020. doi: www.geopolymer.org.

[293] et al. Nurruddin, “Methods of curing geopolymer concrete: A review,” *Int. J. Adv. Appl. Sci.*, vol. 5, no. 1, pp. 31–36, 2018, doi: 10.21833/ijaas.2018.01.005.

[294] ASTM, “ASTM C 666- 97,Standard Test Method for Resistance of Concrete to Rapid

Freezing and Thawing."

[295] C. Shi, Y. L. Mo, and H. B. Dhonde, "High Performance Concrete," *High-Performance Constr. Mater. Sci. Appl.*, pp. 19–90, 2008, doi: 10.1142/9789812797360_0002.

[296] S. EFNARC, "Guidelines for self-compacting concrete," *London, UK Assoc. House*, vol. 32, p. 34, 2002.

[297] W. C. P. James A. Farny, "High-Strength Concrete," *American Concrete Institute, ACI Special Publication*, vol. SP-087. 1985.

[298] Association Française de Normalisation (AFNOR), "Comité de Normalisation Européen, «NF EN 197-5 - Ciment - Partie 5 : Ciment Portland composé CEM II/C-M et Ciment composé CEM VI,»," La Plaine Saint-Denis, 2021.

[299] AFNOR, "NF EN 1015-3, Methods of test for mortar for masonry -Part 3: Determination of consistence of fresh mortar (by flow table)." 1999.

[300] ASTM, "ASTM C143/C143M-12, Standard Test Method for Slump of Hydraulic Cement Concrete.," 2015. doi: 10.1520/C0143_C0143M-12.

[301] AFNOR, "NF EN 196-1, Methods of testing cement- Part 1: Determination of strength," 2016.

[302] "863 Concrete Compressive Strength.Pdf."

[303] AFNOR, "ISO 15901-1, Evaluation of pore size distribution and porosity of solid materials by mercury porosimetry and gas absorption- Part 1: Mercury porosimetry." 2016.

[304] S. Chen *et al.*, "Pore structure of geopolymer materials and its correlations to engineering properties: A review," *Constr. Build. Mater.*, vol. 328, no. March, p. 127064, 2022, doi: 10.1016/j.conbuildmat.2022.127064.

[305] Z. Zhang, H. Wang, Y. Zhu, A. Reid, J. L. Provis, and F. Bullen, "Using fly ash to partially substitute metakaolin in geopolymer synthesis," *Appl. Clay Sci.*, vol. 88–89, pp. 194–201, 2014, doi: https://doi.org/10.1016/j.clay.2013.12.025.

[306] E. Kamseu *et al.*, “Insulating behavior of metakaolin-based geopolymer materials assess with heat flux meter and laser flash techniques,” *J. Therm. Anal. Calorim.*, vol. 108, no. 3, pp. 1189–1199, 2012, doi: 10.1007/s10973-011-1798-9.

[307] Z. Zhang, X. Yao, and H. Zhu, “Potential application of geopolymers as protection coatings for marine concrete: II. Microstructure and anticorrosion mechanism,” *Appl. Clay Sci.*, vol. 49, no. 1, pp. 7–12, 2010, doi: https://doi.org/10.1016/j.clay.2010.04.024.

[308] P. Duan, C. Yan, and W. Zhou, “Influence of partial replacement of fly ash by metakaolin on mechanical properties and microstructure of fly ash geopolymer paste exposed to sulfate attack,” *Ceram. Int.*, vol. 42, no. 2, Part B, pp. 3504–3517, 2016, doi: https://doi.org/10.1016/j.ceramint.2015.10.154.

[309] F. Collins and J. G. Sanjayan, “Microcracking and strength development of alkali activated slag concrete,” *Cem. Concr. Compos.*, vol. 23, no. 4, pp. 345–352, 2001, doi: https://doi.org/10.1016/S0958-9465(01)00003-8.

[310] T. A. Aiken, J. Kwasny, W. Sha, and M. N. Soutsos, “Effect of slag content and activator dosage on the resistance of fly ash geopolymer binders to sulfuric acid attack,” *Cem. Concr. Res.*, vol. 111, no. May, pp. 23–40, 2018, doi: 10.1016/j.cemconres.2018.06.011.

[311] S. Pilehvar *et al.*, “Effect of freeze-thaw cycles on the mechanical behavior of geopolymer concrete and Portland cement concrete containing micro-encapsulated phase change materials,” *Constr. Build. Mater.*, vol. 200, pp. 94–103, 2019, doi: 10.1016/j.conbuildmat.2018.12.057.

[312] A. M. Rashad and D. M. Sadek, “Behavior of alkali-activated slag pastes blended with waste rubber powder under the effect of freeze/thaw cycles and severe sulfate attack,” *Constr. Build. Mater.*, vol. 265, p. 120716, 2020, doi: 10.1016/j.conbuildmat.2020.120716.

[313] ASTM, “ASTM C1585, Standard test method for measurement of standard test method for measurement of rate of absorption of water by hydraulic cement concretes,” 2013.

[314] Astm C1585-13, *Astm C1585-13*. 2013.

[315] AFNOR, “NF EN 196-9 - Methods of testing cement - Part 9: heat of hydration - Semi-adiabatic method,” 2010.

[316] J. Davidovits, “Geopolymers - Inorganic polymeric new materials,” *J. Therm. Anal.*, vol. 37, no. 8, pp. 1633–1656, 1991, doi: 10.1007/BF01912193.

[317] J. Davidovits, “Davidovits, J. (1999) Chemistry of Geopolymeric Systems Terminology. Proceedings of Geopolymer. International Conference, France, 1999.,” *Proc. Geopolymer. Int. Conf.*, p. 1999, 1999, [Online]. Available: https://www.scirp.org/(S(lz5mqp453edsnp55rrgjct55.))/reference/referencespapers.aspx?referenceid=1161598

[318] AFNOR, “NF EN 12457-2: pour lixiviation des déchets fragmentés Lixiviation — Essai de conformité et des boues,” 2022.

[319] D. M. González-García, L. Téllez-Jurado, F. J. Jiménez-Álvarez, L. Zarazua-Villalobos, and H. Balmori-Ramírez, “Evolution of a natural pozzolan-based geopolymer alkalized in the presence of sodium or potassium silicate/hydroxide solution,” *Constr. Build. Mater.*, vol. 321, no. November 2021, 2022, doi: 10.1016/j.conbuildmat.2021.126305.

[320] M. N. S. Hadi, H. Zhang, and S. Parkinson, “Optimum mix design of geopolymer pastes and concretes cured in ambient condition based on compressive strength, setting time and workability,” *J. Build. Eng.*, vol. 23, pp. 301–313, May 2019, doi: 10.1016/j.jobe.2019.02.006.

[321] P. Nath and P. K. Sarker, “Effect of GGBFS on setting, workability and early strength properties of fly ash geopolymer concrete cured in ambient condition,” *Constr. Build. Mater.*, vol. 66, pp. 163–171, 2014, doi: 10.1016/j.conbuildmat.2014.05.080.

[322] S. Kumar, R. Kumar, and S. P. Mehrotra, “Influence of granulated blast furnace slag on the reaction, structure and properties of fly ash based geopolymer,” *J. Mater. Sci.*, vol. 45, no. 3, pp. 607–615, 2010, doi: 10.1007/s10853-009-3934-5.

[323] E. I. Diaz, E. N. Allouche, and S. Eklund, “Factors affecting the suitability of fly ash as source material for geopolymers,” *Fuel*, vol. 89, no. 5, pp. 992–996, 2010, doi:

10.1016/j.fuel.2009.09.012.

[324] N. K. Lee and H. K. Lee, “Influence of the slag content on the chloride and sulfuric acid resistances of alkali-activated fly ash/slag paste,” *Cem. Concr. Compos.*, vol. 72, pp. 168–179, 2016, doi: 10.1016/j.cemconcomp.2016.06.004.

[325] A. Yolcu, M. B. Karakoç, E. Ekinci, A. Özcan, and M. A. Sağır, “Effect of binder dosage and the use of waste rubber fiber on the mechanical and durability performance of geopolymer concrete,” *J. Build. Eng.*, vol. 61, no. September, p. 105162, 2022, doi: 10.1016/j.jobe.2022.105162.

[326] H. Jiang, Z. Qi, E. Yilmaz, J. Han, J. Qiu, and C. Dong, “Effectiveness of alkali-activated slag as alternative binder on workability and early age compressive strength of cemented paste backfills,” *Constr. Build. Mater.*, vol. 218, pp. 689–700, 2019, doi: 10.1016/j.conbuildmat.2019.05.162.

[327] G. Mallikarjuna Rao and T. D. Gunneswara Rao, “A quantitative method of approach in designing the mix proportions of fly ash and GGBS-based geopolymer concrete,” *Aust. J. Civ. Eng.*, vol. 16, no. 1, pp. 53–63, 2018, doi: 10.1080/14488353.2018.1450716.

[328] K. Mermerdaş, Z. Algın, S. M. Oleiwi, and D. E. Nassani, “Optimization of lightweight GGBFS and FA geopolymer mortars by response surface method,” *Constr. Build. Mater.*, vol. 139, pp. 159–171, 2017, doi: 10.1016/j.conbuildmat.2017.02.050.

[329] M. S. Saif *et al.*, “Influence of blended powders on properties of Ultra-High Strength Fibre Reinforced Self Compacting Concrete subjected to elevated temperatures,” *Case Stud. Constr. Mater.*, vol. 18, no. December 2022, p. e01793, 2023, doi: 10.1016/j.cscm.2022.e01793.

[330] N. T. Al-Rawi, “performance of self-compacting geopolymer concrete with and without GGBFS and steel fiber,” *Adv. Concr. Constr.*, vol. 6, no. 4, pp. 323–344, 2018, [Online]. Available: http://link.springer.com/10.1007/978-3-319-76887-8%0Ahttp://link.springer.com/10.1007/978-3-319-93594-2%0Ahttp://dx.doi.org/10.1016/B978-0-12-409517-5.00007-

3%0Ahttp://dx.doi.org/10.1016/j.jff.2015.06.018%0Ahttp://dx.doi.org/10.1038/s41559-019-0877-3%0Aht

[331] P. Pradhan, S. Panda, S. Kumar Parhi, and S. Kumar Panigrahi, "Factors affecting production and properties of self-compacting geopolymer concrete – A review," *Constr. Build. Mater.*, vol. 344, no. June, p. 128174, 2022, doi: 10.1016/j.conbuildmat.2022.128174.

[332] M. A. M. Ariffin, M. A. R. Bhutta, M. W. Hussin, M. Mohd Tahir, and N. Aziah, "Sulfuric acid resistance of blended ash geopolymer concrete," *Constr. Build. Mater.*, vol. 43, pp. 80–86, 2013, doi: 10.1016/j.conbuildmat.2013.01.018.

[333] P. Chindaprasirt, U. Rattanasak, and S. Taebuanhuad, "Resistance to acid and sulfate solutions of microwave-assisted high calcium fly ash geopolymer," *Mater. Struct. Constr.*, vol. 46, no. 3, pp. 375–381, 2013, doi: 10.1617/s11527-012-9907-1.

[334] T. Bakharev, "Resistance of geopolymer materials to acid attack," *Cem. Concr. Res.*, vol. 35, no. 4, pp. 658–670, 2005, doi: 10.1016/j.cemconres.2004.06.005.

[335] P. S. Deb, P. K. Sarker, and S. Barbhuiya, "Sorptivity and acid resistance of ambient-cured geopolymer mortars containing nano-silica," *Cem. Concr. Compos.*, vol. 72, pp. 235–245, 2016, doi: 10.1016/j.cemconcomp.2016.06.017.

[336] A. Aboulayt, M. Riahi, M. Ouazzani Touhami, H. Hannache, M. Gomina, and R. Moussa, "Properties of metakaolin based geopolymer incorporating calcium carbonate," *Adv. Powder Technol.*, vol. 28, no. 9, pp. 2393–2401, 2017, doi: 10.1016/j.apt.2017.06.022.

[337] B. Kim and S. Lee, "Review on characteristics of metakaolin-based geopolymer and fast setting," *J. Korean Ceram. Soc.*, vol. 57, no. 4, pp. 368–377, 2020, doi: 10.1007/s43207-020-00043-y.

[338] L. Chen, Z. Wang, Y. Wang, and J. Feng, "Preparation and properties of alkali activated metakaolin-based geopolymer," *Materials (Basel).*, vol. 9, no. 9, pp. 1–12, 2016, doi: 10.3390/ma9090767.

[339] H. Rahier, B. Van Mele, and J. Wastiels, “Low-temperature synthesized aluminosilicate glasses: Part II. Rheological transformations during low-temperature cure and high-temperature properties of a model compound,” *J. Mater. Sci.*, vol. 31, no. 1, pp. 80–85, 1996, doi: 10.1007/BF00355129.

[340] M. Zhang, H. Guo, T. El-Korchi, G. Zhang, and M. Tao, “Experimental feasibility study of geopolymer as the next-generation soil stabilizer,” *Constr. Build. Mater.*, vol. 47, pp. 1468–1478, 2013, doi: 10.1016/j.conbuildmat.2013.06.017.

[341] R. A. Robayo-Salazar, R. Mejía de Gutiérrez, and F. Puertas, “Effect of metakaolin on natural volcanic pozzolan-based geopolymer cement,” *Appl. Clay Sci.*, vol. 132–133, pp. 491–497, 2016, doi: 10.1016/j.clay.2016.07.020.

[342] V. C. Farmer, Ed., “The Infrared Spectra of Minerals.” Mineralogical Society of Great Britain and Ireland, Jan. 01, 1974. doi: 10.1180/mono-4.

[343] F. Puertas and A. Fernández-Jiménez, “Mineralogical and microstructural characterisation of alkali-activated fly ash/slag pastes,” *Cem. Concr. Compos.*, vol. 25, no. 3, pp. 287–292, 2003, doi: https://doi.org/10.1016/S0958-9465(02)00059-8.

[344] Z. Baščarević *et al.*, “Effects of the concentrated NH4NO3 solution on mechanical properties and structure of the fly ash based geopolymers,” *Constr. Build. Mater.*, vol. 41, no. 3, pp. 570–579, 2013, doi: 10.1016/j.conbuildmat.2012.12.067.

[345] M. Vafaei, A. Allahverdi, P. Dong, N. Bassim, and M. Mahinroosta, “Resistance of red clay brick waste/phosphorus slag-based geopolymer mortar to acid solutions of mild concentration,” *J. Build. Eng.*, vol. 34, no. October 2020, p. 102066, 2021, doi: 10.1016/j.jobe.2020.102066.

[346] N. V. Chukanov and A. D. Chervonnyi, *Infrared Spectroscopy of Minerals and Related Compounds*. Springer, 2016. [Online]. Available: http://link.springer.com/10.1007/978-3-319-25349-7

[347] T. Revathi and R. Jeyalakshmi, “Fly ash–GGBS geopolymer in boron environment: A study on rheology and microstructure by ATR FT-IR and MAS NMR,” *Constr. Build. Mater.*,

vol. 267, p. 120965, 2021, doi: 10.1016/j.conbuildmat.2020.120965.

[348] J. Klinowski, “Nuclear magnetic resonance studies of zeolites,” *Prog. Nucl. Magn. Reson. Spectrosc.*, vol. 16, no. C, pp. 237–309, 1984, doi: 10.1016/0079-6565(84)80007-2.

[349] B. H. W. S. de Jong, C. M. Schramm, and V. E. Parziale, “Polymerization of silicate and aluminate tetrahedra in glasses, melts, and aqueous solutions-V. The polymeric structure of silica in albite and anorthite composition glass and the devitrification of amorphous anorthite,” *Geochim. Cosmochim. Acta*, vol. 48, no. 12, pp. 2619–2629, 1984, doi: 10.1016/0016-7037(84)90310-7.

[350] D. Müller, W. Gessner, H. J. Behrens, and G. Scheler, “Determination of the aluminium coordination in aluminium-oxygen compounds by solid-state high-resolution 27AI NMR,” *Chem. Phys. Lett.*, vol. 79, no. 1, pp. 59–62, 1981, doi: 10.1016/0009-2614(81)85288-8.

[351] E. Ozcelikci *et al.*, “A comprehensive study on the compressive strength, durability-related parameters and microstructure of geopolymer mortars based on mixed construction and demolition waste,” *J. Clean. Prod.*, vol. 396, no. February, p. 136522, 2023, doi: 10.1016/j.jclepro.2023.136522.

[352] I. Lecomte, C. Henrist, M. Liégeois, F. Maseri, A. Rulmont, and R. Cloots, “(Micro)-structural comparison between geopolymers, alkali-activated slag cement and Portland cement,” *J. Eur. Ceram. Soc.*, vol. 26, no. 16, pp. 3789–3797, 2006, doi: 10.1016/j.jeurceramsoc.2005.12.021.

[353] P. Duxson, J. L. Provis, G. C. Lukey, F. Separovic, and J. S. J. Van Deventer, “29Si NMR study of structural ordering in aluminosilicate geopolymer gels,” *Langmuir*, vol. 21, no. 7, pp. 3028–3036, 2005, doi: 10.1021/la047336x.

[354] R. H. Haddad and O. Alshbuol, “Production of geopolymer concrete using natural pozzolan: A parametric study,” *Constr. Build. Mater.*, vol. 114, pp. 699–707, 2016, doi: 10.1016/j.conbuildmat.2016.04.011.

[355] A. Alloul, M. Amar, M. Benzerzour, and N. Abriak, “Developing mortar using limestone flash-calcined dredged sediment / millstone-clay cement binder (LFC),” *J. Build. Eng.*,

vol. 76, no. June, p. 107346, 2023, doi: 10.1016/j.jobe.2023.107346.

[356] H. Slimanou, K. Bouguermouh, and N. Bouzidi, “Synthesis of geopolymers based on dredged sediment in calcined and uncalcined states,” *Mater. Lett.*, vol. 251, pp. 188–191, 2019, doi: https://doi.org/10.1016/j.matlet.2019.05.070.

[357] F. Messina *et al.*, “Synergistic recycling of calcined clayey sediments and water potabilization sludge as geopolymer precursors: Upscaling from binders to precast paving cement-free bricks,” *Constr. Build. Mater.*, vol. 133, pp. 14–26, 2017, doi: https://doi.org/10.1016/j.conbuildmat.2016.12.039.

[358] S. Dashti, “Experimental Evaluation of Beneficial Use of Lake Michigan Dredged Materials in Flyash Based Geopolymer Concrete,” *Theses Diss.*, no. December, 2015, [Online]. Available: https://dc.uwm.edu/etd/1046

[359] R. Karam Cabrerizo, D. Bulteel, T. Wattez, and D. Deneele, “Effect of marine sediments incorporation on the behaviour of alkali-activated GGBFS,” *Mater. Struct.*, vol. 52, 2019, doi: 10.1617/s11527-019-1408-z.

[360] S. Lekshmi and J. Sudhakumar, “An assessment on the durability performance of fly ash-clay based geopolymer mortar containing clay enhanced with lime and GGBS,” *Clean. Mater.*, vol. 5, p. 100129, 2022, doi: https://doi.org/10.1016/j.clema.2022.100129.

[361] G. Huang, Y. Ji, J. Li, Z. Hou, and Z. Dong, “Improving strength of calcinated coal gangue geopolymer mortars via increasing calcium content,” *Constr. Build. Mater.*, vol. 166, pp. 760–768, 2018, doi: https://doi.org/10.1016/j.conbuildmat.2018.02.005.

[362] L. Long, Y. Zhao, G. Lv, Y. Duan, X. Liu, and X. Jiang, “Improving stabilization/solidification of MSWI fly ash with coal gangue based geopolymer via increasing active calcium content,” *Sci. Total Environ.*, vol. 854, p. 158594, 2023, doi: https://doi.org/10.1016/j.scitotenv.2022.158594.

[363] S. Chen, C. Wu, and D. Yan, “Binder-scale creep behavior of metakaolin-based geopolymer,” *Cem. Concr. Res.*, vol. 124, p. 105810, 2019, doi: https://doi.org/10.1016/j.cemconres.2019.105810.

[364] M. Albitar, M. S. Mohamed Ali, P. Visintin, and M. Drechsler, “Durability evaluation of geopolymer and conventional concretes,” *Constr. Build. Mater.*, vol. 136, pp. 374–385, 2017, doi: 10.1016/j.conbuildmat.2017.01.056.

[365] O. Ayeni, A. P. Onwualu, and E. Boakye, “Characterization and mechanical performance of metakaolin-based geopolymer for sustainable building applications,” *Constr. Build. Mater.*, vol. 272, p. 121938, 2021, doi: 10.1016/j.conbuildmat.2020.121938.

[366] M. H. Al-Majidi, A. Lampropoulos, A. Cundy, and S. Meikle, “Development of geopolymer mortar under ambient temperature for in situ applications,” *Constr. Build. Mater.*, vol. 120, pp. 198–211, 2016, doi: 10.1016/j.conbuildmat.2016.05.085.

[367] F. V. C., “the infrared spectra of minerals.,” *Mineral. Soc. Monogr.*, vol. 4, pp. 331–363, 1974, Accessed: Aug. 03, 2023. [Online]. Available: https://cir.nii.ac.jp/crid/1571417124190337792.bib?lang=en

[368] S. Borhan, S. Hesaraki, and S. Ahmadzadeh-Asl, “Evaluation of colloidal silica suspension as efficient additive for improving physicochemical and in vitro biological properties of calcium sulfate-based nanocomposite bone cement,” *J. Mater. Sci. Mater. Med.*, vol. 21, no. 12, pp. 3171–3181, 2010, doi: 10.1007/s10856-010-4168-4.

[369] A. Putnis, B. Winkler, and L. Fernandez-Diaz, “In situ IR spectroscopic and thermogravimetric study of the dehydration of gypsum,” *Mineral. Mag.*, vol. 54, no. 374, pp. 123–128, 1990, doi: 10.1180/minmag.1990.054.374.14.

[370] W. H. S. Bragg and W. L. S. Bragg, *The crystalline state*. G. Bell & Sons. Accessed: Aug. 03, 2023. [Online]. Available: https://cir.nii.ac.jp/crid/1130000793818604928.bib?lang=en

[371] M. E. Sultan, S. A. Abo-El-Enein, A. Z. Sayed, T. M. EL-Sokkary, and H. A. Hammad, “Incorporation of cement bypass flue dust in fly ash and blast furnace slag-based geopolymer,” *Case Stud. Constr. Mater.*, vol. 8, no. December 2017, pp. 315–322, 2018, doi: 10.1016/j.cscm.2018.02.009.

[372] O. A. Abdulkareem, A. M. Mustafa Al Bakri, H. Kamarudin, I. Khairul Nizar, and A. A. Saif, “Effects of elevated temperatures on the thermal behavior and mechanical

performance of fly ash geopolymer paste, mortar and lightweight concrete," *Constr. Build. Mater.*, vol. 50, pp. 377–387, 2014, doi: 10.1016/j.conbuildmat.2013.09.047.

[373] H. M. Khater and M. Gharieb, "Synergetic effect of nano-silica fume for enhancing physico-mechanical properties and thermal behavior of MK-geopolymer composites," *Constr. Build. Mater.*, vol. 350, no. August, p. 128879, 2022, doi: 10.1016/j.conbuildmat.2022.128879.

[374] M. Bastami, M. Baghbadrani, and F. Aslani, "Performance of nano-Silica modified high strength concrete at elevated temperatures," *Constr. Build. Mater.*, vol. 68, pp. 402–408, 2014, doi: 10.1016/j.conbuildmat.2014.06.026.

[375] S. K. Padmanabhan and A. Licciulli, "Synthesis and characteristics of fl y ash and bottom ash based geopolymers – A comparative study," *Ceram. Int.*, vol. 40, no. 2, pp. 2965–2971, 2014, doi: 10.1016/j.ceramint.2013.10.012.

[376] L. Alarcon-Ruiz, G. Platret, E. Massieu, and A. Ehrlacher, "The use of thermal analysis in assessing the effect of temperature on a cement paste," *Cem. Concr. Res.*, vol. 35, no. 3, pp. 609–613, Mar. 2005, doi: 10.1016/J.CEMCONRES.2004.06.015.

[377] Q. Long, Y. Liu, Q. Zhao, M. Zhou, and B. Li, "Effects of GGBFS:FA ratio and humid-heat-treating on the mechanical performance and microstructure of the steel slag-based ternary geopolymer," *Constr. Build. Mater.*, vol. 392, no. June, p. 131750, 2023, doi: 10.1016/j.conbuildmat.2023.131750.

[378] W. Feng, Y. Jin, D. Zheng, Y. Fang, Z. Dong, and H. Cui, "Study of triethanolamine on regulating early strength of fly ash-based chemically foamed geopolymer," *Cem. Concr. Res.*, vol. 162, no. May, p. 107005, 2022, doi: 10.1016/j.cemconres.2022.107005.

[379] M. Fang, Y. Yi, W. Ma, Y. Lin, J. Li, and W. Liu, "Performance analysis of coagulation hardening effect of geopolymer prepared from high calcium-based ladle furnace slag," *Constr. Build. Mater.*, vol. 374, no. September 2022, p. 130963, 2023, doi: 10.1016/j.conbuildmat.2023.130963.

[380] A. Kashani, T. D. Ngo, B. Walkley, and P. Mendis, "Thermal performance of calcium-rich

alkali-activated materials: A microstructural and mechanical study," *Constr. Build. Mater.*, vol. 153, pp. 225–237, 2017, doi: 10.1016/j.conbuildmat.2017.07.119.

[381] P. C. J. Wongpa, K. Kiattikomol, C. Jaturapitakkul, "Compressive strength, modulus of elasticity, and water permeability of inorganic polymer concrete," *Mater. Des.*, vol. 31, pp. 4748–4754, 2010, [Online]. Available: https://doi.org/10.1016/j. %0Amatdes.2010.05.012.

[382] V. Ducman and L. Korat, "Characterization of geopolymer fly-ash based foams obtained with the addition of Al powder or H2O2 as foaming agents," *Mater. Charact.*, vol. 113, pp. 207–213, 2016, doi: https://doi.org/10.1016/j.matchar.2016.01.019.

[383] K. Dhasindrakrishna, K. Pasupathy, S. Ramakrishnan, and J. Sanjayan, "Effect of yield stress development on the foam-stability of aerated geopolymer concrete," *Cem. Concr. Res.*, vol. 138, p. 106233, 2020, doi: https://doi.org/10.1016/j.cemconres.2020.106233.

[384] L. Ricciotti, A. Occhicone, A. Petrillo, C. Ferone, R. Cioffi, and G. Roviello, "Geopolymer-based hybrid foams: Lightweight materials from a sustainable production process," *J. Clean. Prod.*, vol. 250, p. 119588, 2020, doi: https://doi.org/10.1016/j.jclepro.2019.119588.

[385] B. B. Jindal, T. Alomayri, A. Hasan, and C. R. Kaze, "Geopolymer concrete with metakaolin for sustainability: a comprehensive review on raw material's properties, synthesis, performance, and potential application," *Environ. Sci. Pollut. Res. 2021 3010*, vol. 30, no. 10, pp. 25299–25324, Jan. 2022, doi: 10.1007/S11356-021-17849-W.

[386] Z. Yunsheng, S. Wei, and L. Zongjin, "Composition design and microstructural characterization of calcined kaolin-based geopolymer cement," *Appl. Clay Sci.*, vol. 47, no. 3, pp. 271–275, 2010, doi: https://doi.org/10.1016/j.clay.2009.11.002.

[387] P. De Silva, K. Sagoe-Crenstil, and V. Sirivivatnanon, "Kinetics of geopolymerization: Role of Al2O3 and SiO2," *Cem. Concr. Res.*, vol. 37, no. 4, pp. 512–518, 2007, doi: https://doi.org/10.1016/j.cemconres.2007.01.003.

[388] R. A. Fletcher, K. J. D. MacKenzie, C. L. Nicholson, and S. Shimada, "The composition range of aluminosilicate geopolymers," *J. Eur. Ceram. Soc.*, vol. 25, no. 9, pp. 1471–1477, 2005, doi: https://doi.org/10.1016/j.jeurceramsoc.2004.06.001.

[389] M. Rowles and B. O'Connor, "Chemical optimisation of the compressive strength of aluminosilicate geopolymers synthesised by sodium silicate activation of metakaolinite," *J. Mater. Chem.*, vol. 13, no. 5, pp. 1161–1165, 2003, doi: 10.1039/B212629J.

[390] M. Lizcano, A. Gonzalez, S. Basu, K. Lozano, and M. Radovic, "Effects of Water Content and Chemical Composition on Structural Properties of Alkaline Activated Metakaolin-Based Geopolymers," *J. Am. Ceram. Soc.*, vol. 95, no. 7, pp. 2169–2177, 2012, doi: https://doi.org/10.1111/j.1551-2916.2012.05184.x.

[391] A. Kamalloo, Y. Ganjkhanlou, S. H. Aboutalebi, and H. Nuranian, "Modeling of compressive strength of Metakaolin based geopolymers by the use of artificial neural network," *Int. J. Eng. Trans. A Basics*, vol. 23, pp. 145–152, 2010.

[392] D. L. Y. Kong, J. G. Sanjayan, and K. Sagoe-Crentsil, "Comparative performance of geopolymers made with metakaolin and fly ash after exposure to elevated temperatures," *Cem. Concr. Res.*, vol. 37, no. 12, pp. 1583–1589, 2007, doi: https://doi.org/10.1016/j.cemconres.2007.08.021.

[393] J. Bao *et al.*, "Thermal resistance, water absorption and microstructure of high-strength self-compacting lightweight aggregate concrete (HSSC-LWAC) after exposure to elevated temperatures," *Constr. Build. Mater.*, vol. 365, no. 777, p. 130071, 2023, doi: 10.1016/j.conbuildmat.2022.130071.

[394] R. Niry Razafinjato, A.-L. Beaucour, R. L. Hebert, B. Ledesert, R. Bodet, and A. Noumowe, "High temperature behaviour of a wide petrographic range of siliceous and calcareous aggregates for concretes," *Constr. Build. Mater.*, vol. 123, pp. 261–273, 2016, doi: https://doi.org/10.1016/j.conbuildmat.2016.06.097.

[395] A. Krishnan and S. S. Subramanian, "Effect of green gram pod ash (GGPA) as supplementary cementitious material (SCM) in mechanical and durability properties of concrete," *Constr. Build. Mater.*, vol. 411, no. September 2023, p. 134663, 2024, doi: 10.1016/j.conbuildmat.2023.134663.

[396] J. M. Medina, I. F. Sáez del Bosque, M. Frías, M. I. Sánchez de Rojas, and C. Medina,

"Durability of new blended cements additioned with recycled biomass bottom ASH from electric power plants," *Constr. Build. Mater.*, vol. 225, pp. 429–440, 2019, doi: https://doi.org/10.1016/j.conbuildmat.2019.07.176.

[397] S. Prasanphan, K. Hemra, A. Wannagon, T. Kobayashi, S. Onutai, and S. Jiemsirilers, "29Si and 27Al NMR study of the structural transformation of calcined kaolin residue-based geopolymer using low alkali activator content for sustainable construction materials," *J. Build. Eng.*, vol. 70, no. March, p. 106332, 2023, doi: 10.1016/j.jobe.2023.106332.

[398] G. Moutaoukil, S. Alehyen, I. Sobrados, and M. Taibi, "Microstructural and 29 Si and 27 Al MAS NMR spectroscopic evaluations of alkali cation and curing effects on Class C fly ash-based geopolymer," *Chem. Data Collect.*, vol. 41, no. June, p. 100898, 2022, doi: 10.1016/j.cdc.2022.100898.

[399] Z. Fang, Z. Li, X. Zhang, S. Pan, M. Wu, and B. Pan, "Enhanced Arsenite Removal from Silicate-containing Water by Using Redox Polymer-based Fe(III) Oxides Nanocomposite," *Water Res.*, vol. 189, p. 116673, 2021, doi: 10.1016/j.watres.2020.116673.

[400] J. Stefaniak, A. Dutta, B. Verbinnen, M. Shakya, and E. R. Rene, "Selenium removal from mining and process wastewater: A systematic review of available technologies," *J. Water Supply Res. Technol. - AQUA*, vol. 67, no. 8, pp. 903–918, 2018, doi: 10.2166/aqua.2018.109.

[401] A. M. Mansour and M. I. Al Biajawi, "The effect of the addition of metakaolin on the fresh and hardened properties of blended cement products: A review," *Mater. Today Proc.*, vol. 66, pp. 2811–2817, 2022, doi: https://doi.org/10.1016/j.matpr.2022.06.521.

[402] J. J. Brooks and M. A. Megat Johari, "Effect of metakaolin on creep and shrinkage of concrete," *Cem. Concr. Compos.*, vol. 23, no. 6, pp. 495–502, 2001, doi: https://doi.org/10.1016/S0958-9465(00)00095-0.

[403] A. el Mahdi Safhi, P. Rivard, A. Yahia, M. Benzerzour, and K. H. Khayat, "Valorization of dredged sediments in self-consolidating concrete: Fresh, hardened, and microstructural properties," *J. Clean. Prod.*, vol. 263, p. 121472, 2020, doi:

https://doi.org/10.1016/j.jclepro.2020.121472.

[404] J. M. Khatib, “Metakaolin concrete at a low water to binder ratio,” *Constr. Build. Mater.*, vol. 22, no. 8, pp. 1691–1700, 2008, doi: https://doi.org/10.1016/j.conbuildmat.2007.06.003.

[405] I. Mehdipour and K. H. Khayat, “Effect of particle-size distribution and specific surface area of different binder systems on packing density and flow characteristics of cement paste,” *Cem. Concr. Compos.*, vol. 78, pp. 120–131, Apr. 2017, doi: 10.1016/j.cemconcomp.2017.01.005.

[406] H. Mehdizadeh, M.-Z. Guo, and T.-C. Ling, “Ultra-fine sediment of Changjiang estuary as binder replacement in self-compacting mortar: Rheological, hydration and hardened properties,” *J. Build. Eng.*, vol. 44, p. 103251, Dec. 2021, doi: 10.1016/j.jobe.2021.103251.

[407] S. H. Kang, Y. H. Kwon, and J. Moon, “Influence of calcination temperature of impure kaolinitic clay on hydration and strength development of ultra-high-performance cementitious composite,” *Constr. Build. Mater.*, vol. 326, no. December 2021, p. 126920, 2022, doi: 10.1016/j.conbuildmat.2022.126920.

[408] A. M. Salman, M. A. Akinpelu, I. T. Yahaya, and H. M. Salami, “Workability and strengths of ternary cementitious concrete incorporating calcined clay and limestone powder,” *Mater. Today Proc.*, no. xxxx, 2023, doi: 10.1016/j.matpr.2023.02.249.

[409] G. Sua-iam and N. Makul, “Use of limestone powder during incorporation of Pb-containing cathode ray tube waste in self-compacting concrete,” *J. Environ. Manage.*, vol. 128, pp. 931–940, 2013, doi: 10.1016/j.jenvman.2013.06.031.

[410] J. F. Burroughs, J. Shannon, T. S. Rushing, K. Yi, Q. B. Gutierrez, and D. W. Harrelson, “Potential of finely ground limestone powder to benefit ultra-high performance concrete mixtures,” *Constr. Build. Mater.*, vol. 141, pp. 335–342, 2017, doi: 10.1016/j.conbuildmat.2017.02.073.

[411] J. Seo, S. Park, H. N. Yoon, and H. K. Lee, “Effect of CaO incorporation on the microstructure and autogenous shrinkage of ternary blend Portland cement-slag-silica

fume," *Constr. Build. Mater.*, vol. 249, p. 118691, 2020, doi: https://doi.org/10.1016/j.conbuildmat.2020.118691.

[412] M. S. Kim, Y. Jun, C. Lee, and J. E. Oh, "Use of CaO as an activator for producing a price-competitive non-cement structural binder using ground granulated blast furnace slag," *Cem. Concr. Res.*, vol. 54, pp. 208–214, 2013, doi: https://doi.org/10.1016/j.cemconres.2013.09.011.

[413] Y. A. Al-Noaimat *et al.*, "3D printing of limestone-calcined clay cement: A review of its potential implementation in the construction industry," *Results Eng.*, vol. 18, no. April, p. 101115, 2023, doi: 10.1016/j.rineng.2023.101115.

[414] M. Yudenfreund, K. M. Hanna, J. Skalny, I. Older, and S. Brunauer, "Hardened Portland cement pastes of low porosity V. Compressive strength," *Cem. Concr. Res.*, vol. 2, no. 6, pp. 731–743, 1972, doi: 10.1016/0008-8846(72)90008-7.

[415] H. Du and S. D. Pang, "High-performance concrete incorporating calcined kaolin clay and limestone as cement substitute," *Constr. Build. Mater.*, vol. 264, p. 120152, 2020, doi: https://doi.org/10.1016/j.conbuildmat.2020.120152.

[416] S. Etris *et al.*, "Capillary Porosity in Hardened Cement Paste," *J. Test. Eval.*, vol. 1, no. 1, p. 74, 1973, doi: 10.1520/jte11604j.

[417] S. J. Pantazopoulou and R. H. Mills, "Microstructural aspects of the mechanical response of plain concrete," *ACI Mater. J.*, vol. 92, no. 6, pp. 605–616, 1995, doi: 10.14359/9780.

[418] X. Chen, S. Wu, and J. Zhou, "Influence of porosity on compressive and tensile strength of cement mortar," *Constr. Build. Mater.*, vol. 40, pp. 869–874, 2013, doi: 10.1016/j.conbuildmat.2012.11.072.

[419] R. A. Cook and K. C. Hover, "Mercury porosimetry of cement-based materials and associated correction factors," *Constr. Build. Mater.*, vol. 7, no. 4, pp. 231–240, 1993, doi: 10.1016/0950-0618(93)90007-Y.

[420] S. Djaknoun, E. Ouedraogo, and A. Ahmed Benyahia, "Characterisation of the behaviour

of high performance mortar subjected to high temperatures," *Constr. Build. Mater.*, vol. 28, no. 1, pp. 176–186, Mar. 2012, doi: 10.1016/j.conbuildmat.2011.07.063.

[421] A. Machner, M. Zajac, M. Ben Haha, K. O. Kjellsen, M. R. Geiker, and K. De Weerdt, "Chloride-binding capacity of hydrotalcite in cement pastes containing dolomite and metakaolin," *Cem. Concr. Res.*, vol. 107, no. February, pp. 163–181, 2018, doi: 10.1016/j.cemconres.2018.02.002.

[422] M. G. Pineaud A, Rmond S, Cabrillac R, Menou A, Boussa H, "Etude expérimentale de l'influence des hautes températures sur l'énergie de fissuration des BHP," no. (1), pp. 257–64, 2003.

[423] K. De Weerdt, M. Ben Haha, G. Le Saout, K. O. Kjellsen, H. Justnes, and B. Lothenbach, "Hydration mechanisms of ternary Portland cements containing limestone powder and fly ash," *Cem. Concr. Res.*, vol. 41, no. 3, pp. 279–291, 2011, doi: https://doi.org/10.1016/j.cemconres.2010.11.014.

[424] R.-S. Lin, H.-S. Lee, Y. Han, and X.-Y. Wang, "Experimental studies on hydration–strength–durability of limestone-cement-calcined Hwangtoh clay ternary composite," *Constr. Build. Mater.*, vol. 269, p. 121290, 2021, doi: https://doi.org/10.1016/j.conbuildmat.2020.121290.

[425] H. Caetano, G. Ferreira, J. P. C. Rodrigues, and P. Pimienta, "Effect of the high temperatures on the microstructure and compressive strength of high strength fibre concretes," *Constr. Build. Mater.*, vol. 199, pp. 717–736, 2019, doi: https://doi.org/10.1016/j.conbuildmat.2018.12.074.

[426] N. Blouch, K. Rashid, and M. Ju, "Exploring low-grade clay minerals diving into limestone calcined clay cement (LC3): Characterization − Hydration − Performance," *J. Clean. Prod.*, vol. 426, no. September, p. 139065, 2023, doi: 10.1016/j.jclepro.2023.139065.

[427] S. Drissi, C. Shi, N. Li, Y. Liu, J. Liu, and P. He, "Relationship between the composition and hydration-microstructure-mechanical properties of cement-metakaolin-limestone ternary system," *Constr. Build. Mater.*, vol. 302, Oct. 2021, doi:

10.1016/j.conbuildmat.2021.124175.

[428] F. Bahman-Zadeh, A. A. Ramezanianpour, and A. Zolfagharnasab, “Effect of carbonation on chloride binding capacity of limestone calcined clay cement (LC3) and binary pastes,” *J. Build. Eng.*, vol. 52, Jul. 2022, doi: 10.1016/j.jobe.2022.104447.

[429] D. A. Silva, H. R. Roman, and P. J. P. Gleize, “Evidences of chemical interaction between EVA and hydrating Portland cement,” *Cem. Concr. Res.*, vol. 32, no. 9, pp. 1383–1390, 2002, doi: https://doi.org/10.1016/S0008-8846(02)00805-0.

[430] T.-H. Ahn, K.-B. Shim, K.-H. So, and J.-S. Ryou, “Influence of lead and chromium ions as toxic heavy metals between AFt and AFm phases based on C3A and C4A3S,” *J. Ceram. Process. Res.*, vol. 15, pp. 539–544, 2014.

[431] “SOLID STATE *‘Si AND nAl NMR AND FTIR STUDY,” *Science (80-.).*, vol. 25, no. 7, pp. 1435–1444, 1995.

[432] M. Y. A. Mollah, W. Yu, R. Schennach, and D. L. Cocke, “Fourier transform infrared spectroscopic investigation of the early hydration of Portland cement and the influence of sodium lignosulfonate,” *Cem. Concr. Res.*, vol. 30, no. 2, pp. 267–273, 2000, doi: 10.1016/S0008-8846(99)00243-4.

[433] C. F. Chang and J. W. Chen, “The experimental investigation of concrete carbonation depth,” *Cem. Concr. Res.*, vol. 36, no. 9, pp. 1760–1767, 2006, doi: 10.1016/j.cemconres.2004.07.025.

[434] J. M. Marangu, “Effects of sulfuric acid attack on hydrated calcined clay–limestone cement mortars,” *J. Sustain. Cem. Mater.*, vol. 10, no. 5, pp. 257–271, 2021, doi: 10.1080/21650373.2020.1810168.

[435] J. M. Marangu, T. Karanja, and J. Muthengia, “Properties of activated blended cement containing high content of calcined clay,” *Heliyon*, vol. 4, p. e00742, 2018, doi: 10.1016/j.heliyon.2018.e00742.

[436] Y. Dhandapani and M. Santhanam, “Investigation on the microstructure-related

characteristics to elucidate performance of composite cement with limestone-calcined clay combination," *Cem. Concr. Res.*, vol. 129, p. 105959, 2020, doi: 10.1016/j.cemconres.2019.105959.

[437] J. M. Marangu, J. Thiong'o, and W. Muthengia, "Chloride Ingress in Chemically Activated Calcined Clay- Based Cement," *J. Chem.*, vol. 2018, 2018, doi: 10.1155/2018/1595230.

Appendix

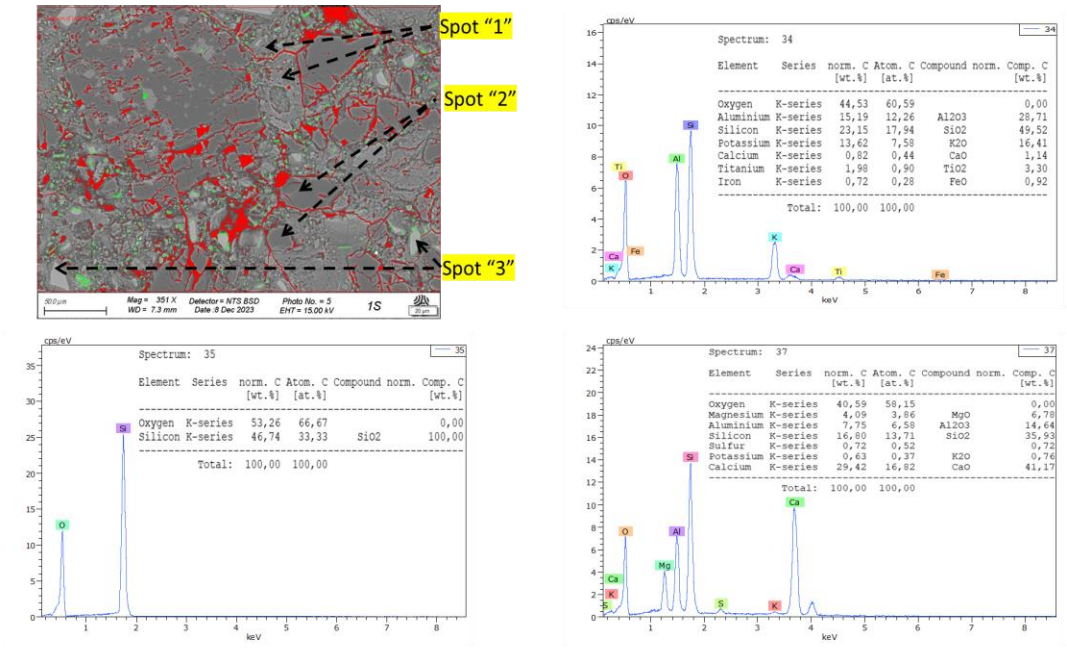

Fig. 149. SEM/EDS for S1.

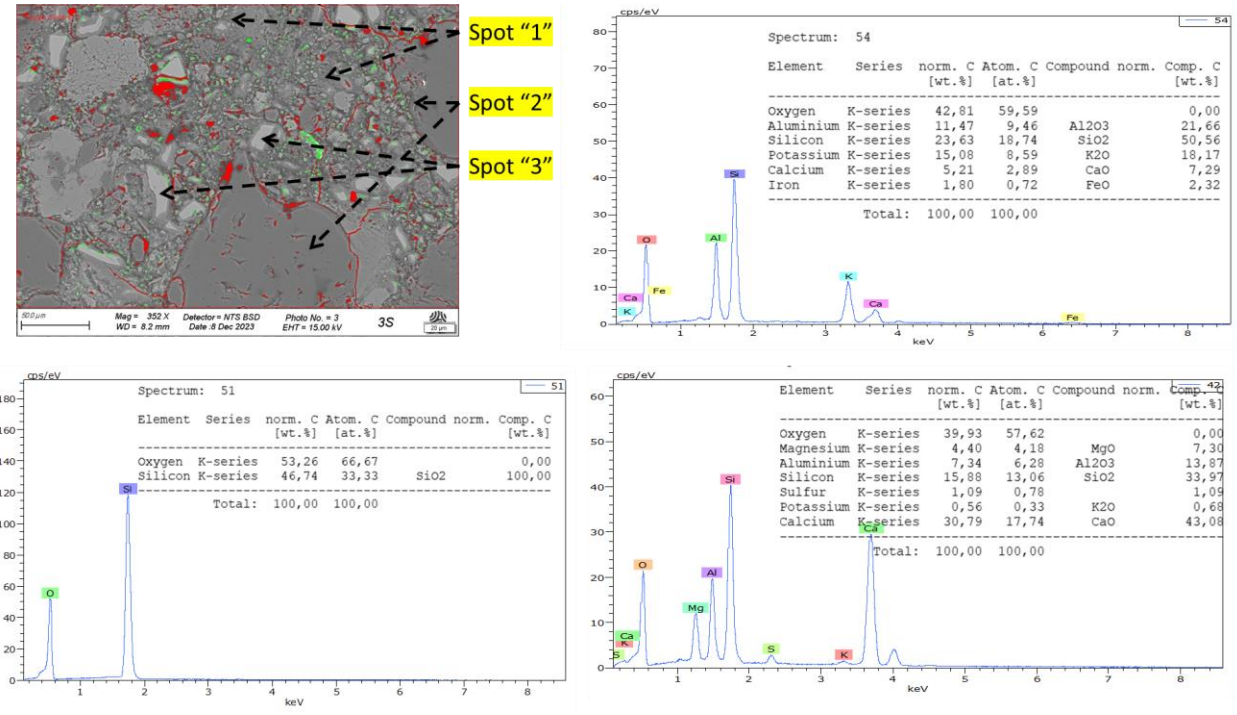

Fig. 150. SEM/EDS for S3.

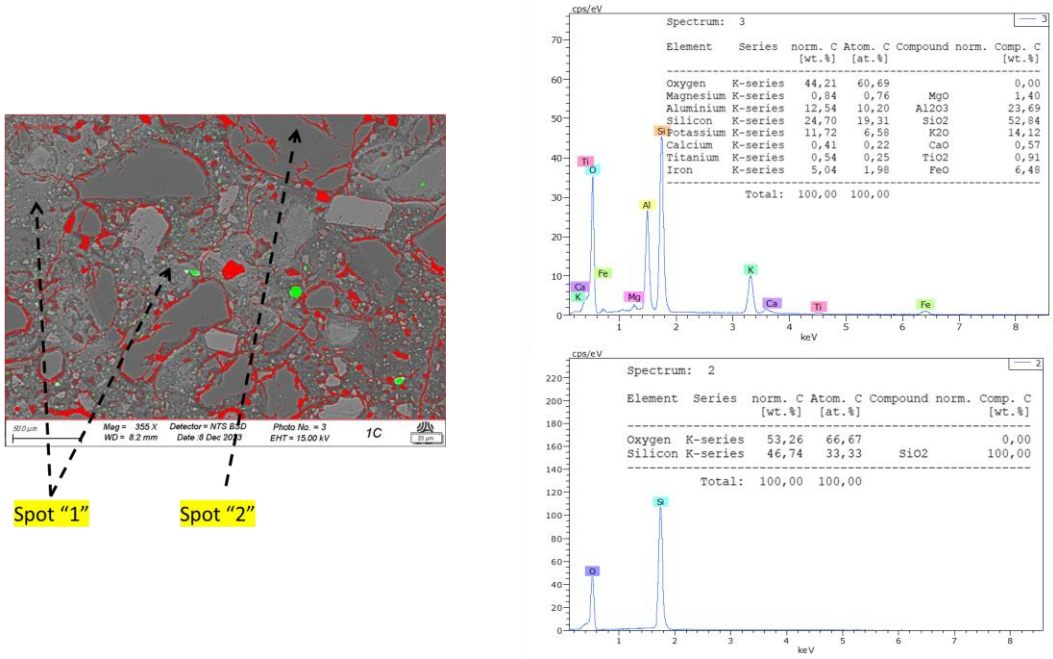

Fig. 151. SEM/EDS for C1.

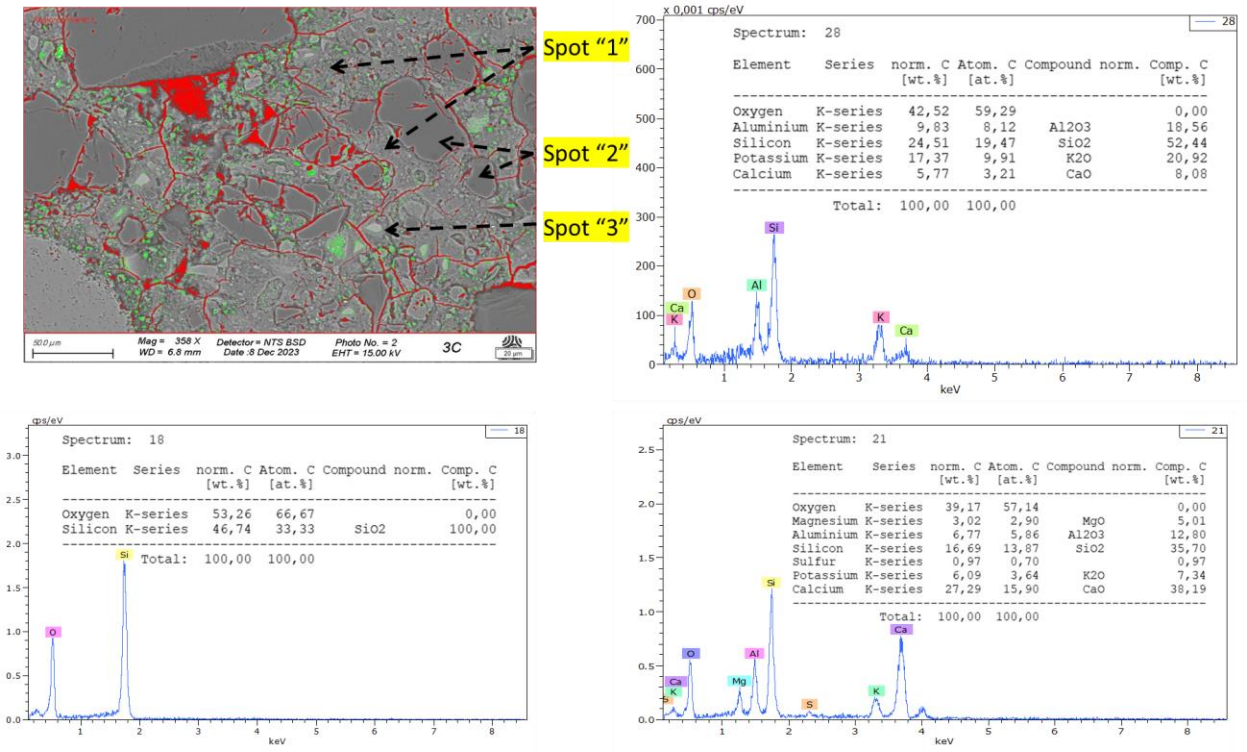

Fig. 152. SEM/EDS for C3.